ISTITUTO ITALIANO DI TECNOLOGIA

A Thesis submitted for the degree of Doctor of Philosophy at

Università degli Studi di Genova

And

Istituto Italiano di Tecnologia

Curriculum: Nanochemistry – XXXVIII cycle

Colloidal Indium Arsenide Quantum dots

Precursor Chemistry, Synthesis strategies, and Core/Shell Architectures for Short-Wave Infrared Optoelectronics

by

Satyaprakash Panda

Supervisor:

Prof. Liberato Manna (IIT)

Co-Supervisor:

Dr. Luca De Trizio (IIT)

Dr. Diego Colombara (UniGe)

Genova, December 2025

Declaration by Supervisor

To Whom It May Concern

As the supervisor of Mr. Satyaprakash Panda, PhD candidate at University of Genova, I hereby certify he has made significant contributions to the research work presented in his doctoral thesis entitled

"Colloidal Indium Arsenide Quantum dots - Precursor Chemistry, Synthesis strategies, and Core/Shell Architectures for Short-Wave Infrared Optoelectronics".

Specifically, with regard to the works presented in Chapter 2 and Chapter 3 of this thesis, which correspond to the following publications:

- *J. Am. Chem. Soc.* **2025**, *147*, 40389−40397
- *Adv. Optical Mater.* **2025**, *13*, e01512

I confirm that Mr. Satyaprakash Panda was the primary contributor to these works. This includes performing the main research activities, such as designing and conducting the study, analyzing the data, and drafting and revising the manuscripts in accordance with the authorship contributions detailed in the respective chapters.

This declaration is provided to fulfill the requirements of University of Genova regarding the incorporation of published works in the doctoral thesis and to confirm the candidate's substantial role in the research presented.

Sincerely,

Prof. Liberato Manna

Genova, December 2025

This page is intentionally left blank

Overview of the Thesis

Short-wave infrared (SWIR) technologies were historically developed for defense, aerospace, and scientific instrumentation, where their ability to operate under low-light conditions and penetrate atmospheric obscurants such as fog, smoke, and haze enabled critical functions including surveillance, night-time imaging, and target identification. For several decades, the development and deployment of SWIR technologies remained largely confined to these specialized sectors. Consequently, epitaxially grown III-V semiconductor detectors, particularly those based on indium gallium arsenide (InGaAs), became the dominant platform for SWIR technologies. In such stringent applications, performance requirements generally outweighed economic constraints, allowing the widespread use of these high-performance but costly detector technologies.

However, in recent years the application landscape of SWIR technologies has expanded significantly beyond traditional defense applications toward industrial inspection, biomedical diagnostics, environmental monitoring, automotive sensing, and consumer electronics. This shift from specialized instrumentation to broader commercial deployment has created a strong demand for scalable and economically viable sensing technologies. The high fabrication costs associated with epitaxial semiconductor growth therefore represent a major barrier to large-scale adoption. Consequently, significant research efforts have focused on developing alternative material platforms capable of enabling lower-cost SWIR devices. Among these approaches, solution-processable nanomaterials have emerged as particularly promising candidates, as they offer compatibility with scalable manufacturing techniques and the potential to substantially reduce device fabrication costs while maintaining the desirable optoelectronic properties required for SWIR applications.

Colloidal indium arsenide (InAs) quantum dots (QDs) are a leading class of RoHS-compliant infrared nanomaterials owing to their large exciton Bohr radius, which enables deep spectral tunability, as well as their high chemical stability. However, the synthesis of high-quality InAs QDs remains challenging because of the strong covalency of the In-As bond and the limited availability of suitable arsenic precursors. Current synthetic strategies rely predominantly on two arsenic sources: tris(trimethylsilyl)arsine ($(TMS)_3$-As) and tris(dimethylamino)arsine (amino-As). Although substantial progress has been achieved using both approaches, each route still suffers from intrinsic limitations associated with precursor chemistry, reaction scalability and reproducibility, which collectively hinder the broader adoption of InAs QDs in commercial SWIR technologies.

This thesis addresses the major bottlenecks associated with both the $(TMS)_3$-As and amino-As routes by introducing mechanistic insights and innovative scientific modifications. Through these advancements, the work establishes pathways for producing high-quality InAs QDs with excitonic absorption and emission in the SWIR region, thereby laying the groundwork for scalable and industrially relevant InAs QD platforms for future infrared optoelectronic applications.

The thesis is divided into three chapters:

Chapter 1 provides the scientific and technological context for this thesis by introducing the SWIR spectral region and its rapidly expanding relevance across a wide range of applications, which is driving increasing commercial and consumer demand. It discusses current market trends and highlights how today's SWIR technologies rely mainly on expensive epitaxial III-V semiconductors, motivating the need for solution-processable SWIR nanomaterials. The chapter then provides a brief history of colloidal nanomaterials and outlines the key principles governing their size-dependent properties, surface chemistry, ligand interactions, core-shell structures, and common synthesis strategies. Building on this foundation, it reviews the classes of nanomaterials that operate in the SWIR region, their historical development, and the role of RoHS compliance in guiding material choices.

Finally, the chapter focuses on colloidal InAs QDs, summarizing their synthetic historical background, the precursors that have enabled their synthesis, and the remaining challenges that motivate the studies presented in Chapters 2 and 3.

In **Chapter 2**, we investigate the synthesis of InAs QDs using the $(TMS)_3$-As precursor and examine the mechanistic limitations associated with the procedures commonly employed in the literature. Although state-of-the-art methodologies based on this precursor can produce high-quality InAs QDs with excellent optical properties, they are hampered by the *in-situ* generation of water during the reaction, which necessitates extensive post-synthetic purification and complicates the workflow. Through a combination of optical, structural, and NMR analyses, we show that the commonly employed dioctylamine (DOA)-oleic acid system undergoes acid-base condensation, leading to the in-situ generation of water, that reacts with the silyl-precursors leading to TMS-derived impurities that contaminate the QDs. By substituting DOA with a tertiary amine, namely trioctylamine (TOA), we suppress these side reactions and obtain cleaner, higher-quality InAs QDs with markedly improved optical properties. The chapter further presents a systematic comparison between the conventional and modified synthetic approaches, providing clear experimental evidence that the proposed strategy effectively resolves the water-generation problem in a mechanistically informed manner.

Despite the improved reaction control and enhanced optical quality achieved using the $(TMS)_3$-As precursor, its high cost and extreme pyrophoricity pose significant challenges for large-scale and industrial implementation. These limitations motivate the work presented in Chapter 3, where we explore a safer and more economically viable arsenic precursor system as an alternative route for the synthesis of high-quality InAs quantum dots.

In **Chapter 3** we investigate the synthetic route based on amino-As precursor. Although this precursor has been explored as a safer alternative to $(TMS)_3$-As, its use still presents intrinsic challenges that hinder the controlled growth of large InAs quantum dots. In this route, a reducing agent is required to convert As^{3+} to As^{3-}, and the strength and stability of this reagent play a critical role in determining the nucleation and growth behavior of the nanocrystals. Conventional

reducing agents are typically supplied in low-boiling solvents, which can cause boiling bursts during high-temperature injections, leading to safety concerns and poor reaction reproducibility. In this chapter, we introduced a new reducing agent, an amino-alane (TOA-AlH_3), that overcomes key limitations of the amino-As route and enables more stable reaction conditions at elevated temperatures. Using this reagent in both hot-injection and seeded-growth methods, we synthesize large, monodisperse InAs cores that, after ZnSe shelling, exhibit efficient SWIR photoluminescence. The chapter also shows that TOA-AlH_3 is fully compatible with $ZnCl_2$, an essential additive for achieving high PLQY in InAs@ZnSe QDs.

Together, these topics establish the scientific framework for the thesis, which aims to develop improved precursor chemistries and synthetic strategies for colloidal InAs quantum dots and their core/shell architectures, enabling high-quality SWIR nanomaterials suitable for future optoelectronic technologies.

Table of Contents

List of Figures

Chapter 1. Introduction

1.1 Infrared and Short-Wave Infrared region of the spectrum

The short-wave infrared (SWIR) region of the spectrum nominally spans the wavelength range of 1000-2500 nm (Figure 1.1.1), bridging the near and mid infrared (NIR and MIR, respectively) regions. This spectral window represents a transitional domain where light retains the reflectance characteristics of visible radiation while exhibiting the propagation advantages of infrared light.[1] SWIR photons penetrate deeper than visible light through scattering and absorbing media such as fog, smoke, or biological tissues while preserving high image contrast and spatial detail (see Section 1.1.1 for further details). Because of these properties, SWIR has become indispensable in remote sensing, industrial inspection, telecommunications, and biomedical imaging applications to cite a few.[2] Furthermore, SWIR radiation is invisible to the human eye and can be used safely at relatively high-power levels, allowing illumination from eye-safe sources such as passive atmospheric 'airglow' and active laser emitters, making it ideal for applications such as Light Detection and Ranging (LiDAR), night-vision, and free-space optical communications. These combined properties make the SWIR window one of the most versatile and technologically relevant regions of the electromagnetic spectrum.

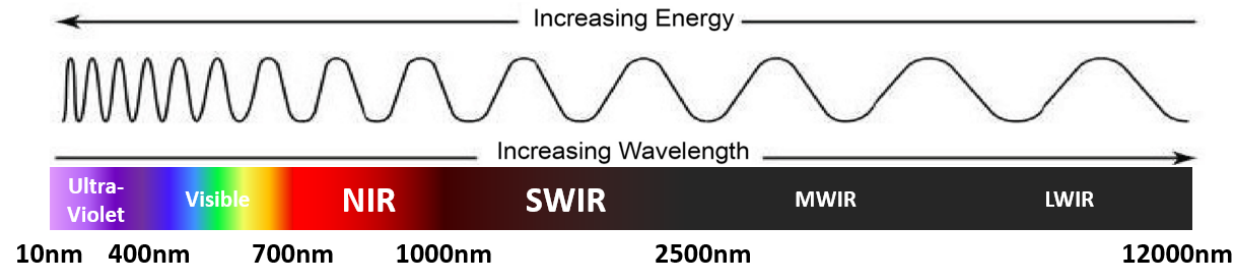

***Figure 1.1.1**. Schematic representation of the electromagnetic spectrum highlighting the NIR and SWIR regions. Wavelength increases from left to right, while photon energy decreases accordingly.*

1.1.1 Physical basis and the advantages

The broad utility of SWIR stems from several fundamental optical and physical advantages that distinguish it from both visible and longer-wavelength infrared radiation.

Reduced light scattering and deeper penetration than visible light.

Light scattering decreases strongly with increasing wavelength ($\propto 1/\lambda^4$) allowing SWIR photons to penetrate deeper than visible ones into turbid or heterogeneous media such as fog, aerosols, or biological tissue[3]. This leads to clearer imaging and higher contrast under degraded visibility, enabling applications where visible cameras fail.

Reduced autofluorescence in biological tissues.

Biological tissues exhibit intense autofluorescence when probed with visible or NIR light, but this effect diminishes drastically when employing SWIR light.[4] Also, biological tissues are transparent

in specific IR regions such as 1000-1350 and 1500-1700 nm. Consequently, SWIR imaging provides high signal-to-noise ratios in fluorescence microscopy and deep-tissue visualization.

Chemical specificity via overtone absorption

SWIR wavelengths correspond to overtone and combination band absorptions of O-H, C-H, and N-H bonds, which are ubiquitous in organic materials, enabling non-destructive determination of moisture, lipid, and protein content in applications ranging from medical diagnostics to agricultural monitoring of crops, fruits and vegetables[5].

Atmospheric transparent windows

Importantly, the SWIR range includes atmospheric and optical transmission windows (1.0-1.35 µm, 1.55 µm, 2.1-2.3 µm) that overlap with the low-loss telecom bands, allowing the use of mature and cost-effective fiber-optic and detector technologies[6] for high performance imaging, sensing, and communication systems.

Eye safety

Light beyond 1.4 µm is strongly absorbed in the cornea and lens rather than the retina (Figure 1.1.2), making it eye-safe at intensities much higher than those permitted in the visible or NIR ranges. This allows high-power illumination for LiDAR, active imaging, and covert surveillance[7].

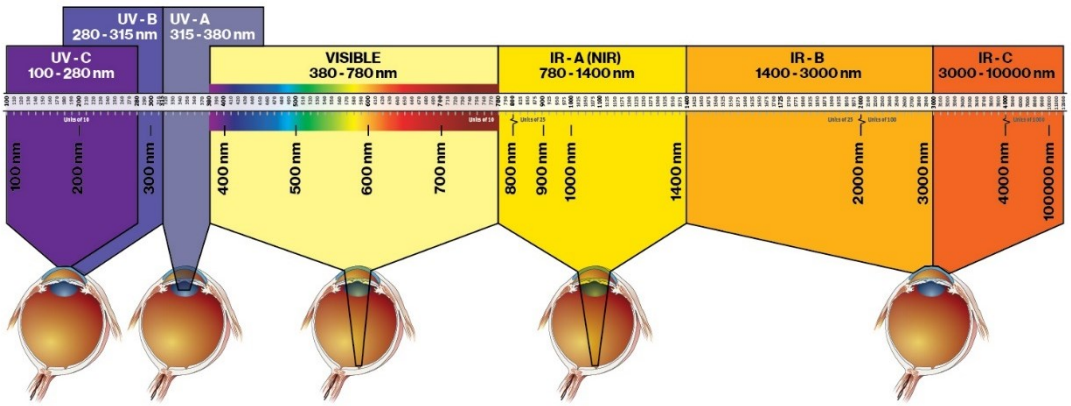

Figure 1.1.2: *Depth of penetration of electromagnetic radiation in the human eye. Adapted from ref[8].*

1.1.2 SWIR in optical and free-space communications.

Global data transmission relies on extremely low-loss propagation in silica optical fibers, whose attenuation minimum occurs near 1.3 µm and 1.55 µm, both within the SWIR window. At about 1.55 µm, fiber losses reach 0.2 dB km^{-1}, close to the theoretical Rayleigh scattering limit (Figure 1.1.3 a, b)[9]. The chromatic dispersion of silica at this wavelength also supports dense wavelength-division multiplexing and ultrahigh-bit-rate transmission. As a result, the global telecommunication infrastructure, including lasers, erbium-doped fiber amplifiers[10], photodiodes, modulators and multiplexers, is fundamentally working in the SWIR[6, 11].

The advantages of the SWIR window extend beyond guided optics to free-space optical (FSO) communication, where laser beams transmit data through the atmosphere between terminals (Figure 1.1.3 c)[12]. Operating around 1.55 µm, FSO systems enable high-capacity links for building-to-building, aircraft-to-ground and satellite communication[13]. Because of reduced scattering and favorable eye-safety limits around 1.55 µm, SWIR wavelengths enable more reliable signal transmission under adverse atmospheric conditions[14, 15]. SWIR-based FSO systems also use mature and cost-effective telecom components, including InGaAs detectors working at room-temperature, which provide reliable performance without the cryogenic cooling required for mid-infrared sensors.

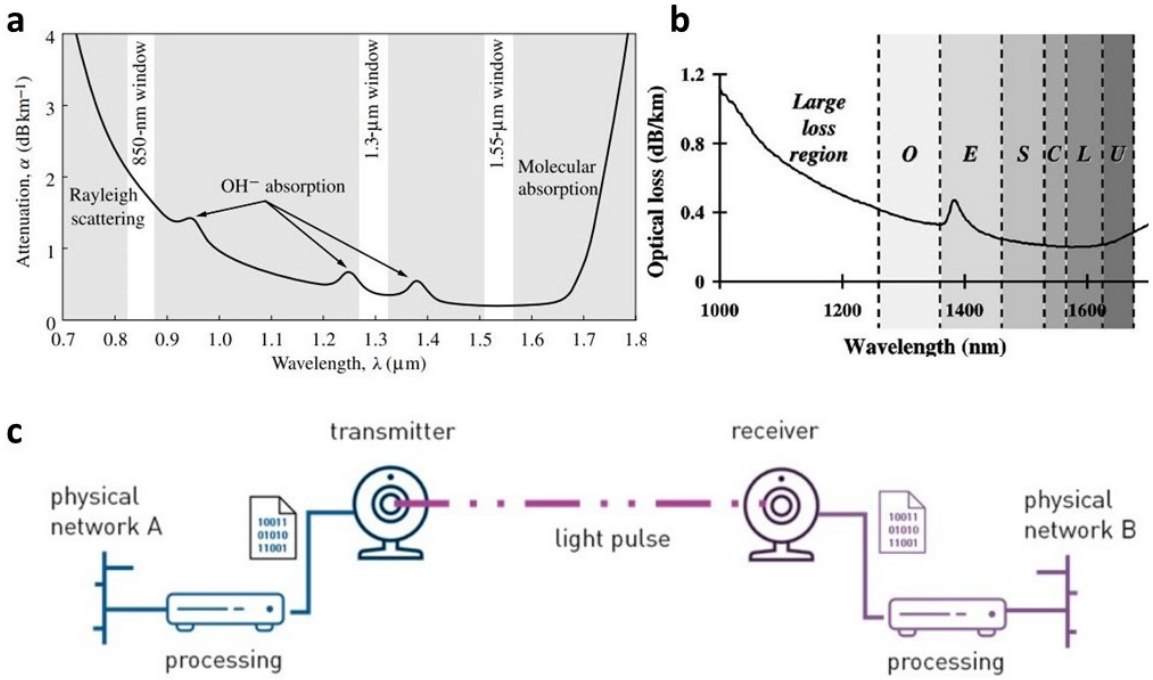

Figure 1.1.3. *(a) Optical attenuation in silica fibers as a function of wavelength, indicating the key loss mechanisms and (b) the corresponding low-loss transmission windows that define the conventional telecom bands (O, E, S, C, L, U) used for signal transmission[6]. (c) Schematic illustration of a Free Space Optical communications system[16].*

1.1.3 SWIR in industrial quality control and product inspection.

SWIR imaging and spectroscopy provide powerful tools for industrial quality control by enabling non-destructive visualization of internal features and chemical contrast that are often inaccessible under visible illumination.

Photovoltaic and semiconductor industry.

The semiconductor and photovoltaic industries rely extensively on SWIR imaging for non-destructive inspection and process control (Figure 1.1.4). Since silicon becomes transparent above ~1150 nm, SWIR cameras can detect internal inclusions, voids, or misaligned layers that

are invisible in the visible range, enabling inline wafer alignment, crystal inspection, and early detection of defects that could damage diamond saws during slicing[2, 17]. In photovoltaics, SWIR electroluminescence and photoluminescence imaging (1100-1550 nm) provide rapid, millisecond-scale mapping of microcracks, dislocations, and shunts, while supporting quality control of silicon wafers[18, 19], solar modules[20], and lithium-ion battery components[21] without physical contact or material destruction (Figure 1.1.4).

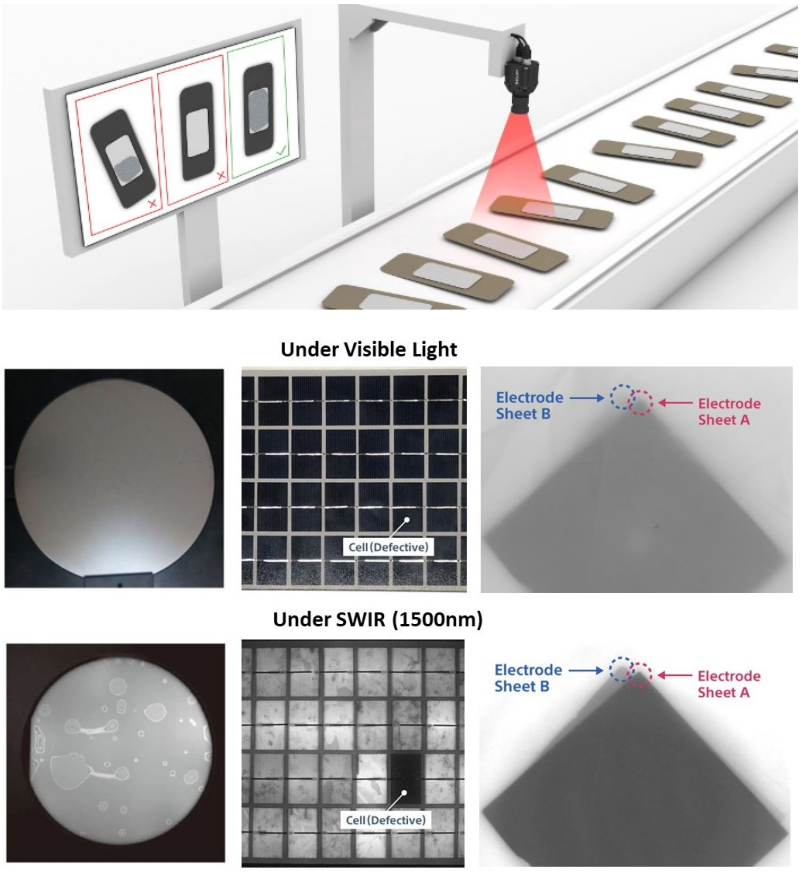

Figure 1.1.4. *(top) Schematic of an industrial inspection setup using machine-vision imaging to identify defective components on a production line[22]. Comparison of visible and SWIR (1500nm) imaging for defect detection showing enhanced contrast of subsurface features, defective cells, and electrode layers under SWIR illumination[23].*

Food industry.

The food industry increasingly employs SWIR hyperspectral imaging (HSI) for non-destructive, real-time quality control (Figure 1.1.5)[24]. Operating typically between 900 and 1700 nm, SWIR enables rapid chemical and structural assessment by exploiting molecular overtone absorptions of O-H, C-H, and N-H bonds[25, 26]. Water absorption peaks near 1450 nm and 1940 nm reveal local variations in moisture, allowing early detection of bruising, ripeness, or fungal damage in fruits and vegetables (Figure 1.1.5 c)[27]. Similarly, SWIR imaging quantifies fat and protein content in cereals and meat[28], detects foreign contaminants such as plastics, stones, or bone fragments,

and differentiates between organic and inorganic materials (Figure 1.1.5 c)[23]. Commercial systems achieve over 95% accuracy in sorting high value products such as dates at industrial line speeds[29]. Moreover, advanced SWIR-HSI combined with chemometric models enables rapid detection of harmful additives (e.g., melamine) in powdered foods[30], offering a safe and efficient alternative to conventional chemical analysis[31].

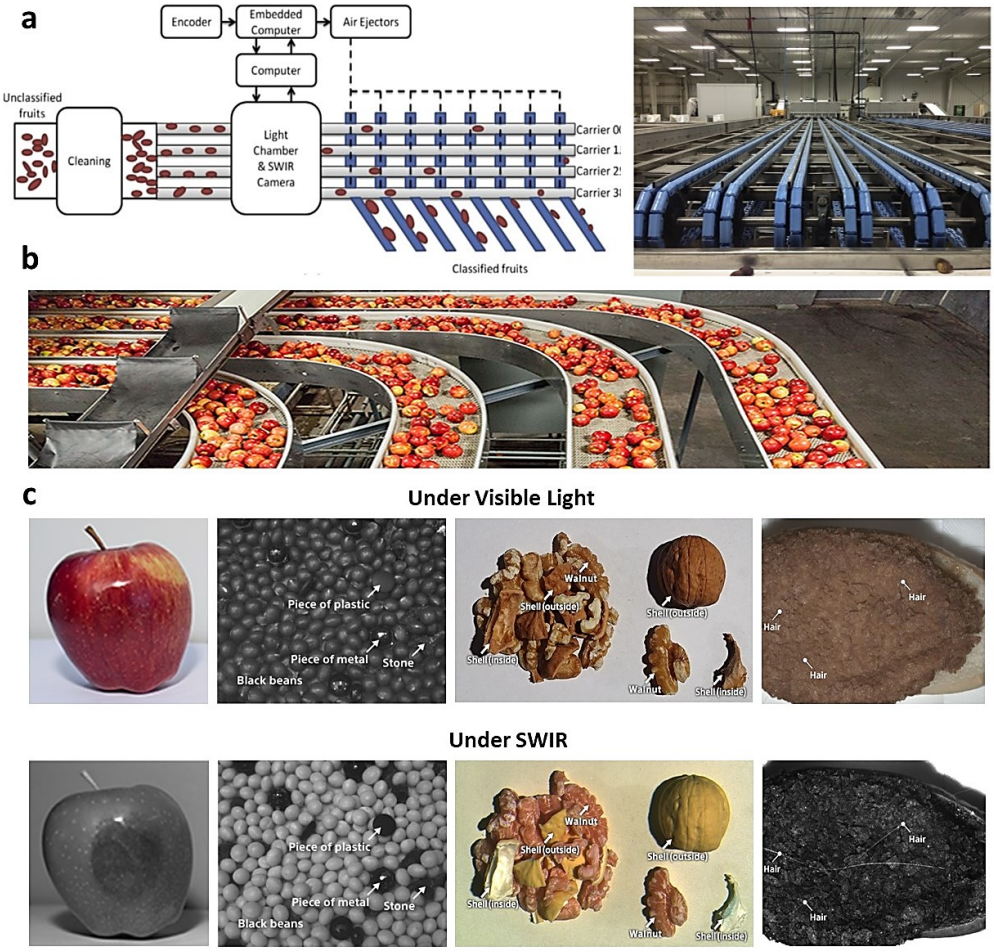

Figure 1.1.5. *(a) Schematic of an automated fruit-sorting system integrating a SWIR imaging module[29], with (b) field operational view. (c) Comparison of visible-light and SWIR (1500 nm) imaging for detecting contaminants and internal defects in food products[23, 32].*

Pharmaceutical industry

SWIR-HSI are vital tools for process analytical technology and real-time quality assurance[33]. SWIR enables non-destructive quantification of active pharmaceutical ingredient distribution, coating uniformity, and moisture content in tablets and capsules[34]. It is extensively used for content uniformity testing, ensuring consistent dosage with prediction errors below 2%. SWIR-HSI also maps API distribution and detects defects or contaminants during production[35, 36]. Integrated into continuous manufacturing, SWIR provides real-time feedback control, enhancing process efficiency and supporting the quality by design framework[37].

Plastic recycling industry

The plastic recycling industry employs SWIR-HSI for rapid, non-destructive polymer identification and automated sorting[38]. Each polymer type like polyethylene terephthalate (PET), polyvinyl chloride (PVC), polyethylene (PE), and polypropylene (PP) exhibits a unique spectral fingerprint in the 1000-2500 nm range, enabling accurate identification and sorting independent of color or contamination[39]. Integrated with high-speed imaging and air-jet systems, SWIR-based sorting prevents cross-contamination, detects hazardous additives, and ensures high-purity recyclates, promoting efficient closed-loop recycling and advancing the circular economy[40, 41].

Glass and metal industry

SWIR imaging is widely applied for high-temperature processes monitoring and defect detection. SWIR cameras can visualize temperature gradients, cooling uniformity, and surface imperfections in materials at 250-800°C[2]. In the glass industry, SWIR systems monitor molten streams, detect inclusions, cracks, and bubbles, and ensure uniform wall thickness in bottles while imaging through flames and glass surfaces[42]. In metal processing, SWIR cameras provide emissivity-independent measurements of weld pools, slag, and oxidation layers, enabling precise evaluation of melt pool uniformity, surface defects, and coating variations[2, 43].

1.1.4 SWIR in agriculture and forestry

SWIR imaging and spectroscopy play a crucial role in precision agriculture, forestry, and soil management due to their sensitivity to moisture and biochemical composition[44]. Reflectance in the 1400-1600 nm range correlates directly with leaf and soil moisture, enabling detection of crop water stress and optimization of irrigation and nutrient management. Absorption features near 2100-2300 nm, associated with lignin and cellulose, provide insight into plant health, biomass, and residue cover[44]. In forestry, SWIR spectroscopy can be used to quantify wood moisture, density and the cellulose-to-lignin ratio, supporting timber quality evaluation without destructive sampling. Furthermore, satellite and UAV-based SWIR sensors (e.g., Landsat, and Sentinel)[45, 46] enable large-scale mapping of soil carbon, non-photosynthetic vegetation, and microplastic contamination, contributing to sustainable agriculture and climate-resilient land management[47].

1.1.5 SWIR in anticounterfeiting, surveillance and biometric authentication

SWIR imaging can distinguish inks, coatings, and polymers that appear identical under visible light but exhibit distinct spectral fingerprints under SWIR light, enabling detection of forgeries in documents, currency, and packaging. Hyperspectral SWIR systems provide rapid, non-contact verification by capturing subtle reflectance and absorption differences, supporting automated forensic identification of counterfeit materials[48]. Moreover, SWIR-emissive materials such as quantum dot inks enable covert tagging through wavelength- or lifetime-encoded luminescence, creating machine-readable markers for product authentication, pharmaceutical traceability, and high-value asset protection (Figure 1.1.6 a-c).

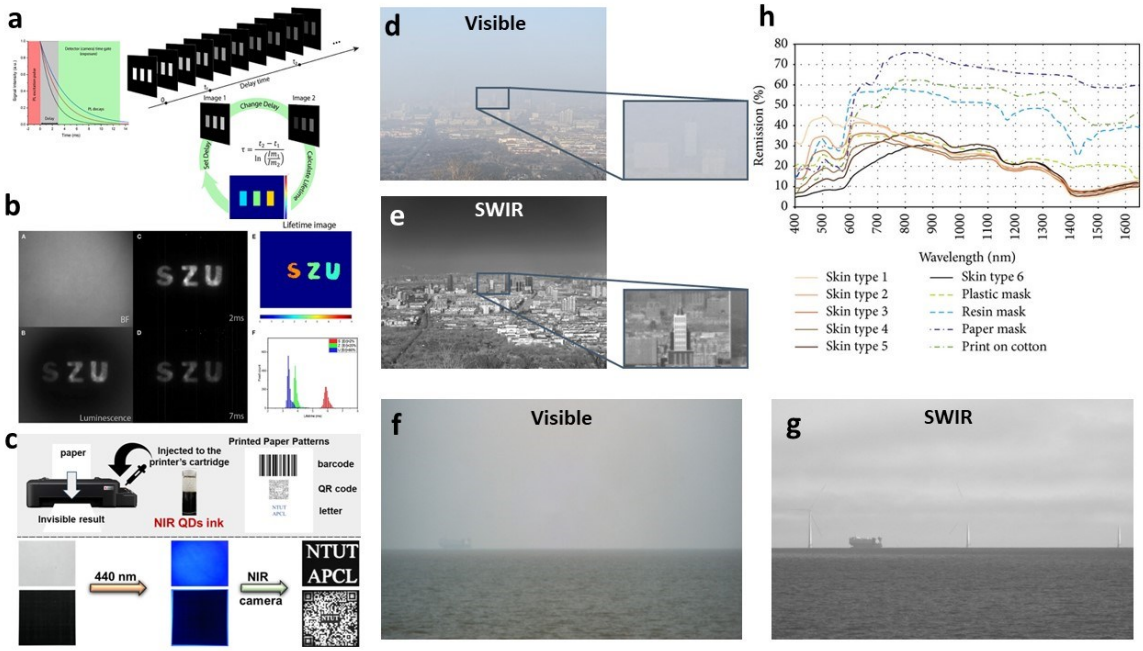

Figure 1.1.6. *(a, b) Time-domain PL filtering, gated imaging, and rapid lifetime-based authentication using SWIR-emissive materials. (c) Inkjet-printed NIR-emissive patterns and QR codes visualized using infrared imaging[48, 49]. (d-g) Visible versus SWIR imaging in haze and fog, with SWIR offering superior contrast and long-range visibility[23]. (h) Spectral reflectance profiles of human skin (types I-VI) and various mask materials, illustrating strong contrast differences in the SWIR range relevant for spoof detection and biometric security[50].*

SWIR imaging has become increasingly important in surveillance and security systems due to its ability to function under both passive and active illumination. In passive mode, cameras exploit atmospheric airglow for night vision in complete darkness, while under active illumination, eye-safe lasers at 1.55 µm enable covert, long-range imaging through haze, fog, or glass[51]. These capabilities make SWIR suitable for border monitoring, maritime observation, and aerial reconnaissance under adverse conditions (Figure 1.1.6 d-g).

In biometric applications, SWIR enhances identification accuracy by offering deeper tissue penetration and reduced sensitivity to melanin pigmentation, enabling consistent iris and facial recognition across all skin tones[52]. The distinct absorption and reflection characteristics of human skin, hair, and subdermal structures in this range allow imaging of vein patterns and subsurface features that are difficult to replicate artificially[50]. These properties enhance liveness detection, preventing fraud using printed images or silicone masks (Figure 1.1.6 h)[53].

1.1.6 SWIR in LiDAR and consumer electronics

SWIR technology has become a cornerstone of modern Light Detection and Ranging (LiDAR) systems, offering key advantages in eye safety, atmospheric transmission, and imaging performance[54]. SWIR-based LiDAR employs high-power, eye-safe lasers that enable long-range detection and high depth resolution under Class 1 safety standards. Because SWIR light scatters less it provides superior signal quality and reliable operation in degraded visibility. Range-gated

detection further improves contrast and accuracy by filtering backscatter from fog or dust[55]. These features make SWIR indispensable for autonomous and driver-assistance systems, where combining reflectance imaging with distance data enhances perception, obstacle detection, and navigation in complex environments. Cameras operating near 1.55 µm can image through glass, detect pedestrians, and maintain visibility in low light or haze, complementing long-wave thermal sensors for safe, all-weather driving[56].

Beyond automotive applications, SWIR LiDAR and imaging systems are increasingly integrated into consumer electronics. Compact time-of-flight and micro-LiDAR sensors in robotic vacuum cleaners, home-mapping robots enable precise 3D mapping and obstacle avoidance, while SWIR imaging in security systems enhances monitoring performance under low-light or obscured conditions. SWIR modules in smartphones, and tablets support augmented reality, gesture and facial recognition, and in wearables for non-invasive monitoring of glucose, blood oxygen, and vascular health, driving intelligent, connected consumer technologies[57].

1.1.7 SWIR in biological and biomedical imaging

SWIR imaging and spectroscopy have become powerful tools in biological and biomedical research owing to their superior optical properties compared to visible and near-infrared (NIR-I, 700–950 nm) based ones. In the SWIR range, known in biology as the second near-infrared (NIR-II) window, photon scattering and tissue autofluorescence are greatly reduced, while absorption from chromophores such as hemoglobin is minimal and water absorption remains moderate (Figure 1.1.7 a-c)[5]. These conditions enable deep tissue penetration and high-contrast visualization of vascular structures, lymphatic networks, and internal organs. In vivo fluorescence imaging using SWIR emitters/probes enables deep-tissue angiography, lymphatic mapping, and organ-level imaging with high signal-to-background ratios and fast frame rates allowing real-time acquisition (Figure 1.1.7 d)[58]. Beyond fluorescence, SWIR reflectance and absorption imaging exploit characteristic absorptions of water (around 1450 and 1940 nm), lipid (around 1700nm), and collagen (which fall around 1150-1300 and 1600-1700 nm), providing intrinsic contrast for assessing hydration, lipid accumulation, and collagen denaturation. This capability enables non-contact evaluation of burn depth, tissue viability, and pathological changes such as edema and atherosclerosis[59]. Recent advances in InGaAs detectors and portable fiber-probe systems have expanded access to SWIR-based in vivo and ex vivo diagnostics, positioning it as an essential modality for quantitative biomedical imaging and clinical monitoring.

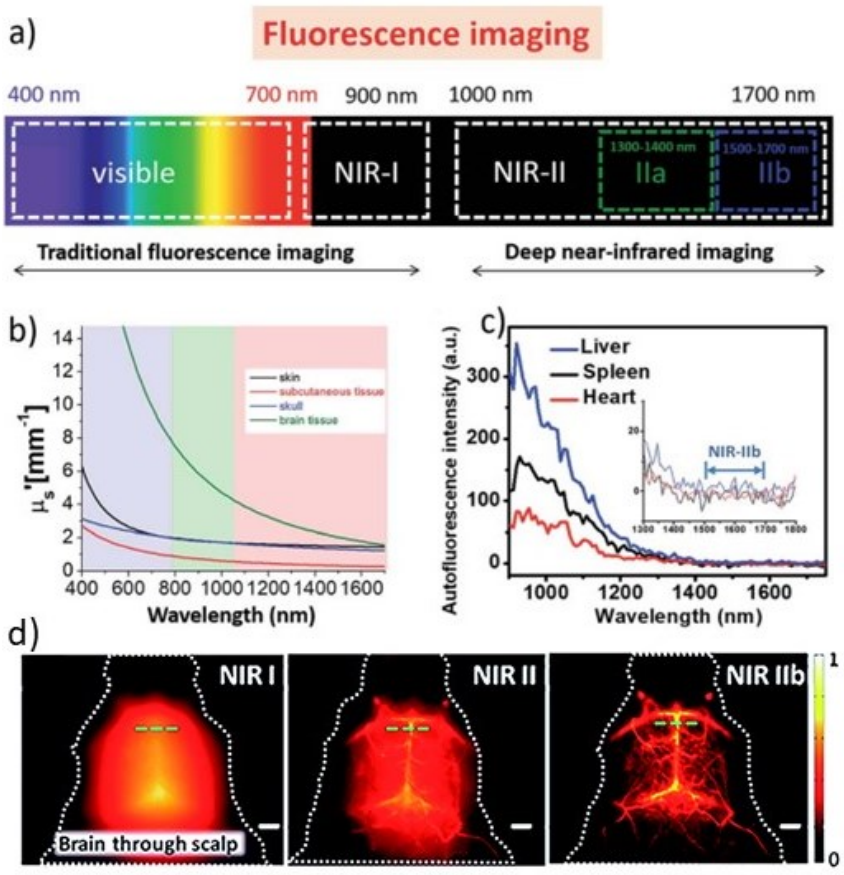

Figure 1.1.7. *(a) Wavelengths for fluorescence imaging, (b) Reduced scattering coefficients of skin, brain tissue, skull, and subcutaneous tissue from 400-1700 nm. (c) Autofluorescence spectra of ex vivo mouse liver, spleen, and heart. (d) In vivo fluorescence images of mouse brain vasculature acquired through the scalp in NIR-I, NIR-II, and NIR-IIb*[58]*.*

1.2 Current market trends and outlook

The SWIR technology market is undergoing rapid expansion, transitioning from specialized military applications to broad adoption across industrial, biomedical, and consumer sectors. Valued at approximately USD 603 million in 2024, the global SWIR market is projected to reach USD 1.2 billion by 2030, growing at a compound annual growth rate of about 12% (Figure 1.2.1). This growth is driven by the increasing use of SWIR systems in a wide range of applications which are explained from Section 1.1.2 to section 1.1.7.[60]

A key driver of this expansion is the industrial sector, which accounted for 39.14% of the global SWIR market share in 2024[61]. In manufacturing environments, SWIR cameras support reliable, high-throughput inspection and monitoring, making them essential in sectors mentioned previously in section 1.1. Concurrently, sensor miniaturization and cost reductions, particularly in indium gallium arsenide (InGaAs) and quantum-dot-based detectors, are accelerating SWIR's integration into autonomous vehicles, robotics, and consumer electronics.

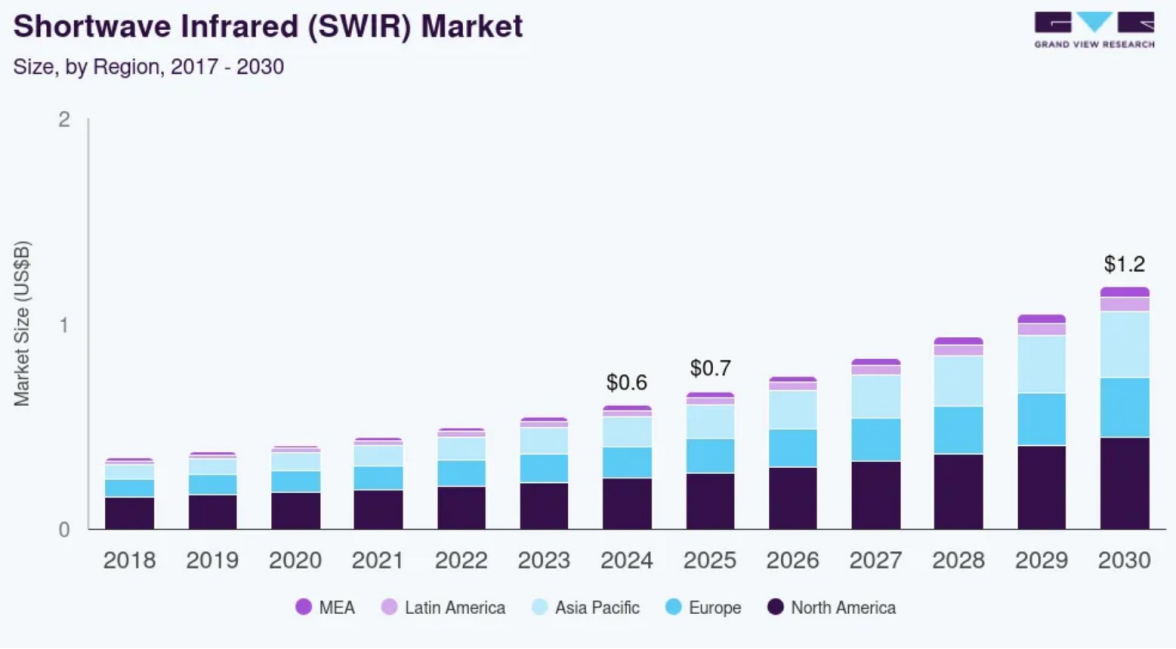

Figure 1.2.1. *Global SWIR market size by region from 2018 to 2030, showing steady growth across all major markets[60].*

A growing synergy between SWIR and artificial intelligence is further driving innovation, enabling automated defect recognition, agricultural analytics, and real-time surveillance[62]. The ongoing development of compact, lightweight SWIR cameras supports portable applications, including environmental monitoring and wearable biomedical diagnostics[63]. By 2030, SWIR technology is expected to achieve mainstream commercial adoption, propelled by technological advancements, regulatory support, and diversification across multiple sectors, positioning it as one of the most dynamic segments in the global photonics industry.

1.2.1 Growth hindrances and possible solution

Despite the rapidly increasing demand for SWIR technologies across industrial, biomedical, and consumer sectors, their widespread adoption is still limited by factors such as high system cost, limited spectral range, integration difficulties, low market awareness, and growing geopolitical complexities associated with the supply of critical raw materials. The foremost limitation, however, lies in the high manufacturing cost of conventional SWIR detectors, which rely on epitaxially grown materials such as InGaAs or HgCdTe that require expensive substrates and complex fabrication processes. InGaAs wafer costs, often exceeding USD 5,000 per wafer, significantly elevate the bill of materials, restricting commercial use to high-value segments such as defense optics and semiconductor inspection[61].

1.2.2 Conventional epitaxial manufacturing

SWIR detectors and cameras have been conventionally fabricated using epitaxially grown semiconductors such as InGaAs, InSb, and HgCdTe on lattice-matched substrates like InP or GaAs, typically via molecular beam epitaxy (MBE) or metal-organic chemical vapor deposition

(MOCVD). Although these methods ensure excellent crystal quality and low dark current, it is complex, costly, and difficult to scale due to the need for ultra-high vacuum conditions, high temperatures, and sophisticated precursor control[64].

A major contributor to the high cost comes also from the reliance on expensive, small-diameter substrates such as InP wafers, typically limited to 3-4 inches in size, which limit throughput and yield due to brittleness and defect sensitivity. In addition, electrical interfacing between the detectors and silicon readout integrated circuits is achieved through flip-chip bonding using indium bumps, a complex and alignment-sensitive process that raises fabrication costs and lowers production yield (Figure 1.2.2)[64, 65].

In addition to economic barriers, epitaxial SWIR materials exhibit restricted bandgap tunability. For instance, lattice-matched $In_{0.53}Ga_{0.47}As$/InP has a fixed cutoff near 1.7 µm, while extending to longer wavelengths via indium-rich alloys introduces lattice mismatch and dislocations, increasing dark current and degrading performance[66].

Collectively, these limitations in cost, scalability, spectral tunability, and integration render epitaxial manufacturing unsuitable for low-cost, large-scale SWIR production, confining its use mainly to defense and specialized industrial applications.

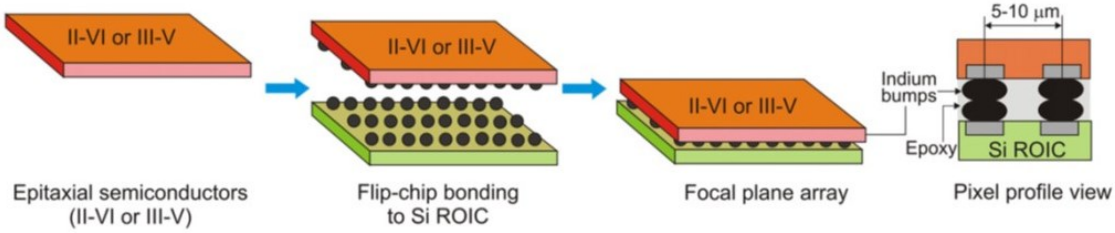

Figure 1.2.2. *Schematic of II-VI or III-V semiconductor layers being flip-chip bonded onto a silicon readout integrated circuit (ROIC) to form a focal plane array, with a pixel cross-section showing indium bump interconnects. Adapted with permission from ref.[64]*

1.2.3 Manufacturing based on Colloidal QDs (CQDs)

Colloidal QDs (CQDs) offer a transformative approach to SWIR photodetection by providing a low-cost, scalable, and complementary metal-oxide semiconductor (CMOS)-compatible alternative to conventional epitaxially grown semiconductors. They are synthesized via wet-chemical methods, where careful control of precursor concentration, ligand environment, and reaction temperature allows precise tuning of their size and composition. This synthetic flexibility enables direct bandgap engineering across the SWIR range (1.0-2.5 µm), allowing tailored spectral response beyond the inherent limitations of lattice-matched epitaxial materials[64, 67].

One of the main advantages of CQDs is their excellent solution processability, allowing film deposition through simple, low-temperature methods such as spin coating, dip coating, or inkjet printing on large-area and flexible substrates for cost-effective, scalable manufacturing (Figure 1.2.3)[67]. CQDs can be directly deposited onto silicon readout integrated circuits in a back-end-of-line process, eliminating the need for costly indium bump bonding used in epitaxial systems. This

monolithic integration simplifies fabrication, increases pixel density, and supports submicron pixel sizes with reduced parasitic capacitance. Furthermore, CQD films can be printed on flexible or transparent substrates using roll-to-roll methods, enabling lightweight and portable SWIR sensors for next-generation autonomous, consumer, and biomedical technologies (Figure 1.2.4).

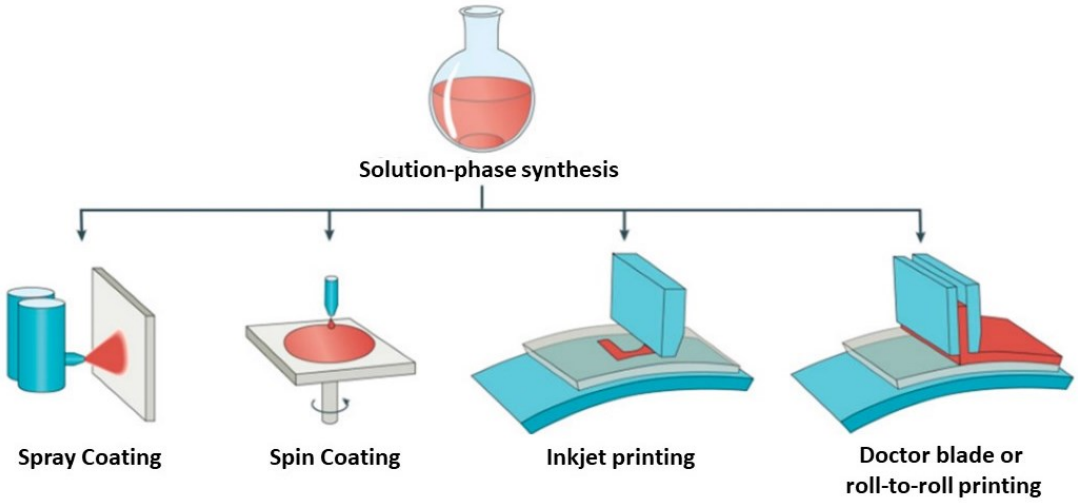

Figure 1.2.3. *Solution-phase synthesis followed by various deposition techniques for forming thin films, including spray coating, spin coating, inkjet printing, and doctor-blade or roll-to-roll coating*[67].

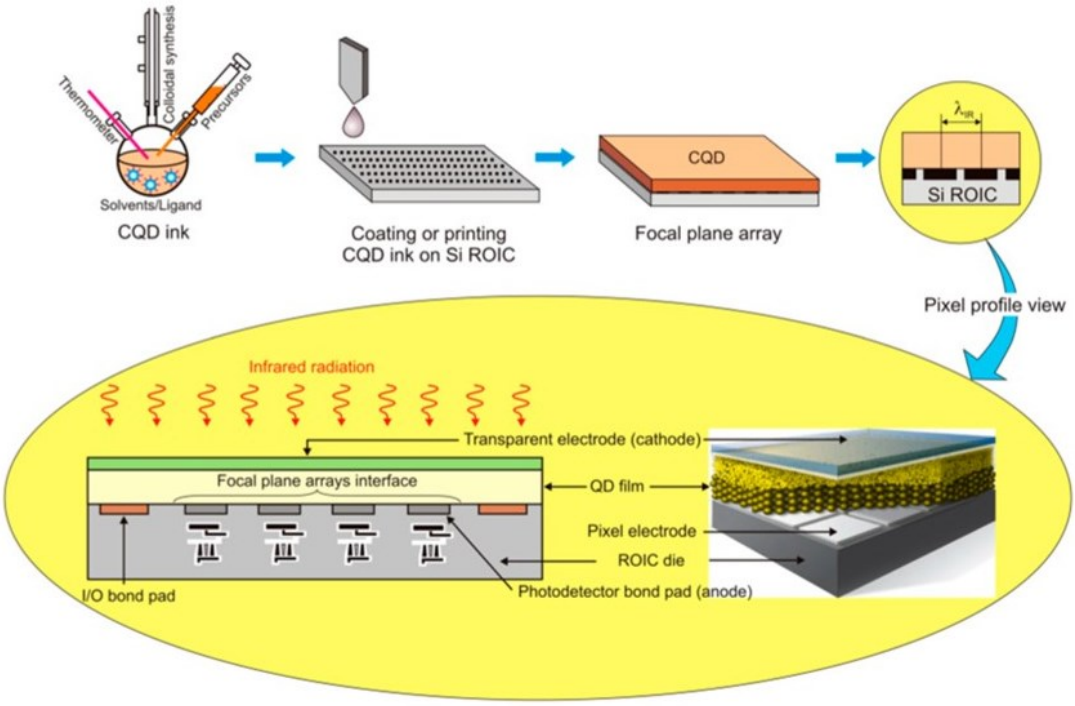

Figure 1.2.4. *Process flow for CQD focal plane arrays, from CQD ink synthesis to printing on a silicon ROIC. Highlighted area shows cross-section of the CQD photodetector architecture, including the transparent electrode, CQD layer, and ROIC readout circuitry. Adapted with permission from ref.*[64]

Thus, CQD-based SWIR detectors are poised to democratize infrared imaging as the foundation for the fourth generation of infrared technologies, offering a pathway toward compact, low-cost, and high-performance devices that unify advanced functionality with large-scale manufacturability[68, 69].

1.3 Nanomaterials

Materials featuring at least one dimension in the 1-100 nm range are broadly defined as nanomaterials. They are commonly classified into four categories based on how their length, width, and height are confined at the nanoscale (Figure 1.3.1)[70]. Zero-dimensional (0D) nanomaterials are confined in all three spatial dimensions, forming particle-like structures such as QDs, nanoclusters, and fullerenes, where strong quantum confinement produces discrete electronic states. One-dimensional (1D) nanomaterials, including nanowires, nanotubes, and nanorods, have two dimensions in the nanoscale while extending in the third, which enables directional charge transport. Two-dimensional (2D) nanomaterials such as graphene, nanosheets, and colloidal nanoplatelets are confined only in thickness, exhibiting large lateral dimensions, and enhanced in-plane electronic and mechanical properties. Three-dimensional (3D) nanomaterials do not have all dimensions within the nanoscale but contain nanoscale grains, pores, or structural features, as in nanocomposites and nanoporous materials[71].

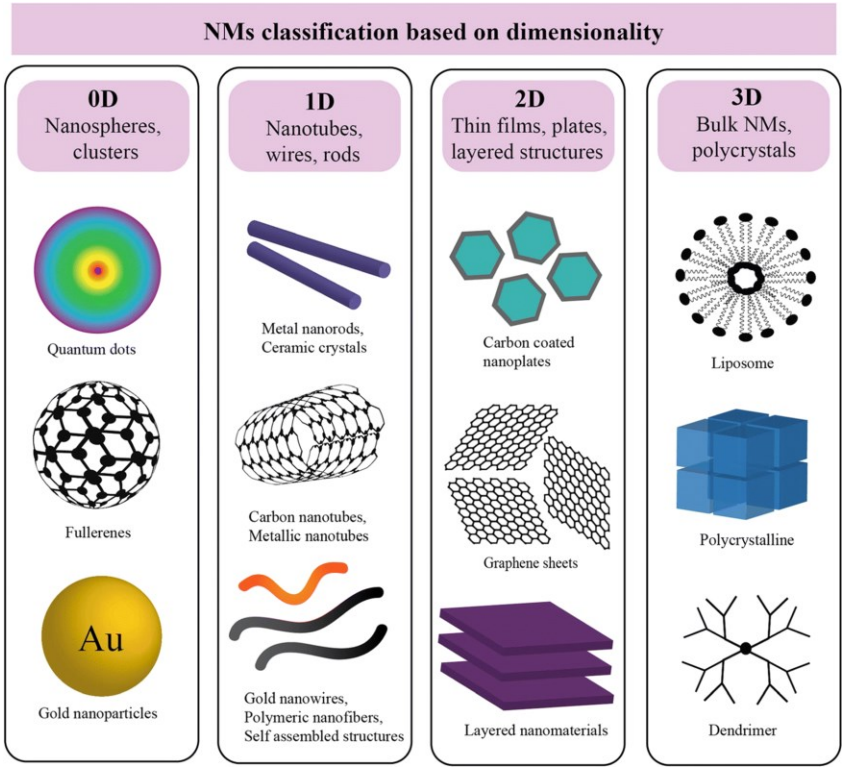

Figure 1.3.1. *Classification of nanomaterials based on dimensionality, illustrating examples of 0D, 1D, 2D, and 3D*[72]***.***

1.3.1 Ancient history of nanomaterials

The origins of nanocrystals can be traced back to prehistoric times, long before the concept of atoms or nanoscale materials existed. Early humans regularly encountered carbon-based nanoparticles such as fullerenes, graphene fragments, and carbon nanotubes in soot generated by fires, and these combustion-derived nanomaterials were unknowingly incorporated into pigments for cave paintings, including the hand stencils found in the caves of Sulawesi, Indonesia (Figure 1.3.2)[73]. By 4000 BC, ancient Egyptians had already developed chemical processes that produced nanoscale compounds: a black hair dye made from lead oxide, lime, and water generated approximately 5 nm PbS nanoparticles through reactions between lead ions and sulfur-rich amino acids in keratin[74]. This tradition of unintentionally producing nanocrystals continued into antiquity and the Middle Ages, most famously exemplified by the Roman Lycurgus Cup (4th century CE). This dichroic chalice appears green in reflected light and deep red in transmission due to gold and silver nanoparticles embedded within the glass, whose plasmonic responses give rise to its striking optical effects. Medieval stained-glass windows also owe their vivid reds, purples, and yellows to copper and gold nanoclusters formed during high-temperature glassmaking (Figure 1.3.2)[75]. At the same time, advanced materials such as Damascus steel, produced from Indian Wootz ingots, derived their exceptional sharpness and resilience from nanoscale features including cementite nanowires and carbon nanotubes formed during repeated forging and thermal cycling[76]. Although ancient artisans and metallurgists had no knowledge of nanoscience, their empirical command of heat, chemistry, and materials processing enabled the creation of nanostructured materials with remarkable optical and mechanical properties. These examples illustrate that the use of nanocrystals long predates modern scientific understanding and that nanoscale phenomena have been exploited unknowingly for millennia (Figure 1.3.2).

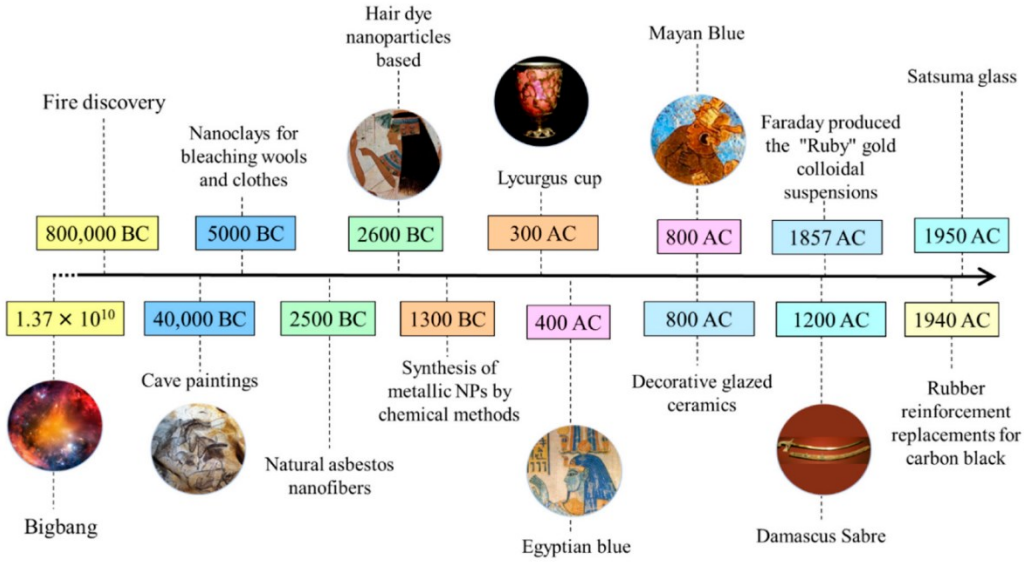

Figure 1.3.2. *Historical timeline highlighting early uses and discoveries related to nanomaterials, from natural nanostructures and ancient pigments to metal colloids and modern engineered nanoparticles[73].*

1.3.2 Birth of Modern Nanoscience and QDs

The conceptual bridge from the unintentional nanotechnology of ancient civilizations to modern nanoscience was first established in the mid-19th century. In 1857, Michael Faraday's systematic studies on colloidal gold revealed that particle size controlled the color of gold dispersions, providing the first scientific evidence of size-dependent properties at sub-microscopic dimensions[77]. A century later, Richard Feynman's 1959 lecture, "There's Plenty of Room at the Bottom," articulated the revolutionary idea of manipulating matter atom by atom, laying the conceptual foundation for nanotechnology[75]. Throughout the early 20th century, advances in physical chemistry, X-ray diffraction (1895), and the development of electron microscopy in the 1930s enabled the direct visualization and characterization of structures at nanometer length scales[78]. These tools revealed that many unusual optical, catalytic, and mechanical properties in materials originated from nanoscale features, further reinforcing the importance of size as a fundamental design parameter[79].

Beginning in the late 1970s and early 1980s, modern nanoscience advanced rapidly with landmark discoveries across multiple classes of nanomaterials. One major direction was the emergence of semiconductor nanocrystals through the first intentional demonstrations of quantum confinement. Alexei Ekimov showed that CuCl nanocrystals precipitated in glass exhibited size-dependent absorption, providing the earliest experimental evidence of quantum-confined behavior[80]. Shortly thereafter, Louis Brus extended these findings to colloidal solutions, demonstrating that the optical and electronic properties of CdS and CdSe nanocrystals could be tuned by controlling particle size[81]. This work established colloidal QDs as deliberately engineered nanomaterials. In parallel, transformative breakthroughs were occurring in carbon-based nanostructures. In 1985, Curl, Kroto, and Smalley discovered C_{60} fullerenes, triggering intense interest in low-dimensional carbon systems[82]. This momentum led to the discovery of carbon nanotubes in 1991[83] and the isolation of graphene in 2004[84], discoveries recognized with Nobel Prizes in 1996 and 2010. Collectively, advances in semiconductor and carbon nanomaterials highlighted the crucial role of size and dimensionality, establishing the foundation of modern nanoscience.

This foundation was reinforced in 1993 when Moungi Bawendi and co-workers introduced the hot-injection organometallic synthesis method, enabling the production of highly crystalline, monodisperse QDs with exceptional optical properties[85]. This breakthrough transformed colloidal nanocrystals into a practical materials platform for applications in optoelectronics, displays, photodetectors, bioimaging, and emerging quantum technologies. Today, QDs are among the most influential nanomaterials, a significance reflected in the 2023 Nobel Prize in Chemistry awarded to Alexei Ekimov, Louis Brus, and Moungi Bawendi for their discovery and synthesis. This progression, from accidental nanoscale artefacts in antiquity to precise atomic-level engineering, marks the full evolution of nanocrystals into a central pillar of modern materials science and technology.

1.3.3 Semiconductor Colloidal QDs

QDs are nanoscale semiconductor crystals whose electronic and optical behavior is governed by quantum confinement, which occurs when at least one-dimension approaches or falls below the exciton Bohr radius of the material. At sizes of roughly 2-10 nm, the continuous band structure of the bulk semiconductor transforms into discrete, atom-like energy levels, producing size-dependent absorption and emission as well as modified carrier interactions. CQDs are a specific class of QDs produced through solution-based wet-chemical synthesis. They consist of nanocrystalline semiconductor cores capped with organic or inorganic ligands that bind to the surface, providing colloidal stability, passivating surface defects, and enabling controlled nucleation and growth. Their solution processability makes CQDs highly versatile for integration into optoelectronic, photonic, and sensing applications.

1.3.3.1 Exciton Bohr Radius

Semiconductors are materials whose electrical and optical properties lie between those of metals and insulators. Their defining characteristic is the presence of a bandgap, an energy separation between the valence band and the conduction band, across which electrons can be promoted through photon absorption. When a semiconductor absorbs a photon with energy greater than its bandgap, an electron is excited to the conduction band, leaving behind a positively charged hole in the valence band. The electron and hole attract each other through the Coulomb force and form a bound quasiparticle known as an exciton, which behaves similarly to a hydrogen-like system in which the hole acts as an effective nucleus and the electron orbits around it[86].

The spatial extent of this bound electron-hole pair is defined by the exciton Bohr radius a_B, which represents the average separation between the electron and hole in the bulk material. In a hydrogen-like effective mass approximation, this radius is given by:

$$a_{B=}\frac{4\pi\varepsilon_0\varepsilon\hbar^2}{\mu e^2}$$

(Equation 1.1)

Where ε is the dielectric constant of the semiconductor, and μ is the reduced effective mass of the electron-hole pair, defined by $\mu^{-1} = m_e^{*-1} + m_h^{*-1}$as m_e^* the electron and m_h^*hole effective masses. The exciton Bohr radius is a fundamental material property and can extend from few nanometers to tens of nanometers. This characteristic length scale determines whether a semiconductor nanocrystal behaves like the bulk or exhibits quantum mechanical size effects.

1.3.3.2 Quantum Confinement Effect

The quantum confinement effect is the fundamental phenomenon that governs the behavior of semiconductor QDs and arises when the physical radius of a nanocrystal (R) becomes comparable to or smaller than the exciton Bohr radius a_B. In this regime, the motion of electrons and holes is restricted by the finite boundaries of the material, and they can no longer be treated as free,

delocalized carriers as in the bulk. Instead, their energies and wavefunctions become quantized, transforming the continuous valence and conduction bands of the bulk semiconductor into discrete, atom-like energy levels. This confinement-induced modification originates from a characteristic widening of the bandgap as the size of the nanocrystal decreases (Figure 1.3.3)[87].

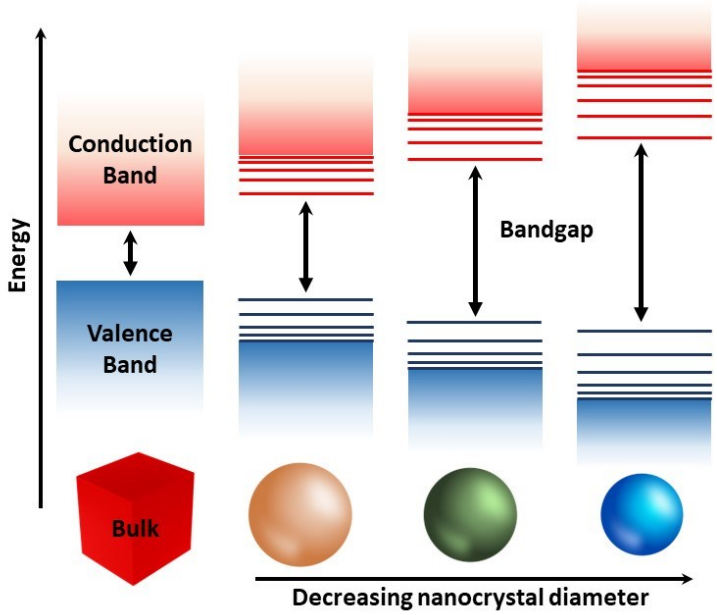

Figure 1.3.3. *Quantum confinement effect on the band structure of semiconductor materials as the nanocrystal size decreases, shown in comparison with the bulk semiconductor.*

The effect can be rationalized using the *particle in a box* model, where an electron is confined within a potential well of size L. For a one-dimensional box of length L, solving the Schrödinger equation for an electron under the boundary conditions that the wavefunction vanishes at the walls yields a set of quantized solutions. These solutions take the form of discrete standing waves, each corresponding to a specific allowed energy level given by:

$$E_n = \frac{n^2\pi^2\hbar^2}{2mL^2}$$

(Equation 1.2)

Where E_n is the energy level, n is the integer quantum number, $\hbar$ is the reduced Plank's constant, m is the mass of the electron, and L is the size of the box. As the dimension L becomes smaller, the allowed wavelengths shorten, increasing the electron's momentum ($p = h/\lambda$) and therefore its kinetic energy.

From equation 1.2, the energy levels (E_n) are inversely proportional to L^2, so reducing the size of the confining region forces the energy states to shift upwards and increases the separation between them (ΔE). In semiconductor nanocrystals, this manifests as an upward shift of the

lowest conduction-band state and a downward shift of the highest valence-band state as the particle size decreases, leading to an overall widening of the bandgap.

A more quantitative description is provided by the effective mass approximation, which treats electrons and holes as particles confined in a spherical potential well. The size-dependent bandgap $E_{QD}(R)$ of a nanocrystal of radius R is commonly expressed using the Brus equation[88]:

$$E_{QD}(R) = E_{bulk} + \frac{\hbar^2\pi^2}{2R^2}\left(\frac{1}{m_e^*} + \frac{1}{m_h^*}\right) - \frac{1.8e^2}{4\pi\varepsilon_0\varepsilon R}$$

(Equation 1.3)

Where E_{bulk} is the bulk bandgap, m_e^* and m_h^* are the electron and hole effective masses and ε is the dielectric constant. The confinement term, scaling as $1/R^2$ dominates at small sizes and is responsible for the pronounced blue-shift in optical absorption and emission as the nanocrystal becomes smaller. The Coulombic attraction (proportional to $1/R$) provides a smaller corrective term. Together, these effects illustrate that quantum confinement fundamentally reshapes the behavior of semiconductor nanocrystals, establishing size as a powerful and tunable parameter that governs their electronic structure, optical response, and overall functional properties.

1.3.3.3 Density of States

The density of states (DOS) describes the number of available electronic energy levels per unit energy and is fundamental for understanding the electronic and optical behavior of materials. In bulk three-dimensional (3D) semiconductors, the DOS is a continuous function that increases smoothly with energy, following a $\sqrt{E}$ dependence (Figure 1.3.4). This continuity reflects the free translational motion of charge carriers enabled by the extended periodic lattice.

When the dimensions of a semiconductor are reduced to the nanoscale and the quantum confinement regime is reached, the nature of the DOS changes profoundly. In zero-dimensional (0D) QDs, where electrons and holes are confined in all three spatial dimensions, translational degrees of freedom are eliminated. The carrier wavefunctions are restricted to a finite region and can only adopt specific standing-wave solutions of the Schrödinger equation. Therefore, the continuous band structure of the bulk semiconductor collapses into a discrete set of quantized, atom-like energy levels. Mathematically, the DOS of an ideal quantum dot is described as a series of Dirac delta functions:

$$D(E) = \sum_n \delta(E - E_n)$$

(Equation 1.4)

which indicates that electronic states exist only at specific allowed energies E_n, with no available states in-between. Each quantized level may exhibit degeneracy associated with spin, orbital symmetry, or valence-band structure (Figure 1.3.4).

The discretization of the DOS in QDs has significant implications for their optical and electronic behavior. By concentrating available electronic states at specific quantized energies, QDs exhibit sharp optical transitions, efficient radiative recombination, and strongly size-dependent absorption and emission, features that differ markedly from the continuous band structure of bulk semiconductors[89].

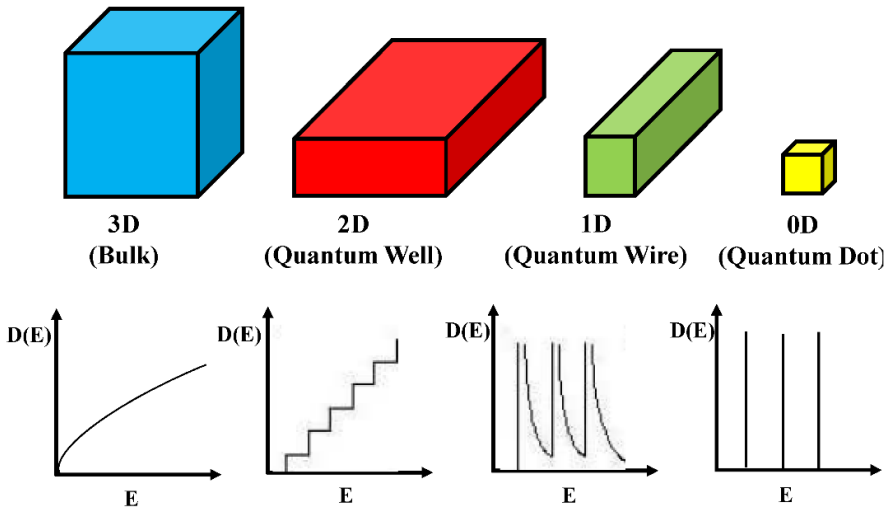

Figure 1.3.4. *Schematic diagram of density of states for 3D, 2D, 1D and 0D systems. Adapted from ref.* [89]

1.3.4 Optical properties of QDs

The discrete electronic structure that emerges from strong quantum confinement and the resulting quantized density of states fundamentally shapes the way QDs interact with light. Because their energy levels resemble those of artificial atoms, QDs display optical transitions that are sharply defined, highly tunable, and strongly dependent on size, composition, and surface quality. These characteristics give rise to distinctive absorption features and efficient, spectrally narrow photoluminescence, making QDs uniquely versatile among semiconductor nanomaterials.

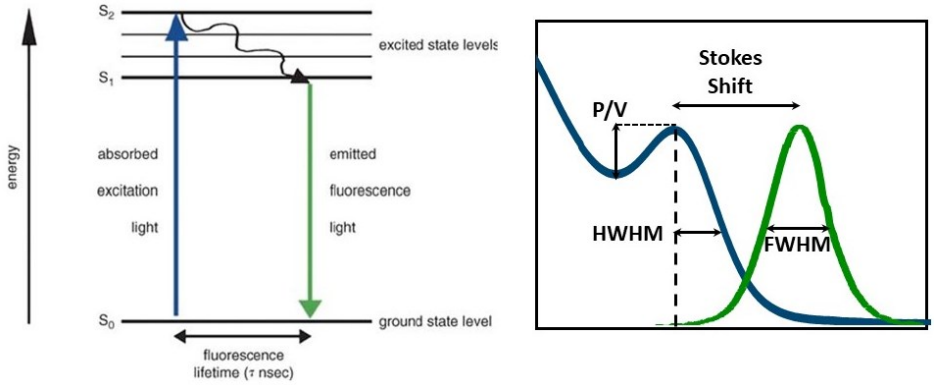

Figure 1.3.5. *(Left) Jablonski diagram illustrating electronic excitation, nonradiative relaxation, and fluorescence emission from excited states. (Right) Excitonic absorption and fluorescence spectra showing key parameters including Stokes shift, HWHM, FWHM, and (P/V) ratio.*

1.3.4.1 Excitonic absorption

The optical absorption properties of semiconductor QDs arise from their discrete electronic structure and quantized density of states. When a QD absorbs light, electrons are promoted from confined valence-band levels to quantized conduction-band states, giving rise to distinct absorption features that contrast sharply with the smooth absorption edge of bulk semiconductors. Because optical transitions occur only between specific quantized states, the absorption spectrum displays well-defined excitonic peaks. The lowest and most prominent of these corresponds to the $1S_h \rightarrow 1S_e$ transition (Figure 1.3.5)[90].

The widening of the bandgap with decreasing size has already been described in the context of quantum confinement, and its optical consequence is directly reflected in the excitonic absorption spectrum. As the nanocrystal radius becomes smaller, the increased confinement energy shifts the excitonic transitions to higher energies, producing a clear blue-shift in the absorption onset. Conversely, larger QDs exhibit reduced confinement, bringing the quantized levels closer together and shifting the excitonic features toward lower energies, progressively approaching the bulk bandgap. This strong size dependence enables precise spectral tunability across a wide wavelength range, from the visible to the near-infrared and the short-wave infrared, simply by adjusting the nanocrystal dimensions within a given semiconductor system.

Beyond the spectral position of the excitonic transitions, the shape and width of the first excitonic peak provide valuable information about ensemble uniformity. A narrow, well-resolved peak indicates a narrow size distribution, whereas broader or less distinct absorption features arise from variations in nanocrystal dimensions (i.e., a polydisperse NC sample) or might be due to NC featuring defects. Two metrics are commonly used to quantify these characteristics: the half-width at half-maximum (HWHM) and the peak-to-valley (P/V) ratio (Figure 1.3.5).

The HWHM, defined as half of the peak width at half its maximum amplitude, serves as a sensitive measure of inhomogeneous broadening. A small HWHM reflects a uniform ensemble with minimal size dispersion and consistent confinement across particles, while a larger HWHM indicates greater variability in nanocrystal dimensions or structural quality. The P/V ratio is defined as the ratio of the absorption intensity at the first excitonic peak to the intensity at the local minimum (valley) immediately following this peak and preceding the next higher-energy transition. A high P/V denotes a sharply defined excitonic transition with minimal background or disorder-related absorption, whereas a low P/V points to overlapping electronic states, weaker confinement, or trap-induced broadening.

Together, HWHM and P/V offer a powerful measure of QDs quality and strongly correlate with device performance. Well-defined excitonic peaks enhance absorption uniformity, spectral purity, and optical gain, while indicating low trap densities and good surface passivation[91]. These metrics are therefore widely used to assess synthesis quality for optoelectronic applications.

1.3.4.2 Photoluminescence in QDs

Photoluminescence (PL) is one of the most characteristic properties of semiconductor QDs, which arises when a photoexcited electron-hole pair (exciton) recombines and emits a photon. Owing to their discrete, atom-like energy levels, QDs exhibit narrow and well-defined emission peaks whose positions and intensities are highly sensitive to particle size, composition, and surface quality. The emission wavelength is primarily determined by the energy difference between the quantized electron and hole ground states (i.e., it follows the $1S_e \rightarrow 1S_h$ transition) and therefore displays strong size dependence (Figure 1.3.5). Smaller QDs emit at shorter wavelengths due to larger confinement energies, whereas larger QDs show red-shifted emission as they approach bulk-like behavior[92].

Following absorption, excited carriers undergo ultrafast intraband relaxation to the lowest conduction band states, typically within hundreds of femtoseconds. This phonon-mediated cooling ensures that emission arises almost entirely from the band-edge exciton. The emitted photon generally has slightly lower energy than the absorbed one, giving rise to a Stokes shift[93]. This shift results from lattice relaxation, exciton-phonon coupling, and small energy differences between closely packed excitonic states. Because its magnitude depends on surface quality (which can introduce trap states, as discussed in section 1.3.5) and the presence of trap or localized states, the Stokes shift is often used as a diagnostic indicator of QD structural and electronic uniformity[94].

Following rapid relaxation to the band-edge states, an exciton may recombine radiatively, emitting a photon. The rate of this process depends strongly on the spatial overlap of the electron and hole wavefunctions, which is enhanced under strong quantum confinement. As a result, smaller QDs typically exhibit faster radiative rates and shorter intrinsic radiative lifetimes, whereas larger or weakly confined dots show slower radiative decay. Radiative lifetimes may also vary with the dielectric environment, the local optical density of states, or coupling to optical cavities and plasmonic structures.

Non-radiative recombination competes directly with radiative decay and arises mainly from carrier trapping at surface or interface defects. Trap states capture electrons or holes and dissipate their energy through phonon emission rather than light, thereby reducing the PL quantum yield (PLQY) and shortening the exciton lifetime[95]. Because a large fraction of atoms in a QD lie at the surface, trap-mediated decay is highly sensitive to surface chemistry, ligand coverage, and structural quality. Poor passivation, ligand loss, oxidation, or defects at the QDs surface can significantly increase non-radiative rates, whereas effective passivation with strongly bound ligands or high-quality inorganic materials, typically referred as “shell”, passivates surface traps and allows radiative recombination to dominate.

The PLQY in QDs is determined by the balance between radiative and non-radiative recombination pathways and is defined by:

$$PLQY = \frac{k_r}{k_r + k_{nr}}$$

(Equation 1.5)

where k_r and k_{nr} are the radiative and non-radiative rate constants. High PLQY therefore requires both strong radiative overlap and effective suppression of trap-mediated losses.

Another important parameter for assessing QDs optical quality is the full width at half maximum (FWHM) of the PL peak (Figure 1.3.5). The FWHM reflects the homogeneity of the emissive states: narrow FWHM values indicate uniform particle size, well-defined electronic structure, and minimal spectral diffusion, whereas broader emission suggests increased polydispersity, surface disorder, or strong carrier-phonon coupling[96].

In addition to trap-assisted non-radiative decay, QDs exhibit another significant non-radiative pathway that becomes prominent at high excitation densities, Auger recombination. In this process, the recombination energy of an electron-hole pair is transferred to a third carrier instead of being emitted as a photon, after which the energized carrier relaxes through phonon emission. Because carriers are confined within a very small volume, their wavefunction overlap is strong, making Auger recombination extremely fast, typically on the picosecond timescale. This process shortens multiexciton lifetimes, reduces PLQY, suppresses multiexciton emission, contributes to PL blinking, and limits the achievement of optical gain[97, 98].

Taken together, a narrow and efficient PL, and suppressed Auger recombination rates serve as the primary hallmarks of high-quality QDs. These characteristics ensure spectrally pure, efficient, and stable emission, making such QDs well suited for demanding optoelectronic applications including LEDs, lasers and quantum light sources.

1.3.5 Surface properties of QDs

Semiconductor QDs possess an exceptionally high surface-to-volume ratio, with 30-50% of their atoms located in the outermost layers of a 3-5 nm nanocrystal[99]. These surface atoms experience incomplete coordination and distorted bonding environments, giving rise to dangling bonds, vacancies, and non-stoichiometric sites. Such under-coordinated atoms create localized electronic states within the bandgap that trap charge carriers and act as efficient non-radiative recombination centers, reducing PLQY, shortening exciton lifetimes, and broadening emission linewidths. In addition to degrading optical properties, the high surface energy associated with these reactive sites makes unpassivated QDs highly prone to colloidal instability, allowing attractive van der Waals forces to promote aggregation, and precipitation. To maintain dispersion in solution and simultaneously suppress surface defects, QDs must be coated with suitable ligands that bind to surface atoms and provide both steric or electrostatic repulsion and effective electronic passivation[100].

1.3.5.1 Surface trap states

The surface dangling bonds and under coordinated atoms cause disruptions to the periodic crystal potential, breaking the translational symmetry of the semiconductor and generating electronic states that do not belong to the intrinsic conduction or valence bands. These defect-derived states are collectively known as surface states or trap states[95]. Such trap states form when exposing the nanocrystals to external environment (e.g. air, humidity), which can lead to the reaction of the surface with oxygen or moisture and induce partial surface oxidation,[101] or when removing surface ligands when washing the nanocrystals, and thus leaving under-coordinated surface atoms behind[102]. Additionally, the dielectric contrast between the semiconductor core and its surrounding medium can shift the energetic position of surface-localized orbitals, influencing whether they behave as shallow or deep traps.

Surface traps can be broadly classified by the type of carrier they capture and their position within the bandgap. Electron traps generally originate from under-coordinated metal atoms, cation vacancies, or oxide species and often reside near the mid-gap region. Hole traps typically arise from anion vacancies or under-coordinated chalcogen or pnictogen atoms and tend to lie near the valence-band edge. Deep mid-gap traps efficiently capture carriers and strongly suppress emission, whereas shallow traps located close to the band edges can temporarily localize electrons or holes, producing delayed fluorescence or long-lived tail components in time-resolved measurements. Additional traps may form through ligand loss, surface etching, or incorporation of external chemical species that disrupt coordination[95].

The presence of these trap states profoundly affects the optical and electronic performance of QDs. They introduce fast non-radiative decay pathways that compete with radiative recombination, lowering the PLQY and shortening exciton lifetimes. Trap-mediated carrier capture also broadens emission linewidths, reduces spectral stability, and contributes to PL intermittency (blinking) in single-particle measurements[103].

1.3.5.2 Surface passivation

Surface passivation aims to complete the coordination of under-coordinated atoms, neutralize dangling bonds, and eliminate trap states that would otherwise introduce fast non-radiative decay pathways. Achieving this requires strategies that both prevent aggregation and maintain a defect-free electronic structure at the NC surface. This can be accomplished through ligand engineering, core/shell architectures, or a combination of both. Together, these approaches form powerful and widely used methods for producing high-quality QDs with excellent optoelectronic properties.

1.3.5.3 Ligands

Ligands are organic molecules or molecular assemblies that bind to the surface atoms of NCs, forming a critical interface that governs their structural, chemical, and optoelectronic properties. Because a large fraction of atoms in a NC lies at the surface, the ligand shell is not merely a

protective coating but an integral part of the nanocrystal. By completing the coordination of surface atoms, ligands suppress dangling bonds and electronic trap states that would otherwise quench PL or inhibit charge transport. They also impart steric or electrostatic repulsion, ensuring colloidal stability during synthesis, purification, and storage. Structurally, ligands typically consist of a binding 'head group', binding the atoms present in the surface of the NCs, and a hydrocarbon 'tail' that controls solubility and interparticle spacing. Beyond stabilization, ligands play an essential role in directing NC growth by modulating precursor reactivity and adsorption kinetics, and they ultimately determine the electronic coupling, surface passivation quality, and overall performance of NCs in optoelectronic applications[104].

Classification of Ligands

Based on the bond that ligand form with NC surface atoms, ligands can be classified into X-type, L-type and Z-type ligands. X-type ligands are ionic species that bind strongly to surface cations or anions by sharing one electron and thus forming ionic or covalent bonds with surface atoms[105]. Common examples include carboxylates ($RCOO^-$), thiolates (RS^-), halides (Cl^-, Br^-) and chalcogenides (S^{2-}, Se^{2-}). They effectively complete the coordination of surface atoms and offer robust passivation of positively charged sites. L-type ligands are neutral Lewis bases that bind by donating an electron pair to empty orbitals on surface atoms. This category includes alkylamines, alkylphosphines, phosphine oxides, thiols, and nitriles. L-type ligands bind more weakly than X-type ligands and can desorb and re-adsorb during heating or purification. They help maintain colloidal stability and solubility but provide only partial surface passivation, often resulting in moderate PLQY for amine capped QDs. Nevertheless, their dynamic binding is crucial during synthesis, where it modulates precursor reactivity and supports controlled, uniform nanocrystal growth. Z-type ligands are neutral Lewis acids that accept 2 electrons density from anion-rich surface sites, restoring surface stoichiometry and suppressing deep trap states. Common examples include metal halides such as $ZnCl_2$, $CdCl_2$, and $InCl_3$, as well as metal carboxylates. Increasingly, these ligands are employed in post-synthetic treatments to improve PLQY and stability by effectively neutralizing surface defects[104, 106].

Ligand Engineering

Ligand engineering is the deliberate control of coordination chemistry at the nanocrystal surface, where the equilibrium between bound and free ligands dictates nucleation, growth, surface stoichiometry, and ultimately the electronic structure of QDs. Native long-chain ligands such as oleate and oleylamine are essential during synthesis because the balance between their steric repulsion and the van der Waals attraction between inorganic cores determines the colloidal stability of the dispersion. However, these ligands are electrically insulating and produce large interparticle separations, leading to poor electronic coupling in solid-state films[107]. Moreover, long-chain ligands bind relatively weakly to the nanocrystal surface and often provide incomplete passivation of trap states, whereas short-chain ligands bind more strongly but compromise colloidal stability due to reduced steric protection. Ligand engineering therefore extends beyond simple passivation: it strategically replaces bulky insulating ligands with shorter, more strongly

binding, or electronically functional species that modulate surface reactivity, enhance charge transport, and improve film stability[108, 109].

The transition from insulating, synthesis-grade colloidal QDs to conductive, device-ready solids is typically achieved through two methodologies: solid-state ligand exchange (SSE) and solution-phase ligand exchange (SPE). SSE has long been the standard for high-performance photovoltaics and relies on a layer-by-layer process. A film of QDs capped with long-chain ligands is spin-coated, then exposed to short ligands such as 1,2 ethanedithiol or tetrabutylammonium iodide, in a solvent that enables ligand replacement without dissolving or damaging the QD film. As these smaller ligands infiltrate the porous film and displace bulky organics, the layer undergoes substantial densification, often shrinking by more than 1 nm in interparticle spacing. Although this compaction improves charge transport, it induces significant tensile stress, generating microcracks and voids. Consequently, multiple deposition-exchange cycles (typically 10–15) are required to achieve a uniform, crack-free absorber layer, making SSE material- and labor-intensive[110, 111].

In contrast to SSE, SPE mitigates scalability and morphological limitations by modifying the ligand shell directly in the colloidal phase before film formation. Incoming ligands such as thiolates, carboxylates, amines, halides are introduced into a QD dispersion, where they compete with native ligands through dynamic adsorption-desorption equilibria, allowing fine control over surface coverage while preserving colloidal stability. A widely used variant is biphasic or interfacial ligand exchange, which exploits the differing solubilities of ligands across two immiscible solvents to efficiently displace hydrophobic ligands and transfer QDs into polar media[112]. This often employs stripping agents such as $NOBF_4$ or Et_3OBF_4 to remove native long-chain ligands and expose surface sites for coordination by inorganic ligands[113]. The resulting polar "conductive inks" can be deposited in a single step to form dense, uniform, crack-free films, offering improved processability and reduced trap densities compared to SSE, and enabling compatibility with scalable roll-to-roll manufacturing.

Overall, ligand engineering provides a powerful platform for tuning band energetics, enhancing charge transport, and suppressing defect-mediated recombination in CQD solids. By precisely designing ligand identity, binding strength, and surface coverage, quantum dot films can be engineered with optimized electronic coupling and minimized trap densities, establishing ligand chemistry as a decisive lever for high-performance optoelectronic devices[109, 114].

1.3.5.4 Core-Shell architecture

Beyond ligand exchange, one of the most powerful strategies for suppressing surface traps and enhancing the optical stability of colloidal QDs is the adoption of core-shell architectures. In this approach, a second semiconductor material with a wider bandgap is grown epitaxially around the initial nanocrystal, creating an inorganic shell that fundamentally reshapes the electronic landscape of the QD. Depending on the band alignment between the core and the shell, the spatial localization of electrons and holes can be precisely controlled, enabling the design of QDs

optimized for specific optical or electronic applications. Even when the shell surface retains some residual trap states, a sufficiently thick and wide-bandgap shell greatly suppresses carrier tunneling, ensuring that the core remains electronically insulated from its surrounding chemical environment[115, 116].

Classification of core-shell architecture

The electronic and optical properties of core-shell nanocrystals are determined by the alignment of the conduction and valence bands at the core-shell interface, which dictates where electrons and holes reside. Based on this band alignment, core-shell structures are broadly classified as Type-I, Type-II, Reverse Type-I, or the intermediate Quasi-Type-II[117, 118].

In a Type-I (straddling-gap) core-shell structure, the core bandgap is completely enclosed within the wider bandgap of the shell, with the shell's conduction band positioned higher in energy and its valence band lower than those of the core (Figure 1.3.6 a). This alignment creates a potential well that confines both electrons and holes within the core, effectively isolating the exciton from surface defects. These architectures primarily passivate dangling bonds and suppress non-radiative recombination, yielding high PLQY and improved stability as demonstrated for InAs@ZnSe systems discussed in Chapter 3. Since both carriers remain confined to the core, the emission wavelength is largely dictated by the core size, with only a slight redshift from minimal wavefunction leakage into the shell.

In contrast, the Type-II (staggered gap) architecture is characterized by a staggered band alignment where the band edges of one material lie effectively lower or higher than the corresponding edges of the other (Figure 1.3.6 c). Consequently, the lowest energy state for the electron is in one material while the lowest energy state for the hole is in the other, creating a spatial separation of charge carriers after photoexcitation. This spatial separation reduces electron-hole overlap, producing long radiative lifetimes and emission at energies below the bandgaps of either material. These properties make Type-II nanocrystals valuable for applications requiring efficient charge separation, such as photovoltaics and photocatalysis.

The Quasi-Type-II regime arises when one carrier is strongly confined while the other experiences only a small band offset and can partially delocalize (Figure 1.3.6 d). In CdSe/CdS, for example, the hole remains confined to the core, whereas the electron spreads into the shell. This partial delocalization, especially in thick-shell structures, reduces electron-hole overlap and suppresses Auger recombination, enabling highly stable, continuous emission.

In the Reverse Type-I architecture, the narrower-bandgap material forms the shell while the wider-bandgap material remains in the core (Figure 1.3.6 b). This inversion drives both carriers into the shell, localizing them near the surface. Although this increases sensitivity to the environment and surface ligands, it enables emission tuning and control over the exciton's effective volume largely independent of the core size.

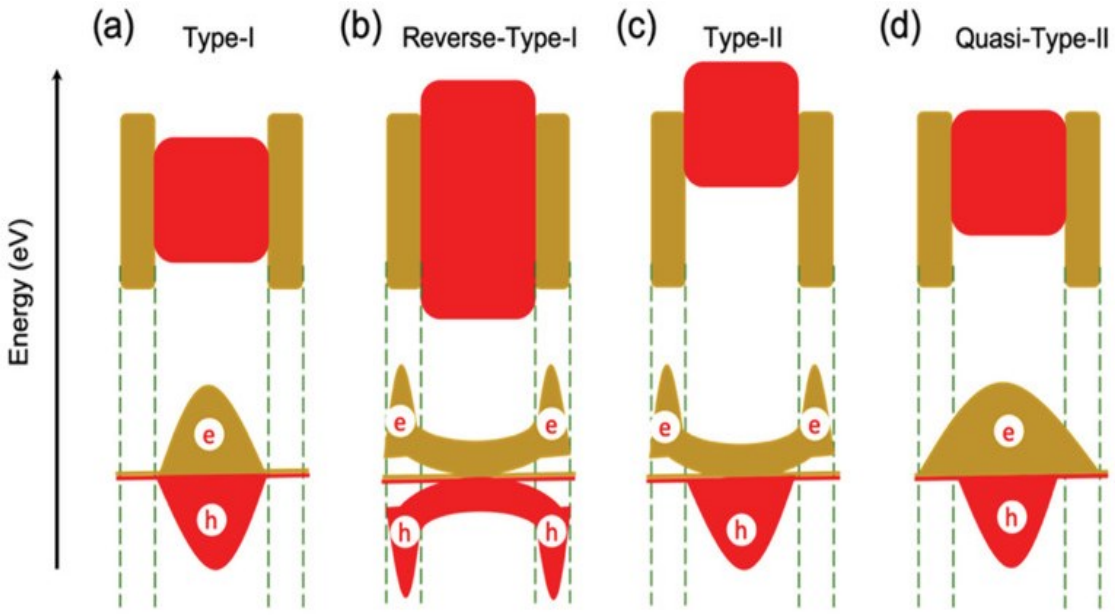

Figure 1.3.6. *Schematic electronic band alignments and corresponding electron (gold) and hole (red) wavefunctions for different classes of core/shell QD systems. The central region represents the core band edges, while the outer regions correspond to the shell in (a) Type-I, (b) reverse Type-I, (c) Type-II, and (d) quasi-Type-II. Adapted with permission from ref.*[118]

1.3.5.5 Lattice mismatch

A critical determinant of the structural and optoelectronic quality of core-shell QDs is the lattice mismatch between the core and shell materials. Lattice mismatch (f) describes the fractional difference between the relaxed lattice constants of the shell (a_s) and the core (a_c) and is expressed as $f = (a_s - a_c)/a_c$. When these lattice parameters differ, the shell must initially deform, either by compressing or stretching to match the in-plane atomic spacing of the core during epitaxial growth. This forced deformation generates coherent elastic strain at the interface, which accumulates as the shell becomes thicker. According to the Matthews-Blakeslee model, such coherent growth is only energetically sustainable up to a specific critical thickness (h_c). Below this threshold, the strain is fully accommodated elastically, enabling the formation of a smooth, defect-free interface essential for high-performance QDs. However, once the shell thickness exceeds h_c, the stored strain energy surpasses the barrier for defect formation, and the heterostructure relaxes through the introduction of misfit dislocations[119]. These dislocations act as deep trap states and non-radiative recombination centers, severely degrading the PLQY and compromising long-term optical stability[120]. Thus, managing lattice mismatch and staying within the critical thickness limit are fundamental requirements for achieving coherent epitaxy and preserving the optoelectronic integrity of core-shell nanocrystals[121].

For material systems with large lattice mismatch, such as CdSe/ZnS (~12%), the critical thickness is theoretically restricted to less than two monolayers, explaining why simple core-shell structures with thick shells often exhibit poor optical quality[122]. To address this limitation,

advanced strain-engineering strategies like alloyed gradient shells and multishell buffer designs are employed to gradually distribute strain across the heterostructure. These approaches increase the effective critical thickness and significantly reduce the likelihood of misfit dislocation formation[123, 124]. Beyond structural stability, strain itself serves as a powerful parameter for band-structure engineering[125]. The hydrostatic pressure imposed by a mismatched shell alters the electronic bandgap through deformation potentials, such as a compressive strain can widen the core bandgap and induce a blue shift, while extreme strain in systems such as CdTe/ZnSe can even drive a transition from Type-I to Type-II alignment[126, 127]. Such strain-induced modulation enables independent tuning of emission wavelength and carrier dynamics beyond what is achievable through size-confinement alone, providing a highly versatile route for tailoring optoelectronic behavior.

1.3.6 Synthesis Methods

The synthesis of colloidal nanomaterials has expanded into a broad and sophisticated toolbox encompassing vapor-phase, solid-state, and solution-based routes, each offering distinct advantages in terms of size control, crystallinity, scalability, and surface chemistry. These methodologies are commonly divided into two overarching paradigms: top-down and bottom-up approaches. Top-down techniques, such as mechanical grinding, lithography, sputtering, and chemical etching, operate by removing material from bulk precursors to produce nanoscale features, which typically require large-scale, high-precision equipment and often yield nanostructures with limited control over size, shape, and surface quality.

Bottom-up approaches, in contrast, assemble atoms or molecular precursors into nanostructures and include techniques such as chemical vapor deposition, sol-gel chemistry, hydrothermal/solvothermal syntheses, high-temperature solid-state reactions, and molten-salt methods[128]. Among these, the solution-phase colloidal synthesis has emerged as the most powerful and economical route for semiconductor QDs, providing precise control over nucleation and growth. Several variations of colloidal synthesis such as solvothermal reactions, microwave-assisted heating, template-directed growth, single-source precursor decomposition, and continuous-flow reactors further expand the available synthetic landscape[129]. Despite the breadth, two distinct methodologies are particularly predominant: the hot-injection method and the heat-up method[130]. These two methodologies are employed extensively throughout this thesis for the synthesis and optimization of the various QDs discussed in the subsequent chapters.

1.3.7 Nucleation and growth kinetics

The formation of colloidal nanocrystals is governed by the interplay between thermodynamics and kinetics, which together determine how precursors convert into monomers, how nuclei emerge, and how NCs evolve in size[131]. A central concept in this framework is supersaturation, arising when the concentration of reactive monomers exceeds their equilibrium solubility. The degree of supersaturation, denoted as S, is quantitatively defined as the ratio of the actual

monomer concentration in solution, C, to the equilibrium monomer concentration between the solid and the solution C_{eq}.

$$S = \frac{C}{C_{eq}}$$

(Equation 1.6)

The chemical potential difference between the supersaturated solution and the equilibrium state drives nucleation and is expressed as:

$$\Delta\mu = k_B T \ln(S)$$

(Equation 1.7)

where k_B is the Boltzmann's constant and T is the absolute temperature. A positive value of $\Delta\mu$ (which occurs when $S > 1$) indicates that the formation of the solid phase is thermodynamically favorable and drives nucleation. The magnitude of this driving force dictates both the critical nucleus size and the overall nucleation rate.

1.3.7.1 Classical Nucleation Theory

The nucleation theory provides the standard theoretical framework for modeling the kinetics of nucleation. Nanoscale systems differ from bulk materials because surface free energy becomes significant[131]. Forming a solid nucleus creates a new solid-liquid interface whose under-coordinated surface atoms carry higher energy, opposing the favorable bulk free-energy gain of crystallization. The total change in Gibbs free energy (ΔG) for the formation of a spherical particle of radius r is thus the sum of two competing terms: the volume free energy term (ΔG_V), which is negative and favors growth, and the surface free energy term (ΔG_S), which is positive and creates a barrier to formation.

$$\Delta G_{total}(r) = \Delta G_V + \Delta G_S$$

$$\Delta G_{total}(r) = \frac{4}{3}\pi r^3 \Delta G_v + 4\pi r^2 \gamma$$

(Equation 1.8)

where γ is the surface energy of the solid-liquid interface ΔG_v is the volume free-energy change per unit volume given by:

$$\Delta G_v = -\frac{k_B T \ln(S)}{v_m}$$

(Equation 1.9)

and v_m is the molar volume of the monomer unit in the crystal lattice. On substituting we get:

$$\Delta G_{total}(r) = 4\pi r^2\gamma - \frac{4}{3}\pi r^3 \frac{k_B T \ln(S)}{v_m}$$

(Equation 1.10)

The shape of this free-energy function reveals a nucleation barrier. At very small radii, the positive surface term dominates, making small clusters unstable and prone to dissolution. As the radius (r) increases, the negative volume term eventually prevails, causing the free energy $\Delta G(r)$ to peak and then decline (Figure 1.3.7). The radius at which $\Delta G(r)$ is maximal is termed the critical radius, r^* and the value of the free energy at this maximum is the nucleation barrier, ΔG^*.

The critical radius, $r^*$is determined by differentiating $\Delta G(r)$ with respect to r and setting the derivative to zero:

$$r^* = \frac{-2\gamma}{\Delta G_v} = \frac{2\gamma v_m}{k_B T \ln(S)}$$

(Equation 1.11)

and the nucleation barrier ΔG^* is given by:

$$\Delta G^* = \frac{16\pi\gamma^3}{3|\Delta G_v|^2} = \frac{16\pi\gamma^3 v_m^2}{3(k_B T \ln(S))^2}$$

(Equation 1.12)

The rate of nucleation, J, defined as the number of stable nuclei formed per unit volume per unit time, follows an Arrhenius-type relationship governed by the height of the energy barrier.

$$J = A \exp\left(-\frac{\Delta G^*}{k_B T}\right)$$

(Equation 1.13)

where A is a kinetic pre-exponential factor.

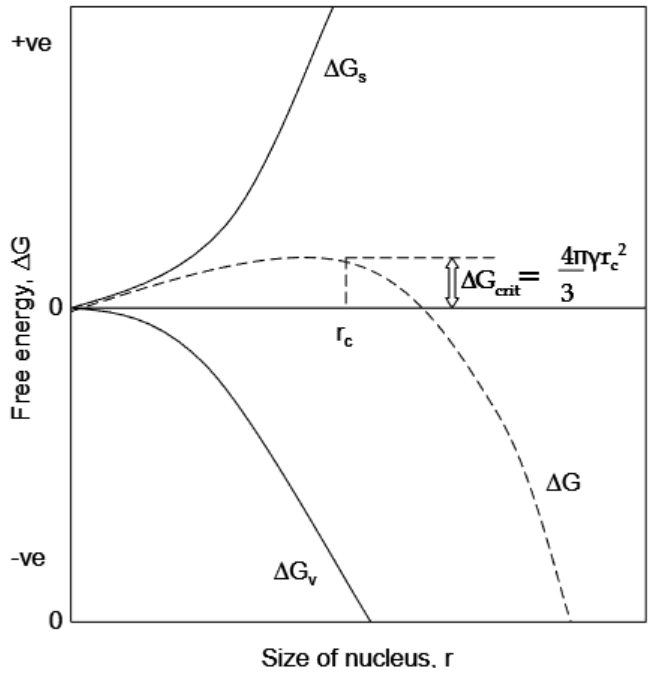

Figure 1.3.7. *Free-energy change as a function of nucleus radius. Adapted from ref.*[132]

1.3.7.2 The LaMer Model

The LaMer model describes how the evolution of monomer concentration controls nucleation and growth in colloidal nanocrystal synthesis (Figure 1.3.8). Originally developed in 1950 for sulfur sols, it remains the central framework for understanding how monodispersity arises from the temporal separation of nucleation and growth[133]. The LaMer model divides the synthesis reaction into three distinct temporal stages based on the monomer concentration $C(t)$.

In the first stage, monomer concentration increases by the conversion of precursors into reactive species. Once the concentration exceeds the equilibrium solubility C_{eq}, the system becomes supersaturated. Nucleation does not yet occur because the nucleation barrier ΔG^* remains high, placing the system in a metastable state.

As monomer generation continues, the concentration eventually reaches a critical supersaturation level C_{crit}, where the nucleation barrier ΔG^* becomes low enough for thermal fluctuations to initiate nucleation. The nucleation rate J rises sharply, producing a burst nucleation. Because these newly formed clusters consume monomers faster than they are generated, the monomer concentration quickly drops below C_{crit}, effectively terminating further nucleation. The solution remains supersaturated, allowing the existing nuclei to grow by consuming the remaining monomers. With no new nuclei forming, all particles share the same growth trajectory, promoting narrow size distributions. This stage of exclusive growth, driven by monomer diffusion to particle surfaces, is essential for achieving monodisperse QDs.

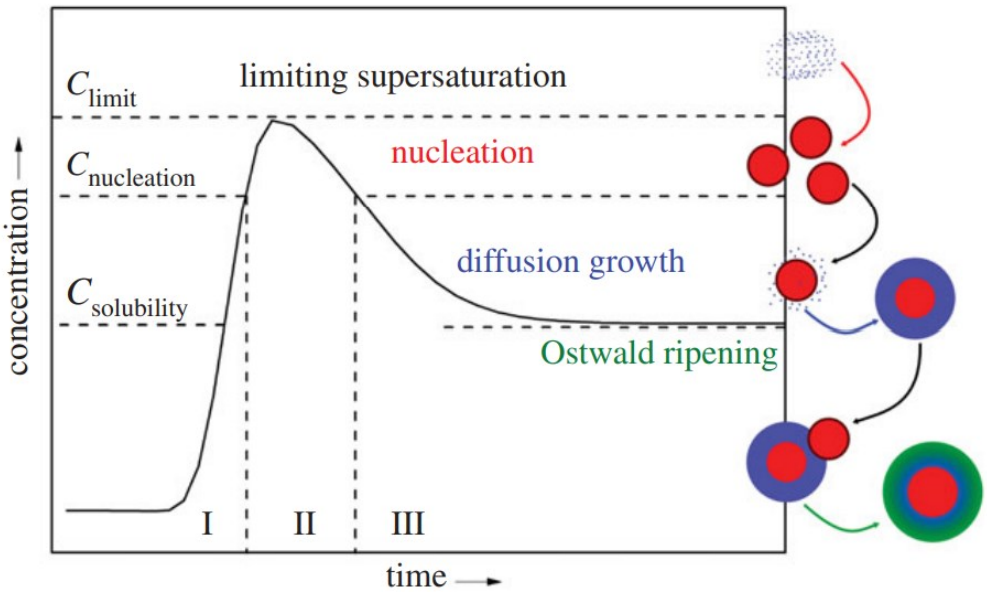

Figure 1.3.8. *Schematic LaMer model describing the evolution of monomer concentration during colloidal nanocrystal formation. Adapted with permission from ref.*[134]

1.3.7.3 Growth Kinetics

Once stable nuclei form, their subsequent size evolution is dictated by the kinetics of growth. The overall growth rate depends on both the transport of monomers to the nanocrystal surface and the surface reaction that incorporates these monomers into the lattice. This rate is governed by the general flux equation given by the Fick-s first law.

The growth of a spherical particle involves monomers diffusing through a boundary layer of thickness δ and then reacting at the surface. The flux J (moles/s) is given by steady-state diffusion:

$$J_{diff} = 4\pi r^2 D \frac{C_b - C_i}{\delta}$$

(Equation 1.14)

where D is the diffusion constant, C_b is concentration in the solution, C_i is the concentration at the particle interface. For small colloidal particles, the diffusion layer thickness δ is approximately equal to the particle radius r, simplifying the flux equation to

$$J_{diff} = 4\pi r D(C_b - C_i)$$

(Equation 1.15)

The reaction flux at the interface of the particle is given by

$$J_{reac} = 4\pi r^2 k_{reac}(C_i - C_r)$$

(Equation 1.16)

where k_{reac} is the surface reaction rate constant and C_r is the equilibrium solubility at the surface of the particle of radius r

Equating the fluxes, we get

$$\frac{dr}{dt} = \frac{v_m\,(C_b - C_r)}{\frac{r}{D} + \frac{1}{k_{reac}}}$$

(Equation 1.17)

Equation 1.17 shows the growth being modulated by two limiting regimes on the relative magnitude of diffusion time (r/D) and reaction time ($1/k_{reac}$).

When surface reaction is slow compared to diffusion ($k_{reac} \ll D/r$), the growth is reaction-limited growth, and the rate is given by:

$$\left(\frac{dr}{dt}\right)_{reac} = v_m k_{reac}(C_b - C_r)$$

(Equation 1.18)

In this regime, the growth is independent of the size, so the size distribution remains constant from nucleation to the growth.

When the surface reaction is fast ($k_{reac} \gg D/r$), the diffusion term dominates, and the growth is diffusion limited with the growth rate.

$$\left(\frac{dr}{dt}\right)_{diff} = \frac{D v_m (C_b - C_r)}{r}$$

(Equation 1.19)

Crucially, the growth rate is inversely proportional to the radius, implying smaller particles grow faster than larger particles, leading to a narrowing of the absolute size distribution. This phenomenon is termed size focusing and is the target regime for high-quality QD synthesis.

1.3.7.4 Growth regime

Once the monomer concentration falls below the nucleation threshold, particle formation stops, and growth becomes governed by surface energy driven mass transfer. Under these conditions, Ostwald ripening sets in, where smaller, high-curvature particles dissolve because their solubility is higher, while larger particles grow by consuming the released monomers[135]. As the bulk concentration decreases, this dissolution-reprecipitation process causes a characteristic broadening of the size distribution. The thermodynamic driving force for this process originates

from the Gibbs–Thomson relation, which states that solubility of a particle increases with decreasing radius[136].

$$C(r) = C_{eq} \exp\left(\frac{2\gamma V_m}{rRT}\right)$$

(Equation 1.20)

Under diffusion-controlled growth, the temporal evolution of particle radius follows:

$$\frac{dr}{dt} = K_D\left(\frac{1}{r} - \frac{1}{r^*}\right)$$

(Equation 1.21)

where K_D is the diffusion-limited growth rate constant and is defined as:

$$K_D = \frac{2\gamma D v_m^2 C_{eq}}{k_B T}$$

(Equation 1.22)

Plotting the $\frac{1}{K_D}\frac{dr}{dt}$ against r, yields a characteristic curve that divides the particle population into defocusing and focusing regimes (Figure 1.3.9).

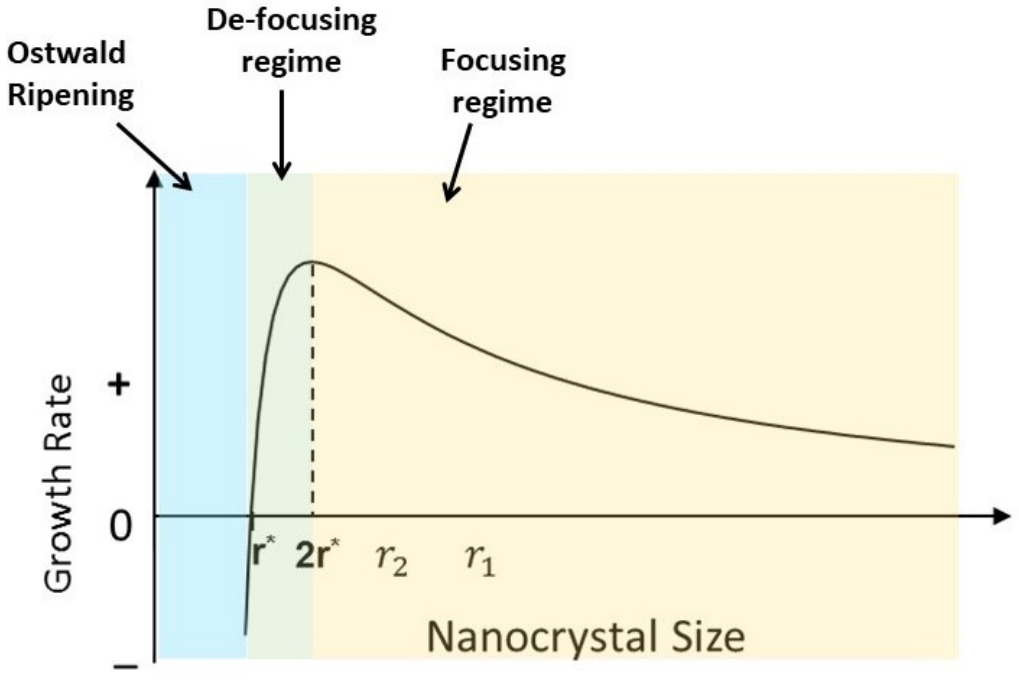

Figure 1.3.9. *Schematic representation of monomer concentration and particle growth dynamics in the classical LaMer mechanism.*

For $r < r^*$, the slope is negative showing negative growth rates i.e. dissolution, while the particles larger than r^* grows.

For $r^* < r < 2r^*$, larger particles grow faster than the smaller ones, which causes broadening in the size distribution. This is called the defocusing zone.

For $r > 2r^*$, the slope of the curvature changes and the larger particles grow slower than the smaller ones causing the size-focusing.

1.3.7.5 Physical Implications

From equation 1.11, the critical radius r^* is inversely proportional to the supersaturation S. Higher supersaturation lowers r^*,producing smaller critical nuclei, whereas reducing the supersaturation increases the r^* and favors larger nuclei. Supersaturation can be modulated either by changing the concentration of reactive monomers or by adjusting the temperature, since C_{eq} increases with temperature and thereby reduces S thermodynamically. However, increasing the temperature also accelerates the kinetics of precursor to monomer conversion, which may raise the monomer concentration and counteract the thermodynamic reduction in supersaturation. Thus, controlling particle size requires balancing these competing thermodynamic and kinetic effects to tune the effective supersaturation during nucleation.

From equation 1.12, the barrier height (ΔG^*) scales with the cube of the surface energy (γ^*). In colloidal synthesis, surface ligands (surfactants) play a crucial role by lowering the γ^* thereby reducing the barrier and promoting nucleation. The choice of ligands thus directly influences the number and size of nuclei formed.

Adjusting the precursor conversion rate is an effective strategy for controlling nanocrystal size. The final size of the QDs is largely determined by the number of nuclei formed during the nucleation burst. Highly reactive precursors convert rapidly to monomers, leading to the formation of large number of nuclei (i.e., small r^*), and consequently smaller final nanocrystals. In contrast, less reactive precursors generate monomers more slowly, produce fewer nuclei (i.e., large r^*), and ultimately yield larger particles (Figure 1.3.10).

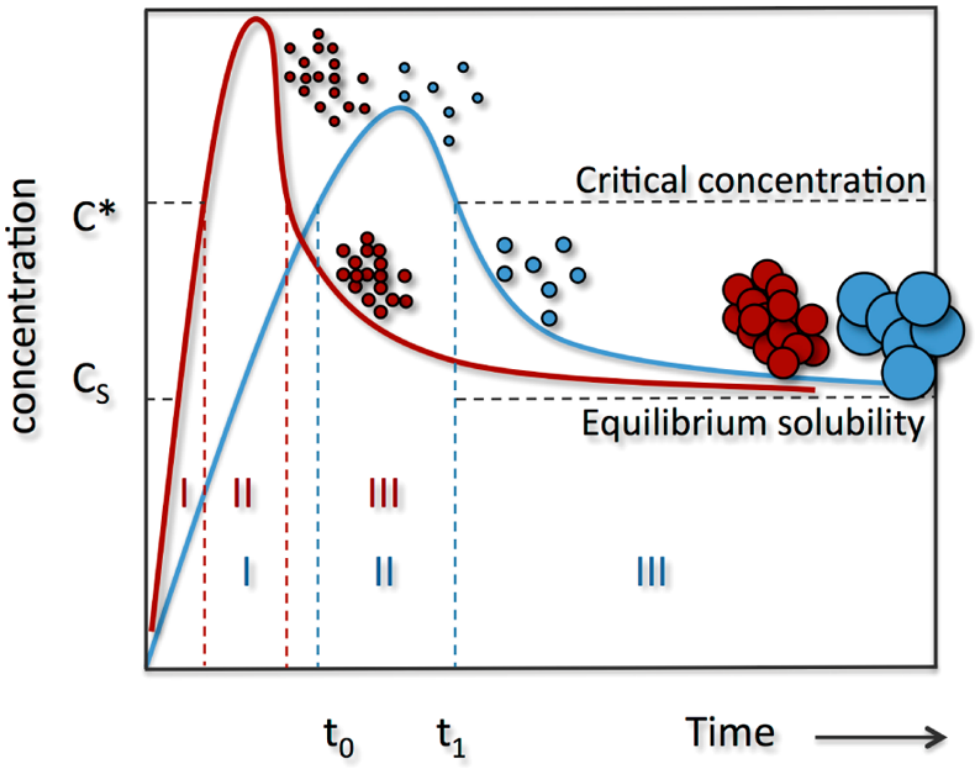

Figure 1.3.10. *LaMer plot comparing monodisperse nanocrystal formation from a highly reactive precursor (red) with rapid monomer generation and a less reactive precursor (blue). Adapted from ref.*[137]

After the available monomers are depleted, nanocrystal growth typically enters the Ostwald ripening regime, which broadens the size distribution. To prolong the growth phase while preserving size focusing, the monomer concentration must be maintained at a level that supports continued particle growth without triggering new nucleation. This can be achieved by supplying a controlled, continuous flux of precursor, ensuring that monomer generation persists as particles grow. Under these conditions, the system can enter a steady-state growth regime in which the rate of monomer formation is balanced by the rate at which growing particles consume monomers.

The concepts and implications outlined above form the basis for understanding the synthesis strategies employed in all subsequent chapters using two main synthesis methodologies.

The hot-injection method is a cornerstone of colloidal nanocrystal synthesis, offering precise control over nucleation and growth by separating these processes in time. In this approach, reactive precursors are rapidly injected into a hot coordinating solvent, producing a sudden supersaturation burst that trigger instantaneous nucleation as described by LaMer's model, followed by controlled growth of a uniform particle population[85]. However, its reliance on steep thermal gradients and millisecond-scale mixing poses major scalability challenges, since temperature inhomogeneity, incomplete mixing, and the reactivity of certain precursors become increasingly difficult to control in larger volumes. Despite these constraints, hot injection remains the most effective route for obtaining high-quality, monodisperse colloidal QDs.

The heat-up (non-injection) method involves mixing all precursors at lower temperature and gradually heating the reaction so that precursor conversion, nucleation, and growth proceed in a thermally controlled sequence rather than through a sudden supersaturation burst. Because nucleation spans a broader temperature range, size distributions can be wider, but the method offers excellent reproducibility and scalability since it avoids rapid injection and relies on gradual thermal activation[138].

1.4 SWIR nanomaterials

1.4.1 Pre-nanomaterials era

William Herschel's discovery of infrared radiation in 1800s laid the foundation for IR science, but practical SWIR detection did not emerge until the mid-twentieth century with the development of narrow-bandgap semiconductors. The first practical infrared photodetectors were based on polycrystalline lead salts. In 1933, Kutzscher demonstrated strong photoconductivity in lead sulfide (PbS) up to roughly 3 µm, marking a decisive shift away from slow thermal detectors. During the 1940s and 1950s, advances in the processing of PbS, PbSe, and PbTe films established these materials as the core of early night-vision and missile-tracking systems. At the same time, germanium photodiodes, including extrinsically doped variants, were developed to extend sensitivity to longer infrared wavelengths[1]. A major milestone occurred in 1959 with Lawson's discovery of the tunable $Hg_{1-x}Cd_xTe$ alloy system, which enabled continuous spectral coverage from the SWIR to the Long-wave Infrared (LWIR)[139]. By the 1960s and 1970s, MCT and InSb photodiodes supported the first infrared focal-plane arrays, although these devices generally required cryogenic operation.

The modern SWIR era emerged with the advancement of III-V epitaxial growth, beginning with liquid-phase epitaxy and later refined through high-precision techniques such as metal-organic chemical vapor deposition and MBE. These developments enabled the high-quality growth of $In_{0.53}Ga_{0.47}As$ lattice-matched to InP, an alloy with a room-temperature bandgap of 0.74 eV and a cutoff near 1.7 µm. Here, the cutoff refers to the maximum wavelength at which the material can absorb or detect photons. This material rapidly became the standard for telecommunications and low-light imaging. By the 1990s, InGaAs focal-plane arrays achieved low dark currents and detectivities exceeding 10^{14}Jones[140, 141]. A recent breakthrough occurred in 2020 with Sony's copper-to-copper hybridization technique, which allowed wafer-level bonding without indium bumps and enabled 5 µm-pitch InGaAs sensors[142].

Despite these advances, epitaxial SWIR materials remain costly and limited by substrate constraints, wafer size, and complex integration as described in section 1.2.2. These limitations prompted the move toward solution-processed nanomaterials, including SWIR absorbing and emitting CQDs.

1.4.2 SWIR CQDs

The development of colloidal SWIR QDs emerged directly from advances in visible CdSe nanocrystals in the 1990s, when reliable hot-injection chemistry enabled precise control over size and optical properties[85]. With these methods established, researchers turned to narrow-bandgap IV-VI semiconductors to achieve CQDs with emission in the infrared. A major breakthrough was achieved by Hines and Scholes in 2003, who reported the organometallic synthesis of high-quality, monodisperse PbS nanocrystals with size-tunable near-infrared emission extending to approximately 1.3-1.4 µm. This work is widely regarded as the first demonstration of practical SWIR-capable colloidal QDs[143]. Shortly thereafter, Bakueva and co-workers showed electroluminescence from PbS nanocrystals spanning 1000-1600 nm in polymer LEDs, providing one of the earliest device examples covering the telecom and SWIR bands[144]. Throughout the 2000s, PbS and PbSe QDs rapidly became the dominant solution-processed SWIR materials, powering early advances in infrared photovoltaics and photodetectors. A pivotal contribution came from Sargent's group, who demonstrated the first solution-processed PbS-based infrared photodetector and showed that colloidal nanocrystals could extend polymer photodiodes well beyond their intrinsic 800 nm limit[145]. Together, these developments established lead chalcogenides as the foundational materials and defined the basic synthetic and electronic principles that guided the first generation of colloidal SWIR QDs[146].

To access longer infrared wavelengths, researchers turned to mercury chalcogenides such as HgTe and HgSe. Early aqueous HgTe QDs with NIR electroluminescence were reported in 2005 by O'Connor et al. marking one of the first demonstrations of HgTe-based colloidal IR LEDs[147]. This was followed by Kovalenko's 2006 synthesis of nanocrystals with ultranarrow, widely tunable bandgaps spanning the telecom to mid-IR range[148]. Keuleyan et al. later in 2011, extended this tunability from ~1.3 to nearly 5 µm[149, 150]. Together, these advances established Hg-chalcogenides as the most spectrally flexible CQDs, enabling SWIR–MWIR detection and room-temperature FPAs.

As Pb- and Hg-based CQDs advanced, their use in NIR-II/SWIR bioimaging emerged, with PbS QDs enabling deep-tissue fluorescence beyond 1000 nm. However, their intrinsic toxicity limited biomedical and consumer applications, prompting a global shift toward environmentally benign, RoHS-compliant SWIR nanomaterials[151]. The first significant "greener" SWIR CQDs were silver chalcogenides. Du et al. (2010) introduced Ag_2S QDs emitting near 1058 nm, and later studies established Ag_2S and Ag_2Se as bright, biocompatible NIR-II probes (1.0-1.4 µm)[152]. In parallel, I-III-VI semiconductors such as $CuInS_2$, $CuInSe_2$ and $AgInSe_2$ offered reduced toxicity and moderate infrared tunability, forming an essential bridge between toxic chalcogenides and fully RoHS-compliant SWIR nanomaterials[153, 154].

A major advance in SWIR nanomaterials came with the emergence of III-V pnictide CQDs, particularly InAs and InSb[155, 156]. Although explored since the late 1990s, early InAs syntheses in the mid-2000s suffered from poor size control and optical quality. This changed in the mid-2010s with continuous-injection strategies, improved arsenic precursors, and refined ligand chemistry,

enabling high-quality InAs CQDs with narrow linewidths and tunability from ~900 to 1800 nm[157]. Further progress in reducing-agent chemistry, seeded growth, and ZnSe passivation enhanced stability and PL efficiency[158, 159]. InSb CQDs, featuring an even narrower band-gap, have more recently emerged as promising candidates for deeper SWIR sensing[160, 161].

1.4.3 The RoHS directive

The EU Restriction of Hazardous Substances (RoHS) Directive is the primary regulatory framework governing the use of toxic materials in electrical and electronic equipment (EEE). The original RoHS 1 (Directive 2002/95/EC) was recast as RoHS 2 (Directive 2011/65/EU), amended by 2015/863/EU, and now applies to nearly all EEE placed on the EU market. Its objective is to protect human health and the environment by restricting hazardous substances and reducing the toxicity of electronic waste, while encouraging the use of safer alternatives. RoHS functions as a negative list, meaning it bans only those substances explicitly named in Annex II; materials not included in this list are considered compliant by default[162, 163].

1.4.3.1 Restricted substances and limit values

Annex II of Directive 2011/65/EU currently restricts ten substances or substance groups: lead (Pb), mercury (Hg), cadmium (Cd), hexavalent chromium [Cr(VI)], polybrominated biphenyls (PBB), polybrominated diphenyl ethers (PBDE), and four phthalates [DEHP, BBP, DBP, DIBP].

The maximum concentration values tolerated **per homogeneous material** are:

- Pb: 0.1 wt%
- Hg: 0.1 wt%
- Cd: 0.01 wt%
- Cr(VI): 0.1 wt%
- PBBs and PBDEs: 0.1 wt%
- DEHP, BBP, DBP, DIBP: 0.1 wt%

1.4.3.2 RoHS restricted SWIR CQDs

SWIR CQDs have historically been based on II-VI and IV-VI semiconductors such as PbS, PbSe, PbTe, and HgTe because of their narrow bandgaps and strong absorption. However, these materials intrinsically contain large amounts of Pb or Hg, placing them far above the RoHS limit of 0.1 wt% per homogeneous material. For example, PbS consists of lead and sulfur in a 1:1 ratio, and lead accounts for ~86% of its molar mass. Even after considering the organic ligands present in colloidal QDs, the lead content of a PbS CQD typically remains between 40% and 70% by weight. Such compositions cannot be engineered below the regulatory threshold without eliminating the material's identity. As a result, any device incorporating Pb- or Hg-based CQDs is inherently non-compliant unless covered by a specific exemption. This regulatory barrier remains a major obstacle to the commercialization of heavy-metal SWIR CQD technologies. RoHS Article 5 permits exemptions only when substitution is technically impossible or when replacing a restricted substance would cause greater environmental, health, or safety harm than it prevents.

This framework creates a major commercial limitation for Pb-based SWIR materials because none of the existing exemptions apply to high-volume consumer electronics. Smartphones, classified under Category 2 or 4, have no standing exemption that allows lead in infrared detectors; the available exemptions apply mainly to medical and industrial equipment (Categories 8 and 9) and are limited to uses such as solders or glass, not the active layers of consumer sensors. Consequently, PbS CQDs are effectively excluded from the consumer market despite their strong performance.

1.4.3.3 Inherent Toxicity of Pb- and Hg- based CQDs

A major regulatory concern with Pb- and Hg-based CQDs arises from their environmental fate when disposed in landfills, where acidic leachates can mobilize toxic ions. The Toxicity Characteristic Leaching Procedure is the standard test simulating a landfill's mildly acidic (~ pH 5) environment and quantifies heavy metal release[164]. Materials with high bond ionicity are especially vulnerable to acid attack, for instance, the Pb-S bond in Lead sulfide (PbS) has a Philips ionicity of ~0.77, rendering the lattice amenable to dissolution and release of Pb^{2+} ions under acidic leaching. Experimental studies demonstrate that PbS films and QDs release significant Pb concentrations under oxidative or acidic stress once organic ligands degrade in landfill conditions. Once released, Pb^{2+} behaves as a potent neurotoxin by mimicking Ca^{2+} and crossing the blood-brain barrier, disrupting neurotransmitter release and synaptic plasticity[165, 166]. On the other hand, Hg^{2+} from degraded HgTe QDs can bind protein sulfhydryl groups, impair enzyme function, and bioaccumulate as methylmercury in aquatic food chains[167]. The release of these ions into soil and groundwater therefore presents long-term ecological and health risks, underpinning the stringent exclusion of Pb and Hg CQDs from consumer-electronics waste streams.

1.4.3.4 RoHS compliant materials

Among RoHS-compliant SWIR materials, three main colloidal QD families have emerged: III–V pnictides, silver chalcogenides, and I-III-VI chalcogenides. I-III-VI chalcopyrites[168] such as $CuInS_2$, $CuInSe_2$, and $AgInSe_2$ are considered low-toxicity alternatives, but their ternary cation lattice introduces substantial compositional disorder and sensitivity to stoichiometry. Small deviations in the Cu:In ratio create off-stoichiometry and defect-rich surfaces, and their emission is dominated by donor-acceptor pair recombination rather than clean band-edge transitions. As a result, these materials exhibit broad linewidths, poorly defined absorption edges, and significant batch-to-batch variability[169, 170].

Silver chalcogenides (Ag_2S, Ag_2Se, Ag_2Te) are attractive for their biocompatibility[171] and low-temperature processing[172], but their electronic structure imposes significant limitations. These QDs exhibit weak quantum confinement, low oscillator strengths, and a strong tendency toward self-doping arising from Ag-deficient stoichiometries. A major challenge is the exceptionally high mobility of Ag^+ ions, which gives these materials superionic character and allows ion migration under light or electrical bias. Such movement destabilizes the lattice, increases dark current, and accelerates structural degradation in operating devices[169].

The III-V semiconductor family includes InP, InAs, and InSb. While InP QDs are well developed, their optical absorption remains largely confined to the UV-visible region, limiting their usefulness in the SWIR[173]. InAs and InSb, by contrast, possess much narrower bandgaps that align with the NIR and SWIR spectral ranges. However, the ultranarrow bulk bandgap of InSb results in inherently high intrinsic carrier densities and elevated dark currents at room temperature, which degrade noise performance and bias stability in photodetectors. In addition, Sb-based precursor chemistries are highly reactive and difficult to control, often producing broader size distributions and surfaces that are more susceptible to oxidation[169].

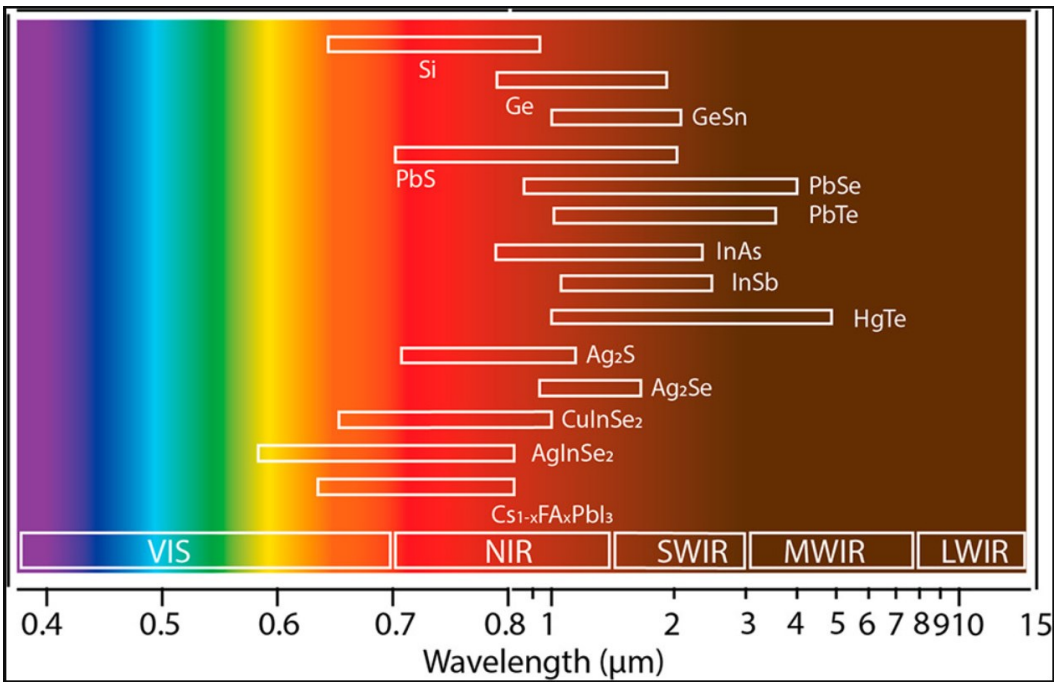

Figure 1.4.1. *Emission wavelength range of representative infrared QDs discussed in section 1.4. Adapted with permission from ref.[168]*

1.4.3.5 InAs and the arsenic paradox

A frequent source of confusion in the field of infrared optoelectronics is the permissibility of InAs QDs under environmental regulations, despite arsenic's well-known toxicity. This so-called "Arsenic Paradox" arises from the differing scopes and mechanisms of EU regulations. The RoHS Directive (2011/65/EU) restricts a fixed list of hazardous substances in electronics, in which arsenic is not included, making InAs RoHS-compliant. In contrast, REACH (Registration, Evaluation, Authorization and Restriction of Chemicals) adopts a broader chemical safety lens. Under REACH Annex XVII, certain arsenic compounds are restricted, primarily in high-exposure contexts such as anti-fouling marine paints, wood preservatives, and water treatment applications[174]. While certain arsenic compounds (e.g., As_2O_3) are listed as Substances of Very High Concern under REACH, the use of III-V materials in sealed electronics is considered to pose negligible exposure risk, and thus remains permitted. From a materials science perspective, the In-As bond is markedly more covalent than that of Pb-S (Phillips ionicity ~0.36 vs. 0.77), resulting

in stronger directional bonding and enhanced chemical stability. This reduced ionicity implies that arsenic remains tightly bound in the InAs lattice, with minimal potential for leaching under typical environmental or physiological conditions. Thus, InAs represents a unique regulatory and chemical exception: a compound containing a toxic element, yet permissible under RoHS and not subject to REACH prohibitions for its current use-case, owing to both its robust lattice chemistry and low exposure profile.

1.4.4 Colloidal InAs QDs

Colloidal InAs QDs have emerged as one of the most promising RoHS-compliant materials for active SWIR optoelectronics because they combine deep spectral tunability, strong quantum confinement, and exceptional chemical stability. InAs possesses a narrow bulk bandgap of 0.35 eV at room temperature, a zinc blende crystal structure, and highly covalent In-As bonds with a low Philips ionicity of 0.36[175]. This high covalency reduces susceptibility to hydrolytic degradation and limits the release of arsenic species in aqueous environments, while also giving rise to a large exciton Bohr radius of about 31 nm[176]. As a result, size-dependent optical properties persist even in relatively large nanocrystals, enabling continuous tuning across the Visible-NIR-SWIR region[177].

Despite these intrinsic advantages, the synthesis of high-quality InAs QDs has historically lagged behind that of Cd-, Pb-, and Hg-based systems due to the limited availability of suitable arsenic precursors. The high covalency of the In-As bond necessitates elevated reaction temperatures for nucleation and growth, making it more difficult to control size, polydispersity, and reaction kinetics compared with II-VI and IV-VI QDs, where a broad range of precursors enables precise tunability[177]. Surface chemistry poses an additional challenge. Unpassivated dangling bonds generate surface states that trap photogenerated carriers and quench emission. While trap states in more ionic semiconductors are relatively shallow and easier to neutralize, their depth increases with covalency, leading InAs to form deep traps that severely reduce PL efficiency. Achieving bright emission typically requires overcoating the core with a type-I shell, but the large lattice mismatch between InAs (6.06 Å) and Cd-free wide-bandgap materials such as ZnSe and ZnS induces significant interfacial strain. This strain fosters defect formation at the core-shell interface, creating additional trap sites and limiting PLQY in conventional core/shell structures.

Given these challenges and opportunities, it becomes important to trace how colloidal InAs QDs have developed over time and how their synthetic foundations were established in the literature.

1.4.4.1 Foundation of colloidal InAs QDs: The $(TMS)_3As$ route

The first wet-chemical synthesis of InAs was reported by Wells and co-workers in 1989 and relied on a dehalosilylation reaction between indium(III) chloride ($InCl_3$) and tris(trimethylsilyl)arsine ($(TMS)_3As$)[156]. In their protocol, a solution of $InCl_3$ and $(TMS)_3As$ in pentane was stirred at room temperature for several days and then heated in benzene at 70–75°C to promote InAs formation. The resulting solids were subsequently heated to 150°C overnight and subjected to a brief high-temperature annealing step to remove volatile byproducts such as Me_3SiCl, ultimately yielding nanocrystalline InAs with purity approaching 99.7% after optimization. Although the material was

essentially non-emissive and exhibited an average crystallite size of about 10 nm, this work marked an important milestone by establishing the first true solution-phase route to III-V semiconductors at a time when such materials were almost exclusively prepared by epitaxial routes[178, 179]. A few years later, in 1996, Guzelian et al. adapted this chemistry to a higher-temperature regime by using TOP as both solvent and coordinating ligand and performing a heat-up synthesis at 240-265 °C[155]. After size-selective precipitation of the products, they isolated InAs QDs with size-tunable band-edge emission between 850 and 1200 nm, providing the first clear demonstration of quantum confinement in colloidal InAs.

Inspired by Murray's seminal hot-injection synthesis of CdSe QDs, Peng, Battaglia, and co-workers introduced the first hot-injection protocols for colloidal InAs in 1998[180, 181]. In this approach, $(TMS)_3As$ was rapidly injected into a hot mixture of indium precursors ($In(Ac)_3$ or $InCl_3$), long-chain carboxylic acids (palmitic or myristic acid), and high-boiling solvents like 1-octadecene (ODE) or TOP. This method quickly replaced the earlier low-temperature dehalosilylation route, offering faster reactions, better control over nucleation and growth, and tunable optical properties extending from the visible-NIR boundary into the SWIR. Over the following decade, the $(TMS)_3As$ hot-injection route became the standard strategy for producing colloidal InAs. However, its effectiveness was constrained by the extremely high reactivity of $(TMS)_3As$, which converts almost instantaneously upon injection, producing a very brief nucleation burst and rapid monomer depletion. As a result, growth proceeds largely through Ostwald ripening, leading to broad size distributions even under optimized conditions[177]. Efforts to moderate precursor reactivity by synthesizing bulkier or less labile silylarsines, such as tris(isopropyldimethylsilyl)arsine and tris(trimethylgermyl)arsine, yielded only modest improvements. Notably, even changes in precursor reactivity spanning 2-3 orders of magnitude produced negligible effects on growth kinetics or size broadening, highlighting the intrinsic limitations of silylarsine-based arsenic chemistry[182].

1.4.4.2 Modified synthetic strategy: the seeded growth approach.

The focus then shifted from altering precursor reactivity to engineering the synthesis kinetics, particularly by modulating the growth phase to suppress ripening and maintain size focusing. A landmark advancement came from Franke et al.[159], who demonstrated a multiple-injection strategy in which only a small, sub-stoichiometric portion of the arsenic precursor (As/In ~10%) was used to nucleate InAs seeds, followed by the slow continuous injection of the remaining precursor, that maintains the reaction in a size-focused regime. Using $(TMGe)_3As$ and indium(III) acetate, this approach produced large, monodisperse InAs QDs with narrow emission linewidths (<135 meV) tunable from 700 to 1200 nm, without post-synthetic size selection. Crucially, they observed identical QD sizes and distribution when using fast-reacting precursors such as $(TMS)_3As$ or slower precursors such as triisopropylsilylarsine, demonstrating that monomer feed rate governs the growth rather than precursor reactivity.

A complementary strategy to continuous injection is the seeded-growth approach that uses pre-formed InAs clusters as controlled monomer reservoirs. In the seminal work of Tamang et al.,~2.5

nm InAs seeds were first obtained by hot injection, while amorphous InAs nanoclusters were generated separately at room temperature from $(TMS)_3As$ and indium oleate in 1-octadecene[183]. These clusters, which exhibit characteristic absorption features at 420-460 nm and behave as atomically precise, magic-sized precursors, were then slowly injected into the seed reaction mixture. Because the clusters release monomers under diffusion control, seed growth proceeded in a strong size-focusing regime, producing InAs QDs of ~5-6 nm with sharply defined excitonic peaks (HWHM 60-80 meV), comparable to high-quality PbS nanocrystals. A key advantage of this method is that the final QD size is governed solely by the total amount of cluster solution delivered, enabling highly tunable synthetic route.

This seeded-growth strategy was further refined by Song et al., who incorporated dioctylamine (DOA) throughout the synthesis, including during cluster preparation, to moderate the high reactivity of $(TMS)_3As$[184]. Although the exact mechanism remains unclear, DOA enabled more controlled nucleation and growth when DOA-derived clusters were added continuously, allowing finer size tunability of both seeds and final QDs. Building on this foundation, Kim et al. introduced a diffusion-dynamics-controlled injection method in which InAs cluster precursors were injected into 1.4 nm seeds at precisely regulated rates[185]. By maintaining the monomer supply rate below the monomer consumption rate of the seeds, the authors ensured that growth remained firmly in a supply-limited, size-focusing regime. This kinetic control allowed growth of larger InAs QDs extending upto 9nm, with excitonic feature around 1600 nm, with remarkably narrow size distributions (HWHM ~60 meV), producing record InAs QDs. Although this represents the most effective synthesis strategy reported to date, it presents intrinsic limitations that are discussed in detail in Chapter 2.

1.4.4.3 Alternative arsenic precursors

Although the $(TMS)_3As$ route yields InAs QDs with excellent optical quality, it is limited by significant practical constraints. $(TMS)_3As$ is highly pyrophoric, extremely expensive with limited commercial availability. Its As^{3-} makes Si-As bonds highly prone to oxidation, and exposure to air or moisture rapidly produces exothermic Si-O bond formation and releases hazardous arsenic hydrides such as arsine (AsH_3). These safety and cost issues severely restrict the scalability of the $(TMS)_3As$ approach and motivate the search for alternative arsenic precursor.

Early efforts to replace $(TMS)_3As$ focused on safer, less reactive organoarsenic precursors, but none yielded high-quality InAs QDs. Uesugi et al. showed that triphenylarsine ($AsPh_3$), an air-stable and commercially accessible precursor, could generate NIR-tunable InAs nanocrystals by heating mixtures of In-oleate and $AsPh_3$[186, 187]. However, its strong As-C bonds release arsenic too slowly, requiring prolonged high-temperature reactions in which nucleation and growth overlap, producing broad size distributions and modest PLQYs. Similar limitations were seen with arsenic silylamides $[(Me_3Si)_2N]_2AsCl$ and dimers such as $[tBu_2As(NEt_2)]_2$. Although they form InAs, their insufficient reactivity prevents sustained size focusing[188-190]. Arsenic halides like $AsCl_3$, used with strong hydride reductants (e.g., $LiEt_3BH$ in oleylamine), avoided organosilicon by-products but reintroduced pyrophoric hazards and still failed to provide adequate nucleation control[190, 191].

1.4.4.4 InAs CQDs through the tris(dimethylamino)arsine route

A major step toward safer and more scalable InAs QD synthesis was achieved with tris(dimethylamino)arsine ($As(NMe_2)_3$, amino-As), a bench-stable and inexpensive precursor. Green et al. showed that heating $InCl_3$ with amino-As could form InAs QDs, though only after long reaction times and with broad dispersity and low PLQY[192]. The crucial advantage of amino-As emerged when its reactivity was controlled by introducing a separate reducing agent. Griegel et al. developed a two-step hot-injection method in which amino-As undergoes transamination with indium halides in oleylamine to generate tris(oleylamino)arsine, followed by the injection of a reducing agent such as tris(dimethylamino)phosphine[193]. The reducing agent plays a central role by converting As^{3+} into As^{3-}, generating the reactive arsenide monomers required for InAs formation. Srivastava et al. demonstrated that tuning the reducing agent's strength directly modulates the rate of monomer release, thereby governing nucleation and growth kinetics and allowing precise control over QD size and size distribution[194, 195].

Although amino-As proved a promising alternative arsenic precursor, it generally did not match the optical quality of $(TMS)_3As$ based QDs. Recent efforts sought to overcome these limitations. Kim et al. extended InAs absorption to ~1700 nm using diisobutylaluminum hydride (DIBAL-H) and lithium bis(trimethylsilyl)amide[157], while Leemans et al. used aminophosphines to produce In(As,P) QDs tunable to ~1600 nm[196]. More recently, Skorotetcky et al. employed a continuous-injection strategy using hexamethyltrisiloxane (HMTS) as the reducing agent, achieving amino-As based InAs QDs absorbing up to ~1550 nm[197]. Although these advances successfully extended size tunability into the SWIR range, they consistently fell short in achieving high PL efficiency. This challenge is analyzed in depth in Chapter 3, where the limitations of the amino-As route are addressed and strategies for achieving high-PLQY SWIR-emissive InAs QDs are presented.

1.5 References

1. Rogalski, A., History of infrared detectors. *Opto-Electronics Review* **2012,** *20* (3), 279-308.
2. Hashagen, J., Seeing Beyond the Visible. *Optik & Photonik* **2015,** *10* (3), 34-37.
3. Craig F. Bohren, D. R. H., Absorption and Scattering by an Arbitrary Particle. In *Absorption and Scattering of Light by Small Particles*, 1998; pp 57-81.
4. Hong, G.; Diao, S.; Antaris, A. L.; Dai, H., Carbon Nanomaterials for Biological Imaging and Nanomedicinal Therapy. *Chemical Reviews* **2015,** *115* (19), 10816-10906.
5. Wilson, R.; Nadeau, K.; Jaworski, F.; Tromberg, B.; Durkin, A., Review of short-wave infrared spectroscopy and imaging methods for biological tissue characterization. *Journal of Biomedical Optics* **2015,** *20* (3), 030901.
6. Nouchi, P.; de Montmorillon, L.-A.; Sillard, P.; Bertaina, A.; Guenot, P., Optical fiber design for wavelength-multiplexed transmission. *Comptes Rendus Physique* **2003,** *4* (1), 29-39.
7. Wang, Y.; Wu, H.; Rodà, C.; Peng, L.; Taghipour, N.; Dosil, M.; Konstantatos, G., Shortwave Infrared Light Detection and Ranging Using Silver Telluride Quantum Dots. *Advanced Materials* **2025,** *37* (21), 2500977.
8. Laser Safety Guide. https://lasersafety.com/resources/laser-safety-guide/ (accessed 02/12/2025).
9. Miya, T.; Terunuma, Y.; Hosaka, T.; Miyashita, T., Ultimate low-loss single-mode fibre at 1.55 µm. *Electronics Letters* **1979,** *15* (4), 106-108.
10. Desurvire, E., *Erbium-Doped Fiber Amplifiers: Principles and Applications*. Wiley: 2002.
11. Kirsch, D. C.; Chen, S.; Sidharthan, R.; Chen, Y.; Yoo, S.; Chernysheva, M., Short-wave IR ultrafast fiber laser systems: Current challenges and prospective applications. *Journal of Applied Physics* **2020,** *128* (18).
12. Manor, H.; Arnon, S., Performance of an optical wireless communication system as a function of wavelength. *Appl. Opt.* **2003,** *42* (21), 4285-4294.
13. Li, L.; Zhang, R.; Zhao, Z.; Xie, G.; Liao, P.; Pang, K.; Song, H.; Liu, C.; Ren, Y.; Labroille, G.; Jian, P.; Starodubov, D.; Lynn, B.; Bock, R.; Tur, M.; Willner, A. E., High-Capacity Free-Space Optical Communications Between a Ground Transmitter and a Ground Receiver via a UAV Using Multiplexing of Multiple Orbital-Angular-Momentum Beams. *Scientific Reports* **2017,** *7* (1), 17427.
14. Fischer, K. W.; Witiw, M. R.; Eisenberg, E., Optical attenuation in fog at a wavelength of 1.55 micrometers. *Atmospheric Research* **2008,** *87* (3), 252-258.
15. Brouillette, C.; Huang, H.; Smith, W.; Farquharson, S., Raman spectroscopy using 1550 nm (retina-safe) laser excitation. *Appl Spectrosc* **2011,** *65* (5), 561-3.
16. Andor, O. I. Free Space Optical Communications and Adaptive Optics with C-RED 3. https://andor.oxinst.com/learning/view/article/free-space-optical-communications-and-adaptive-optics-with-c-red-3 (accessed 02/12/2025).
17. Vandersmissen, R. Short-wave infrared cameras in semiconductor inspection applications. https://www.exosens.com/node/146434 (accessed 02/12/2025).
18. Silicon Block Inspection with SWIR Imaging. https://www.techbriefs.com/component/content/article/12234-silicon-block-inspection-with-swir-imaging (accessed 02/12/2025

).

19. R.J. Wilson, I. SWIR Cameras, Lenses, and Lighting. https://rjwilson.com/cameras-swir-imaging/swir-imaging/ (accessed 02/12/2025).
20. Yan, F.; Johnston, S.; Zaunbrecher, K.; Al-Jassim, M.; Sidelkheir, O.; Blosse, A. In *Defect-bandemission photoluminescence imagingonmulti-crystallinesisolar cells*, 2011 37th IEEE Photovoltaic Specialists Conference, 19-24 June 2011; 2011; pp 002231-002235.
21. Richter, J.; Lorenz, S.; Kaas, A.; Fuchs, M.; Röder, C.; Peuker, U. A.; Heitmann, J.; Gloaguen, R., Spectral Characterization of Battery Components from Li-Ion Battery Recycling Processes. *Metals* **2024,** *14* (2), 147.
22. Crumley, R. How UV and SWIR are Revolutionizing Industrial Vision Systems. https://www.balluff.com/en-us/blog/how-uv-and-swir-are-revolutionizing-industrial-vision-systems (accessed 02/12/2025).
23. Semicon, S. Short-Wavelength InfraRed Image Sensor Technology SenSWIR™. https://www.sony-semicon.com/en/technology/industry/senswir.html#section-12 (accessed 02/12/2025).
24. Wang, W.; Paliwal, J., Near-infrared spectroscopy and imaging in food quality and safety. *Sensing and Instrumentation for Food Quality and Safety* **2007,** *1* (4), 193-207.
25. Allen, T.; Beard, P.; Hall, A.; Dhillon, A.; Owen, J., Spectroscopic photoacoustic imaging of lipid-rich plaques in the human aorta in the 740 to 1400 nm wavelength range. *Journal of Biomedical Optics* **2012,** *17* (6), 061209.
26. Fodor, M.; Matkovits, A.; Benes, E. L.; Jókai, Z., The Role of Near-Infrared Spectroscopy in Food Quality Assurance: A Review of the Past Two Decades. *Foods* **2024,** *13* (21), 3501.
27. Lorente, D.; Aleixos, N.; Gómez-Sanchis, J.; Cubero, S.; García-Navarrete, O. L.; Blasco, J., Recent Advances and Applications of Hyperspectral Imaging for Fruit and Vegetable Quality Assessment. *Food and Bioprocess Technology* **2012,** *5* (4), 1121-1142.
28. Kays, S. E.; Archibald, D. D.; Sohn, M., Prediction of fat in intact cereal food products using near-infrared reflectance spectroscopy. *Journal of the Science of Food and Agriculture* **2005,** *85* (9), 1596-1602.
29. Zhang, D.; Lee, D.-J.; Tippetts, B. J.; Lillywhite, K. D., Date quality evaluation using short-wave infrared imaging. *Journal of Food Engineering* **2014,** *141*, 74-84.
30. Lee, H.; Kim, M. S.; Lohumi, S.; Cho, B.-K., Detection of melamine in milk powder using MCT-based short-wave infrared hyperspectral imaging system. *Food Additives & Contaminants: Part A* **2018,** *35* (6), 1027-1037.
31. Ozturk, S.; Bowler, A.; Rady, A.; Watson, N. J., Near-infrared spectroscopy and machine learning for classification of food powders during a continuous process. *Journal of Food Engineering* **2023,** *341*, 111339.
32. Focus, P. https://www.photonfocus.com/industries/food-processing/quality-control/ (accessed 02/12/2025).
33. Kim, E. J.; Kim, J. H.; Kim, M. S.; Jeong, S. H.; Choi, D. H., Process Analytical Technology Tools for Monitoring Pharmaceutical Unit Operations: A Control Strategy for Continuous Process Verification. *Pharmaceutics* **2021,** *13* (6).
34. Kim, D.-W.; Park, J.-B.; Lee, S.-H.; Weon, K.-Y., Development of a Process Analytical Technology(PAT) method using near-infrared spectroscopy system for evaluating an active coating process for a low-dose drug. *Journal of Drug Delivery Science and Technology* **2017,** *39*, 8-15.

35. Sulub, Y.; LoBrutto, R.; Vivilecchia, R.; Wabuyele, B. W., Content uniformity determination of pharmaceutical tablets using five near-infrared reflectance spectrometers: a process analytical technology (PAT) approach using robust multivariate calibration transfer algorithms. *Anal Chim Acta* **2008,** *611* (2), 143-50.
36. Gendrin, C.; Roggo, Y.; Collet, C., Content uniformity of pharmaceutical solid dosage forms by near infrared hyperspectral imaging: A feasibility study. *Talanta* **2007,** *73* (4), 733-41.
37. Kubota, M.; Kinoshita, Y.; Hirokawa, S.; Shikichi, D.; Izumi, N.; Hagiwara, N.; Sakai, D.; Matsuzaki, Y.; Yamamoto, M.; Takai, L.; Kon, Y.; Aoshima, Y.; Ota, R.; Kosaka, M.; Sun, M.; Kawano, Y.; Li, K., In-line multi-wavelength non-destructive pharma quality monitoring with ultrabroadband carbon nanotubes photo-thermoelectric imaging scanners. *Light: Science & Applications* **2025,** *14* (1), 306.
38. Karaca, A. C.; Ertürk, A.; Güllü, M. K.; Elmas, M.; Ertürk, S. In *Automatic waste sorting using shortwave infrared hyperspectral imaging system*, 2013 5th Workshop on Hyperspectral Image and Signal Processing: Evolution in Remote Sensing (WHISPERS), 26-28 June 2013; 2013; pp 1-4.
39. Mehrubeoglu, M.; Van Sickle, A.; Turner, J., *Detection and identification of plastics using SWIR hyperspectral imaging*. SPIE: 2020; Vol. 11504.
40. Cucuzza, P.; Serranti, S.; Bonifazi, G.; Capobianco, G., Effective Recycling Solutions for the Production of High-Quality PET Flakes Based on Hyperspectral Imaging and Variable Selection. *J Imaging* **2021,** *7* (9).
41. Bonifazi, G.; Fiore, L.; Gasbarrone, R.; Palmieri, R.; Serranti, S., Hyperspectral Imaging Applied to WEEE Plastic Recycling: A Methodological Approach. *Sustainability* **2023,** *15* (14), 11345.
42. Infrared Vision: SWIR Sees the Furnace Through the Flames. https://www.techbriefs.com/component/content/article/13380-5659-122 (accessed 02/12/2025).
43. Grujić, K., A Review of Thermal Spectral Imaging Methods for Monitoring High-Temperature Molten Material Streams. *Sensors (Basel)* **2023,** *23* (3).
44. Daughtry, C. S. T.; Hunt, E. R.; McMurtrey, J. E., Assessing crop residue cover using shortwave infrared reflectance. *Remote Sensing of Environment* **2004,** *90* (1), 126-134.
45. Lamb, B. T.; Dennison, P. E.; Hively, W. D.; Kokaly, R. F.; Serbin, G.; Wu, Z.; Dabney, P. W.; Masek, J. G.; Campbell, M.; Daughtry, C. S. T., Optimizing Landsat Next Shortwave Infrared Bands for Crop Residue Characterization. *Remote Sensing* **2022,** *14* (23), 6128.
46. Hively, W. D.; Lamb, B. T.; Daughtry, C. S. T.; Serbin, G.; Dennison, P.; Kokaly, R. F.; Wu, Z.; Masek, J. G., Evaluation of SWIR Crop Residue Bands for the Landsat Next Mission. *Remote Sensing* **2021,** *13* (18), 3718.
47. Berger, K.; Hank, T.; Halabuk, A.; Rivera-Caicedo, J. P.; Wocher, M.; Mojses, M.; Gerhátová, K.; Tagliabue, G.; Dolz, M. M.; Venteo, A. B. P.; Verrelst, J., Assessing Non-Photosynthetic Cropland Biomass from Spaceborne Hyperspectral Imagery. *Remote Sens (Basel)* **2021,** *13* (22), 4711.
48. Ziniuk, R.; Yakovliev, A.; Li, H.; Chen, G.; Qu, J.; Ohulchanskyy, T. Y., Real-Time Imaging of Short-Wave Infrared Luminescence Lifetimes for Anti-counterfeiting Applications. *Frontiers in Chemistry* **2021,** *Volume 9 - 2021*.

49. Muchlis, A. M. G.; Hu, C.-C.; Nguyen, H.-D.; Devi, R. K.; Tsai, Y.-T.; Lee, Y. C.; Lin, C. C., Emerging Inkjet-Compatible Anti-Counterfeiting Inks Based on Microfluidic-Synthesized NIR PbS/CdS Quantum Dots. *JACS Au* **2025,** *5* (10), 4856-4869.
50. Steiner, H.; Sporrer, S.; Kolb, A.; Jung, N., Design of an Active Multispectral SWIR Camera System for Skin Detection and Face Verification. *Journal of Sensors* **2016,** *2016* (1), 9682453.
51. Oda, N.; Sano, M.; Kagami, S.; Nambu, Y.; Tanaka, T.; Yamamoto, T.; Inada, H.; Iguchi, Y.; Katsuyama, T. In *Performance estimation for SWIR cameras under OH night airglow illumination*, Defense + Security, 2017.
52. Scheer, T.; Rohde, M.; Breithaupt, R.; Jung, N.; Lange, R., Customizable Presentation Attack Detection for Improved Resilience of Biometric Applications Using Near-Infrared Skin Detection. *Sensors* **2024,** *24* (8), 2389.
53. Steiner, H.; Kolb, A.; Jung, N. In *Reliable face anti-spoofing using multispectral SWIR imaging*, 2016 International Conference on Biometrics (ICB), 13-16 June 2016; 2016; pp 1-8.
54. Liang, D.; Zhang, C.; Zhang, P.; Liu, S.; Li, H.; Niu, S.; Rao, R. Z.; Zhao, L.; Chen, X.; Li, H.; Huo, Y., Evolution of laser technology for automotive LiDAR, an industrial viewpoint. *Nature Communications* **2024,** *15* (1), 7660.
55. Duthon, P.; Colomb, M.; Bernardin, F., Light Transmission in Fog: The Influence of Wavelength on the Extinction Coefficient. *Applied Sciences* **2019,** *9* (14), 2843.
56. Bernini, N.; Bertozzi, M.; Cerri, P.; Fedriga, R. I., SWIR Cameras for the Automotive Field: Two Test Cases. *International Scholarly Research Notices* **2014,** *2014* (1), 858979.
57. Hina, A.; Saadeh, W., Noninvasive Blood Glucose Monitoring Systems Using Near-Infrared Technology-A Review. *Sensors (Basel)* **2022,** *22* (13).
58. Ding, F.; Zhan, Y.; Lu, X.; Sun, Y., Recent advances in near-infrared II fluorophores for multifunctional biomedical imaging. *Chemical Science* **2018,** *9* (19), 4370-4380.
59. Mironov, S.; Hwang, C. D.; Nemzek, J.; Li, J.; Ranganathan, K.; Butts, J. T.; Cholok, D. J.; Dolgachev, V. A.; Wang, S. C.; Hemmila, M.; Cederna, P. S.; Morris, M. D.; Berenfeld, O.; Levi, B., Short-wave infrared light imaging measures tissue moisture and distinguishes superficial from deep burns. *Wound Repair and Regeneration* **2020,** *28* (2), 185-193.
60. Research, G. V. Shortwave Infrared Market (2025 - 2030). https://www.grandviewresearch.com/industry-analysis/shortwave-infrared-market-report (accessed 02/12/2025).
61. Intelligence, M. SWIR Camera Market Size & Share Analysis - Growth Trends And Forecast (2025 - 2030) https://www.mordorintelligence.com/industry-reports/shortwave-infrared-market (accessed 02/12/2025).
62. Lucintel SWIR Camera Market Report: Trends, Forecast and Competitive Analysis to 2030. https://www.lucintel.com/swir-camera-market.aspx (accessed 02/12/2025).
63. Emberion Emberion Oy Introduces Groundbreaking Ultra Low-Cost SWIR Sensor. https://www.emberion.com/emberion-oy-introduces-groundbreaking-ultra-low-cost-swir-sensor/ (accessed 02/12/2025).
64. Rogalski, A., Scaling infrared detectors—status and outlook. *Reports on Progress in Physics* **2022,** *85* (12), 126501.
65. Du, J.; Zhao, X.; Su, J.; Li, B.; Duan, X.; Dong, T.; Lin, H.; Ren, Y.; Miao, Y.; Radamson, H. H., Review of Short-Wavelength Infrared Flip-Chip Bump Bonding Process Technology. *Sensors* **2025,** *25* (1), 263.

66. Hoke, W. E.; Lemonias, P. J.; Mosca, J. J.; Lyman, P. S.; Torabi, A.; Marsh, P. F.; McTaggart, R. A.; Lardizabal, S. M.; Hetzler, K., Molecular beam epitaxial growth and device performance of metamorphic high electron mobility transistor structures fabricated on GaAs substrates. *Journal of Vacuum Science & Technology B: Microelectronics and Nanometer Structures Processing, Measurement, and Phenomena* **1999,** *17* (3), 1131-1135.
67. Yu, L.; Tian, P.; Liang, K., Advancements and Challenges in Colloidal Quantum Dot Infrared Photodetectors: Strategies for Short-Wave Infrared, Mid-Wave Infrared, and Long-Wave Infrared Applications. *Quantum Beam Science* **2025,** *9* (1), 9.
68. Wang, Y.; Peng, L.; Schreier, J.; Bi, Y.; Black, A.; Malla, A.; Goossens, S.; Konstantatos, G., Silver telluride colloidal quantum dot infrared photodetectors and image sensors. *Nature Photonics* **2024,** *18* (3), 236-242.
69. Vincent, S.; Nikolaidou, K.; Dalmases, M.; Dosil, M.; Malla, A.; Wang, Y.; Konstantatos, G., Flexible Large Area SWIR Colloidal Quantum Dot Down Converters Based on Scalable Manufacturing Processes. *Advanced Materials Technologies* **2025,** *10* (12), 2401960.
70. Kittel, C.; McEuen, P., *Introduction to Solid State Physics*. Wiley: 2018.
71. Mekuye, B.; Abera, B., Nanomaterials: An overview of synthesis, classification, characterization, and applications. *Nano Select* **2023,** *4* (8), 486-501.
72. Darwish, M. A.; Abd-Elaziem, W.; Elsheikh, A.; Zayed, A. A., Advancements in nanomaterials for nanosensors: a comprehensive review. *Nanoscale Advances* **2024,** *6* (16), 4015-4046.
73. Barhoum, A.; García-Betancourt, M. L.; Jeevanandam, J.; Hussien, E. A.; Mekkawy, S. A.; Mostafa, M.; Omran, M. M.; S. Abdalla, M.; Bechelany, M., Review on Natural, Incidental, Bioinspired, and Engineered Nanomaterials: History, Definitions, Classifications, Synthesis, Properties, Market, Toxicities, Risks, and Regulations. *Nanomaterials* **2022,** *12* (2), 177.
74. Walter, P.; Welcomme, E.; Hallégot, P.; Zaluzec, N. J.; Deeb, C.; Castaing, J.; Veyssière, P.; Bréniaux, R.; Lévêque, J.-L.; Tsoucaris, G., Early Use of PbS Nanotechnology for an Ancient Hair Dyeing Formula. *Nano Letters* **2006,** *6* (10), 2215-2219.
75. Montanarella, F.; Kovalenko, M. V., Three Millennia of Nanocrystals. *ACS Nano* **2022,** *16* (4), 5085-5102.
76. Reibold, M.; Paufler, P.; Levin, A. A.; Kochmann, W.; Pätzke, N.; Meyer, D. C. In *Discovery of Nanotubes in Ancient Damascus Steel*, Physics and Engineering of New Materials, Berlin, Heidelberg, 2009//; Cat, D. T.; Pucci, A.; Wandelt, K., Eds. Springer Berlin Heidelberg: Berlin, Heidelberg, 2009; pp 305-310.
77. Faraday, M., X. The Bakerian Lecture. —Experimental relations of gold (and other metals) to light. *Philosophical Transactions of the Royal Society of London* **1857,** (147), 145-181.
78. Knoll, M.; Ruska, E., Das Elektronenmikroskop. *Zeitschrift für Physik* **1932,** *78* (5), 318-339.
79. Bragg, W. H.; Bragg, W. L., The reflection of X-rays by crystals. *Proceedings of the Royal Society of London. Series A, Containing Papers of a Mathematical and Physical Character* **1913,** *88* (605), 428-438.
80. Ekimov, A. I.; Onushchenko, A. A., Quantum size effect in three-dimensional microscopic semiconductor crystals. *Soviet Journal of Experimental and Theoretical Physics Letters* **1981,** *34*, 345.
81. Brus, L. E., A simple model for the ionization potential, electron affinity, and aqueous redox potentials of small semiconductor crystallites. *Journal of Chemical Physics* **1983,** *79*, 5566-5571.

82. Kroto, H. W.; Heath, J. R.; O'Brien, S. C.; Curl, R. F.; Smalley, R. E., C60: Buckminsterfullerene. *Nature* **1985,** *318* (6042), 162-163.
83. Iijima, S., Helical microtubules of graphitic carbon. *Nature* **1991,** *354* (6348), 56-58.
84. Novoselov, K. S.; Geim, A. K.; Morozov, S. V.; Jiang, D.; Zhang, Y.; Dubonos, S. V.; Grigorieva, I. V.; Firsov, A. A., Electric Field Effect in Atomically Thin Carbon Films. *Science* **2004,** *306* (5696), 666-669.
85. Murray, C. B.; Norris, D. J.; Bawendi, M. G., Synthesis and characterization of nearly monodisperse CdE (E = sulfur, selenium, tellurium) semiconductor nanocrystallites. *Journal of the American Chemical Society* **1993,** *115* (19), 8706-8715.
86. Krahne, R.; Manna, L.; Morello, G.; Figuerola, A.; George, C.; Deka, S., Quantum Effects in Confined Systems. In *Physical Properties of Nanorods*, Krahne, R.; Manna, L.; Morello, G.; Figuerola, A.; George, C.; Deka, S., Eds. Springer Berlin Heidelberg: Berlin, Heidelberg, 2013; pp 1-6.
87. Alivisatos, A. P., Semiconductor Clusters, Nanocrystals, and Quantum Dots. *Science* **1996,** *271* (5251), 933-937.
88. Brus, L., Electronic wave functions in semiconductor clusters: experiment and theory. *The Journal of Physical Chemistry* **1986,** *90* (12), 2555-2560.
89. Kailasa, S. K.; Cheng, K.-H.; Wu, H.-F., Semiconductor Nanomaterials-Based Fluorescence Spectroscopic and Matrix-Assisted Laser Desorption/Ionization (MALDI) Mass Spectrometric Approaches to Proteome Analysis. *Materials* **2013,** *6* (12), 5763-5795.
90. Hawrylak, P.; Narvaez, G. A.; Bayer, M.; Forchel, A., Excitonic Absorption in a Quantum Dot. *Physical Review Letters* **2000,** *85* (2), 389-392.
91. Dou, H.; Yuan, C.; Zhu, R.; Li, L.; Zhang, J.; Weng, T.-C., Impact of Surface Trap States on Electron and Energy Transfer in CdSe Quantum Dots Studied by Femtosecond Transient Absorption Spectroscopy. *Nanomaterials* **2024,** *14* (1), 34.
92. Poudyal, U.; Adhikari, C. M.; Makani, N. H.; Gautam, B. R.; Neupane, T., Size-dependent fluorescence properties of CdSe quantum dots. *Solid State Communications* **2025,** *403*, 115993.
93. Woggon, U.; Giessen, H.; Gindele, F.; Wind, O.; Fluegel, B.; Peyghambarian, N., Ultrafast energy relaxation in quantum dots. *Physical Review B* **1996,** *54* (24), 17681-17690.
94. Bagga, A.; Chattopadhyay, P. K.; Ghosh, S., Origin of Stokes shift in InAs and CdSe quantum dots: Exchange splitting of excitonic states. *Physical Review B* **2006,** *74* (3), 035341.
95. Giansante, C.; Infante, I., Surface Traps in Colloidal Quantum Dots: A Combined Experimental and Theoretical Perspective. *The Journal of Physical Chemistry Letters* **2017,** *8* (20), 5209-5215.
96. Jang, H. M.; Lee, S. H.; Jang, K. Y.; Park, J.; Lee, T.-W., Semi-empirical approach to assess externally-induced photoluminescence linewidth broadening of halide perovskite nanocrystals with particle-size distribution. *Communications Physics* **2023,** *6* (1), 372.
97. Klimov, V. I., Mechanisms for Photogeneration and Recombination of Multiexcitons in Semiconductor Nanocrystals: Implications for Lasing and Solar Energy Conversion. *The Journal of Physical Chemistry B* **2006,** *110* (34), 16827-16845.
98. Klimov, V. I., Optical Nonlinearities and Ultrafast Carrier Dynamics in Semiconductor Nanocrystals. *The Journal of Physical Chemistry B* **2000,** *104* (26), 6112-6123.
99. Kovalenko, M. V.; Manna, L.; Cabot, A.; Hens, Z.; Talapin, D. V.; Kagan, C. R.; Klimov, V. I.; Rogach, A. L.; Reiss, P.; Milliron, D. J.; Guyot-Sionnnest, P.; Konstantatos, G.; Parak, W. J.;

Hyeon, T.; Korgel, B. A.; Murray, C. B.; Heiss, W., Prospects of Nanoscience with Nanocrystals. *ACS Nano* **2015,** *9* (2), 1012-1057.
100. Mo, S.; Shao, X.; Chen, Y.; Cheng, Z., Increasing entropy for colloidal stabilization. *Scientific Reports* **2016,** *6* (1), 36836.
101. Kim, S.; Yeon, S.; Lee, M.; Jin, J.; Shin, S.; Gwak, N.; Jeong, I.; Jang, H.; Hwang, G. W.; Oh, N., Chemically and electronically active metal ions on InAs quantum dots for infrared detectors. *NPG Asia Materials* **2023,** *15* (1), 30.
102. Fisher, A. A. E.; Osborne, M. A.; Day, I. J.; Lucena Alcalde, G., Measurement of ligand coverage on cadmium selenide nanocrystals and its influence on dielectric dependent photoluminescence intermittency. *Communications Chemistry* **2019,** *2* (1), 63.
103. Olshansky, J. H.; Balan, A. D.; Ding, T. X.; Fu, X.; Lee, Y. V.; Alivisatos, A. P., Temperature-Dependent Hole Transfer from Photoexcited Quantum Dots to Molecular Species: Evidence for Trap-Mediated Transfer. *ACS Nano* **2017,** *11* (8), 8346-8355.
104. Daniel-da-Silva, A. L.; Trindade, T., Colloidal Nanocrystals with Surface Organic Ligands. In *Surface Chemistry of Colloidal Nanocrystals*, The Royal Society of Chemistry: 2021; p 0.
105. Green, M. L. H., A new approach to the formal classification of covalent compounds of the elements. *Journal of Organometallic Chemistry* **1995,** *500* (1), 127-148.
106. Nag, A.; Kovalenko, M. V.; Lee, J.-S.; Liu, W.; Spokoyny, B.; Talapin, D. V., Metal-free Inorganic Ligands for Colloidal Nanocrystals: S2–, HS–, Se2–, HSe–, Te2–, HTe–, TeS32–, OH–, and NH2– as Surface Ligands. *Journal of the American Chemical Society* **2011,** *133* (27), 10612-10620.
107. Liu, M.; Tang, G.; Liu, Y.; Jiang, F.-L., Ligand Exchange of Quantum Dots: A Thermodynamic Perspective. *The Journal of Physical Chemistry Letters* **2024,** *15* (7), 1975-1984.
108. Guyot-Sionnest, P., Electrical Transport in Colloidal Quantum Dot Films. *The Journal of Physical Chemistry Letters* **2012,** *3* (9), 1169-1175.
109. Lee, S.; Choi, M.-J.; Sharma, G.; Biondi, M.; Chen, B.; Baek, S.-W.; Najarian, A. M.; Vafaie, M.; Wicks, J.; Sagar, L. K.; Hoogland, S.; de Arquer, F. P. G.; Voznyy, O.; Sargent, E. H., Orthogonal colloidal quantum dot inks enable efficient multilayer optoelectronic devices. *Nature Communications* **2020,** *11* (1), 4814.
110. Tom, A. E.; Thomas, A.; Somakumar, A. K.; Kuriakose, L.; Ison, V. V., Performance enhancement of PbS quantum dot solar cells employing a hybrid solid-state ligand exchange protocol. *Thin Solid Films* **2023,** *787*, 140138.
111. You, H. R.; Park, J. Y.; Lee, D. H.; Kim, Y.; Choi, J., Recent Research Progress in Surface Ligand Exchange of PbS Quantum Dots for Solar Cell Application. *Applied Sciences* **2020,** *10* (3), 975.
112. Dong, A.; Ye, X.; Chen, J.; Kang, Y.; Gordon, T.; Kikkawa, J. M.; Murray, C. B., A Generalized Ligand-Exchange Strategy Enabling Sequential Surface Functionalization of Colloidal Nanocrystals. *Journal of the American Chemical Society* **2011,** *133* (4), 998-1006.
113. Rosen, E. L.; Buonsanti, R.; Llordes, A.; Sawvel, A. M.; Milliron, D. J.; Helms, B. A., Exceptionally Mild Reactive Stripping of Native Ligands from Nanocrystal Surfaces by Using Meerwein's Salt. *Angewandte Chemie International Edition* **2012,** *51* (3), 684-689.
114. Wang, R.; Shang, Y.; Kanjanaboos, P.; Zhou, W.; Ning, Z.; Sargent, E. H., Colloidal quantum dot ligand engineering for high performance solar cells. *Energy & Environmental Science* **2016,** *9* (4), 1130-1143.

115. Reiss, P.; Protière, M.; Li, L., Core/Shell Semiconductor Nanocrystals. *Small* **2009,** *5* (2), 154-168.
116. Sahu, A.; Kumar, D., Core-shell quantum dots: A review on classification, materials, application, and theoretical modeling. *Journal of Alloys and Compounds* **2022,** *924*, 166508.
117. Huang, X.; Tong, X.; Wang, Z., Rational design of colloidal core/shell quantum dots for optoelectronic applications. *Journal of Electronic Science and Technology* **2020,** *18* (2), 100018.
118. Selopal, G. S.; Zhao, H.; Wang, Z. M.; Rosei, F., Core/Shell Quantum Dots Solar Cells. *Advanced Functional Materials* **2020,** *30* (13), 1908762.
119. Matthews, J. W.; Blakeslee, A. E., Defects in epitaxial multilayers: I. Misfit dislocations. *Journal of Crystal Growth* **1974,** *27*, 118-125.
120. Colin, J., Generation of a dipole of misfit dislocations in an axisymmetrical precipitate embedded in a semi-infinite matrix. *International Journal of Solids and Structures* **2016,** *82*, 9-15.
121. Vinayakan, R.; Shanmugapriya, T.; Nair, P. V.; Ramamurthy, P.; Thomas, K. G., An Approach for Optimizing the Shell Thickness of Core−Shell Quantum Dots Using Photoinduced Charge Transfer. *The Journal of Physical Chemistry C* **2007,** *111* (28), 10146-10149.
122. Baranov, A. V.; Rakovich, Y. P.; Donegan, J. F.; Perova, T. S.; Moore, R. A.; Talapin, D. V.; Rogach, A. L.; Masumoto, Y.; Nabiev, I., Effect of ZnS shell thickness on the phonon spectra in CdSe quantum dots. *Physical Review B* **2003,** *68* (16), 165306.
123. McBride, J. R.; Mishra, N.; Click, S. M.; Orfield, N. J.; Wang, F.; Acharya, K.; Chisholm, M. F.; Htoon, H.; Rosenthal, S. J.; Hollingsworth, J. A., Role of shell composition and morphology in achieving single-emitter photostability for green-emitting "giant" quantum dots. *The Journal of Chemical Physics* **2020,** *152* (12).
124. Mulder, J. T.; Kirkwood, N.; De Trizio, L.; Li, C.; Bals, S.; Manna, L.; Houtepen, A. J., Developing Lattice Matched ZnMgSe Shells on InZnP Quantum Dots for Phosphor Applications. *ACS Applied Nano Materials* **2020,** *3* (4), 3859-3867.
125. Jing, L.; Kershaw, S. V.; Kipp, T.; Kalytchuk, S.; Ding, K.; Zeng, J.; Jiao, M.; Sun, X.; Mews, A.; Rogach, A. L.; Gao, M., Insight into Strain Effects on Band Alignment Shifts, Carrier Localization and Recombination Kinetics in CdTe/CdS Core/Shell Quantum Dots. *Journal of the American Chemical Society* **2015,** *137* (5), 2073-2084.
126. Smith, A. M.; Mohs, A. M.; Nie, S., Tuning the optical and electronic properties of colloidal nanocrystals by lattice strain. *Nature Nanotechnology* **2009,** *4* (1), 56-63.
127. Ganguli, N.; Acharya, S.; Dasgupta, I., First-principles study of the electronic structure of CdS/ZnSe coupled quantum dots. *Physical Review B* **2014,** *89* (24), 245423.
128. Kudera, S.; Manna, L., Chapter 3 - Bottom-Up Synthesis of Nanosized Objects. In *Colloidal Foundations of Nanoscience*, Berti, D.; Palazzo, G., Eds. Elsevier: Amsterdam, 2014; pp 47-80.
129. Talapin, D. V.; Lee, J.-S.; Kovalenko, M. V.; Shevchenko, E. V., Prospects of Colloidal Nanocrystals for Electronic and Optoelectronic Applications. *Chemical Reviews* **2010,** *110* (1), 389-458.
130. Kwon, S. G.; Hyeon, T., Formation Mechanisms of Uniform Nanocrystals via Hot-Injection and Heat-Up Methods. *Small* **2011,** *7* (19), 2685-2702.
131. Thanh, N. T. K.; Maclean, N.; Mahiddine, S., Mechanisms of Nucleation and Growth of Nanoparticles in Solution. *Chemical Reviews* **2014,** *114* (15), 7610-7630.
132. Crystal Habit Modification Using Habit Modifiers. *Modern Aspects of Bulk Crystal and Thin Film Preparation* **2012**.

133. Lamer, V. K.; Dinegar, R. H., Theory, Production and Mechanism of Formation of Monodispersed Hydrosols. *Journal of the American Chemical Society* **1950,** *72*, 4847-4854.
134. Dunne, P. W.; Munn, A. S.; Starkey, C. L.; Huddle, T. A.; Lester, E. H., Continuous-flow hydrothermal synthesis for the production of inorganic nanomaterials. *Philosophical Transactions of the Royal Society A: Mathematical, Physical and Engineering Sciences* **2015,** *373* (2057).
135. Voorhees, P. W., The theory of Ostwald ripening. *Journal of Statistical Physics* **1985,** *38*, 231-252.
136. Clark, M. D.; Kumar, S. K.; Owen, J. S.; Chan, E. M., Focusing Nanocrystal Size Distributions via Production Control. *Nano Letters* **2011,** *11* (5), 1976-1980.
137. Tamang, S.; Lincheneau, C.; Hermans, Y.; Jeong, S.; Reiss, P., Chemistry of InP Nanocrystal Syntheses. *Chemistry of Materials* **2016,** *28* (8), 2491-2506.
138. van Embden, J.; Chesman, A. S. R.; Jasieniak, J. J., The Heat-Up Synthesis of Colloidal Nanocrystals. *Chemistry of Materials* **2015,** *27* (7), 2246-2285.
139. Rogalski, A., HgCdTe infrared detector material: history, status and outlook. *Reports on Progress in Physics* **2005,** *68* (10), 2267.
140. Zhang, Y.-G.; Gu, Y.; Shao, X.-M.; Li, X.; Gong, H.-M.; Fang, J.-X., Short-wave infrared InGaAs photodetectors and focal plane arrays*. *Chinese Physics B* **2018,** *27* (12), 128102.
141. Kozlowski, L.; Cabelli, S.; Cooper, D.; Vural, K., *Low-background infrared hybrid focal plane array characterization*. SPIE: 1993; Vol. 1946.
142. Du, J.; Zhao, X.; Su, J.; Li, B.; Duan, X.; Dong, T.; Lin, H.; Ren, Y.; Miao, Y.; Radamson, H. H., Review of Short-Wavelength Infrared Flip-Chip Bump Bonding Process Technology. *Sensors (Basel)* **2025,** *25* (1).
143. Hines, M. A.; Scholes, G. D., Colloidal PbS Nanocrystals with Size-Tunable Near-Infrared Emission: Observation of Post-Synthesis Self-Narrowing of the Particle Size Distribution. *Advanced Materials* **2003,** *15* (21), 1844-1849.
144. Bakueva, L.; Musikhin, S.; Hines, M. A.; Chang, T.-W. F.; Tzolov, M.; Scholes, G. D.; Sargent, E. H., Size-tunable infrared (1000–1600 nm) electroluminescence from PbS quantum-dot nanocrystals in a semiconducting polymer. *Applied Physics Letters* **2003,** *82* (17), 2895-2897.
145. McDonald, S. A.; Konstantatos, G.; Zhang, S.; Cyr, P. W.; Klem, E. J.; Levina, L.; Sargent, E. H., Solution-processed PbS quantum dot infrared photodetectors and photovoltaics. *Nat Mater* **2005,** *4* (2), 138-42.
146. Murphy, J. E.; Beard, M. C.; Norman, A. G.; Ahrenkiel, S. P.; Johnson, J. C.; Yu, P.; Mićić, O. I.; Ellingson, R. J.; Nozik, A. J., PbTe Colloidal Nanocrystals: Synthesis, Characterization, and Multiple Exciton Generation. *Journal of the American Chemical Society* **2006,** *128* (10), 3241-3247.
147. O'Connor, É.; O'Riordan, A.; Doyle, H.; Moynihan, S.; Cuddihy, A.; Redmond, G., Near-infrared electroluminescent devices based on colloidal HgTe quantum dot arrays. *Applied Physics Letters* **2005,** *86* (20).
148. Kovalenko, M. V.; Kaufmann, E.; Pachinger, D.; Roither, J.; Huber, M.; Stangl, J.; Hesser, G.; Schäffler, F.; Heiss, W., Colloidal HgTe Nanocrystals with Widely Tunable Narrow Band Gap Energies: From Telecommunications to Molecular Vibrations. *Journal of the American Chemical Society* **2006,** *128* (11), 3516-3517.
149. Keuleyan, S.; Lhuillier, E.; Brajuskovic, V.; Guyot-Sionnest, P., Mid-infrared HgTe colloidal quantum dot photodetectors. *Nature Photonics* **2011,** *5* (8), 489-493.

150. Keuleyan, S.; Lhuillier, E.; Guyot-Sionnest, P., Synthesis of Colloidal HgTe Quantum Dots for Narrow Mid-IR Emission and Detection. *Journal of the American Chemical Society* **2011,** *133* (41), 16422-16424.
151. Kim, J. H.; Kim, H. R.; Lee, B. R.; Choi, E. S.; In, S. I.; Kim, E., Carcinogenic activity of PbS quantum dots screened using exosomal biomarkers secreted from HEK293 cells. *Int J Nanomedicine* **2015,** *10*, 5513-27.
152. Du, Y.; Xu, B.; Fu, T.; Cai, M.; Li, F.; Zhang, Y.; Wang, Q., Near-Infrared Photoluminescent Ag2S Quantum Dots from a Single Source Precursor. *Journal of the American Chemical Society* **2010,** *132* (5), 1470-1471.
153. van der Stam, W.; Bladt, E.; Rabouw, F. T.; Bals, S.; de Mello Donega, C., Near-Infrared Emitting CuInSe2/CuInS2 Dot Core/Rod Shell Heteronanorods by Sequential Cation Exchange. *ACS Nano* **2015,** *9* (11), 11430-11438.
154. Jose Varghese, R.; Oluwafemi, O. S., The Photoluminescence and Biocompatibility of CuInS2-Based Ternary Quantum Dots and Their Biological Applications. *Chemosensors* **2020,** *8* (4), 101.
155. Guzelian, A. A.; Banin, U.; Kadavanich, A. V.; Peng, X.; Alivisatos, A. P., Colloidal chemical synthesis and characterization of InAs nanocrystal quantum dots. *Applied Physics Letters* **1996,** *69* (10), 1432-1434.
156. Wells, R. L.; Pitt, C. G.; McPhail, A. T.; Purdy, A. P.; Shafieezad, S.; Hallock, R. B., The use of tris(trimethylsilyl)arsine to prepare gallium arsenide and indium arsenide. *Chemistry of Materials* **1989,** *1* (1), 4-6.
157. Kim, M.; Lee, J.; Jung, J.; Shin, D.; Kim, J.; Cho, E.; Xing, Y.; Jeong, H.; Park, S.; Oh, S. H.; Kim, Y.-H.; Jeong, S., Surface-Originated Weak Confinement in Tetrahedral Indium Arsenide Quantum Dots. *Journal of the American Chemical Society* **2024,** *146* (15), 10251-10256.
158. Zhu, D.; Bahmani Jalali, H.; Saleh, G.; Di Stasio, F.; Prato, M.; Polykarpou, N.; Othonos, A.; Christodoulou, S.; Ivanov, Y. P.; Divitini, G.; Infante, I.; De Trizio, L.; Manna, L., Boosting the Photoluminescence Efficiency of InAs Nanocrystals Synthesized with Aminoarsine via a ZnSe Thick-Shell Overgrowth. *Advanced Materials* **2023,** *35* (38), 2303621.
159. Franke, D.; Harris, D. K.; Chen, O.; Bruns, O. T.; Carr, J. A.; Wilson, M. W. B.; Bawendi, M. G., Continuous injection synthesis of indium arsenide quantum dots emissive in the short-wavelength infrared. *Nature Communications* **2016,** *7* (1), 12749.
160. Busatto, S.; de Ruiter, M.; Jastrzebski, J. T. B. H.; Albrecht, W.; Pinchetti, V.; Brovelli, S.; Bals, S.; Moret, M.-E.; de Mello Donega, C., Luminescent Colloidal InSb Quantum Dots from In Situ Generated Single-Source Precursor. *ACS Nano* **2020,** *14* (10), 13146-13160.
161. Liu, Z.; Sun, C.; Wang, Q.; Lu, W.; Liu, Z.; Li, P.; Chen, Y.; Hu, X.; You, H.; Zhang, J.; Hou, X.; Zeng, B.; Li, Q.; Zhu, J.; Dai, N.; Li, Y., Colloidal InSb Quantum Dots Mid-Wave Infrared Photoconductive Detectors via One-Step Strong Acid Surface Treatment Strategy. *Nano Letters* **2025,** *25* (36), 13549-13556.
162. DIRECTIVE 2011/65/EU OF THE EUROPEAN PARLIAMENT AND OF THE COUNCIL of 8 June 2011 on the restriction of the use of certain hazardous substances in electrical and electronic equipment. https://eur-lex.europa.eu/legal-content/EN/TXT/HTML/?uri=CELEX%3A32011L0065#ntr1-L_2011174EN.01008801-E0001 (accessed 02/12/2025

).
163. Directive 2011/65/EU of the European Parliament and of the Council of 8 June 2011 on the restriction of the use of certain hazardous substances in electrical and electronic equipment (recast) Text with EEA relevance. https://eur-lex.europa.eu/eli/dir/2011/65/oj/eng (accessed 02/12/2025).
164. Restriction of Hazardous Substances in Electrical and Electronic Equipment (RoHS). https://environment.ec.europa.eu/topics/waste-and-recycling/rohs-directive_en

(accessed 02/12/2025).
165. Sanders, T.; Liu, Y.; Buchner, V.; Tchounwou, P. B., Neurotoxic effects and biomarkers of lead exposure: a review. *Rev Environ Health* **2009,** *24* (1), 15-45.
166. Bressler, J. P.; Goldstein, G. W., Mechanisms of lead neurotoxicity. *Biochem Pharmacol* **1991,** *41* (4), 479-84.
167. Wu, Y.-S.; Osman, A. I.; Hosny, M.; Elgarahy, A. M.; Eltaweil, A. S.; Rooney, D. W.; Chen, Z.; Rahim, N. S.; Sekar, M.; Gopinath, S. C. B.; Mat Rani, N. N. I.; Batumalaie, K.; Yap, P.-S., The Toxicity of Mercury and Its Chemical Compounds: Molecular Mechanisms and Environmental and Human Health Implications: A Comprehensive Review. *ACS Omega* **2024,** *9* (5), 5100-5126.
168. Lu, H.; Carroll, G. M.; Neale, N. R.; Beard, M. C., Infrared Quantum Dots: Progress, Challenges, and Opportunities. *ACS Nano* **2019,** *13* (2), 939-953.
169. Hu, C.; Channa, A. I.; Xia, L.; Li, X.; Li, Z.; Wang, Z. M.; Tong, X., Colloidal InAs Quantum Dots: Synthesis, Properties, and Optoelectronic Devices. *Advanced Functional Materials* **2025,** *35* (32), 2500280.
170. Berends, A. C.; Mangnus, M. J. J.; Xia, C.; Rabouw, F. T.; de Mello Donega, C., Optoelectronic Properties of Ternary I–III–VI2 Semiconductor Nanocrystals: Bright Prospects with Elusive Origins. *The Journal of Physical Chemistry Letters* **2019,** *10* (7), 1600-1616.
171. Nieves, L. M.; Mossburg, K.; Hsu, J. C.; Maidment, A. D. A.; Cormode, D. P., Silver chalcogenide nanoparticles: a review of their biomedical applications. *Nanoscale* **2021,** *13* (46), 19306-19323.
172. Paul, S. J.; Li, L.; Li, Z.; Kywe, T.; Vataj, A.; Sahu, A., Heavy Metal Free Ag2Se Quantum Dot Inks for Near to Short-Wave Infrared Detection. *ACS Applied Materials & Interfaces* **2025,** *17* (38), 53735-53744.
173. Almeida, G.; Ubbink, R. F.; Stam, M.; du Fossé, I.; Houtepen, A. J., InP colloidal quantum dots for visible and near-infrared photonics. *Nature Reviews Materials* **2023,** *8* (11), 742-758.
174. REACH Regulation https://environment.ec.europa.eu/topics/chemicals/reach-regulation_en (accessed 02/12/2025).
175. R. Heath, J., Covalency in semiconductor quantum dots. *Chemical Society Reviews* **1998,** *27* (1), 65-71.
176. Yu, P.; Beard, M. C.; Ellingson, R. J.; Ferrere, S.; Curtis, C.; Drexler, J.; Luiszer, F.; Nozik, A. J., Absorption Cross-Section and Related Optical Properties of Colloidal InAs Quantum Dots. *The Journal of Physical Chemistry B* **2005,** *109* (15), 7084-7087.
177. Bahmani Jalali, H.; De Trizio, L.; Manna, L.; Di Stasio, F., Indium arsenide quantum dots: an alternative to lead-based infrared emitting nanomaterials. *Chemical Society Reviews* **2022,** *51* (24), 9861-9881.

178. Kuech, T. F., Metal-organic vapor phase epitaxy of compound semiconductors. *Materials Science Reports* **1987,** *2* (1), 1-49.
179. Kubiak, R. A. A.; Parker, E. H. C.; Newstead, S.; Harris, J. J., The morphology and electrical properties of heteroepitaxial InAs prepared by MBE. *Applied Physics A* **1984,** *35* (1), 61-66.
180. Peng, X.; Wickham, J.; Alivisatos, A. P., Kinetics of II-VI and III-V Colloidal Semiconductor Nanocrystal Growth: "Focusing" of Size Distributions. *Journal of the American Chemical Society* **1998,** *120* (21), 5343-5344.
181. Battaglia, D.; Peng, X., Formation of High Quality InP and InAs Nanocrystals in a Noncoordinating Solvent. *Nano Letters* **2002,** *2* (9), 1027-1030.
182. Harris, D. K.; Bawendi, M. G., Improved Precursor Chemistry for the Synthesis of III–V Quantum Dots. *Journal of the American Chemical Society* **2012,** *134* (50), 20211-20213.
183. Tamang, S.; Lee, S.; Choi, H.; Jeong, S., Tuning Size and Size Distribution of Colloidal InAs Nanocrystals via Continuous Supply of Prenucleation Clusters on Nanocrystal Seeds. *Chemistry of Materials* **2016,** *28* (22), 8119-8122.
184. Song, J. H.; Choi, H.; Pham, H. T.; Jeong, S., Energy level tuned indium arsenide colloidal quantum dot films for efficient photovoltaics. *Nature Communications* **2018,** *9* (1), 4267.
185. Kim, T.; Park, S.; Jeong, S., Diffusion dynamics controlled colloidal synthesis of highly monodisperse InAs nanocrystals. *Nature Communications* **2021,** *12* (1), 3013.
186. Uesugi, H.; Kita, M.; Omata, T., Facile synthesis of colloidal InAs nanocrystals using triphenylarsine as an arsenic source. *Journal of Crystal Growth* **2014,** *405*, 39-43.
187. Uesugi, H.; Kita, M.; Omata, T., Synthesis of size-controlled colloidal InAs quantum dots using triphenylarsine as a stable arsenic source. *Journal of Crystal Growth* **2015,** *416*, 134-141.
188. Das, A.; Shamirian, A.; Snee, P. T., Arsenic Silylamide: An Effective Precursor for Arsenide Semiconductor Nanocrystal Synthesis. *Chemistry of Materials* **2016,** *28* (11), 4058-4064.
189. Malik, M. A.; O'Brien, P.; Helliwell, M., A new synthesis of InAs quantum dots from [tBu2AsInEt2]2. *Journal of Materials Chemistry* **2005,** *15* (14), 1463-1467.
190. Sheikh, T.; Mir, W. J.; Nematulloev, S.; Maity, P.; Yorov, K. E.; Hedhili, M. N.; Emwas, A.-H.; Khan, M. S.; Abulikemu, M.; Mohammed, O. F.; Bakr, O. M., InAs Nanorod Colloidal Quantum Dots with Tunable Bandgaps Deep into the Short-Wave Infrared. *ACS Nano* **2023,** *17* (22), 23094-23102.
191. Zhao, T.; Oh, N.; Jishkariani, D.; Zhang, M.; Wang, H.; Li, N.; Lee, J. D.; Zeng, C.; Muduli, M.; Choi, H.-J.; Su, D.; Murray, C. B.; Kagan, C. R., General Synthetic Route to High-Quality Colloidal III–V Semiconductor Quantum Dots Based on Pnictogen Chlorides. *Journal of the American Chemical Society* **2019,** *141* (38), 15145-15152.
192. Green, M.; Norager, S.; Moriarty, P.; Motevalli, M.; O'Brien, P., On the synthesis and manipulation of InAs quantum dots. *Journal of Materials Chemistry* **2000,** *10* (8), 1939-1943.
193. Grigel, V.; Dupont, D.; De Nolf, K.; Hens, Z.; Tessier, M. D., InAs Colloidal Quantum Dots Synthesis via Aminopnictogen Precursor Chemistry. *J Am Chem Soc* **2016,** *138* (41), 13485-13488.
194. Srivastava, V.; Janke, E. M.; Diroll, B. T.; Schaller, R. D.; Talapin, D. V., Facile, Economic and Size-Tunable Synthesis of Metal Arsenide Nanocrystals. *Chemistry of Materials* **2016,** *28* (18), 6797-6802.
195. Srivastava, V.; Dunietz, E.; Kamysbayev, V.; Anderson, J. S.; Talapin, D. V., Monodisperse InAs Quantum Dots from Aminoarsine Precursors: Understanding the Role of Reducing Agent. *Chemistry of Materials* **2018,** *30* (11), 3623-3627.

196. Leemans, J.; Respekta, D.; Bai, J.; Braeuer, S.; Vanhaecke, F.; Hens, Z., Formation of Colloidal In(As,P) Quantum Dots Active in the Short-Wave Infrared, Promoting Growth through Temperature Ramps. *ACS Nano* **2023,** *17* (20), 20002-20012.
197. Skorotetcky, M. S.; Mir, W. J.; Sheikh, T.; Yorov, K. E.; Saidzhonov, B. M.; Daws, S.; Zhou, R.; Hedhili, M. N.; Abulikemu, M.; Mohammed, O. F.; Bakr, O. M., Si-H Hydrosilane Reducing Agents for Size- and Shape-Controlled InAs Colloidal Quantum Dots. *Advanced Materials* **2025,** *37* (4), 2412105.

Chapter 2. Trioctylamine in the Synthesis of Tris(trimethylsilyl)arsine Based InAs Quantum Dots Prevents the Formation of Si-Based Byproducts

2.1. Abstract

The best reported strategy to grow large colloidal InAs quantum dots (QDs) with precise control over size and size distribution is a seeded-growth synthesis that uses di-octylamine (DOA) coupled with tris(trimethylsilyl)arsine ($(TMS)_3$-As) as the arsenic precursor, and oleic acid (OLAc) as the ligand. However, these methods exhibit a recurring yet poorly understood issue, which is the formation of oxygen-containing species that persist with the InAs QDs after the synthesis. In this chapter, we elucidate the origin of these contaminants through detailed nuclear magnetic resonance (NMR) studies. Specifically, we show that DOA and OLAc condense at the high temperatures required for synthesis (>250 °C), releasing water as a byproduct. The released water, in turn, leads to the formation of TMS-OH species, which subsequently condense to form TMS-O-TMS and TMS-OA. As a result, DOA-based InAs QDs do not feature surface indium or arsenic oxide layers, but instead are contaminated, even after multiple washing steps, by unbound TMS-OA and bound TMS-O-based species. We show that these issues can be solved by replacing DOA with tri-n-octylamine (TOA), a tertiary amine, thus not capable of undergoing condensation with OLAc. This prevents the formation of water and leads to clean InAs QDs, which is the novelty of this work. We also show that the procedure we developed allows for the synthesis of TOA-based InAs QDs with excellent control over their optical features: excitonic absorption peaks as narrow as 50 meV (half-width at half-maximum) and peak-to-valley ratios as high as ~2, the latter representing a record for InAs QDs.

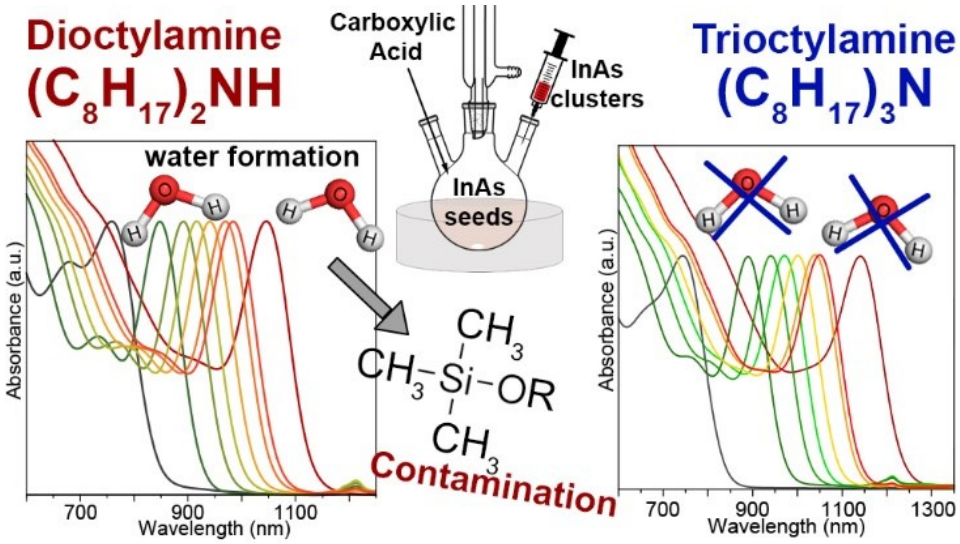

2.2. Introduction

Colloidal quantum dots (QDs) that absorb and emit in the infrared (IR) region have emerged as promising active materials for next-generation optoelectronic technologies[1, 2]. Their compatibility with established complementary metal oxide semiconductor (CMOS) processing presents a cost-effective route toward scalable IR devices[3, 4] such as photodetectors, solar cells[5, 6], light-emitting diodes (LEDs)[7-10], lasers[11, 12], and optical sensors[13]. These devices underpin a wide range of existing and rapidly expanding application areas, including security authentication[14], optogenetics[15], agricultural monitoring[16], Li-Fi communication[17], surveillance and automotive imaging, night-vision and all-weather cloud vision systems[18], industrial inspection, and broadband optical communication[19]. Historically, IR-emissive colloidal semiconductors based on II-VI (Cd- and Hg-chalcogenides)[20, 21] and IV-VI (Pb-chalcogenides)[22, 23] compounds have dominated this landscape due to their well-developed syntheses and favorable electronic structures. However, the intrinsic toxicity of these heavy-metal based materials[24, 25] poses significant barriers to their integration into consumer electronics, motivating the development of safer, RoHS-compliant alternatives.

Among the emerging RoHS-compliant materials, colloidal InAs QDs are particularly attractive because their bandgap can be continuously tuned from the visible region to approximately 0.7 eV (~1700 nm) through quantum confinement[2, 26-31]. The most mature and widely adopted synthetic route to InAs QDs employs tris(trimethylsilyl)arsine ($(TMS)_3$-As) or its tris(trimethylgermyl)-arsine analogue as the arsenic precursor[32-35]. These highly reactive precursors facilitate the growth of InAs QDs with exceptionally narrow size distributions, yielding high-quality optical features such as first excitonic absorption peaks with half-widths at half-maximum (HWHM) as low as ~50 meV (at ~1300 nm) and peak-to-valley (P/V) ratios reaching ~1.6[28]. Such metrics such as narrow HWHM and high P/V ratio serve as direct indicators of the structural and electronic uniformity of the QDs, reflecting minimized polydispersity, reduced trap densities, and enhanced carrier confinement[36]. These properties are essential for high-performance infrared optoelectronic devices, particularly photodetectors, where spectral purity translates into efficient carrier extraction, reduced dark current, and improved detectivity and responsivity[37]. By contrast, alternative arsenic precursors including tris(dimethylamino)arsine[27, 38, 39], arsenic halides[40, 41], and triphenylarsine[42, 43] have consistently produced InAs QDs with broader excitonic linewidths (HWHM ~100 meV at ~800 nm) and P/V ratios close to unity, underscoring the unique effectiveness of $(TMS)_3$-As based chemistries in achieving high optical fidelity[39, 44].

In the conventional $(TMS)_3$-As based synthesis of InAs QDs, the arsenic precursor is rapidly injected into a hot reaction mixture containing indium acetate, oleic acid as the coordinating ligand, and 1-octadecene (ODE) as the non-coordinating solvent[32, 33]. While this protocol reliably produces high-quality nanocrystals, it suffers from a fundamental limitation arising from the extremely high reactivity of $(TMS)_3$-As. Upon injection, $(TMS)_3$-As undergoes rapid precursor-to-monomer conversion, generating a sharp nucleation burst that quickly consumes most of the

available monomers. As a result, the subsequent growth phase is severely monomer-starved, preventing the QDs from growing to larger sizes while maintaining a narrow size distribution (Figure 2.2.1c). To circumvent this issue, researchers have developed seeded-growth strategies that supply precursors continuously during the reaction, allowing monomer concentrations to be sustained over extended periods and enabling controlled growth of larger, monodisperse InAs QDs. Notable advances in this direction were made by Franke et al. and Tamang et al., who demonstrated that seeded-growth strategies based on continuous precursor injection could effectively sustain monomer availability during the reaction, thereby enabling the growth of larger InAs QDs while preserving narrow size distributions (Figure 2.2.1)[26, 31].

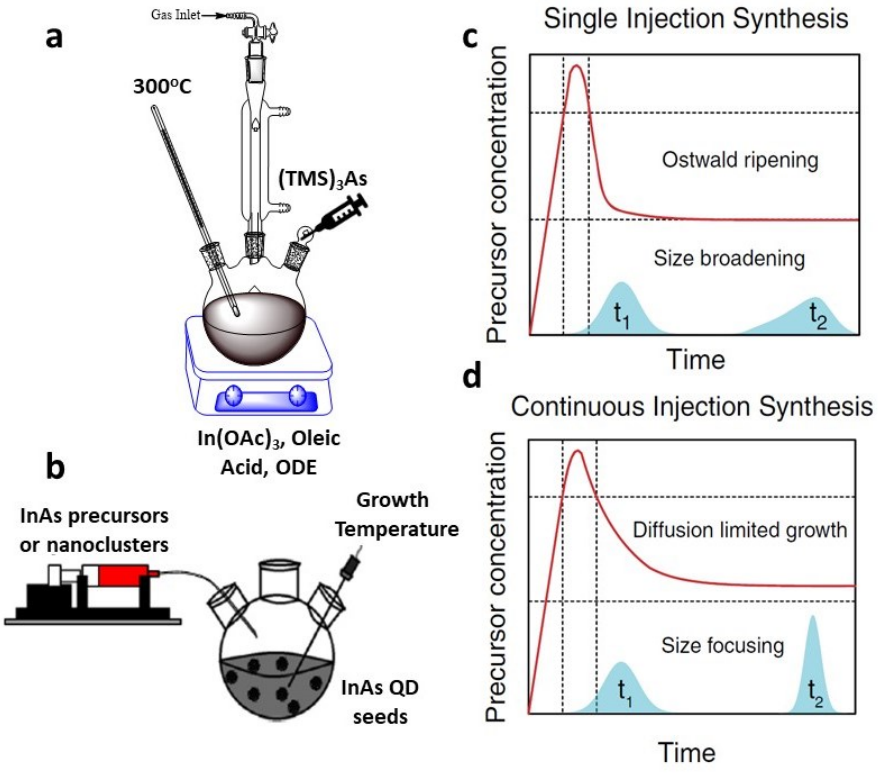

Figure 2.2.1: *(a) Schematics showing hot-injection synthesis and (b) subsequent continuous injection method. Temporal evolution of precursor concentration during (c) a typical hot-injection synthesis and (d) during a combination of hot and continuous injection.*

Amines are known to play a critical role in modulating the reaction kinetics of III-V semiconductor nanocrystals, with primary amines such as octylamine functioning as either reaction inhibitors or activators depending on the specific reaction environment[45]. Building on this concept, Song et al. refined the continuous-injection approach by incorporating dioctylamine (DOA) throughout all stages of the synthesis, including the preparation of the initial InAs clusters to lower the reactivity of $(TMS)_3$-As[30]. These clusters are ultrasmall, atomically precise nanocrystals exhibiting discrete absorption features and well-defined atomic arrangements and are often described as magic-sized nanoclusters. They were originally generated at room temperature by reacting $(TMS)_3$-As

with indium oleate in ODE, and Song et al. advanced this methodology by incorporating DOA directly into this cluster-forming step, thereby modulating the nucleation and early growth pathways from the outset.

Although the mechanism by which DOA moderates precursor reactivity remains unclear, its use enables fine control over the size of the initial InAs seeds and their subsequent growth during continuous cluster injection. This strategy yielded QDs with HWHM values as low as 57 meV at 1100 nm[30, 31]. Further optimization of the cluster injection rate allowed the excitonic absorption to be extended to ~1600 nm, with linewidths of ~60 meV and P/V ratios around 1.12 (Figure 2.2.2 a-d)[28]. Despite representing one of the most effective methods reported to date, this approach has an intrinsic limitation: the simultaneous presence of a secondary amine (i.e. DOA) and a carboxylic acid (i.e. OLAc) at high reaction temperatures (~300 °C). Under these conditions, DOA and OLAc can undergo condensation to form an amide and water[45]. The generation of water during synthesis is detrimental, as it can induce surface oxidation and degrade the optical quality of III-V QDs[45, 46]. This possibility had not been systematically investigated, and the role of in-situ formed water in DOA-based InAs syntheses remained unknown. Based on previous reports showing In_2O_3 and/or surface As_2O_3 impurities, we hypothesized that these oxides may arise from water generated during the amine-acid condensation (Figure 2.2.2 e, f)[30, 47].

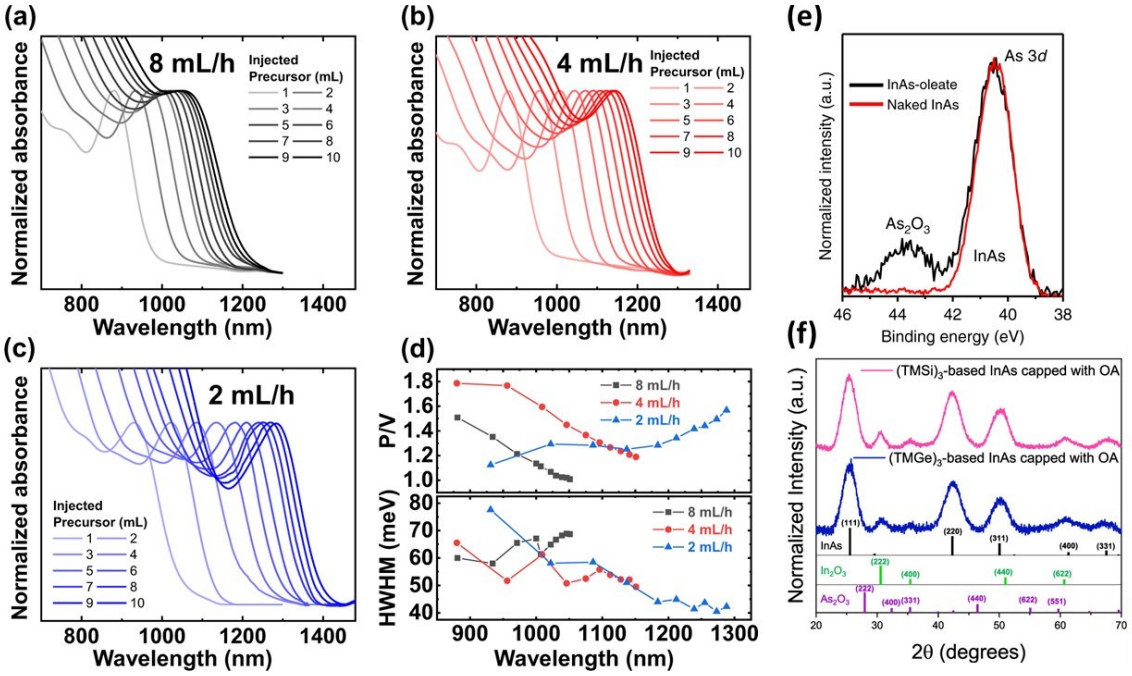

Figure 2.2.2: *(a-c) Normalized absorption spectra of aliquots under various precursor injection rates. (d) Peak-to-valley ratio and HWHM of 1st excitonic peaks of (a-c). (e) XPS spectra of As 3d from InAs QDs. (f) XRD patterns of InAs CQDs made using DOA based $(TMS)_3$-As route.*

In this chapter, we shed light onto these points by directly comparing the optical, structural, and chemical properties of InAs QDs synthesized through two analogous seeded-growth strategies that differ only in the amine employed: DOA, the commonly used secondary amine and TOA, a

tertiary amine introduced here as the key innovation. TOA was specifically selected because, unlike secondary amines, it lacks N-H bonds and therefore cannot undergo condensation with oleic acid. Its use should thus suppress the formation of water during synthesis and eliminate water-mediated side reactions. Under the optimized reaction conditions developed in this study, we successfully synthesized InAs QDs using both DOA and TOA, achieving excellent control over particle size and uniformity, with excitonic absorption peaks tunable up to 1100 nm, HWHM values as low as ~50 meV, and P/V ratios approaching 2, the latter representing a record value for colloidal InAs QDs. Despite exhibiting similarly high optical quality, the two samples differed markedly in several critical aspects:

(i) Purifying DOA-based InAs QDs from the crude reaction mixture proved to be particularly difficult, often resulting in the formation of a gel-like precipitate that led to substantial material loss or, in many cases, the complete failure of the purification step. In sharp contrast, TOA-based InAs QDs could be isolated cleanly using standard washing procedures, yielding stable and well-dispersed nanocrystals with no abnormal aggregation or gelation.

(ii) Thermogravimetric analysis (TGA) further revealed that DOA-based InAs QDs, even if cleaned thoroughly, exhibited significantly higher weight loss compared to their TOA-based counterparts. This mass loss is most likely attributable to the presence of metal-organic byproducts that remained bound to the QD surface or trapped within the organic matrix and could not be eliminated through conventional purification.

(iii) Si-based byproducts were detected exclusively in DOA-derived InAs QDs, as evidenced by X-ray photoelectron spectroscopy (XPS) and further confirmed through scanning transmission electron microscopy coupled with energy-dispersive X-ray spectroscopy (STEM-EDS). Such signatures were absent in the TOA-based samples, reinforcing the conclusion that DOA promotes the formation of silicon-oxygen species during synthesis.

To elucidate the origin of the Si-containing impurities, we performed nuclear magnetic resonance (NMR) spectroscopy on DOA-derived InAs QDs, which revealed clear signatures of TMS-based species. A series of control experiments, in which $(TMS)_3$-As was heated at 250°C in the presence of DOA, OLAc, or both, confirmed that water is indeed generated under the reaction conditions used for DOA-based InAs QDs syntheses. Notably, this in-situ formed water did not produce any detectable In-O or As-O surface oxides, as verified by both XPS and XRD analyses. Instead, it reacted with $(TMS)_3$-As to form trimethylsilanol (TMS-OH), which subsequently underwent self-condensation to yield hexamethyldisiloxane (TMS-O-TMS) and reacted with OLAc to produce the corresponding silyl ester (TMS-OLAc). Consistent with these reaction pathways, NMR spectra of the purified DOA-based QDs showed the presence of free TMS-OLAc as well as bound TMS-derived moieties, confirming that these silicon-oxygen species constitute the primary Si-based contaminants.

Overall, our findings demonstrate that the quality of $(TMS)_3$-As based InAs QDs can be significantly improved by employing tertiary amines, such as TOA, in place of primary or secondary amines. Tertiary amines prevent amine-acid condensation and thus eliminate water

formation during synthesis, ultimately yielding cleaner QDs with superior optical and chemical purity.

2.3. Results and discussion

InAs QDs were synthesized following the procedure reported by Song et al. with several modifications[30]. In detail, to prepare the starting InAs QDs, DOA was mixed with $(TMS)_3$-As and ODE, and the resulting solution was injected in a reaction flask containing In-oleate and ODE at 280 °C (see the Experimental section). Quenching the reaction after 10 min yielded InAs QDs with a first excitonic absorption peak at ~755 nm, a HWHM of 97.2 meV, and a P/V ratio of 1.36 (Figure 2.3.1a-c, time = 0 h). These seeds were subsequently grown larger through a continuous-injection growth phase in which DOA-based InAs clusters were introduced into the reaction mixture at 280°C over approximately 3.5 h. This controlled monomer supply red-shifted the excitonic peak to 937 nm and improved the optical quality, yielding a narrower HWHM of 64 meV and an enhanced P/V ratio of 2.4 (Figure 2.3.1a-c, time = 3.5 h). Following a cleaning step, a second seeded-growth step was carried out at 280°C for an additional 20 h. The resulting InAs QDs exhibited an excitonic absorption at 1045 nm, with an HWHM of 53 meV and a P/V ratio of 2.2 (Figure 2.3.1a-c, time = 23.5 h).

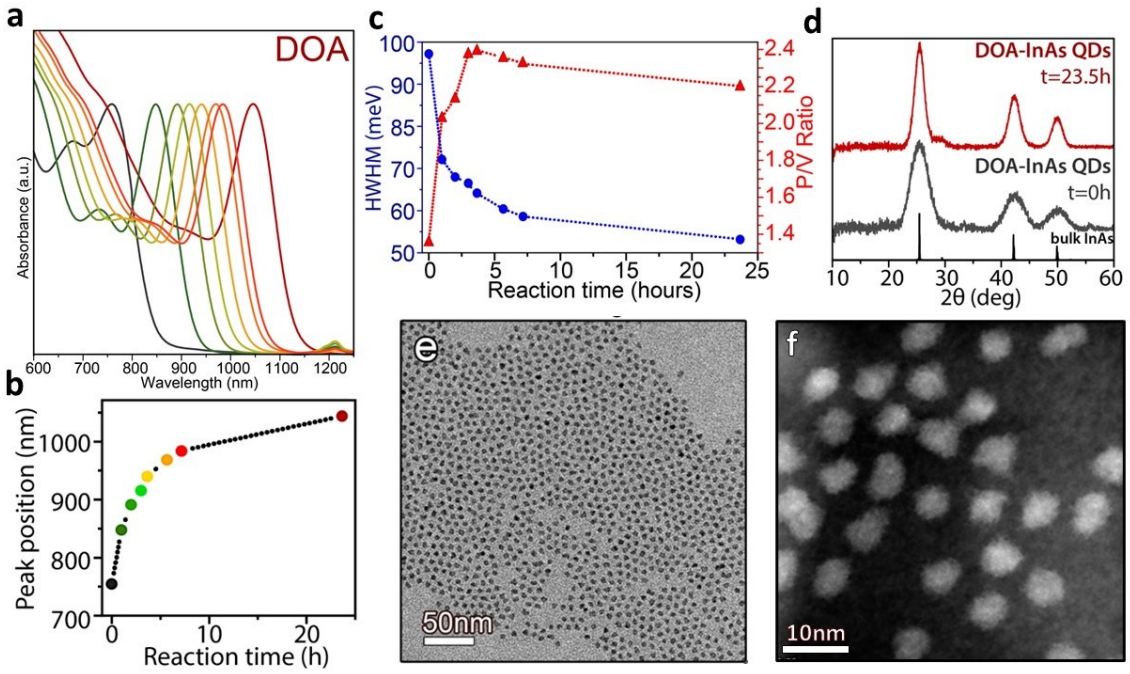

Figure 2.3.1. *(a) Evolution of the optical absorption spectra of InAs QDs synthesized with DOA at different (b) reaction times, along with their corresponding (c) HWHM and P/V ratios. The reaction time 0 corresponds to the time at which the seeded growth starts. (d) XRD patterns of final InAs QDs after the seeded growth. (e) BF-TEM image of the final InAs QDs and (f) the corresponding high-resolution STEM images.*

These optical parameters, particularly the narrow excitonic absorption peak and high P/V ratio, confirm excellent control over the QDs size distribution. Such performance was achieved by using

DOA-based clusters prepared with a DOA:$(TMS)_3$-As ratio of 6:1, in contrast to the 3:1 ratio originally reported by Song et al., and by precisely regulating the injection rate of the clusters (details in experimental section). Powder X-ray diffraction (XRD) of the final DOA-based QDs displayed reflections consistent with cubic zinc-blende InAs (ICSD 98-002-4518), with no detectable signatures of secondary phases (Figure 2.3.1 d). Importantly, unlike some previous reports, no indium oxide or arsenic oxide peaks were observed[30, 47]. Transmission electron microscopy (TEM) revealed faceted nanocrystals with a uniform size distribution of 5.7 ± 0.5 nm calculated from the high-resolution scanning transmission electron microscopy (STEM) (Figure 2.3.1 e-f), in agreement with the narrow excitonic linewidth observed spectroscopically.

We next carried out the synthesis of InAs QDs using TOA in place of DOA. To enable a direct and meaningful comparison between the two approaches, all reaction parameters were kept identical, with the sole modification being the substitution of the secondary amine (DOA) with the tertiary amine (TOA). Similar to DOA, TOA was found to moderate the reactivity of $(TMS)_3$-As, producing initial InAs QDs with optical properties comparable to those obtained using DOA (Figure 2.3.2 a). After a 10 min reaction, the TOA-derived seeds exhibited a first excitonic absorption peak at ~750 nm, with an HWHM of 114 meV and a P/V ratio of 1.44 (Figure 2.3.2 a-c, time = 0 h).

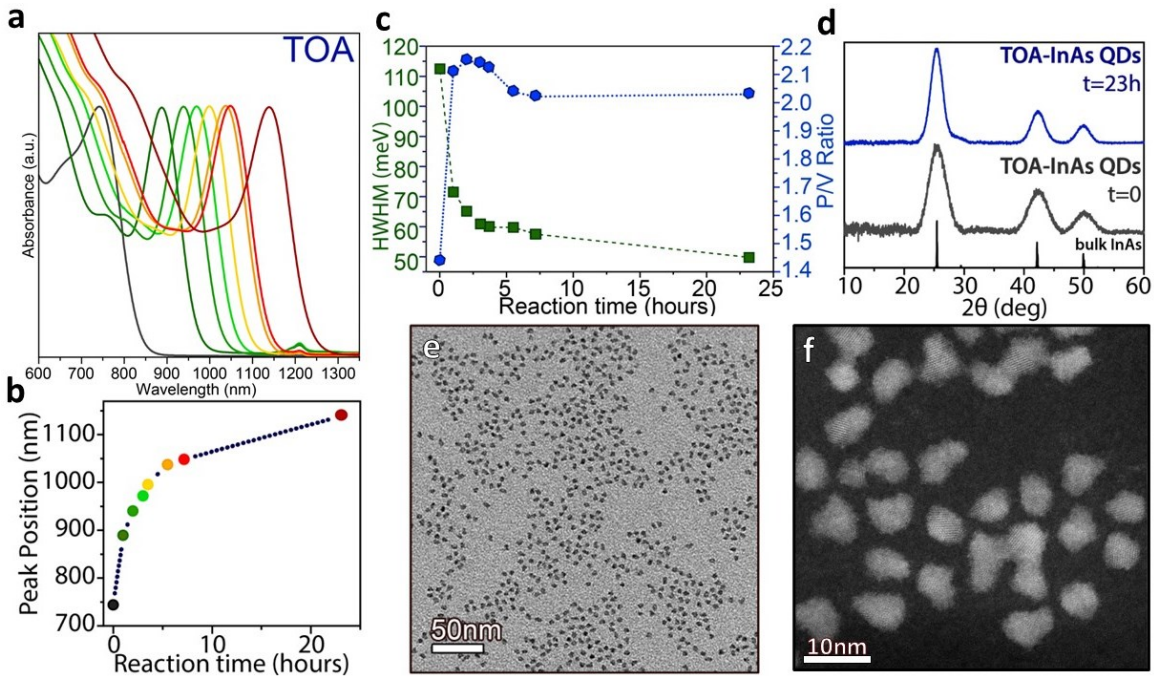

Figure 2.3.2. *(a) Evolution of the optical absorption spectra of InAs QDs synthesized with TOA at different (b) reaction times, along with their corresponding (c) HWHM and P/V ratios. The reaction time 0 corresponds to the time at which the seeded growth starts. (d) XRD patterns of final InAs QDs after the seeded growth. (e) BF-TEM image of the final InAs QDs and (f) the corresponding high-resolution STEM images.*

These seeds were subsequently grown larger through continuous injection of TOA-based InAs clusters, following the same growth protocol used for the DOA system. After the first seeded-growth stage at 280°C for 3 h, the excitonic peak red-shifted to 972 nm and the optical quality improved significantly, yielding a linewidth of 61 meV and a P/V ratio of 2.14 (Figure 2.3.2 a-c, time = 3 h). A second seeded-growth step, performed at 280°C for an additional 20 h, produced InAs QDs with an excitonic absorption centered at 1140 nm and exhibiting an HWHM of 55 meV and a P/V ratio of 2.03.

As in the DOA case, the XRD pattern of the TOA-grown QDs matched that of cubic zinc-blende InAs (ICSD 98-002-4518), with no detectable secondary phases (Figure 2.3.2 d). TEM analysis confirmed that these QDs were faceted nanocrystals with a uniform size distribution, averaging 6.0 ± 0.6 nm in diameter (Figure 2.3.2 e-f), consistent with the narrow excitonic linewidths observed spectroscopically.

A comparison between the DOA- and TOA-derived InAs QDs shows that both amines effectively regulate the nucleation and growth processes, yielding nanocrystals of similarly high optical and structural quality. In both cases, the QDs exhibited (i) exceptionally high P/V ratios of approximately 2 and remarkably narrow HWHM values of ~50 meV, which are record metrics for colloidal InAs QDs reported till date (Table 2.1); and (ii) no detectable secondary crystalline phases or additional QD populations.

Table 2. 1. *Comparison of excitonic peak position, HWHM and P/V ratios of InAs QD samples reported in the present work and in literature.*

Precursor system	**Excitonic peak position (nm)**	**HWHM (meV)**	**P/V ratio**	
$(TMS)_3$-As + DOA	1045	53	2.2	This work
$(TMS)_3$-As + TOA	1140	55	2.03	This work
$(TMS)_3$-As + DOA	~1140	55	1.3	Song et. al.[30]
$(TMS)_3$-As	1200	92	---	Franke et. al.[26]
$(TMS)_3$-As	1100	~70	---	Tamang et.al.[31]

Despite the similar optical and structural quality achieved with both amines, pronounced differences emerged during the purification of the resulting QD products. DOA-based InAs QDs proved challenging to clean, frequently forming gel-like agglomerates during the washing steps (Figure 2.3.3 a-c). This behavior made the purification procedure highly sensitive to the amount of antisolvent used, as excessive addition often triggered complete precipitation and resulted in the loss of the entire batch. (Figure 2.3.3 b-c). Even when a stable colloidal dispersion was ultimately obtained, the purified DOA-based QDs still showed clear signs of organic

contamination. In contrast, TOA-based QDs underwent purification smoothly. Organic residues were readily removed without the need for special precautions, and the resulting dispersions produced cleaner QDs.

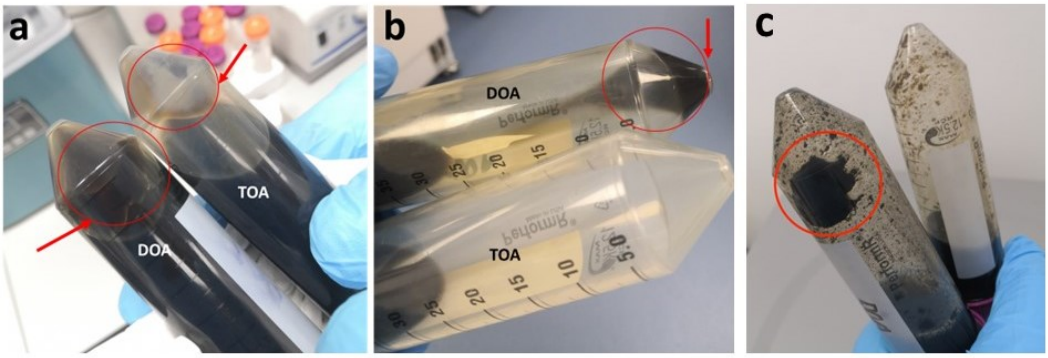

Figure 2.3.3. *Photographs of the InAs QD products obtained using either DOA or TOA are shown after a) addition of the antisolvent to the crude reaction solution and b) upon the first washing step and redispersion in hexane, while the TOA-based QDs could be fully redispersed in hexane, showing no signs of precipitated byproducts, a portion of the DOA-based sample remained trapped in a sticky, gel-like precipitate that could not be redispersed, indicating incomplete purification and residual contamination. (c) Loss of DOA-based QD product upon improper washing.*

Upon drop-casting, DOA-based QDs exhibited a visibly "sticky" residue consistent with persistent organic byproducts and displayed poor electrical conductivity, whereas TOA-based QDs formed clean, uniform films with significantly higher conductivity (Figure 2.3.4).

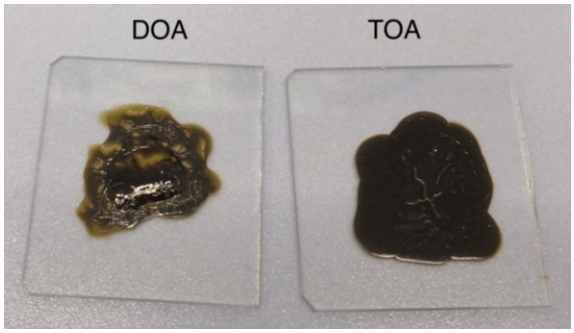

Figure 2.3.4. *Drop-cast films of (left) DOA-based and (right) TOA-based QDs. The DOA-based QDs form a sticky film indicative of residual organic contamination, while the TOA-based QDs yield a powdery film consistent with a cleaner product.*

To systematically assess the influence of these byproducts on charge transport, we carried out electrical measurements on films of DOA- and TOA-derived InAs QDs without applying any ligand-exchange treatment. InAs QD films were deposited on pre-patterned Si substrates with thermal oxide (n++ Si/90 nm SiO_2) and interdigitated Au electrodes. We prepared two device variants: as deposited and baked (with post-heat treatment at 200°C for 30 min) (Figure 2.3.5 a-d). All fabrication steps were performed inside a nitrogen glovebox.

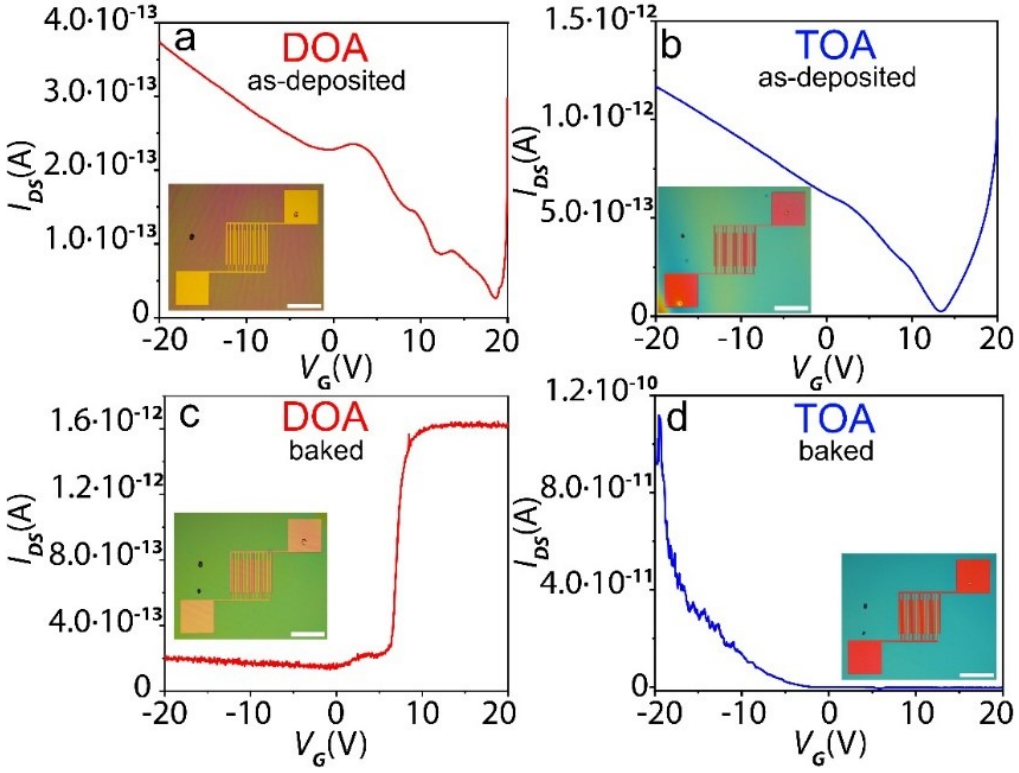

Figure 2.3.5. *FET transfer characteristics (at 300 K) of InAs QDs samples: (a) DOA and (b) TOA as deposited, (c) DOA and (d) TOA after baking. A plan-view optical image of each FET device is shown for each transfer curve (scale bars are all 0.5 mm).*

Electrical characterization revealed that TOA-based QDs consistently exhibited higher carrier mobilities compared to DOA-based QDs. Moreover, the FET on/off ratios clearly demonstrated superior conductivity in TOA-derived films, with the baked TOA devices displaying conductivities approximately two orders of magnitude higher than their DOA counterparts (Table 2.2)

Table 2. 2. *FET data for DOA- and TOA-based InAs QD films.*

Sample	**Transport**	**Electron mobility ($cm^2/V{\cdot}s$)**	**Hole mobility ($cm^2/V{\cdot}s$)**
DOA- QDs, as deposited	Ambipolar	$1.6 \cdot 10^{-9}$	$7.79 \cdot 10^{-10}$
DOA- QDs, baked	Unipolar (electron)	$6.52 \cdot 10^{-9}$	-
TOA- QDs, as deposited	Ambipolar	$3.08 \cdot 10^{-9}$	$2.44 \cdot 10^{-9}$
TOA- QDs, baked	Unipolar (hole)	-	$7.74 \cdot 10^{-8}$

To further probe the structural and compositional differences between the two InAs QD samples, we performed thermogravimetric analysis (TGA) on the final products obtained from the two seeded-growth procedures, that is, the DOA-based QDs with an excitonic absorption at 1045 nm and the TOA-based QDs absorbing at 1140 nm. In agreement with the qualitative purification behavior described earlier, TGA revealed that the DOA-derived QDs contained a considerably larger fraction of organic or metal-organic species than their TOA-based counterparts (Figure 2.3.6 a, b). Specifically, DOA-based InAs QDs displayed an initial mass loss of approximately 5% at 134 °C, followed by a substantial 41% loss at 373 °C (Figure 2.3.6 a), consistent with previous reports on similar systems[47]. In contrast, the TOA-based QDs exhibited a markedly smaller total weight loss of only 29% occurring around 380 °C, indicating a significantly cleaner surface composition.

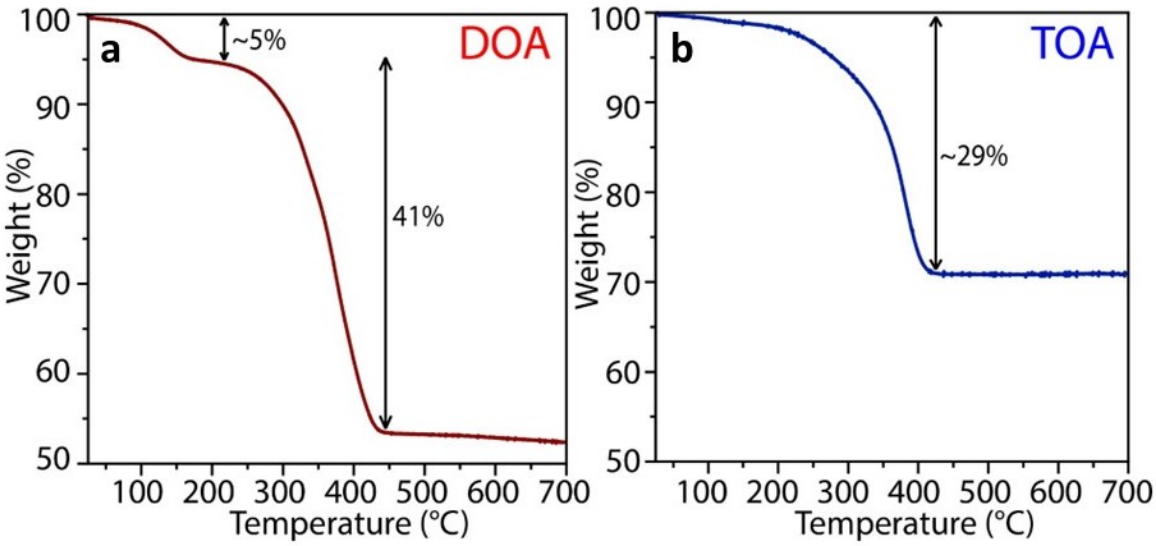

Figure 2.3.6. *TGA curves of (a) DOA- and (b) TOA-based InAs QDs.*

XPS analysis was subsequently performed on the final QDs obtained from both synthetic routes. Notably, neither sample showed evidence of surface oxides, an important result given that oxide formation has commonly been reported for DOA-based InAs QDs in prior studies. The In 3d region similarly confirmed the presence of InAs, with the primary In $3d_{5/2}$ component appearing at 444.3 ± 0.2 eV for both samples (Figure 2.3.7 a, b)[48]. However, the DOA-derived sample exhibited a pronounced asymmetric broadening on the high-binding-energy side of the In 3d peaks, a feature largely absent in the TOA-based QDs. Peak deconvolution (Figure 2.3.7 b) revealed a second indium species with an In $3d_{5/2}$ component at 445.2 ± 0.2 eV. This binding energy, together with the accompanying O 1s peak at 531.8 ± 0.2 eV (Figure 2.3.7 d), is characteristic of indium carboxylates, which likely originate from oleate ligands present at the QD surface[49]. A second low-intensity oxygen component, centered at approx. 530.8 eV, was also needed to better reproduce the experimental O 1s signal. This is most likely to be attributed to adventitious organic species, as C-OH groups, and not to oxygen in In_2O_3, for which a oxygen signal is expected at 529.5 eV.[50]

In both cases, the As 3d peak was centered at ~41 eV, consistent with arsenide species, and no signal was detected in the 42-46 eV binding-energy range associated with As_2O_3 (Figure 2.3.7. c)[44, 48, 51]. A key distinguishing feature between the two samples was observed in the Si 2p region. The DOA-based QDs displayed a clear Si 2p peak at ~102 eV, consistent with silicone or siloxane-type species containing Si-O bonds[52]. This peak was entirely absent in the TOA-derived QDs (Figure 2.3.7 f), indicating that silicon-containing byproducts are specific to the DOA route.

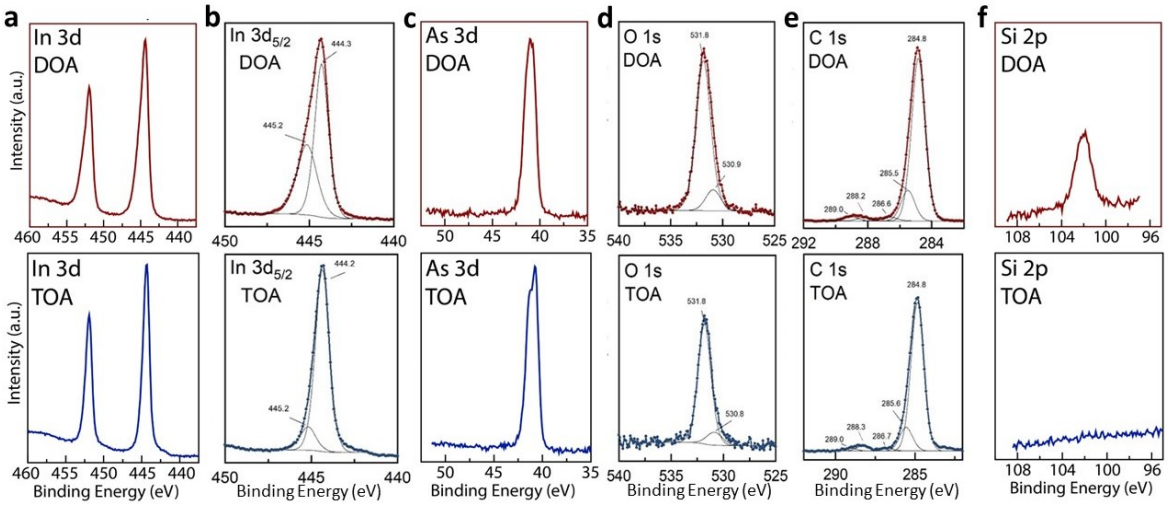

Figure 2.3.7. *(a) In 3d, (b) In $3d_{5/2}$, (c) As 3d, (d) O 1s, (e) C 1s, and (f) Si 2p XPS spectra collected on DOA- (top row) and TOA- (bottom row) based InAs QDs samples.*

The presence of Si-based species in the DOA sample was further corroborated by STEM-EDS compositional mapping, which revealed a diffuse Si signal distributed across the carbon support film rather than colocalized with the InAs QDs (Figure 2.3.8), confirming that these species are extrinsic byproducts rather than part of the QD lattice.

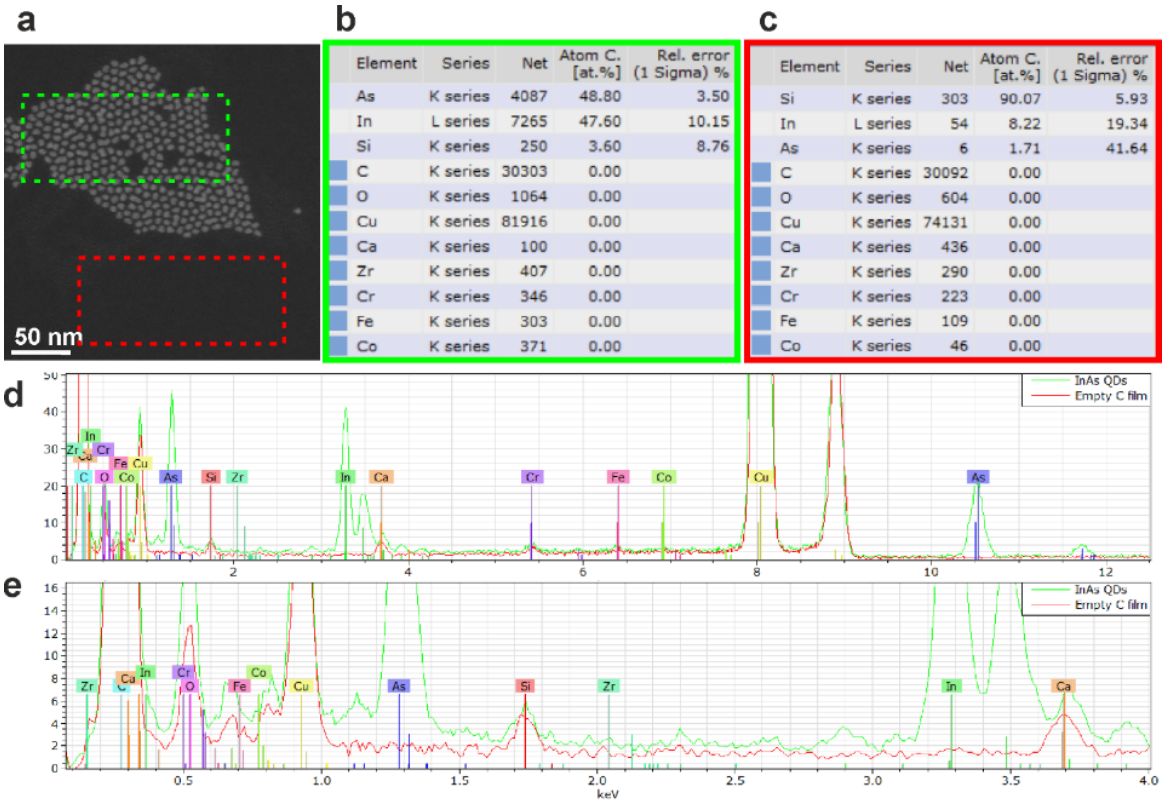

Element	Series	Net	Atom C. [at.%]	Rel. error (1 Sigma) %
As	K series	4087	48.80	3.50
In	L series	7265	47.60	10.15
Si	K series	250	3.60	8.76
C	K series	30303	0.00	
O	K series	1064	0.00	
Cu	K series	81916	0.00	
Ca	K series	100	0.00	
Zr	K series	407	0.00	
Cr	K series	346	0.00	
Fe	K series	303	0.00	
Co	K series	371	0.00	

Element	Series	Net	Atom C. [at.%]	Rel. error (1 Sigma) %
Si	K series	303	90.07	5.93
In	L series	54	8.22	19.34
As	K series	6	1.71	41.64
C	K series	30092	0.00	
O	K series	604	0.00	
Cu	K series	74131	0.00	
Ca	K series	436	0.00	
Zr	K series	290	0.00	
Cr	K series	223	0.00	
Fe	K series	109	0.00	
Co	K series	46	0.00	

Figure 2.3.8. *STEM-EDS quantitative analysis of Si in final InAs QDs synthesized with DOA. (a) High-angle annular dark field (HAADF)-STEM image of QDs and (b) quantification obtained in areas containing a large number of QDs, compared with (c) quantification in neighboring empty regions, with identical area (e.g., see panel (a)), showing no significant difference in net counts for Si (column "Net"). (d,e) Raw spectra obtained by summing areas (green) with and (red) without QDs, selected as shown in panel (a). The X-rays peaks of Cu, Ca, Zr, Cr and Fe are due to the TEM grid and components of the experimental setup hit by back-scattered electrons.*

To further elucidate the nature of the Si-containing species, we acquired ^{1}H NMR and HSQC spectra of the DOA-derived InAs QDs. These measurements revealed a sharp resonance at 0.25 ppm and a broader signal centered around 0.70 ppm, both consistent with the presence of TMS-based moieties (Figure 2.3.9 a). In particular, analysis of the edited HSQC spectrum, together with chemical shift considerations, allowed us to assign the broad resonance at 0.70 ppm in the ^{1}H NMR and -2.58 ppm in the ^{13}C spectrum to a CH_3 group belonging to TMS-based species bound to the surface of the QDs (Figure 2.3.9 b).

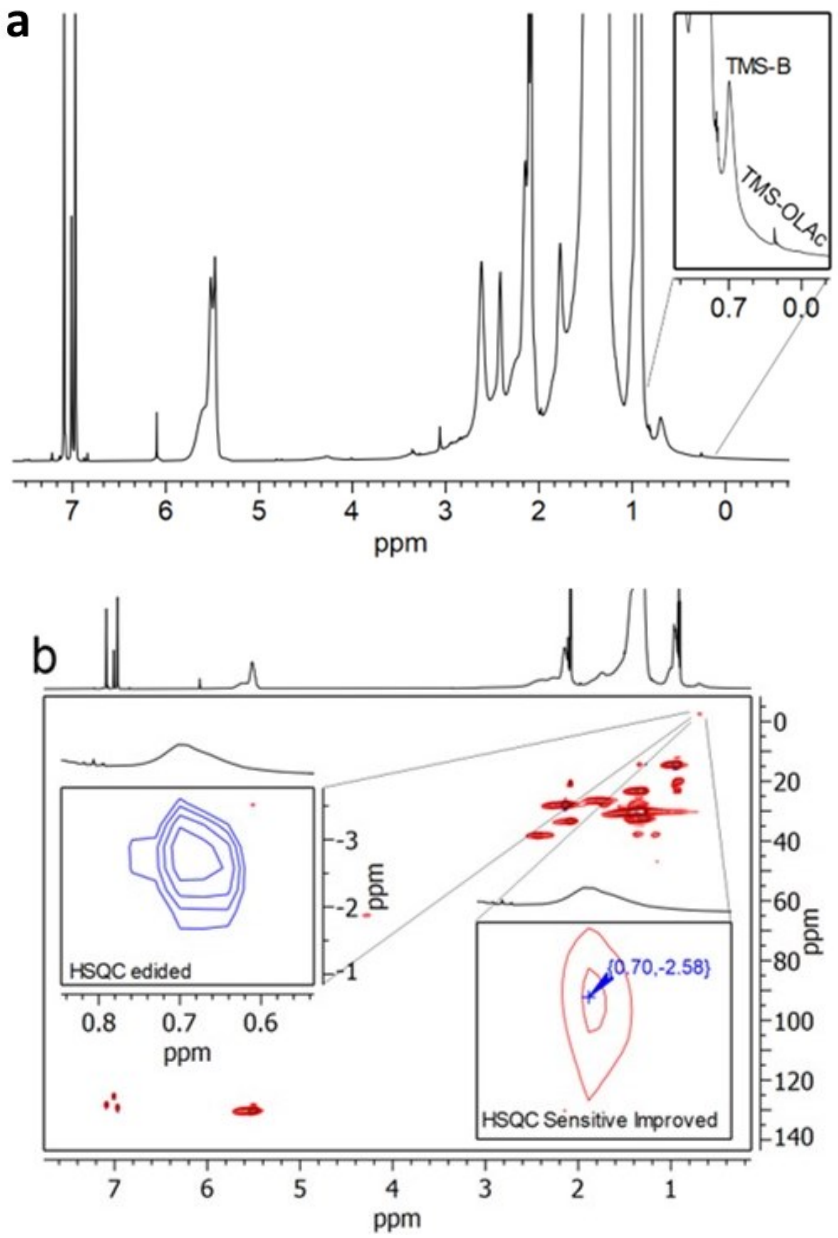

Figure 2.3.9. *a) ^{1}H NMR and b) ^{1}H-^{13}C HSQC NMR spectra of DOA-based InAs QDs in toluene-d. The insets show the edited version (left inset), in which CH_3 groups are represented in blue, and the sensitive improved (right inset).*

To determine the identity of these species, elucidate their formation pathway, and uncover possible side reactions occurring during InAs QD synthesis, we conducted a series of control experiments and characterized the resulting products using ^{1}H and ^{13}C NMR spectroscopy. These control experiments consisted of reacting either $(TMS)_3$-As or trimethylsilanol (TMS-OH) with DOA, OLAc, or mixtures of DOA + OLAc or TOA + OLAc at elevated temperatures (250 °C). The reaction products were identified by spiking the crude mixtures with authentic reference compounds, commercially available when possible or otherwise freshly synthesized and fully

characterizing them by ^{1}H and ^{13}C NMR spectroscopy. The structural assignments of all reference compounds and reaction products are provided in the Appendices section.

In the first control experiment, we investigated the direct reaction between $(TMS)_3$-As and OLAc under typical growth conditions. Specifically, OLAc (2 mL, 6 mmol) was loaded into a three-neck flask, degassed at 120 °C for 1 h, and subsequently heated to 250 °C under nitrogen. At this temperature, $(TMS)_3$-As (140 µL, 0.5 mmol) was injected, and the mixture was allowed to react for 1 h. An aliquot of the crude product was then diluted in toluene-d for ^{1}H and ^{13}C NMR analysis. The NMR spectra (Figure 2.3.10 and 2.3.11) revealed the clean formation of trimethylsilyl oleate (TMS-OLAc), confirming that $(TMS)_3$-As undergoes nucleophilic displacement by OLAc to generate the corresponding silyl ester under these conditions as shown in Equation 2.1

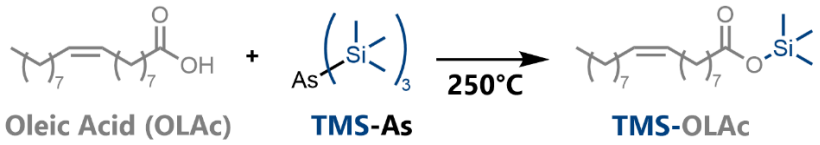

(Equation 2.1)

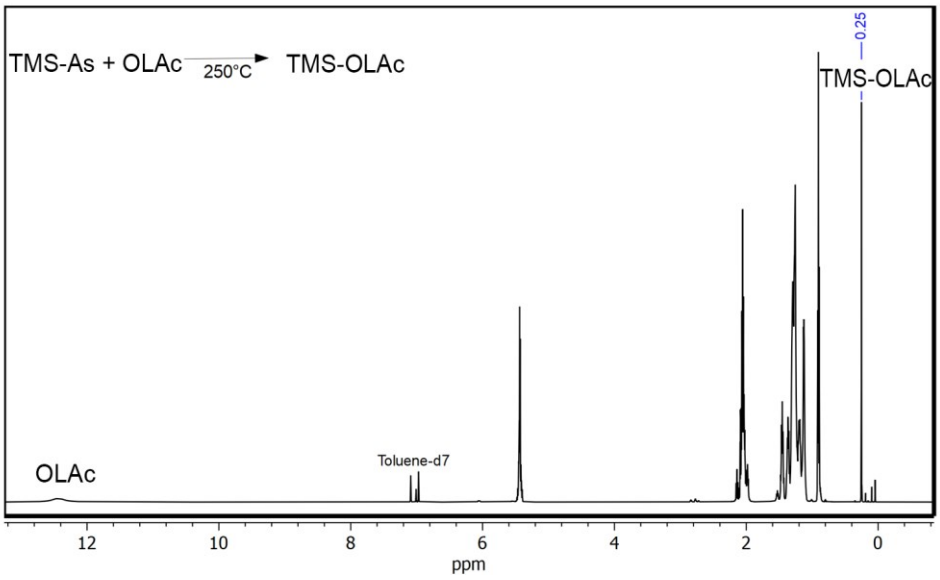

Figure 2.3.10. *^{1}H NMR spectrum of the reaction of $(TMS)_3$-As with OLAc in toluene-d, diagnostic peaks are labeled.*

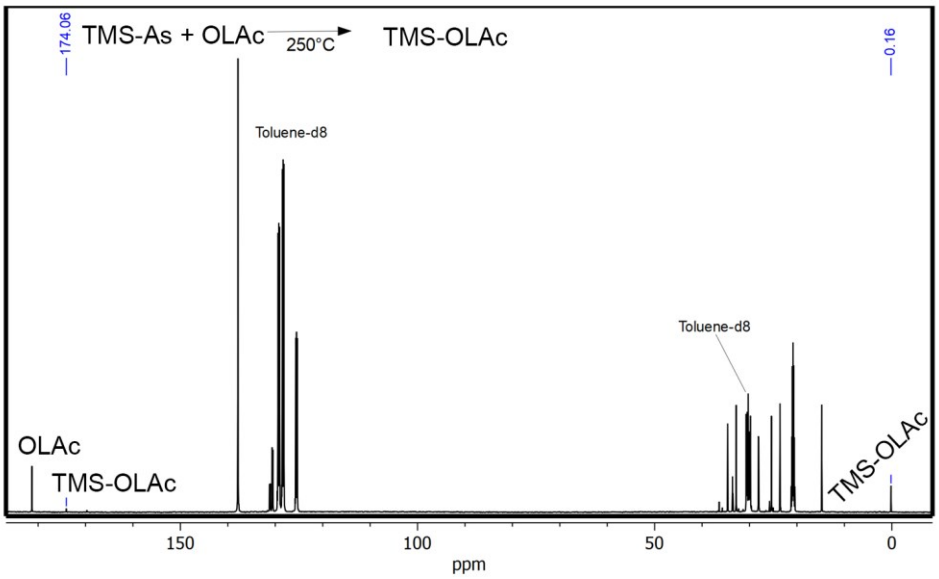

Figure 2.3.11. *^{13}CNMR spectrum of the reaction of $(TMS)_3$-As with OLAc in toluene-d, diagnostic peaks are labeled.*

Having established that $(TMS)_3$-As readily forms the corresponding silyl ester with OLAc, we next examined the reactivity of its hydrolysis product, trimethylsilanol (TMS-OH), toward the same carboxylic acid. In this control experiment, OLAc (2 mL, 6 mmol) was loaded into a three-neck round-bottom flask, degassed at 120 °C for 1 h, and then heated to 250 °C under nitrogen. At this temperature, TMS-OH (160 µL, 1.5 mmol) was slowly injected to avoid excessive volatilization and boiling. The reaction was allowed to proceed for 1 h under a continuous nitrogen flow, after which a small aliquot (30 µL) was withdrawn, diluted in dry toluene-d, and analyzed by ^{1}H and ^{13}C NMR spectroscopy (Figure 2.3.12 and 2.3.13).

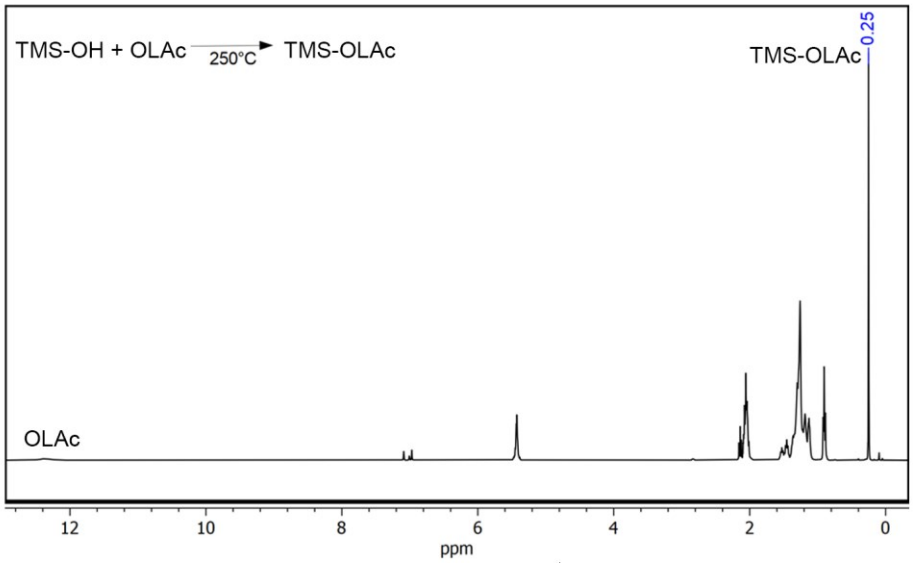

Figure 2.3.12. *^{1}H NMR spectrum of the reaction of TMS-OH with OLAc in toluene-d, diagnostic peaks are labeled.*

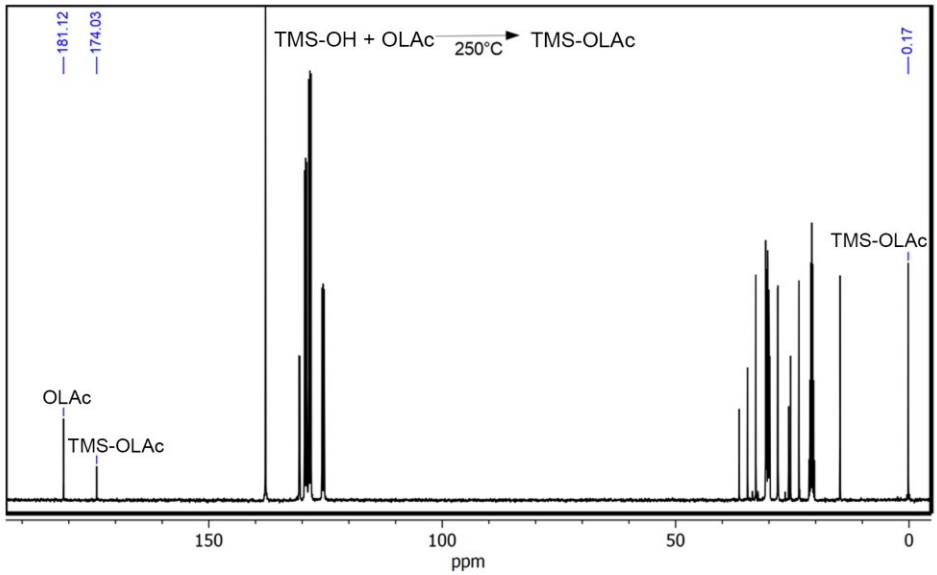

Figure 2.3.13. *^{13}C NMR spectrum of the reaction of TMS-OH with OLAc in toluene-d, diagnostic peaks are labeled.*

The NMR spectra revealed that TMS-OH undergoes a clean esterification reaction with OLAc to form trimethylsilyl oleate (TMS-OLAc), mirroring the behavior observed for $(TMS)_3$-As in the previous experiment. In addition, a minor secondary reaction was detected in which TMS-OH partially condensed with itself to yield hexamethyldisiloxane (TMS-O-TMS). These outcomes, illustrated in Equation 2.2 and supported by the spectra in Figure 2.3.12 and 2.3.13, confirm that both $(TMS)_3$-As and TMS-OH are competent precursors for generating TMS-OLAc under the thermal conditions used for InAs QD growth.

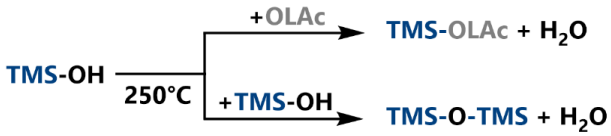

(Equation 2.2)

To investigate whether interactions between TMS-derived species and DOA could lead to amide formation or other side products, we next examined the reactivity of both $(TMS)_3$-As and TMS-OH with DOA under typical synthesis conditions. In the first experiment, DOA (900 µL, 3 mmol) was loaded into a three-neck flask, degassed at 120 °C for 1 h, and heated to 250 °C under nitrogen. $(TMS)_3$-As (140 µL, 0.5 mmol) was then injected, and the mixture was allowed to react for 1 h before a small aliquot was collected and analyzed by ^{1}H and ^{13}C NMR spectroscopy (Figure 2.3.14 a, b). An analogous procedure was used to probe the reactivity of TMS-OH with DOA: DOA (900 µL, 3 mmol) was degassed and heated to 250 °C, after which TMS-OH (160 µL, 1.5 mmol) was slowly injected to minimize boiling, followed by a 1 h reaction period under a high nitrogen flow. NMR analysis of the crude products revealed that neither reaction produced the corresponding silylamine (TMS-DOA). Instead, in the TMS-OH + DOA experiment, the dominant

product was hexamethyldisiloxane (TMS-O-TMS), arising from the self-condensation of TMS-OH. These results indicate that DOA does not undergo silylation under these conditions and that TMS-OH preferentially reacts with itself rather than forming amide- or silylamine-type species (Figure 2.3.14).

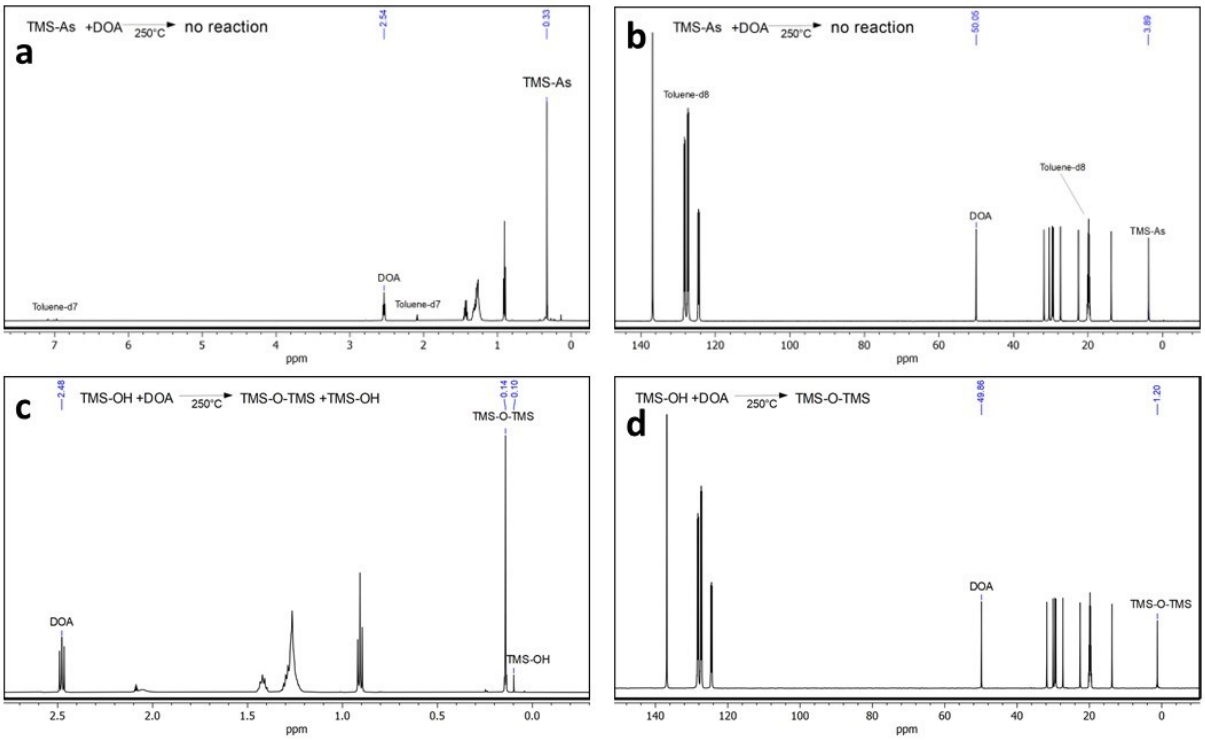

Figure 2.3.14. *(a, c) ^{1}H NMR spectrum of the reaction of $(TMS)_3$-As and TMS-OH with DOA in toluene-d and (b, d) their corresponding ^{13}C NMR spectrum.*

Having assessed the reactivity of $(TMS)_3$-As and TMS-OH with individual components of the synthesis mixture, we next recreated conditions more closely resembling the actual InAs QD growth environment by examining their behavior in the presence of both DOA and OLAc. Of particular interest was the reaction between $(TMS)_3$-As and a mixture of DOA and OLAc. In this experiment, OLAc (2 mL, 6 mmol) and DOA (900 µL, 3 mmol) were introduced into a three-neck round-bottom flask, degassed at 120°C for 1 h, and then heated to 250°C under nitrogen. At this temperature, $(TMS)_3$-As (140 µL, 0.5 mmol) was injected, and the reaction was allowed to proceed for 1 h. A 30 µL aliquot of the crude mixture was collected and analyzed by ^{1}H and ^{13}C NMR spectroscopy. The spectra revealed the simultaneous formation of several products, including N,N-dioctyloleamide (DOA-OLAc), TMS-OLAc, TMS-OH, and its condensation product TMS-O-TMS (Figure 2.3.15). The coexistence of these species confirms that, under typical synthesis temperatures, DOA and OLAc readily undergo amide-forming condensation, generating water in situ, which subsequently reacts with $(TMS)_3$-As to produce the various TMS-based byproducts observed.

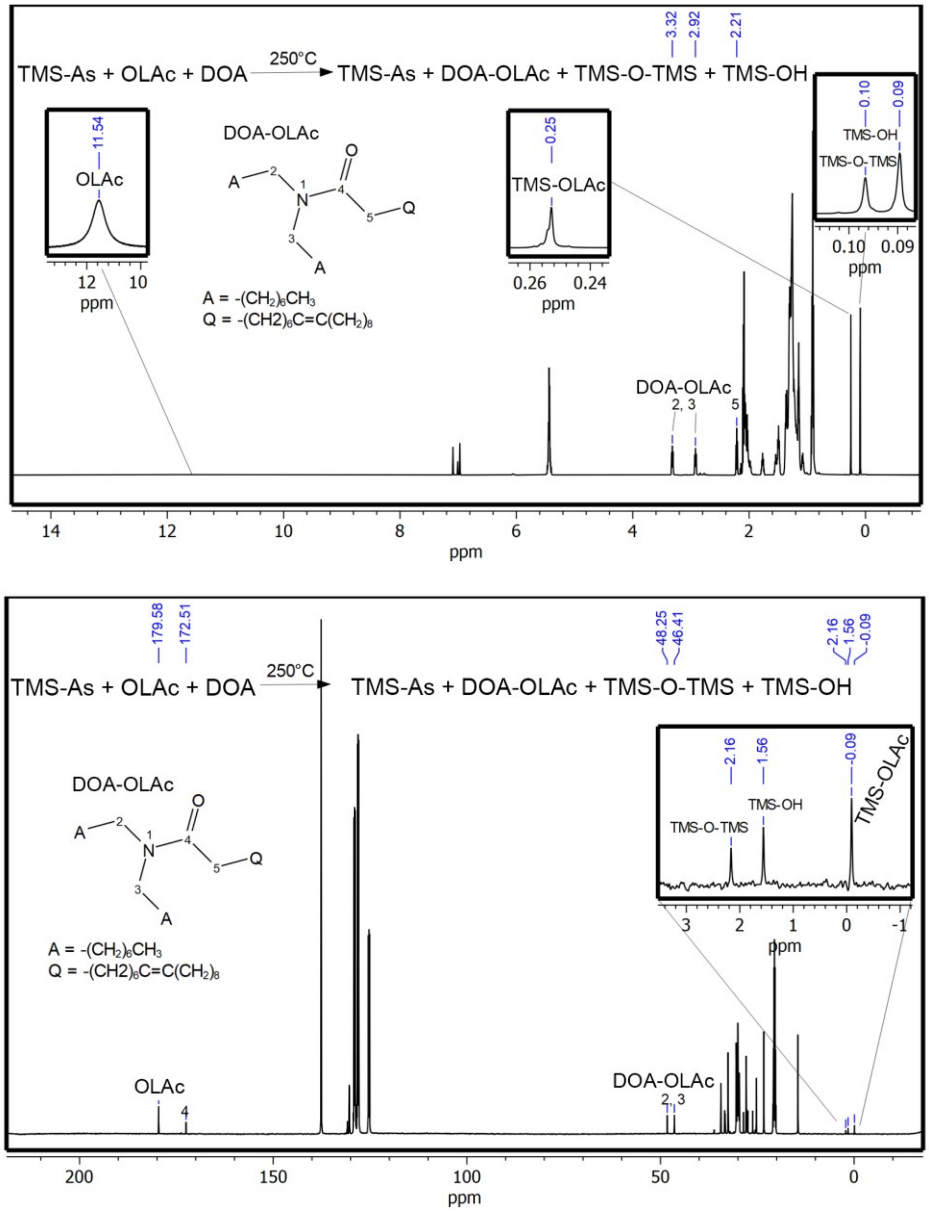

Figure 2.3.15: *^{1}H and ^{13}C NMR spectrum of the reaction of $(TMS)_3$-As with OLAc and DOA in toluene-d, diagnostic peaks are labeled.*

To further validate the structural assignments of the products formed in the $(TMS)_3$-As + DOA + OLAc reaction, we performed two-dimensional NMR analyses (Figure 2.3.16) and spiking experiments (Figure 2.3.17). ^{1}H-^{13}C Heteronuclear Multiple Bond Correlation (HMBC) spectroscopy confirmed the presence of the amide functionality originating from DOA-OLAc condensation, while ^{1}H NMR spiking with authentic reference compounds enabled unambiguous identification of the TMS-derived species observed in the crude mixture.

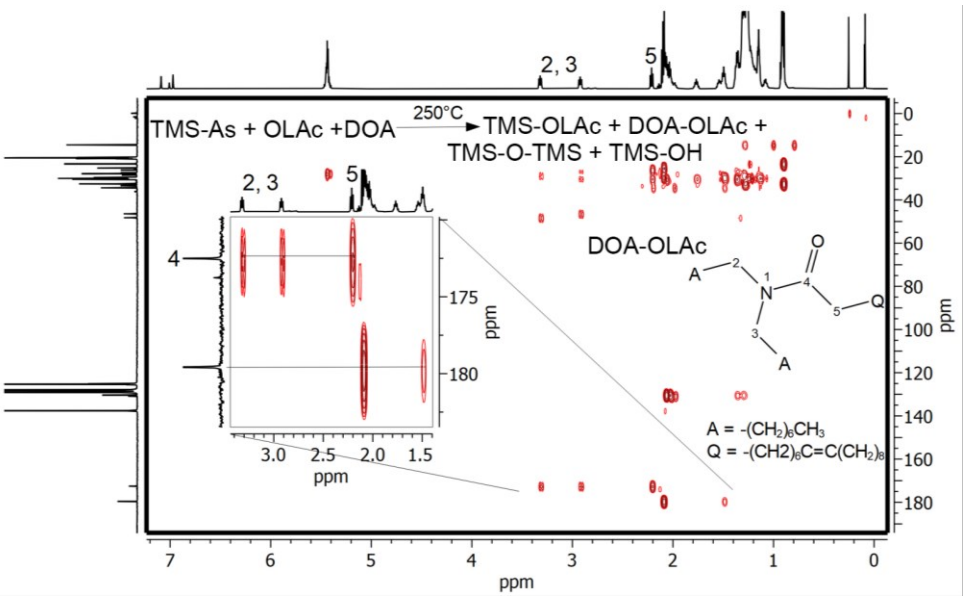

Figure 2.3.16. *^{1}H-^{13}C HMBC NMR spectrum of the reaction of $(TMS)_3$-As with OLAc and DOA, as proof of the structure identity, the cross correlation HMBC peaks between both the CH_2 in position 2 and 3 and the one in position 5 with the carbon at 172.51 ppm, diagnostic of amide group, inset.*

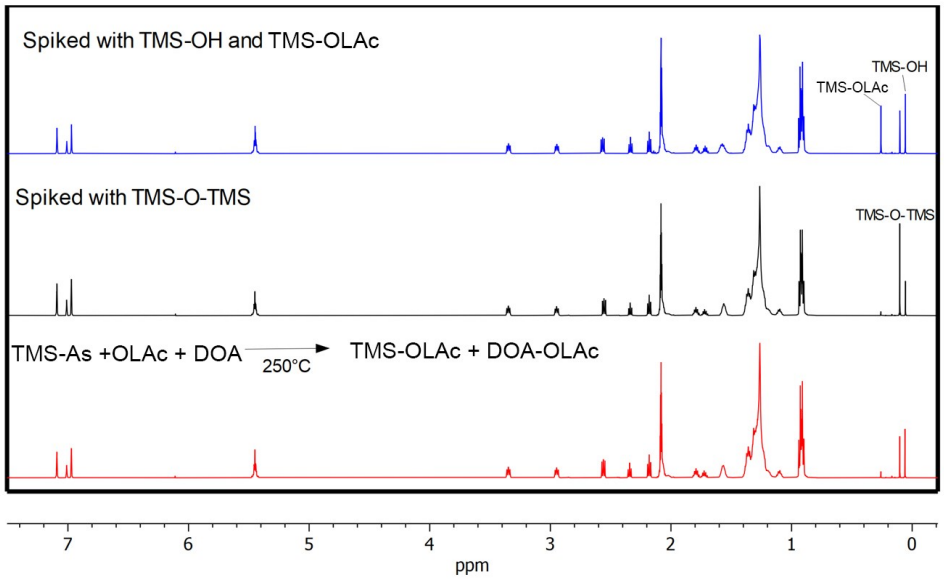

Figure 2.3.17. *^{1}H NMR spectrum of the reaction of $(TMS)_3$-As +DOA+ OLAc, spiked with TMS-OLAc, TMS-O-TMS and TMS-OH authentic compound. Peaks increasing confirmed the attribution.*

To assess how the reaction chemistry changes when TOA is used instead of DOA, we also examined the reactivity of $(TMS)_3$-As in the presence of a TOA and OLAc mixture under the same conditions. In this experiment, OLAc (2 mL, 6 mmol) and TOA (1.3 mL, 3 mmol) were added to a three-neck round-bottom flask, degassed at 120 °C for 1 h, and then heated to 250 °C under nitrogen. $(TMS)_3$-As (140 µL, 0.5 mmol) was injected at this temperature, and the reaction was allowed to proceed for 1 h. A 30 µL aliquot of the crude mixture was then diluted in dry toluene-

d for ^{1}H and ^{13}C NMR analysis. The spectra showed that the main reaction product was trimethylsilyl oleate (TMS-OLAc), with only a small amount of hexamethyldisiloxane (TMS-O-TMS) detected. The minor formation of TMS-O-TMS, despite TOA being incapable of condensation with OLAc, likely originates from the hydrolysis of reactive TMS-containing intermediates by trace moisture present in the reagents or solvent environment.

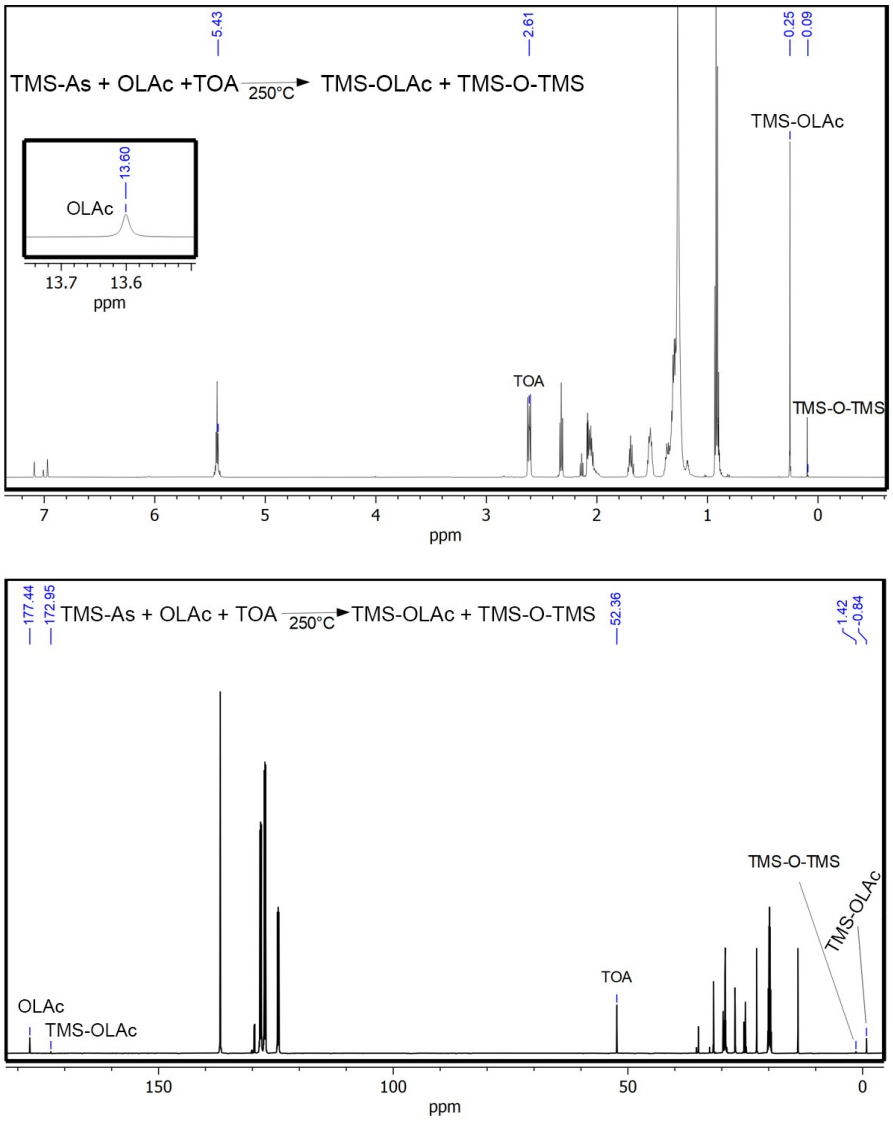

Figure 2.3.18. *^{1}H and ^{13}C NMR spectrum of the reaction of $(TMS)_3$-As with OLAc and TOA in toluene-d, diagnostic peaks are labeled.*

To further validate the structural assignments of products formed in the $(TMS)_3$-As + TOA + OLAc reaction, we performed spiking experiments using authentic reference compounds (Figure 2.3.17).

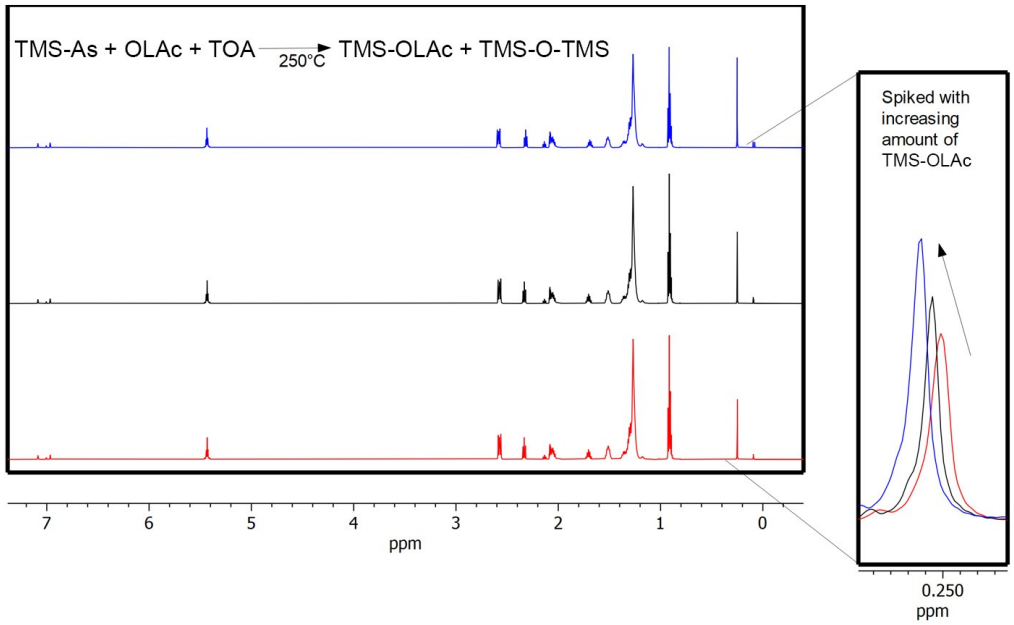

Figure 2.3.19. *^{1}H NMR spectrum of the reaction of $(TMS)_3$-As +TOA+ OLAc, spiked with TMS-OLAc, authentic compound. Peaks increasing confirmed the attribution.*

Overall, the control experiments revealed several important insights into the side reactions occurring during DOA-based InAs QD synthesis:

(i) DOA and OLAc undergo condensation even at temperatures lower than those used during QD growth (250 °C vs 280 °C), producing water as a byproduct.

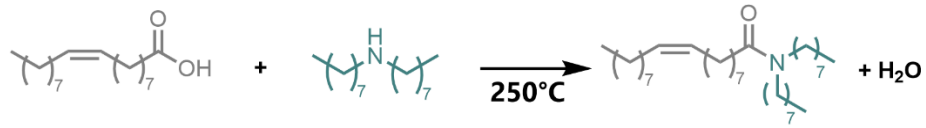

Oleic Acid (OLAc) N,N-dioctylamine (DOA) DOA-OLAc

(Equation 2.3)

(ii) No ketones were detected in any of the reaction mixtures, ruling out OLAc ketonization as previously hypothesized by other group as a source of water[47].

(iii) the water formed through amide condensation readily reacts with TMS-containing species to generate substantial amounts of TMS-OH, which can subsequently condense with itself or react with OLAc, leading to the formation of TMS-O-TMS, TMS-OLAc, and additional water in a self-propagating cascade[53].

(iv) the sharp resonance at 0.25 ppm observed in the ^{1}H NMR spectrum of DOA-based InAs QDs was unambiguously assigned to free TMS-OLAc.

(v) the broad signal at 0.69 ppm (denoted TMS-B in Figure 2.3.9 a) was attributed, based on HSQC correlations, to TMS-derived species bound to the QD surface, although a precise structural assignment could not be made.

These results can be rationalized by considering the reaction environment characteristic of DOA-based InAs QD synthesis. Under these conditions, the in-situ formation of water through the

condensation of DOA with OLAc drives the generation of several TMS-derived byproducts including DOA-OLAc, TMS-OLAc, and TMS-O-TMS, that accumulate in significant amounts. These species are possibly difficult to remove during purification, explaining the washing challenges observed experimentally for DOA-derived QDs. In contrast, the synthesis conducted with TOA largely suppresses the formation of TMS-OLAc and related byproducts, likely because the absence of water prevents the hydrolysis of TMS-containing intermediates and their subsequent reaction with OLAc. It should be noted, however, that under slightly different reaction conditions reported by other groups for DOA-based syntheses, surface indium or arsenic oxides have been detected. This suggests that the fate of the in situ generated water is sensitive to subtle variations in reaction parameters and may not always lead to the same chemical outcomes.

2.4. Conclusions

In conclusion, we have demonstrated that trioctylamine (TOA), much like dioctylamine (DOA), is capable of moderating the reactivity of $(TMS)_3$-As, thereby enabling precise control over the growth of InAs QDs while maintaining narrow size distributions. Under the optimized conditions developed in this work, we achieved InAs QDs with excitonic absorption peaks tunable up to 1100 nm, HWHM values as low as ~50 meV, and peak-to-valley ratios above 2, representing record optical figures of merit for colloidal InAs QDs.

Crucially, we have shown that TOA offers a major advantage over DOA by preventing the in-situ formation of water, which arises from the high-temperature condensation reaction between DOA and oleic acid (OLAc) at 280 °C. The water produced under DOA-based conditions triggers a cascade of reactions involving TMS-containing intermediates, leading to the formation of TMS-O-TMS and TMS-OLAc species that contaminate the resulting QDs. These contaminants complicate purification, frequently causing gelation or complete loss of product, and persist even after extensive washing, in some cases remaining as free TMS-OLAc or as TMS-derived moieties bound to the QD surface. In contrast, TOA-based InAs QDs are substantially cleaner, easier to purify, and free from silicon-oxygen byproducts.

Overall, our findings highlight the importance of amine selection in $(TMS)_3$-As based InAs QD syntheses and demonstrate that tertiary amines offer a robust strategy to suppress unwanted side reactions. We anticipate that further tuning of tertiary amine sterics, by systematically varying the alkyl substituents on the nitrogen center, could provide an additional handle for manipulating precursor reactivity and refining control over QD size and size distribution in future synthetic developments.

2.5. Experimental Section

Chemicals

Indium(III) acetate (InOAc, 99.99%), Oleic acid (OLAc), 1-octadecene (ODE, 90%), dioctylamine (DOA, 98%), tri-n-octylamine (TOA, 98%), toluene (anhydrous, 99.8%), hexane (anhydrous, 99%), butanol (anhydrous, 99.8%), toluene-d8 (99.6 atom% D). The above chemicals were purchased from Sigma-Aldrich and used without further purification. Tris(trimethylsilyl)arsine $(TMS)_3$-As, 99%) was purchased from Dock chemicals and used without further purification. DOA, TOA, and ODE were degassed at 120°C under vacuum for 1h before use.

Synthesis of InAs QDs using DOA

The synthesis method is based on the study previously reported by Song *et al.,* with some modifications. The synthesis of InAs QDs is carried out in three steps: first, starting InAs QDs are prepared, which are then grown larger through two subsequent steps involving the continuous injection of InAs clusters.

First step. We first prepared indium oleate by mixing 580 mg (2 mmol) of indium acetate, 2 mL of oleic acid (6 mmol) and 3 mL of ODE in a 100mL round bottom flask. The mixture was degassed at 120°C for 2 h under vacuum. The As precursor solution was prepared inside an argon filled glovebox by mixing 140 µL of $(TMS)_3$-As (0.5 mmol) with 450 µL of DOA (1.5 mmol) and 1 mL of ODE at room temperature in a 4 mL glass vial for ~5min. This solution was rapidly injected into the reaction flask, which was previously heated up to 280°C under nitrogen. The InAs QDs were allowed to grow for 10 min after the injection.

Second step. We prepared a dispersion of DOA-based InAs clusters by mixing an indium oleate solution (prepared by degassing at 120°C under vacuum for 2 h a mixture of 870 mg, 3 mmol, of indium acetate, 2.35 mL of oleic acid, 9 mmol, and 15 mL of ODE in a 100 mL round bottom flask) with an As-precursor solution (prepared inside a glovebox by mixing 215 µL of $(TMS)_3$-As, 0.75 mmol, 1.375 mL of DOA, 4.5 mmol, and 3 mL of ODE at room temperature in a 10 mL glass vial for ~5min).

InAs QDs were grown larger by the continuous injection of the DOA-based InAs cluster dispersion into the crude reaction solution of InAs QDs heated up to 280 °C. The injection rate was 8 mL/h for the first hour, followed by a 4 mL/h rate until all the InAs cluster dispersion was completely injected (this step lasted ~3 hours). The reaction was quenched by cooling it to room temperature, and the resulting QDs were purified by adding 15 mL of hexane and 60 mL of butanol, followed by centrifugation at 8000 rpm for 5 minutes. The precipitate was discarded. Next, 60 mL of butanol was added to the supernatant and the resulting mixture was centrifuged again at 8000 rpm for 5 minutes. The precipitate was collected and re-dispersed in 10 mL of hexane, then precipitated again by adding 40 mL of butanol. This cleaning step was repeated twice. Finally, the precipitate was re-dispersed in 3 mL of hexane. All purification steps were carried out in a glove box under an argon atmosphere.

Third step. A second DOA-based InAs clusters dispersion was prepared as described in the *second step*. The InAs QDs prepared in the *second step* were mixed with 3 mL of ODE in a 100 mL flask and degassed at 120 °C for 1 hour under vacuum to remove the hexane, leaving the QDs in the ODE solution. The temperature of the flask was then increased to 280 °C under nitrogen, and the dispersion of DOA-based InAs clusters was injected continuously using a syringe pump. The injection rate was varied over time: for the first 2 hours, the injection rate was 2 mL/h, followed by a 1 mL/h rate until all the InAs clusters were injected (the overall injection process lasted ~20 hours). The reaction was then stopped, and the flask was allowed to cool to room temperature. The resulting QDs were purified similarly to the method used in the *second step*. The washed final InAs QDs were dispersed in a nonpolar solvent such as octane, toluene, or hexane for further processing.

Synthesis of InAs QDs using TOA

The synthesis of InAs QDs using TOA followed the same procedure as that used for DOA, with the only modification being the substitution of DOA with TOA in equivalent molar amounts. Specifically, 656 µL of TOA (1.5 mmol) was used for the synthesis of InAs starting QDs, and 1.96 mL (4.5mmol) for the preparation of the TOA-based InAs cluster solution. The cleaning procedures were also analogous to those employed for DOA-based InAs QDs.

Optical Measurements

The absorption spectra were recorded using a Varian Cary 5000 UV-Vis-NIR spectrophotometer. Samples were prepared by diluting the QD dispersions in 3 mL of tetrachloroethylene and measuring them in standard 1 cm path-length quartz cuvettes, , sealed with airtight screw caps, inside a N_2 filled glovebox. Aliquots were taken directly from the reaction mixture using a glass syringe, diluted with toluene, and their absorption was measured under ambient conditions.

X-ray Diffraction (XRD)

XRD patterns were collected using a PANanalytical Empyrean X-ray diffractometer equipped with a 1.8 kW Cu Kα ceramic X-ray tube and a PIXcel3D 2×2 area detector, operating at 45 kV and 40 mA. For XRD measurements, specimens were prepared by depositing a concentrated QDs solution onto a silicon zero-diffraction single crystal substrate. Diffraction patterns were recorded under ambient conditions utilizing parallel beam geometry and symmetric reflection mode. The XRD data were analyzed using PANalytical's HighScore 4.1 software.

X-Ray Photoelectron Spectroscopy (XPS)

Specimens for XPS were prepared in a glove box by drop casting a few microliters of a concentrated QD solution onto freshly cleaved highly oriented pyrolytic graphite (HOPG, ZYB grade). The specimens were then transferred to the vacuum chamber, avoiding air exposure through an *ad hoc* transfer vessel, to reduce air-induced oxidation. The XPS analyses were carried out with a Kratos Axis Ultra^{DLD} spectrometer, using a monochromatic Al Kα source operated at 20mA and 15kV. Wide scans were carried out at a pass energy of 160 eV over an analysis area of

300 x 700 μm^2. High-resolution analyses were carried out at a pass energy of 20 eV. The Kratos charge neutralizer system was used on all specimens. Spectra were charge corrected to the main line of the carbon 1s spectrum (C-C bonds) set to 284.8 eV. Spectra were analyzed using CasaXPS software (version 2.3.24).

Bright Field Transmission Electron Microscopy (BF-TEM)

Diluted QDs solutions were drop-cast onto copper TEM grids with an ultrathin carbon film. Overview bright-field TEM images were acquired on a JEOL JEM-1400Plus microscope with a thermionic gun (LaB_6) operated at an acceleration voltage of 120 kV.

STEM-EDS

DOA-based InAs QDs were drop cast onto an ultrathin C/lacey C/Cu grid, previously plasma-treated to remove any residues from film preparation. The analysis was performed employing an image-Cs-corrected JEOL JEM-2200FS TEM, equipped with a Bruker X-Flash 5060 EDS system, operated at 200 kV. The EDS quantification was obtained from the summed spectra acquired from a large number of QDs, using the Cliff-Lorimer method for the Kα peaks of C, Si and As and the Lα peak of In.

High resolution scanning transmission electron microscopy images were acquired at an acceleration voltage of 300 kV in a Thermo Fisher Spectra 300 S/TEM, acquiring the high-angle annular dark field (HAADF) signal. The current was set to 200 pA and the convergence angle to 25 mrad. Samples were dispersed on ultra-thin carbon films for analysis.

Thermogravimetric analysis (TGA)

Thermal gravimetric analysis (TGA) was conducted with a TA instruments Q500 thermal analyzer under a 50 mL/min nitrogen flux on ∼5 mg of nanocrystals powders. The samples were analyzed after a 5 min equilibration at 30 °C, and then the temperature was increased by a 10 °C/min ramp up to 700 °C.

FET Characterizations

InAs QD films were deposited on pre-patterned Si substrates with thermal oxide (n++ Si/90 nm SiO_2) and interdigitated Au electrodes. Two device variants were prepared as deposited and baked (with post-heat treatment at 200°C for 30 min). All the FET fabrication steps were carried out inside a glovebox. The FET transfer characteristic measurements were performed using Keithley 4200-SCS Semiconductor Characterization System. The carrier mobility was extracted from the linear regime of the FET transfer curve. It was calculated by fitting the experimental data to the following equation: $\mu = \frac{L}{WC_iV_D}\frac{dI_D}{dV_G}$, where L, W, C_i, V_D, I_D, and V_G are the channel length (i.e., 10 µm), channel width (i.e., 10 mm), capacitance per unit area (i.e., 3.84×10^{-4} $F.m^{-2}$), drain voltage (i.e., 1 V), drain current, and gate voltage, respectively.

Nuclear Magnetic Resonance (NMR)

All NMR experiments were acquired on a Bruker (Bruker, Rheinstetten, Germany) 600 MHz spectrometer fitted with a 5 mm QCI cryoprobe, at 298 K. The lock, matching and tuning, shimming, and the 90° pulse optimization, were performed automatically on each sample tube, by using Bruker's routines. The NMR samples were prepared by drying under vacuum a 30 µL aliquot of each InAs QD dispersion. After drying, 1.5 mL of toluene-d8 was added to the QDs to redisperse them. A 600 µL portion of this solution was then used for NMR analysis.

^{1}H NMR. 32 scans were accumulated, without steady ones and spinning, at a fixed receiver gain (4.5), with 65536 digit points and an inter-pulse delay of 30 s, over a spectral width of 20.83 ppm with the offset positioned at 6.18 ppm. A smoothing exponential function equivalent to 0.3 Hz was applied to FID (Free Induction Decays) before the Fourier transform.

^{1}H-^{13}C HSQC (*Heteronuclear Single-Quantum Correlation*) experiment (edited version) was performed with 64 scans, 1024 digit points, 256 increments and $^{1}J_{CH}$ of 145 Hz, over a spectral width of 15.15 ppm for ^{1}H and 165.0 ppm for ^{13}C, with a transmitter frequency offset positioned at 7.0 and 75 ppm, respectively. ^{1}H-^{13}C *HSQC sensitive improved* experiment was run with the same parameters except for the spectral width of 13.02 ppm for ^{1}H and 165.0 ppm for ^{13}C, with a transmitter frequency offset positioned at 4.7 and 70 ppm, respectively.

The ^{1}H-^{13}C HMBC experiment was recorded by using 16 FIDs, 4096 digit points, 128 increments, and $^{1}J_{CH}$ long range of 10 Hz, a spectral width of 15.15 ppm for ^{1}H and 220.00 ppm for ^{13}C, with a transmitter frequency offset at 7.00 and 100.00 ppm, respectively.

Precursor Chemistry

Indium(III) acetate in oleic acid

In the $(TMS)_3As$ synthesis route, indium acetate ($In(OAc)_3$) is first mixed with oleic acid and ODE and degassed under vacuum. This step is not simple dissolution but a deliberate chemical activation that converts $In(OAc)_3$ into a reactive, soluble indium-oleate complex suitable for high-temperature reaction. When $In(OAc)_3$ is combined with excess oleic acid, an acidolysis ligand-exchange reaction occurs in which oleate replaces acetate on the indium center. Although acetic and oleic acid have comparable pKa values, the exchange is driven forward by the continuous removal of acetic acid, a volatile byproduct that boils at 118°C and is easily stripped under mild vacuum. As the mixture is heated to >100°C, the evaporation of acetic acid appears as vigorous bubbling, and a clear solution of indium(III) oleate forms once degassing is complete. This transformation is crucial because acetate ligands do not provide adequate steric stabilization or solubility in the nonpolar ODE medium, whereas the long-chain oleate ligands keep indium species well dispersed.

$(TMS)_3$-As

The precursor chemistry of $(TMS)_3$-As is dictated by the reversed polarity and thermodynamic lability of the Si-As bond. The markedly lower electronegativity of silicon (χ_{Si} = 1.9) compared to arsenic (χ_{As} = 2.1) polarizes the bond as ($Si^{\delta+}$ - $As^{\delta-}$)[54], imparting substantial anionic character to the arsenic center and pre-activating it for nucleophilic behavior. Because Si-As bonds are relatively labile than the Si-heteroatom (Si-O) bond, this precursor is highly reactive and pyrophoric and hence should only be handled under inert atmosphere. Upon injection, heterolytic Si-As scission releases arsenide (As^{3-}) that drives InAs nucleation. This strong thermodynamic drive toward Si-O bond formation accelerates Si-As scission and accounts for the extreme reactivity of $(TMS)_3As$.

2.6. References

1. Lu, H.; Carroll, G. M.; Neale, N. R.; Beard, M. C., Infrared Quantum Dots: Progress, Challenges, and Opportunities. *ACS Nano* **2019,** *13* (2), 939-953.
2. Bahmani Jalali, H.; De Trizio, L.; Manna, L.; Di Stasio, F., Indium arsenide quantum dots: an alternative to lead-based infrared emitting nanomaterials. *Chemical Society Reviews* **2022,** *51* (24), 9861-9881.
3. Lhuillier, E.; Keuleyan, S.; Liu, H.; Guyot-Sionnest, P., Mid-IR Colloidal Nanocrystals. *Chemistry of Materials* **2013,** *25* (8), 1272-1282.
4. Rogalski, A., Scaling infrared detectors—status and outlook. *Reports on Progress in Physics* **2022,** *85* (12).
5. Zhou, R.; Xu, J.; Luo, P.; Hu, L.; Pan, X.; Xu, J.; Jiang, Y.; Wang, L., Near-Infrared Photoactive Semiconductor Quantum Dots for Solar Cells. *Advanced Energy Materials* **2021,** *11* (40), 2101923.
6. Chen, J.; Zheng, S.; Jia, D.; Liu, W.; Andruszkiewicz, A.; Qin, C.; Yu, M.; Liu, J.; Johansson, E. M. J.; Zhang, X., Regulating Thiol Ligands of p-Type Colloidal Quantum Dots for Efficient Infrared Solar Cells. *ACS Energy Letters* **2021,** *6* (5), 1970-1979.
7. De Franco, M.; Zhu, D.; Asaithambi, A.; Prato, M.; Charalampous, E.; Christodoulou, S.; Kriegel, I.; De Trizio, L.; Manna, L.; Bahmani Jalali, H.; Di Stasio, F., Near-Infrared Light-Emitting Diodes Based on RoHS-Compliant InAs/ZnSe Colloidal Quantum Dots. *ACS Energy Letters* **2022,** *7* (11), 3788-3790.
8. Müller, T.; Skiba-Szymanska, J.; Krysa, A. B.; Huwer, J.; Felle, M.; Anderson, M.; Stevenson, R. M.; Heffernan, J.; Ritchie, D. A.; Shields, A. J., A quantum light-emitting diode for the standard telecom window around 1,550 nm. *Nature Communications* **2018,** *9* (1), 862.
9. Roshan, H.; Zhu, D.; Piccinotti, D.; Dai, J.; De Franco, M.; Barelli, M.; Prato, M.; De Trizio, L.; Manna, L.; Di Stasio, F., Near Infrared Light-Emitting Diodes Based on Colloidal InAs/ZnSe Core/Thick-Shell Quantum Dots. *Advanced Science* **2024,** *11* (23), 2400734.
10. Vasilopoulou, M.; Fakharuddin, A.; García de Arquer, F. P.; Georgiadou, D. G.; Kim, H.; Mohd Yusoff, A. R. b.; Gao, F.; Nazeeruddin, M. K.; Bolink, H. J.; Sargent, E. H., Advances in solution-processed near-infrared light-emitting diodes. *Nature Photonics* **2021,** *15* (9), 656-669.
11. Christodoulou, S.; Ramiro, I.; Othonos, A.; Figueroba, A.; Dalmases, M.; Özdemir, O.; Pradhan, S.; Itskos, G.; Konstantatos, G., Single-Exciton Gain and Stimulated Emission Across the Infrared Telecom Band from Robust Heavily Doped PbS Colloidal Quantum Dots. *Nano Letters* **2020,** *20* (8), 5909-5915.
12. Ahn, N.; Livache, C.; Pinchetti, V.; Jung, H.; Jin, H.; Hahm, D.; Park, Y.-S.; Klimov, V. I., Electrically driven amplified spontaneous emission from colloidal quantum dots. *Nature* **2023,** *617* (7959), 79-85.
13. Pejović, V.; Georgitzikis, E.; Lee, J.; Lieberman, I.; Cheyns, D.; Heremans, P.; Malinowski, P. E., Infrared Colloidal Quantum Dot Image Sensors. *IEEE Transactions on Electron Devices* **2022,** *69* (6), 2840-2850.
14. Zhang, Z.; Chang, H.; Xue, B.; Zhang, S.; Li, X.; Wong, W.-K.; Li, K.; Zhu, X., Near-infrared and visible dual emissive transparent nanopaper based on Yb(III)–carbon quantum dots grafted oxidized nanofibrillated cellulose for anti-counterfeiting applications. *Cellulose* **2018,** *25* (1), 377-389.

15. Kaberniuk, A. A.; Baloban, M.; Monakhov, M. V.; Shcherbakova, D. M.; Verkhusha, V. V., Single-component near-infrared optogenetic systems for gene transcription regulation. *Nature Communications* **2021,** *12* (1), 3859.
16. Tsuchikawa, S.; Ma, T.; Inagaki, T., Application of near-infrared spectroscopy to agriculture and forestry. *Analytical Sciences* **2022,** *38* (4), 635-642.
17. Tsonev, D.; Videv, S.; Haas, H., *Light fidelity (Li-Fi): towards all-optical networking*. SPIE: 2014; Vol. 9007.
18. Kwon, H.-J.; Lee, S.-H., Visible and Near-Infrared Image Acquisition and Fusion for Night Surveillance. *Chemosensors* **2021,** *9* (4), 75.
19. Haigh, P. A.; Bausi, F.; Ghassemlooy, Z.; Papakonstantinou, I.; Le Minh, H.; Fléchon, C.; Cacialli, F., Visible light communications: real time 10 Mb/s link with a low bandwidth polymer light-emitting diode. *Opt. Express* **2014,** *22* (3), 2830-2838.
20. Keuleyan, S.; Lhuillier, E.; Guyot-Sionnest, P., Synthesis of Colloidal HgTe Quantum Dots for Narrow Mid-IR Emission and Detection. *Journal of the American Chemical Society* **2011,** *133* (41), 16422-16424.
21. Bansal, A. K.; Antolini, F.; Zhang, S.; Stroea, L.; Ortolani, L.; Lanzi, M.; Serra, E.; Allard, S.; Scherf, U.; Samuel, I. D. W., Highly Luminescent Colloidal CdS Quantum Dots with Efficient Near-Infrared Electroluminescence in Light-Emitting Diodes. *The Journal of Physical Chemistry C* **2016,** *120* (3), 1871-1880.
22. McDonald, S. A.; Konstantatos, G.; Zhang, S.; Cyr, P. W.; Klem, E. J. D.; Levina, L.; Sargent, E. H., Solution-processed PbS quantum dot infrared photodetectors and photovoltaics. *Nature Materials* **2005,** *4* (2), 138-142.
23. Pietryga, J. M.; Schaller, R. D.; Werder, D.; Stewart, M. H.; Klimov, V. I.; Hollingsworth, J. A., Pushing the Band Gap Envelope: Mid-Infrared Emitting Colloidal PbSe Quantum Dots. *Journal of the American Chemical Society* **2004,** *126* (38), 11752-11753.
24. Sobhanan, J.; Jones, P.; Kohara, R.; Sugino, S.; Vacha, M.; Subrahmanyam, C.; Takano, Y.; Lacy, F.; Biju, V., Toxicity of nanomaterials due to photochemical degradation and the release of heavy metal ions. *Nanoscale* **2020,** *12* (43), 22049-22058.
25. Schubert, J.; Riley, E. J.; Tyler, S. A., Combined effects in toxicology-a rapid systematic testing procedure: Cadmium, mercury, and lead. *Journal of Toxicology and Environmental Health* **1978,** *4* (5-6), 763-776.
26. Franke, D.; Harris, D. K.; Chen, O.; Bruns, O. T.; Carr, J. A.; Wilson, M. W. B.; Bawendi, M. G., Continuous injection synthesis of indium arsenide quantum dots emissive in the short-wavelength infrared. *Nature Communications* **2016,** *7* (1), 12749.
27. Grigel, V.; Dupont, D.; De Nolf, K.; Hens, Z.; Tessier, M. D., InAs Colloidal Quantum Dots Synthesis via Aminopnictogen Precursor Chemistry. *Journal of the American Chemical Society* **2016,** *138* (41), 13485-13488.
28. Kim, T.; Park, S.; Jeong, S., Diffusion dynamics controlled colloidal synthesis of highly monodisperse InAs nanocrystals. *Nature Communications* **2021,** *12* (1), 3013.
29. Leemans, J.; Respekta, D.; Bai, J.; Braeuer, S.; Vanhaecke, F.; Hens, Z., Formation of Colloidal In(As,P) Quantum Dots Active in the Short-Wave Infrared, Promoting Growth through Temperature Ramps. *ACS Nano* **2023,** *17* (20), 20002-20012.
30. Song, J. H.; Choi, H.; Pham, H. T.; Jeong, S., Energy level tuned indium arsenide colloidal quantum dot films for efficient photovoltaics. *Nature Communications* **2018,** *9* (1), 4267.

31. Tamang, S.; Lee, S.; Choi, H.; Jeong, S., Tuning Size and Size Distribution of Colloidal InAs Nanocrystals via Continuous Supply of Prenucleation Clusters on Nanocrystal Seeds. *Chemistry of Materials* **2016,** *28* (22), 8119-8122.
32. Peng, X.; Wickham, J.; Alivisatos, A. P., Kinetics of II-VI and III-V Colloidal Semiconductor Nanocrystal Growth: "Focusing" of Size Distributions. *Journal of the American Chemical Society* **1998,** *120* (21), 5343-5344.
33. Battaglia, D.; Peng, X., Formation of High Quality InP and InAs Nanocrystals in a Noncoordinating Solvent. *Nano Letters* **2002,** *2* (9), 1027-1030.
34. Harris, D. K.; Bawendi, M. G., Improved Precursor Chemistry for the Synthesis of III–V Quantum Dots. *Journal of the American Chemical Society* **2012,** *134* (50), 20211-20213.
35. Wells, R. L.; Pitt, C. G.; McPhail, A. T.; Purdy, A. P.; Shafieezad, S.; Hallock, R. B., The use of tris(trimethylsilyl)arsine to prepare gallium arsenide and indium arsenide. *Chemistry of Materials* **1989,** *1* (1), 4-6.
36. Dou, H.; Yuan, C.; Zhu, R.; Li, L.; Zhang, J.; Weng, T.-C., Impact of Surface Trap States on Electron and Energy Transfer in CdSe Quantum Dots Studied by Femtosecond Transient Absorption Spectroscopy. *Nanomaterials* **2024,** *14* (1), 34.
37. Hou, B.; Cho, Y.; Kim, B. S.; Hong, J.; Park, J. B.; Ahn, S. J.; Sohn, J. I.; Cha, S.; Kim, J. M., Highly Monodispersed PbS Quantum Dots for Outstanding Cascaded-Junction Solar Cells. *ACS Energy Letters* **2016,** *1* (4), 834-839.
38. Leemans, J.; Pejović, V.; Georgitzikis, E.; Minjauw, M.; Siddik, A. B.; Deng, Y.-H.; Kuang, Y.; Roelkens, G.; Detavernier, C.; Lieberman, I.; Malinowski, P. E.; Cheyns, D.; Hens, Z., Colloidal III–V Quantum Dot Photodiodes for Short-Wave Infrared Photodetection. *Advanced Science* **2022,** *9* (17), 2200844.
39. Srivastava, V.; Dunietz, E.; Kamysbayev, V.; Anderson, J. S.; Talapin, D. V., Monodisperse InAs Quantum Dots from Aminoarsine Precursors: Understanding the Role of Reducing Agent. *Chemistry of Materials* **2018,** *30* (11), 3623-3627.
40. Sheikh, T.; Mir, W. J.; Nematulloev, S.; Maity, P.; Yorov, K. E.; Hedhili, M. N.; Emwas, A.-H.; Khan, M. S.; Abulikemu, M.; Mohammed, O. F.; Bakr, O. M., InAs Nanorod Colloidal Quantum Dots with Tunable Bandgaps Deep into the Short-Wave Infrared. *ACS Nano* **2023,** *17* (22), 23094-23102.
41. Zhao, T.; Oh, N.; Jishkariani, D.; Zhang, M.; Wang, H.; Li, N.; Lee, J. D.; Zeng, C.; Muduli, M.; Choi, H.-J.; Su, D.; Murray, C. B.; Kagan, C. R., General Synthetic Route to High-Quality Colloidal III–V Semiconductor Quantum Dots Based on Pnictogen Chlorides. *Journal of the American Chemical Society* **2019,** *141* (38), 15145-15152.
42. Uesugi, H.; Kita, M.; Omata, T., Facile synthesis of colloidal InAs nanocrystals using triphenylarsine as an arsenic source. *Journal of Crystal Growth* **2014,** *405*, 39-43.
43. Uesugi, H.; Kita, M.; Omata, T., Synthesis of size-controlled colloidal InAs quantum dots using triphenylarsine as a stable arsenic source. *Journal of Crystal Growth* **2015,** *416*, 134-141.
44. Zhu, D.; Bellato, F.; Bahmani Jalali, H.; Di Stasio, F.; Prato, M.; Ivanov, Y. P.; Divitini, G.; Infante, I.; De Trizio, L.; Manna, L., ZnCl2 Mediated Synthesis of InAs Nanocrystals with Aminoarsine. *Journal of the American Chemical Society* **2022,** *144* (23), 10515-10523.
45. Tamang, S.; Lincheneau, C.; Hermans, Y.; Jeong, S.; Reiss, P., Chemistry of InP Nanocrystal Syntheses. *Chemistry of Materials* **2016,** *28* (8), 2491-2506.

46. Xie, L.; Harris, D. K.; Bawendi, M. G.; Jensen, K. F., Effect of Trace Water on the Growth of Indium Phosphide Quantum Dots. *Chemistry of Materials* **2015,** *27* (14), 5058-5063.
47. Ban, H. W.; Vafaie, M.; Levina, L.; Xia, P.; Imran, M.; Liu, Y.; Najarian, A. M.; Sargent, E. H., Resurfacing of InAs Colloidal Quantum Dots Equalizes Photodetector Performance across Synthetic Routes. *Journal of the American Chemical Society* **2024**.
48. Poirier, D. M.; Weaver, J. H., InAs(110) by XPS. *Surface Science Spectra* **1993,** *2* (3), 224-231.
49. Henderson, Jeffrey D.; Pearson, L.; Nie, H.-Y.; Biesinger, Mark C., X-Ray Photoelectron Spectroscopy Analysis of Indium and Indium-Containing Compounds. *Surface and Interface Analysis* **2025,** *57* (1), 81-97.
50. Henderson, Jeffrey D.; Pearson, L.; Nie, H.-Y.; Biesinger, Mark C., X-Ray Photoelectron Spectroscopy Analysis of Indium and Indium-Containing Compounds. *Surf. Interface Anal.* **2024,** *57* (1), 81-97.
51. Zhu, D.; Bahmani Jalali, H.; Saleh, G.; Di Stasio, F.; Prato, M.; Polykarpou, N.; Othonos, A.; Christodoulou, S.; Ivanov, Y. P.; Divitini, G.; Infante, I.; De Trizio, L.; Manna, L., Boosting the Photoluminescence Efficiency of InAs Nanocrystals Synthesized with Aminoarsine via a ZnSe Thick-Shell Overgrowth. *Advanced Materials* **2023,** *35* (38), 2303621.
52. Jakša, G.; Štefane, B.; Kovač, J., XPS and AFM characterization of aminosilanes with different numbers of bonding sites on a silicon wafer. *Surface and Interface Analysis* **2013,** *45* (11-12), 1709-1713.
53. Gogoi, N.; Wahyudi, W.; Mindemark, J.; Hernández, G.; Broqvist, P.; Berg, E. J., Reactivity of Organosilicon Additives with Water in Li-ion Batteries. *The Journal of Physical Chemistry C* **2024,** *128* (4), 1654-1662.
54. Information, N. C. f. B. Electronegativity in the Periodic Table of Elements. https://pubchem.ncbi.nlm.nih.gov/ptable/electronegativity/ (accessed 02/12/2025).
55. Schneider, C. A.; Rasband, W. S.; Eliceiri, K. W., NIH Image to ImageJ: 25 years of image analysis. *Nature Methods* **2012,** *9* (7), 671-675.

2.7. Appendices

NMR characterizations of the reference compounds.

The appendix reports the ^{1}H NMR ^{13}C NMR spectra of all reference compounds used for the structural assignments throughout the Chapter 2. The analyzed compounds include:

i. Commercially available compounds: TMS-OH, TMS-O-TMS and TMS-As.
ii. Synthesized compounds: TMS-OLAc and TMS-DOA

These spectra were collected to validate the identity of products formed in the control reactions and to support the mechanistic interpretation of TMS-derived species observed during the synthesis of InAs quantum dots. Each NMR dataset is accompanied by relevant peak assignments and acquisition details to ensure reproducibility.

A1. Tris(trimethylsilyl)arsine ((TMS$_3$-OH), Dock Chemicals, 99%)

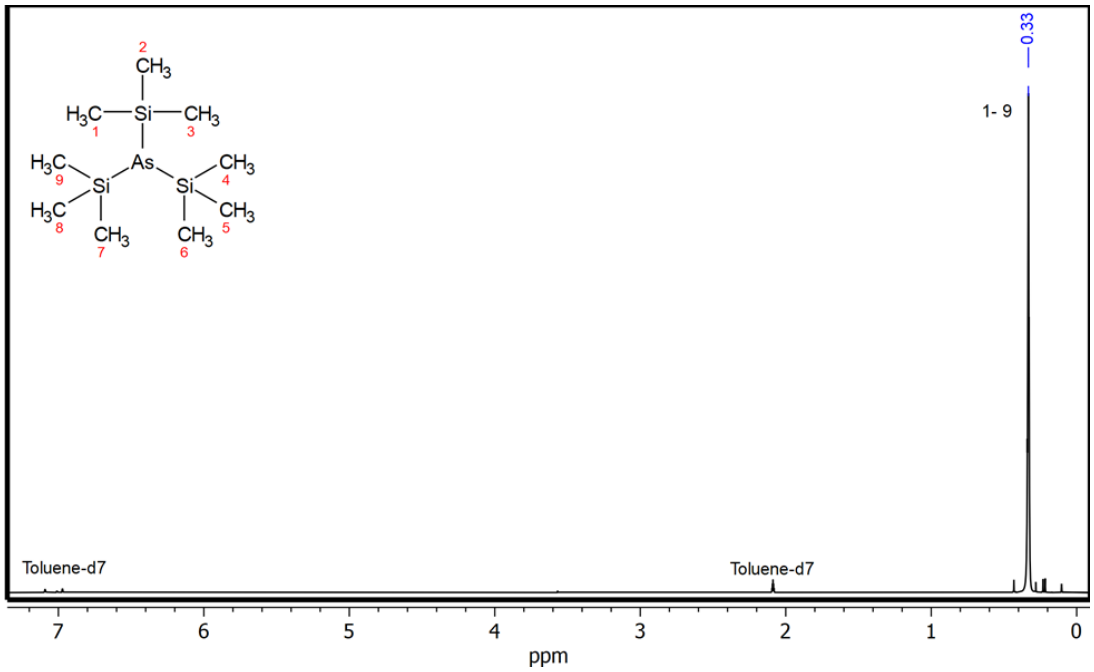

Appendix 2.7.1. *^{1}H NMR spectrum of (TMS)$_3$-As (Dock Chemicals, 99%) in toluene-d, the structure and peaks assignment are embedded.*

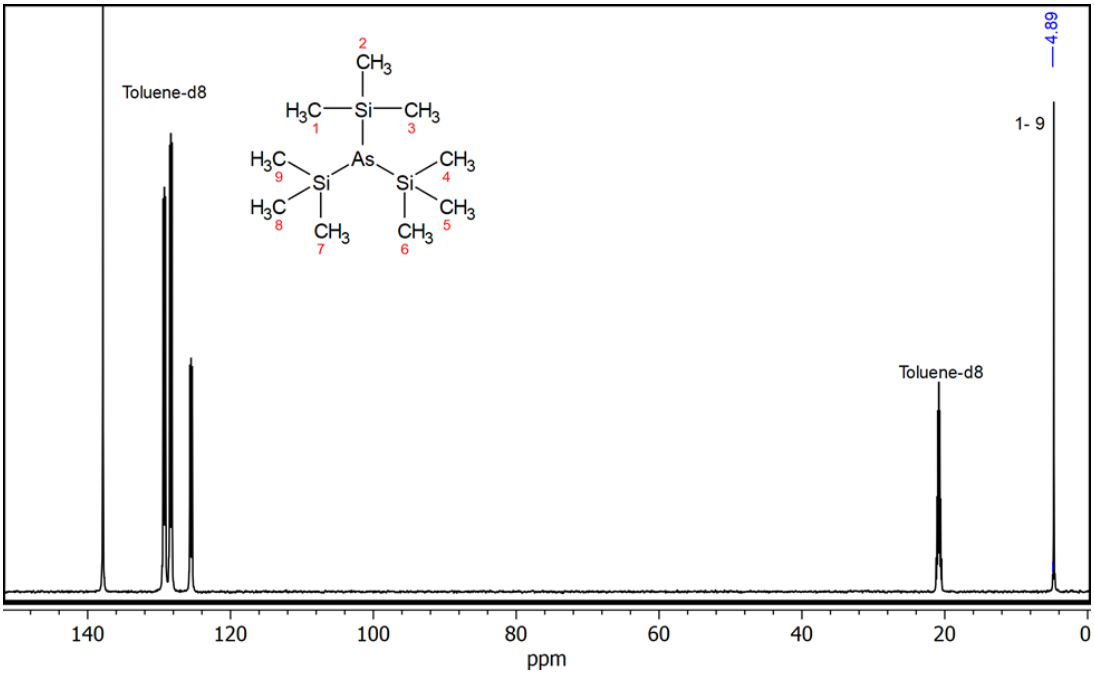

Appendix 2.7.2. *^{13}C NMR spectrum of TMS-As (Dock Chemicals, 99%) in toluene-d, the structure and peaks assignment are embedded.*

A2. Trimethylsilanol (TMS-OH, Sigma Aldrich, 97.5%)

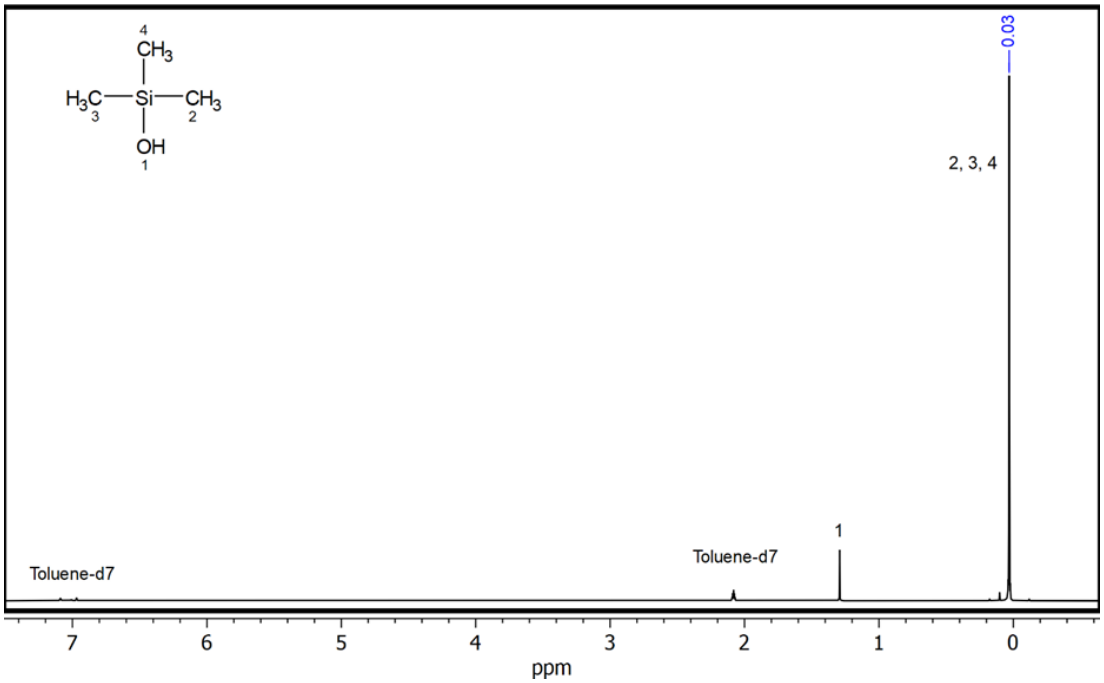

Appendix 2.7.3. *^{1}H NMR spectrum of TMS-OH (Sigma Aldrich, 97.5%) in toluene-d, the structure and peaks assignment are embedded.*

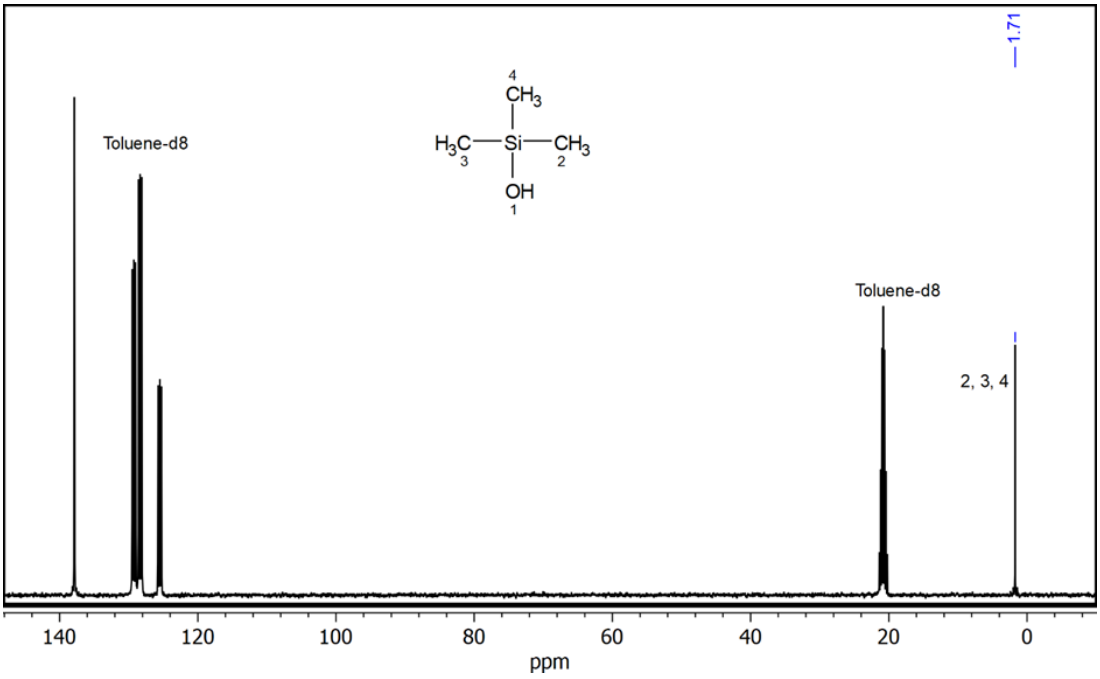

Appendix 2.7.4. *^{13}C NMR spectrum of TMS-OH (Sigma Aldrich, 97.5%) in toluene-d, the structure and peaks assignment are embedded.*

A2. Hexamethyldisiloxane (TMS-O-TMS, Sigma Aldrich, 98%)

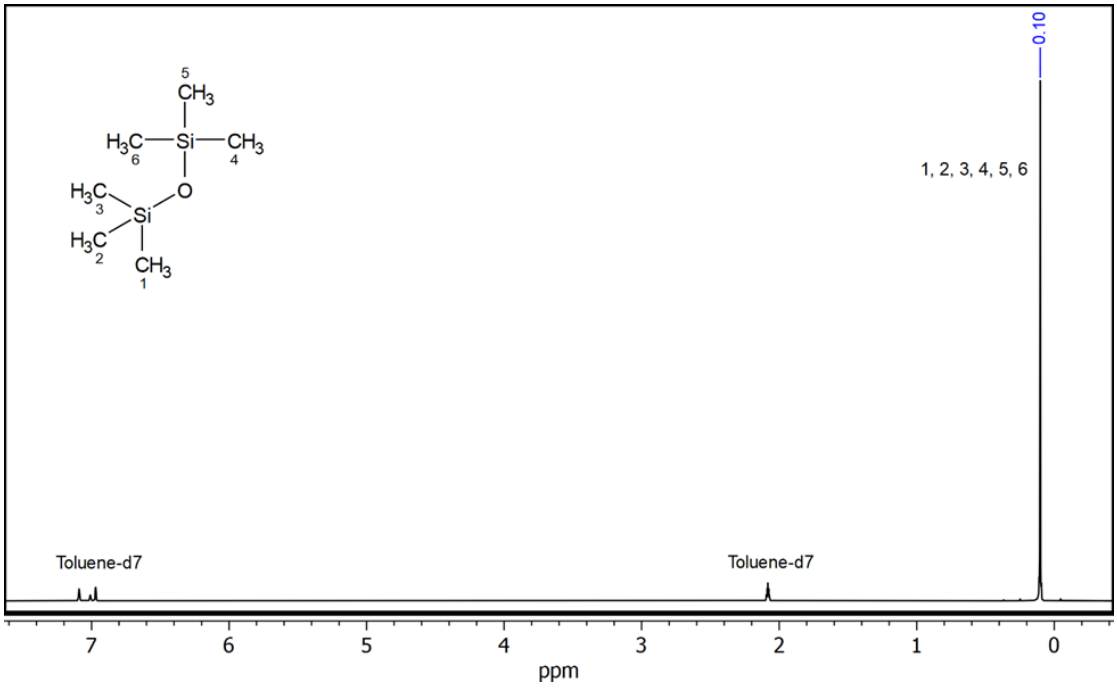

Appendix 2.7.5. *^{1}H NMR spectrum of TMS-O-TMS (Sigma Aldrich, 98%) in toluene-d, the structure and peaks assignment are embedded.*

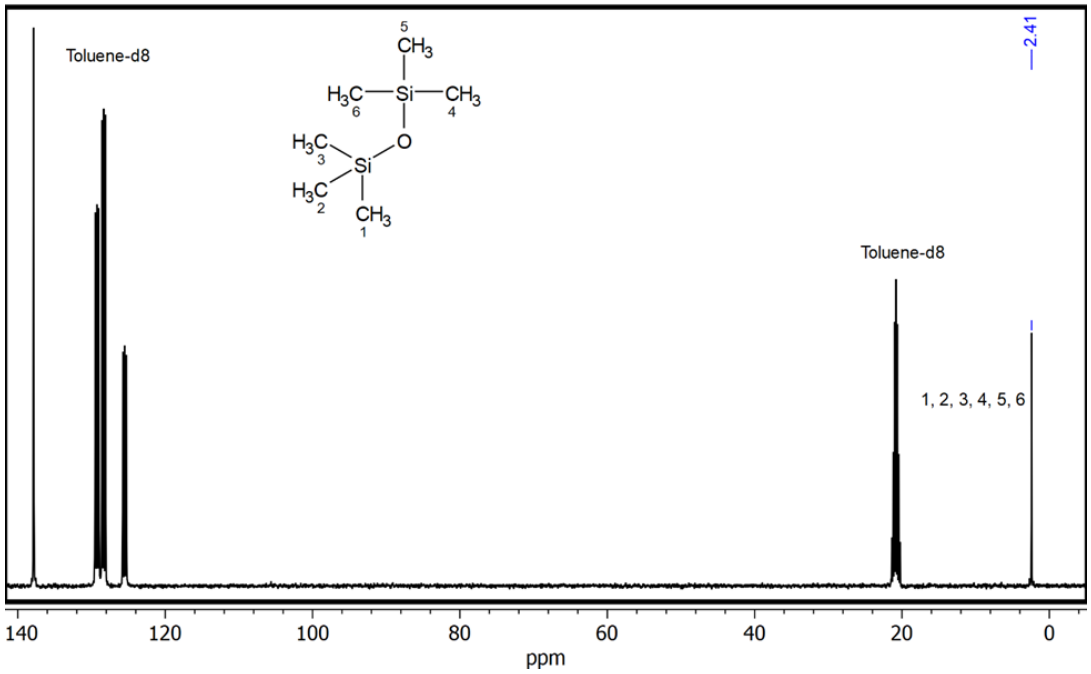

Appendix 2.7.6. *^{13}C NMR spectrum of TMS-O-TMS (Sigma Aldrich, 98%) in toluene-d, the structure and peaks assignment are embedded.*

NMR characterizations of the synthesized compounds.

Chemicals

Dry tetrahydrofuran (Sigma Aldrich, 99.9%), dry pyridine (Sigma Aldrich, 99.8%), diisopropylethylamine (Sigma Aldrich, 98.0%), chlorotrimethylsilane (Sigma Aldrich, 99.0%), cyclohexane (Sigma Aldrich, 99.5%), dry dichloromethane (Thermo Scientific, 99.9%), triethylamine (Sigma Aldrich, 99.5%).

Procedure for the synthesis of TMS-Oleate (TMS-OLAc)

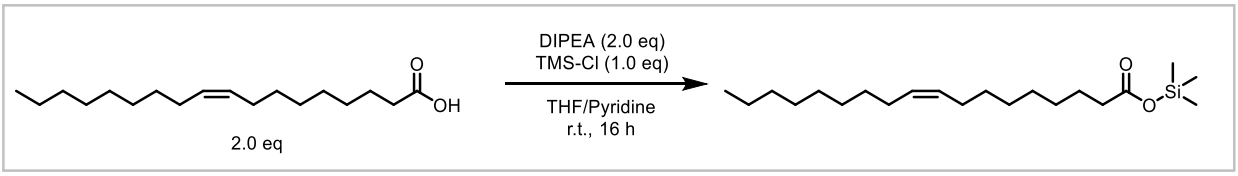

In a screwcap vial with septum, oleic acid (1.0 mmol, 316 µL, 2.0 equivalents) was dissolved in dry tetrahydrofuran (THF, 0.3 ml) and dry pyridine (0.2 ml) under nitrogen atmosphere. To this solution N,N-diisopropylethylamine (DIPEA, 1.0 mmol, 175 µL, 2.0 equivalents) and chlorotrimethylsilane (0.5 mmol, 70 µL, 1.0 equivalents) were subsequently added. The reaction was left stirring overnight at room temperature. Cyclohexane was then added to the reaction mixture and the slurry was filtered. The volatiles were then removed, and the resulting pale-

yellow oil was characterized without further purification. The product was stored in a -20°C freezer under nitrogen atmosphere.

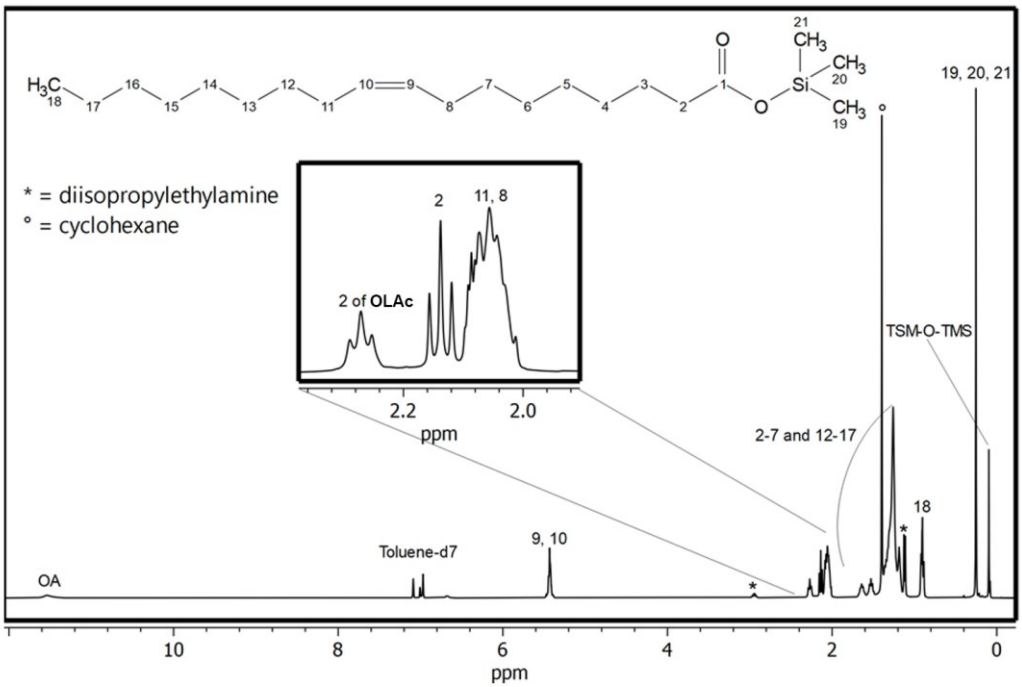

Appendix 2.7.7. *^{1}H NMR spectrum of TMS-OLAc in toluene-d, the structure and peaks assignment are embedded.*

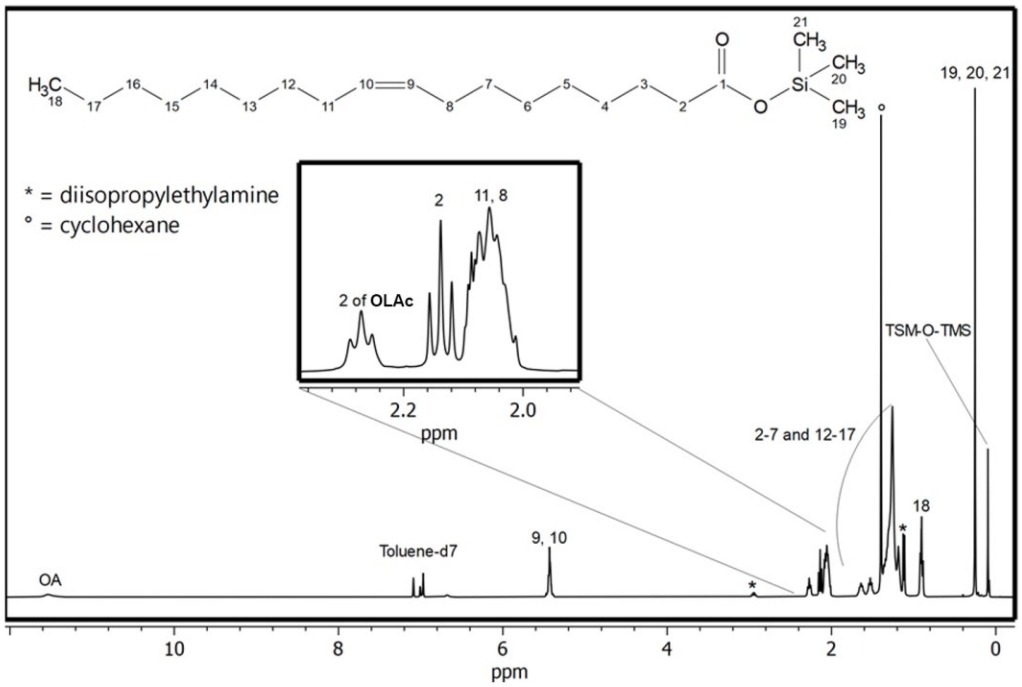

Appendix 2.7.8. *^{13}C NMR spectrum of TMS-OLAc in toluene-d, the structure and peaks assignment are embedded.*

The presence of a small amount of TMS-O-TMS alongside TMS-OLAc in the NMR spectra can be attributed to the hydrolysis of TMS-based species or reactive TMS intermediates by trace moisture present either in the reaction mixture or the solvent environment.

Procedure for the synthesis of TMS-dioctylamine (TMS-DOA)

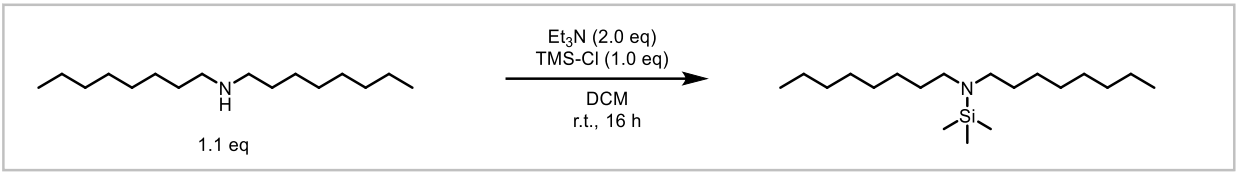

In a screwcap vial with septum, N,N-dioctylamine (0.3 mmol, 90 µL, 1.1 equivalents) was dissolved in dry Dichloromethane (DCM, 1.0 ml) under nitrogen atmosphere. Triethylamine (Et_3N, 0.6 mmol, 66 µL, 2.0 equivalents) was added followed by chlorotrimethylsilane (0.27 mmol, 34 µL, 1.0 equivalents). The reaction was left stirring overnight at room temperature. Cyclohexane was then added to the reaction mixture and the slurry was filtered. The volatiles were then removed, and the resulting orange oil was characterized without further purification. The product was stored in a -20°C freezer under nitrogen atmosphere.

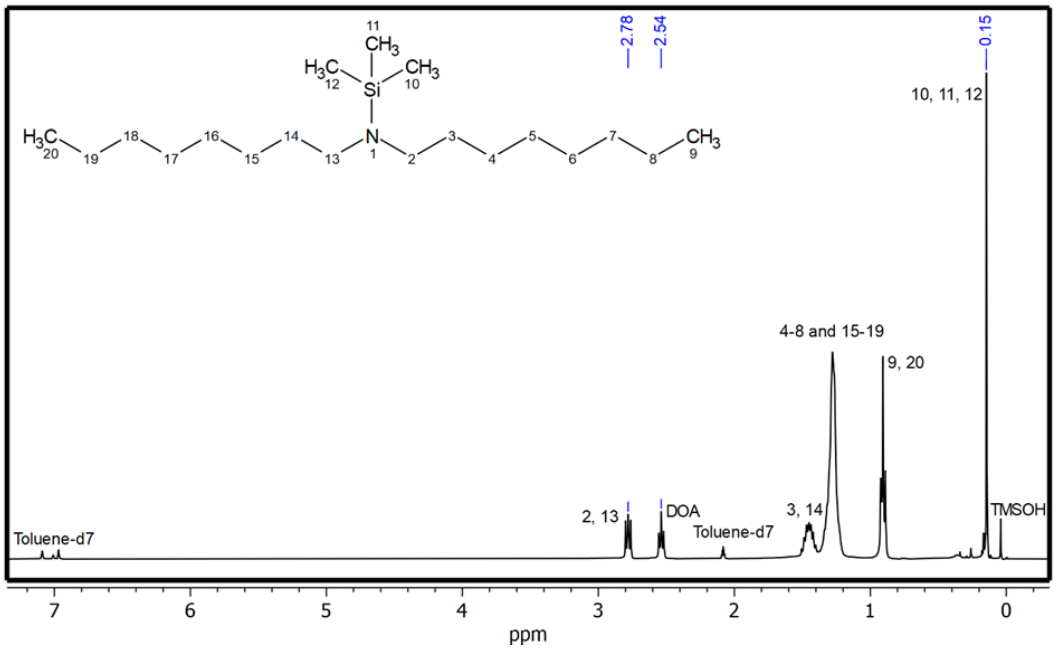

Appendix 2.7.9. *^{1}H NMR spectrum of TMS-DOA in toluene-d, the structure and peaks assignment are embedded.*

The NMR experiments were done in ambient conditions. Overtime, TMS-DOA was observed to readily decompose to form TMS-OH, as evidenced by the appearance of the characteristic peak of TMS-OH in Appendix 2.7.9.

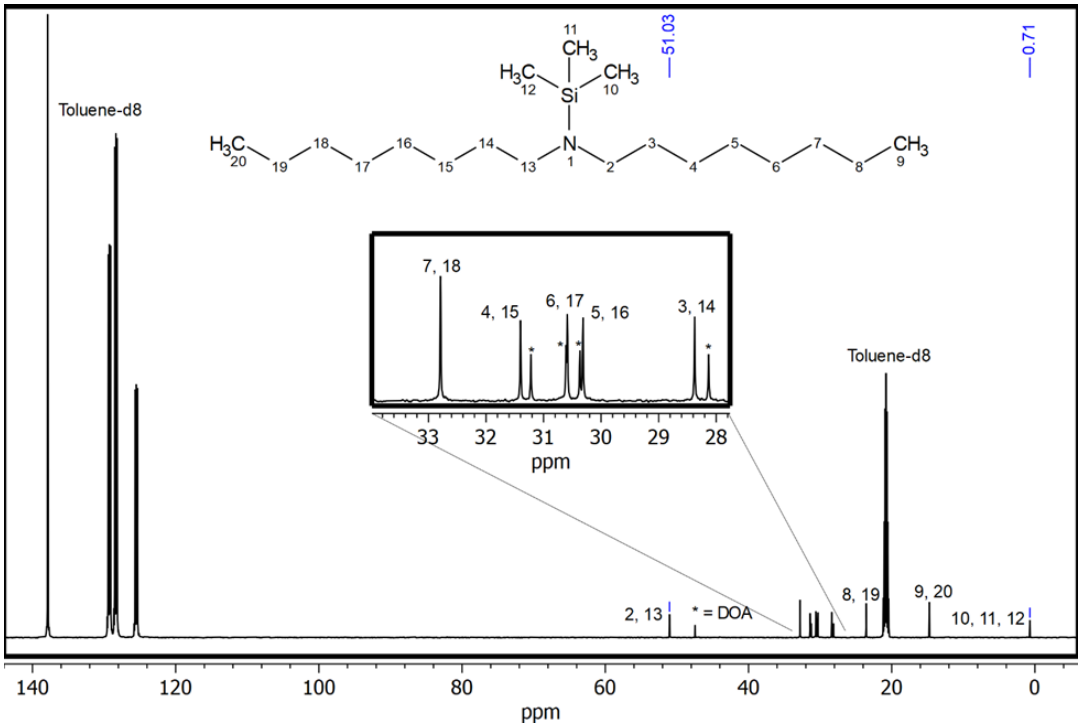

Appendix 2.7.10. *^{13}C NMR spectrum of TMS-DOA in toluene-d, the structure and peaks assignment are embedded.*

Size distribution curves calculated from TEM images using ImageJ software

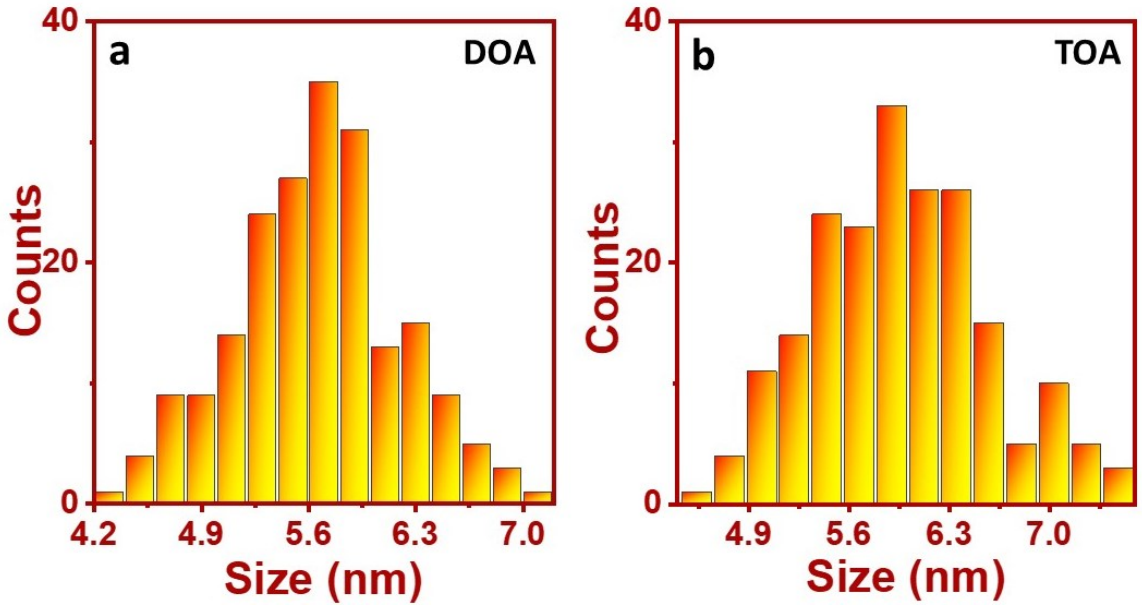

Appendix 2.7.11. *Size distribution histograms for the (a) InAs-DOA, and (b) InAs-TOA QD samples measured using ImageJ software.*[55]

Chapter 3. Overcoming the Short-Wave Infrared Barrier in the Photoluminescence of Amino-As-Based InAs Quantum Dots.

3.1 Abstract

In Chapter 2, we found that $(TMS)_3$-As, when combined with trioctylamine, enables the synthesis of high-quality InAs quantum dots (QDs) with excellent size control and optical properties. However, despite its synthetic advantages, $(TMS)_3$-As is highly pyrophoric and expensive, making it unsuitable for large-scale or industrial implementation. This limitation motivated the transition to safer and more practical arsenic precursors, such as tris(dimethylamino)arsine (amino-As). Although amino-As is non-pyrophoric and commercially available, its effective use requires an external reducing agent to convert and release the reactive As^{3-} monomers. The synthesis of amino-As-based InAs QDs with narrow excitonic absorption features and efficient photoluminescence (PL) beyond 1000 nm remains a considerable challenge. A key limitation lies in the use of conventional reducing agents, which release low-boiling byproducts causing temperature fluctuations and unstable reaction conditions that are detrimental in seeded growth strategies. In this chapter, we introduce trioctylamine-alane (TOA-AlH_3) as a high-boiling reducing agent that overcomes these limitations and enables the one-pot synthesis of amino-As-based InAs QDs with narrow excitonic features up to 935 nm. After ZnSe shelling, these QDs reach PLQY of 75% at 905 nm and 60% at 1000 nm, record values for amino-As-derived InAs@ZnSe QDs. We further show that TOA-AlH_3 enables the seeded growth of InAs QDs, allowing the preparation of large QDs with excitonic peaks extendable to 1350 nm. Following ZnSe shell growth, the PLQYs reach 46%, 38%, 32%, and 23% at 1160, 1250, 1335, and 1430 nm, respectively. Importantly, TOA-AlH_3 is compatible with the use of $ZnCl_2$ as a reaction additive, which is essential for trap passivation and high luminescence. Together, these results establish a safe, scalable, and high-performance synthetic route for SWIR-emitting InAs QDs based on amino-As chemistry.

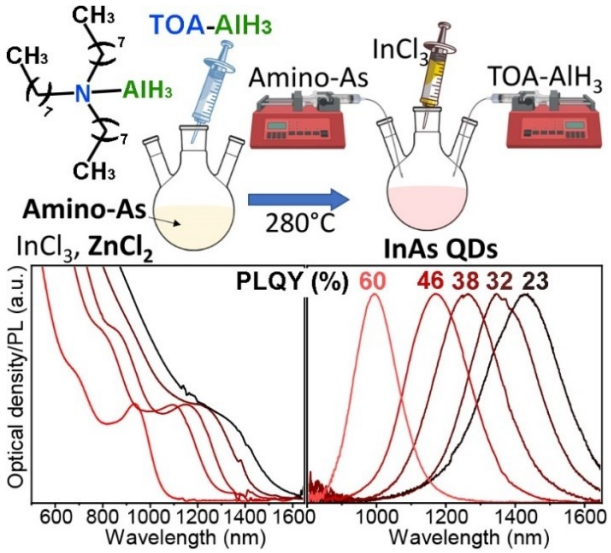

3.2 Introduction

Future consumer markets for infrared (IR) technologies will require materials that are not only efficient but also inexpensive and compatible with scalable manufacturing, supporting the broad range of applications discussed in Chapter 1[1-11]. Colloidal quantum dots (CQDs) are especially promising because they can be synthesized cost-effectively and integrated into devices through solution-processed methods[2, 4-6, 9-13]. Indeed, IR-emitting QDs have already been incorporated into prototype lasers, sensors, LEDs, and other optoelectronic devices[2, 9-12, 14-16].

To date, the highest IR device performance has been achieved with Pb- and Hg-based QDs, but their intrinsic toxicity[17, 18] makes them unsuitable for consumer applications[19-22]. This limitation has accelerated efforts toward developing RoHS-compliant alternatives[23 24, 25], including Ag- and Cu-based I-III-VI semiconductors ($AgInSe_2$, $CuInSe_2$, $CuInS_2$), as well as III-V compounds such as InSb and InAs QDs[26-28]. Among these, InAs QDs stand out due to their wide quantum-confinement tunability, enabling the optical bandgap to be adjusted across a broad spectral range from approximately 540 to 1700 nm[8, 15, 16, 29-39].

Out of the two major colloidal synthesis routes that exist for InAs QDs, the tris(trimethylsilyl)arsine ($(TMS)_3$-As) route discussed in Chapter 2 has enabled the preparation of high-quality nanocrystals, and our modified protocol produced QDs with excellent optical properties. However, the photoluminescence (PL) efficiency of these larger-core TMS-As–derived QDs has not yet been investigated in detail[4, 8, 35]. Due to the high cost, toxicity, and pyrophoricity of the $(TMS)_3$-As precursor, the use of amino-As, a much cheaper and less reactive arsenic precursor, has gained popularity in recent years[37, 40-45].

To fully exploit amino-As-based InAs QDs in optoelectronic devices, substantial improvements in their optical properties are still required. Key parameters include not only the position and linewidth of the first excitonic absorption feature[34, 35, 46], but also the PL quantum yield (PLQY), particularly at wavelengths exceeding 1000 nm[38, 47]. Achieving efficient PL in this SWIR region remains one of the central challenges in amino-As-based InAs QD synthesis. Although PLQYs approaching 70% have been reported for amino-As-derived InAs QDs emitting near 950 nm[42, 43, 48], larger QDs with absorption and emission extending beyond 1000 nm generally exhibit little to no detectable PL.

Several strategies have attempted to address this limitation, yet with limited success. For example, Kim et al. prepared amino-As-based InAs QDs with absorption edges reaching 1700 nm using diisobutylaluminum hydride (DIBAL-H) as the reducing agent together with lithium bis(trimethylsilyl)amide as an additive[49]; however, no PL was observed from these samples. Leemans et al. employed amino-phosphines as in situ reducing agents to synthesize amino-As-based In(As,P) QDs with absorption tunable to 1600 nm, but again no PLQY values were reported[37]. More recently, Skorotetcký et al. demonstrated a continuous-injection method using 1,1,3,3,5,5-hexamethyltrisiloxane (HMTS) as the reducing agent, yielding amino-As-based InAs QDs with absorption peaks up to 1550 nm; yet their PL characteristics were not discussed[45].

These considerations motivated the present work, which aims to overcome the long-standing limitations of amino-As chemistry and achieve efficient, tunable emission above 1000 nm from amino-As-based InAs QDs. To attain this goal, we developed a synthetic strategy enabling the preparation of InAs@ZnSe QDs with photoluminescence (PL) extending to 1400 nm and PLQYs as high as 60% at 1000 nm, 46% at 1160 nm, 38% at 1250 nm, 32% at 1335 nm, and 23% at 1430 nm. This progress builds on our recently established amino-As-based InAs synthesis platform[42, 43, 48], which highlights the crucial role of $ZnCl_2$ as a Z-type ligand additive for enhancing surface passivation and PL efficiency.

The novelty of the present work lies in the introduction of a new reducing agent, trioctylamine alane (TOA-AlH_3), which we synthesized as a replacement for dimethylethylamine alane (DMEA-AlH_3). DMEA-AlH_3 is currently regarded as the most effective reducing agent when paired with amino-As to achieve optimal control over the size distribution of InAs QDs[39, 40, 43]. However, the maximum achievable InAs QDs size is limited to ~3 nm, corresponding to a PL peaked at most at 950-970 nm[40, 42, 43, 48]. The synthesis of larger InAs QDs with DMEA-AlH_3, via either one-pot procedures or seeded growth approaches, is impeded by the following drawbacks:

1) DMEA-AlH_3 is commercially available only dissolved in low-boiling solvents, such as toluene, hence, when injected into a hot mixture (typically at 240-280°C), it can cause a boiling burst.
2) upon cleavage of the Al-N bond, which occurs at ~130°C[50], DMEA is released into the reaction mixture, also causing vigorous boiling.

The combined presence of low-boiling solvents and liberated amines makes it difficult to maintain the thermal stability required for seeded growth and poses significant safety concerns. Notably, other reducing agents reported for amino-As systems present analogous limitations: DIBAL-H is typically supplied in low-boiling solvents (toluene, hexane, THF), while amino-phosphines and HMTS possess boiling points (150 °C and 128 °C, respectively) well below the temperatures required for InAs QD growth (240-260 °C).

TOA-AlH_3 effectively addresses all these issues. As an amino-alane, its reduction kinetics toward As^{3+} are comparable to those of DMEA-AlH_3 the Al-N bond cleaves in a similar temperature range (130-150 °C)[50], releasing AlH_3 as the active reducing species. Crucially, however, the byproduct trioctylamine (TOA) has a high boiling point (365 °C), and TOA-AlH_3 dissolves readily in high-boiling, non-coordinating solvents such as octadecene (ODE). As a result, its use does not induce temperature fluctuations or vapor formation, enabling a stable reaction environment essential for both one-pot and seeded-growth strategies.

Using TOA-AlH_3, we first established a one-pot synthesis yielding amino-As based InAs QDs with excitonic peaks tunable up to 935 nm with exceptionally narrow absorption linewidths (HWHM as low as 85 meV), which is among the lowest reported values for this precursor system[39, 40, 42-44]. Subsequent ZnSe shell growth produced InAs@ZnSe QDs with PLQYs of 75% at 900 nm and 60% at 1000 nm, matching or surpassing state-of-the-art values for amino-As-based approaches.

Building on this success, we next developed a seeded-growth method to further enlarge the InAs QDs. This optimized procedure involves injecting $InCl_3$ into the crude InAs reaction mixture, followed by simultaneous co-injection of TOA-AlH_3 and amino-As at 240 °C. This strategy enabled the synthesis of InAs QDs with absorption tunable to 1340 nm. After ZnSe shell growth, these samples exhibited record PLQY values of 46% at 1160 nm, 38% at 1250 nm, 32% at 1335 nm, and 23% at 1430 nm. Importantly, such high PL efficiencies were achieved only when $ZnCl_2$ was employed from the beginning of the synthesis of the InAs QDs. In its absence, the resulting InAs@ZnSe systems showed either negligible PL or dramatically reduced PLQYs, underscoring the essential role of $ZnCl_2$ mediated passivation in enabling efficient SWIR emission.

3.3 Results and discussions

Our study began with the synthesis of the new high-boiling reducing agent which is TOA-AlH_3. The synthesis follows a standard amino-alane formation route, in which TOA was added dropwise to a mixture of $AlCl_3$ and $LiAlH_4$ in pentane, followed by filtration and removal of pentane (see Equation 3.1 and the experimental section for details)

$$AlCl_{3\,(s)} + 3LiAlH_{4\,(s)} + 4TOA_{(l)} \rightarrow 4\left(TOA - AlH_{3\,(l)}\right) + 3LiCl_{(s)}$$

(Equation 3.1)

Using an excess of both $AlCl_3$ and $LiAlH_4$ ensured the complete conversion of TOA into the corresponding TOA-AlH_3 amino-alane adduct, with a synthesis yield of ~94% (details in the experimental section). The ^{1}H NMR spectrum of the product displayed peaks corresponding to TOA, shifted downfield to 2.60 ppm compared to pure TOA (2.47 ppm). This desheilding is characteristic of the formation of a Lewis adduct between the nitrogen atom of TOA and the electron-deficient AlH_3 moiety (Figure 3.3.1 and 3.3.2). Moreover, the product featured a broad peak at 4.39 ppm ascribable to the AlH_3 unit[50] (integrating to 3 hydrogen atoms), consistent with similar compounds (Figure 3.3.2).

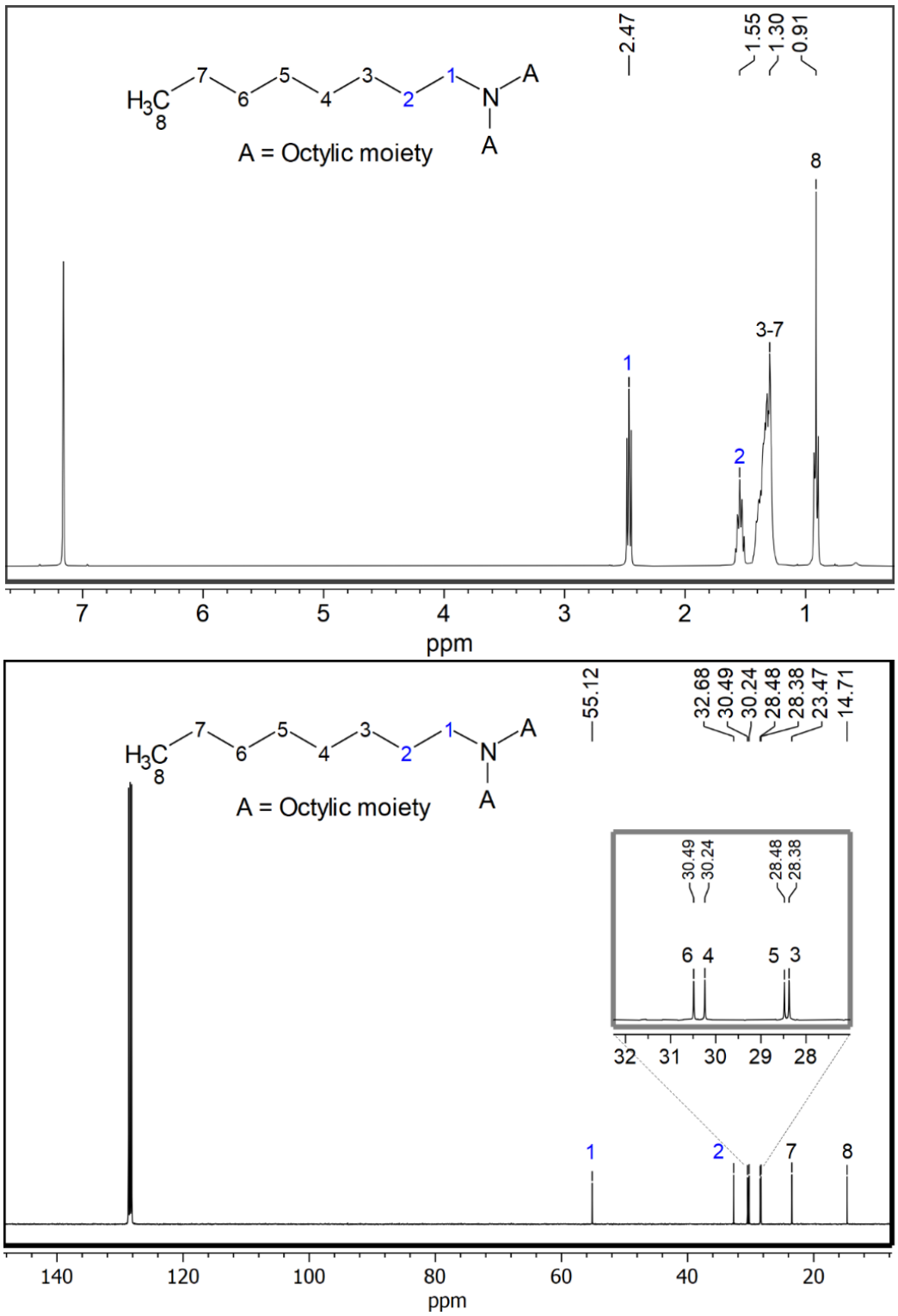

Figure 3.3.1. *^{1}H NMR (top) and ^{13}C NMR (below) spectra of TOA in benzene-d6, the structure and peak assignment are embedded.*

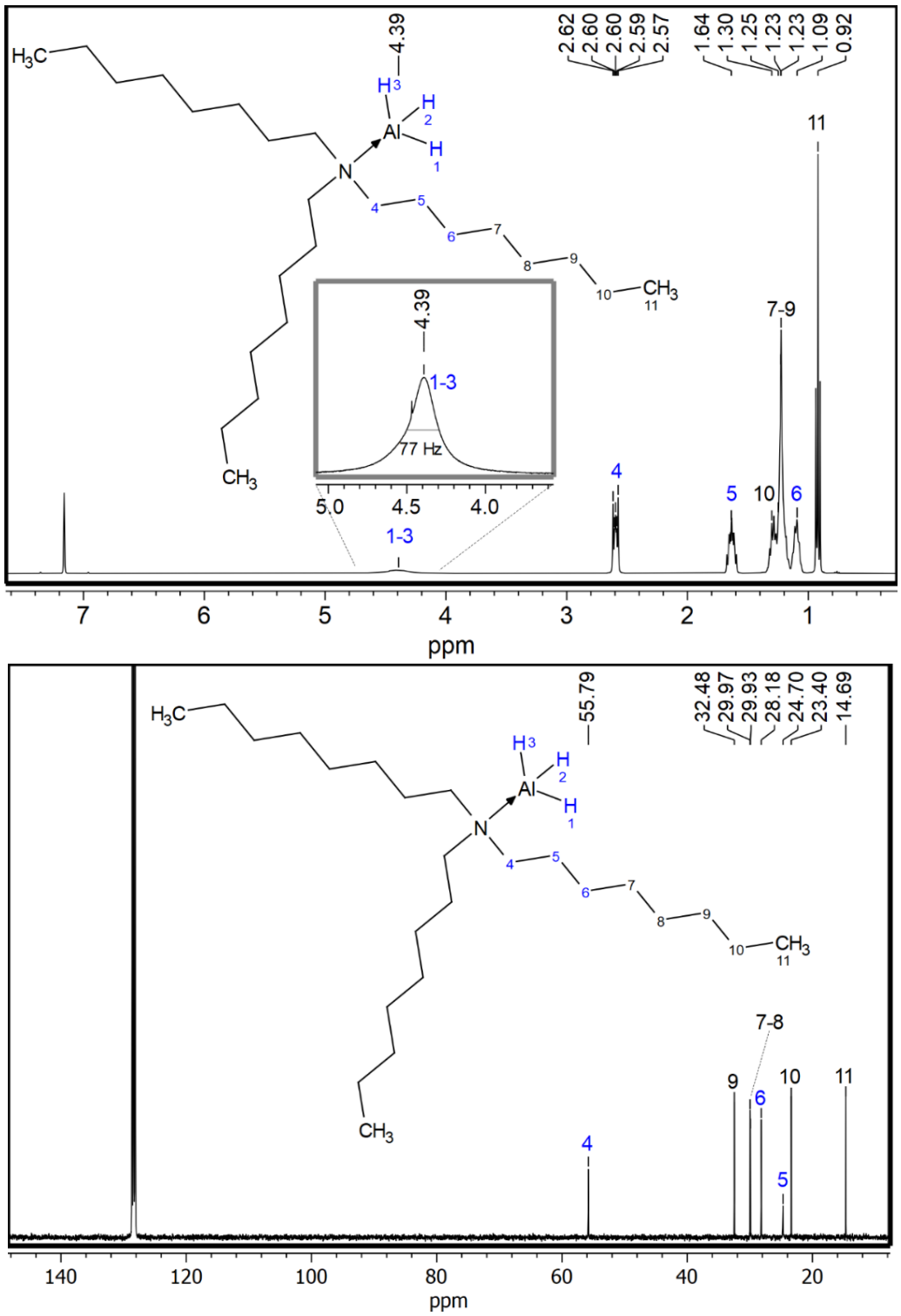

Figure 3.3.2. *^{1}H NMR (top) and ^{13}C NMR (below) spectra of TOA-AlH_3 in benzene-d6, the structure and peak assignment are embedded. Diagnostic broad peak of AlH_3 appears at 4.39 ppm with a FWHM (Full Width at Half Maximum of 77Hz).*

^{1}H NMR (300.13 MHz in C_6D_6): δ (ppm) = 4.39 (*br s,* 3H, AlH_3, FWHM = 77 Hz), 2.60, (*m*, 6H), 1.64 (*m*, 6H), 1.29 (*m*, 6H), 1.23 (*br s*, 18), 1.10 (*m*, 6H), 0.92 (*ps t*, 9H). The peak assignment is reported in Figure 3.3.2.

^{13}C NMR (100.62 MHz in in C_6D_6): δ (ppm) = 55.79, 32.48, 29.97, 29.93, 28.18, 24.70, 23.40, 14.69. The peak assignment is reported in Figure 3.3.2.

The absolute purity of the TOA-AlH_3 product was assessed by quantitative ^{1}H NMR spectroscopy and subsequently used to calculate the overall synthetic yield. Quantitative NMR measurements were carried out using the PULCON (Pulse Length–Based Concentration Determination) method[51], in which the integrated intensity of the CH_2-N resonance of TOA-AlH_3 was compared to that of an external standard, namely a 100.6 mM solution of 1,2,4,5-tetramethylbenzene (TraceCERT, 99.99%), with each peak normalized to the number of contributing protons. For this analysis, a 100.06 mM TOA-AlH_3 solution in benzene-d (22 mg in 573.5 µL) was prepared. The analysis returned an actual concentration of 100.77 mM, corresponding to 91.7% TOA-AlH_3 and 8.35% free TOA. The presence of fast exchange between TOA and TOA-AlH_3 prevented a direct quantification of the two species within a single NMR spectrum, making the external-standard approach necessary (Figure 3.3.3).

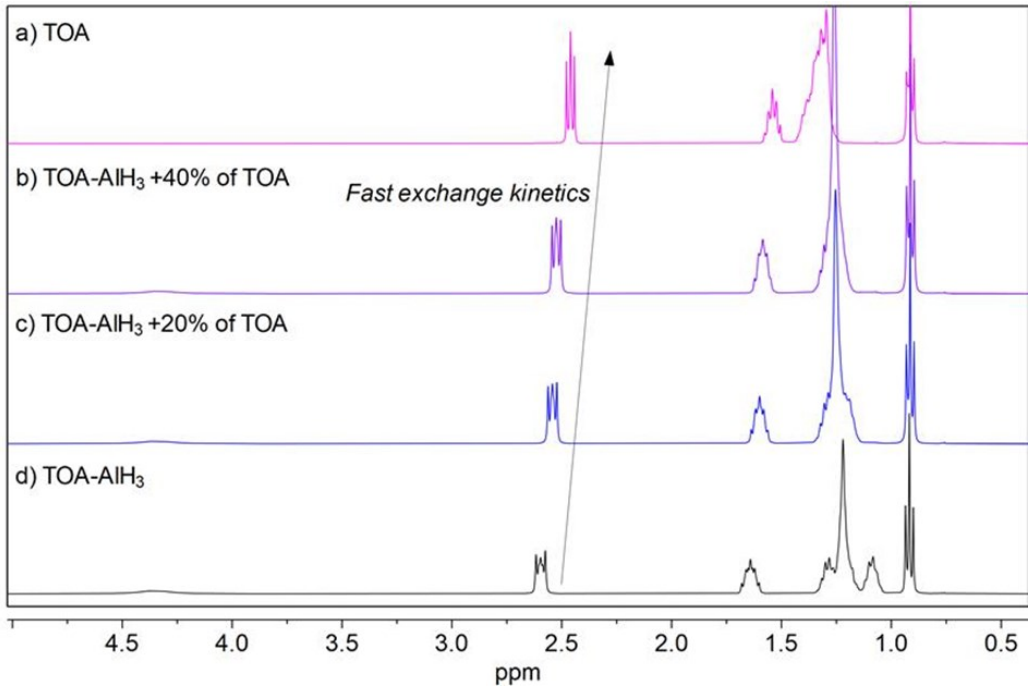

Figure 3.3.3. *^{1}H NMR spectra in benzene-D of a) TOA, d) TOA-AlH_3 and different amount of TOA added to TOA-AlH_3 b) and c). Only a single CH_2-N signal is detected, reveling a fast exchange kinetics regime between the TOA-AlH_3 adduct and the free TOA, in comparison to the NMR time scale. After subsequent addition increasing amount of free TOA the CH_2N peak gets up-field shifted.*

After filtration and removal of pentane, the crude TOA-AlH_3 product weighed 33.06 g. Since TOA is the limiting reagent in the synthesis (with $AlCl_3$ and $LiAlH_4$ used in excess; Equation 3.1), the

theoretical amount of TOA-AlH_3 obtainable from the reaction is 93mmol corresponding to 35.68 g (M.W. of TOA-AlH_3 = 383.67 g mol^{-1}). The product yield is given by:

$$\%\, Yield = \frac{Experimental\ yield}{Theoretical\ yield} * (\%\, Purity) * 100\%$$

(Equation 3.2)

This calculation yields an overall product yield of 84.9%.

Beyond its straightforward preparation, TOA-AlH_3 offers two major advantages over conventional reducing agents used in amino-As-based InAs QD synthesis, such as DMEA-AlH_3, DIBAL-H, or HMTS.

i. the TOA released upon cleavage of the N-Al bond is a high-boiling compound (365-367^oC at 1 atm) unlike other commonly used reducing agents, which thermally decompose into low-boiling species
ii. TOA-AlH_3 can be dispersed/mixed with a high-boiling non-coordinating solvent, whereas commonly used reducing agents are commercially available in low-boiling solvents.

ODE was selected as a suitable high-boiling non-coordinating solvent to dilute TOA-AlH_3 for two main reasons: i) to reduce TOA-AlH_3 high viscosity, thereby enabling smooth and consistent injection during the QD synthesis; ii) ODE is non-reactive toward TOA-AlH_3 to avoid unwanted side reactions that could degrade the precursor or alter its reducing power.

The newly synthesized TOA-AlH_3 reducing agent was next implemented in place of DMEA-AlH_3 within our established amino-As-based one-pot InAs QD synthesis protocol[42, 43], which incorporates $ZnCl_2$ as a crucial additive (see Experimental Section for details). Our objective at this stage was to optimize the reaction conditions to obtain the largest possible QD size while preserving a narrow size distribution. To do so, we maintained constant amounts of $InCl_3$ (0.2 mmol), $ZnCl_2$ (2 mmol), and amino-As (0.2 mmol), and systematically varied key reaction parameters. These included the injection and growth temperatures, the relative quantities of TOA-AlH_3, oleylamine (Olam), and non-coordinating solvent (ODE), as well as the overall reaction time.

We first optimized the amount of TOA-AlH_3 while keeping all other reaction parameters constant, namely an injection temperature of 240 °C, a reaction temperature of 300 °C, 0.2 mmol of $InCl_3$, 2 mmol of $ZnCl_2$, and 5 mL of Olam, together with the injection of 0.2 mmol amino-As dissolved in 0.5 mL of Olam. The desired amount of TOA-AlH_3 was premixed with 0.5 mL of ODE inside an N_2-filled glovebox and injected at 240 °C. Systematic variation of the TOA-AlH_3 quantity revealed:

i. low TOA-AlH_3 amount led to poor precursor reduction and limited InAs growth, producing QDs with broad size distributions (HWHM ≥ 120 meV; deep-blue curve Figure 3.3.4 a, b).
ii. Excess TOA-AlH_3 (1.5 mmol) resulted in reduction of indium precursors, leading to the formation of metallic indium byproducts (Figure 3.3.4 c).

iii. An intermediate amount of 0.8 mmol TOA-AlH_3 afforded the best results, yielding InAs QDs with excitonic peaks above 800 nm and the narrowest size distributions in this series (HWHM ~100 meV), with no detectable byproduct formation (light blue curve, Figure 3.3.4 a-c).

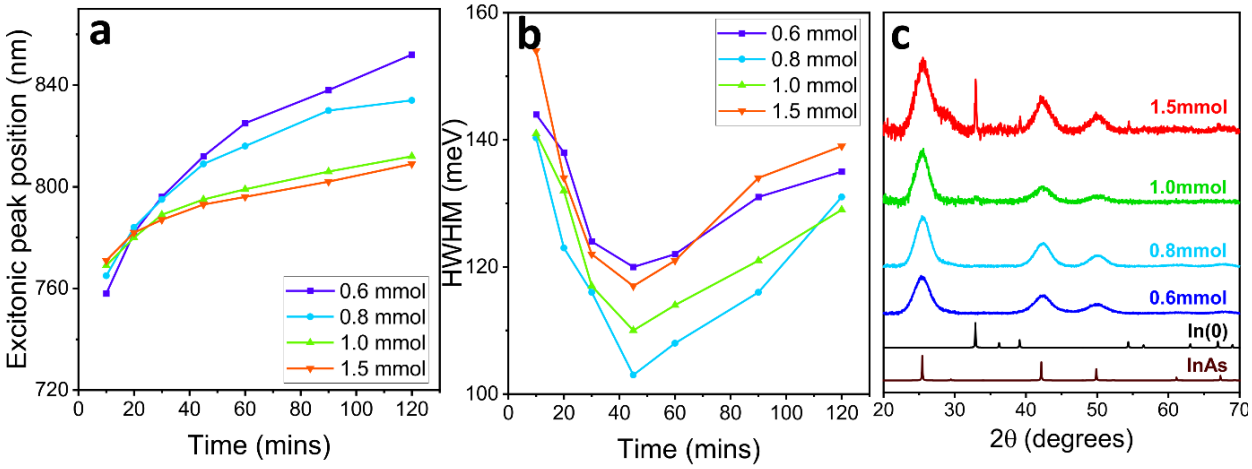

Figure 3.3.4. *Evolution of (a) excitonic peak position and (b) HWHM with time by varying the amount of TOA-AlH_3 from 0.6 to 1.5 mmol. (c) X-ray diffraction (XRD) patterns of the resulting InAs QD products.*

We next investigated the effect of injection (inj.) and reaction (reac.) temperatures while maintaining a fixed amount of TOA-AlH_3 (0.8 mmol) and keeping all other parameters constant (0.2 mmol $InCl_3$, 2 mmol $ZnCl_2$, 0.2 mmol amino-As, and 5 mL Olam). The results revealed clear temperature-dependent trends:

i. Low inj. and reac. temperatures (180 °C) led to the formation of small QDs (i.e., having an excitonic peak position located at ~700 nm, purple curve Figure 3.3.5 a).
ii. High inj. and reac. temperatures (280 °C) resulted in the aggregation of the QDs (light blue curve, Figure 3.3.5 a).
iii. Performing the inj. at relatively low temperature (240°C) and the reac. at high temperatures (280°C), yielded the best results in terms of QDs growth (reaching an excitonic peak position of 785nm) and lowest HWHM (as low as ~100meV at 45 min, orange curve; Figure 3.3.5 a, b).

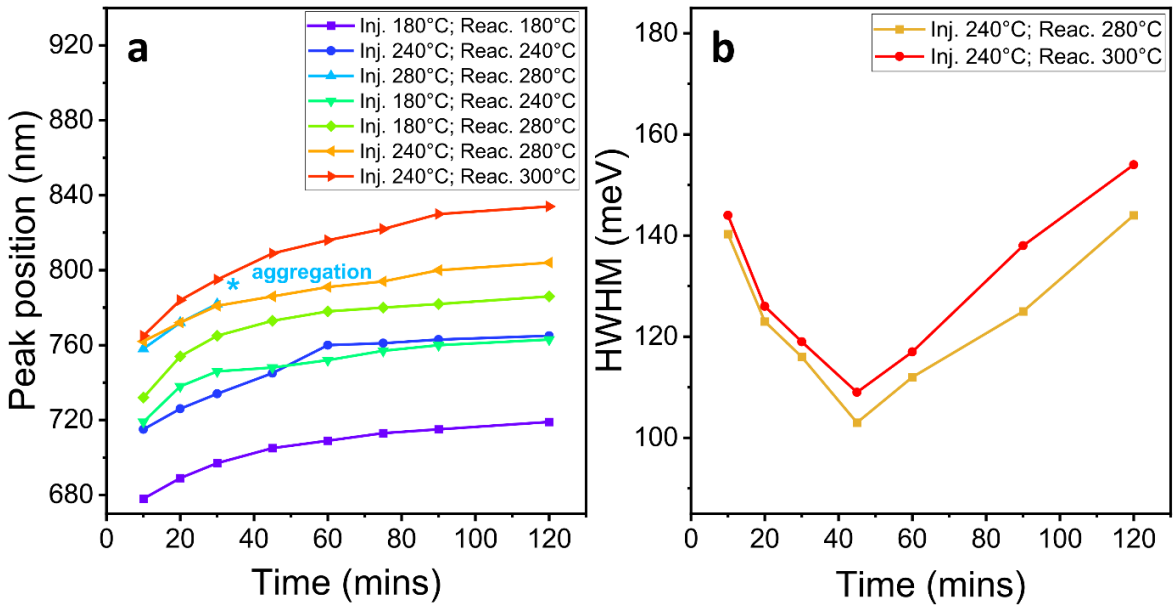

Figure 3.3.5. *Evolution of (a) excitonic peak position and (b) HWHM with reaction time by varying the injection and reaction temperature.*

By employing 0.8 mmol of TOA-AlH_3 and setting the injection and reaction temperatures to 240°C and 280°C, respectively, the most significant effects on QD growth were observed when varying the relative amounts of ODE and Olam. Specifically, reducing the Olam amount from 5 ml to 2.5 ml while increasing the ODE volume from 0 ml to 7.5 ml resulted in InAs QDs with excitonic absorption peak tunable from roughly 750 to 1025 nm (Figure 3.3.6 a) with HWHM values ranging from 100 meV up to more than 150meV (Figure 3.3.6 b). These observations are consistent with previous findings showing that achieving larger InAs QDs with narrow size distributions requires an optimal balance between the amount of Olam and the precursor concentration, the latter being controlled by the volume of ODE[37, 39]. The underlying physical rationale for this behavior is discussed in Section 1.3.7.5.

Using 5 mL of both Olam and ODE and a reaction time of 40 min (green curves in Figure 3.3.6 a, b), we obtained InAs QDs (sample InAs825) featuring an excitonic absorption peak at 825 nm with a HWHM of 100 meV (Figure 3.3.6 c and Table 3.1). These optical characteristics closely match those previously obtained using DMEA-AlH_3, where a HWHM of 115 meV was reported at 827 nm[42, 43]. It is important to note that the HWHM values extracted directly from the reaction aliquots (Figure 3.3.6 b) are systematically broader than those measured after purification (Table 3.1), a trend consistent with earlier reports by Leemans et al[37].

Optimizing the solvent ratio to 3.3 mL Olam and 6.7 mL ODE (red curves in Figure 3.3.6 a, b) enabled further red-shifting of the excitonic absorption peak to 935 nm, while achieving an even narrower linewidth of ~85 meV (sample InAs935), one of the smallest reported for amino-As based InAs QDs[40, 42-44, 46]. This sample required a longer growth time of approximately 60 minutes

(Figure 3.3.6 d). Notably, the HWHM of InAs935 is significantly narrower than that obtained using DMEA-AlH_3 at comparable wavelengths, which typically exceed ~100 meV[42].

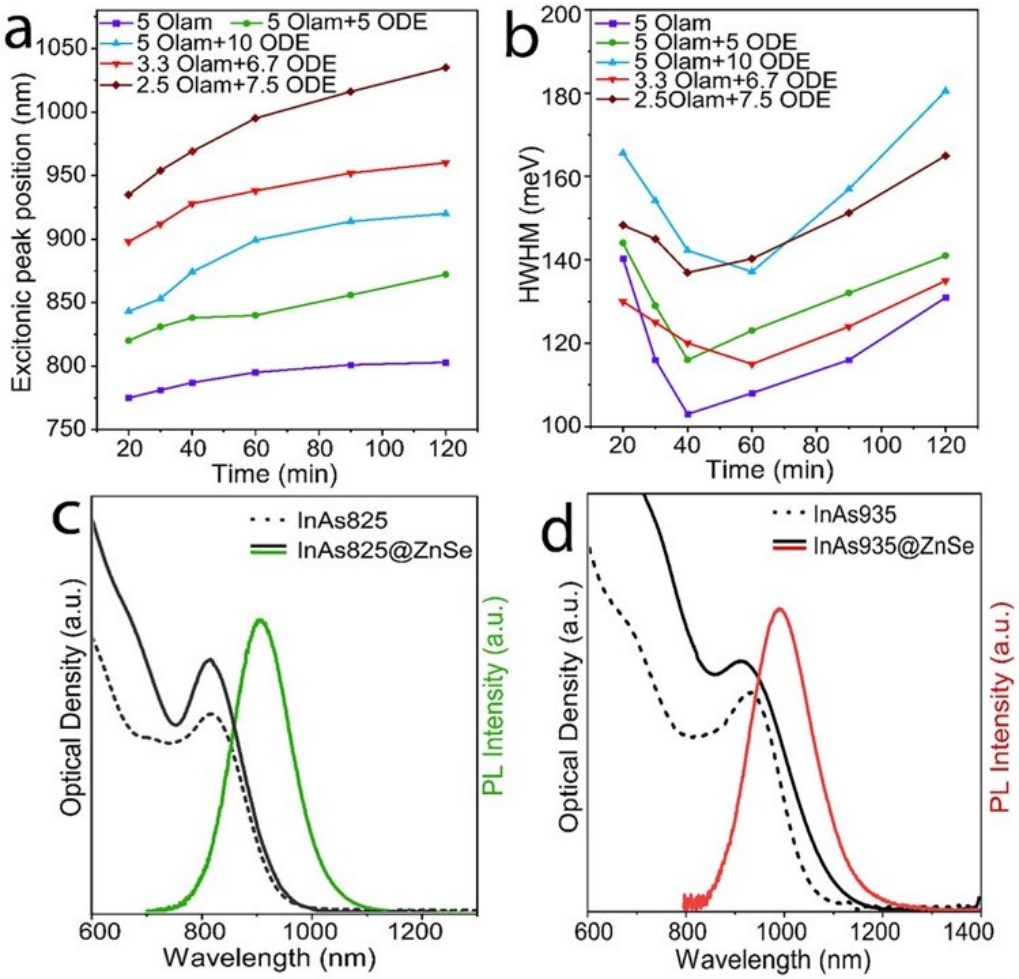

Figure 3.3.6. *a) Variation of the excitonic peak position and b) the corresponding HWHM as a function of the reaction time when employing different Olam and ODE volumes (in mL) and working with 0.8 mmol of TOA-AlH_3 and setting the injection and reaction temperatures to 240°C and 280°C, respectively. Absorption and PL curves of c) InAs825 and d) InAs935 QDs and the corresponding core@shell structures.*

Bright-field TEM images further revealed that the QDs are well dispersed and monodisperse, with average sizes of approximately ~2.9 nm for InAs825 and ~3.8 nm for InAs935 (Figure 3.3.7 a-c). XRD analysis of both InAs825 and InAs935 confirmed that the nanocrystals adopt the cubic zinc-blende InAs structure (ICSD 98-002-4518), with no detectable secondary phases (Figure 3.3.7 f).

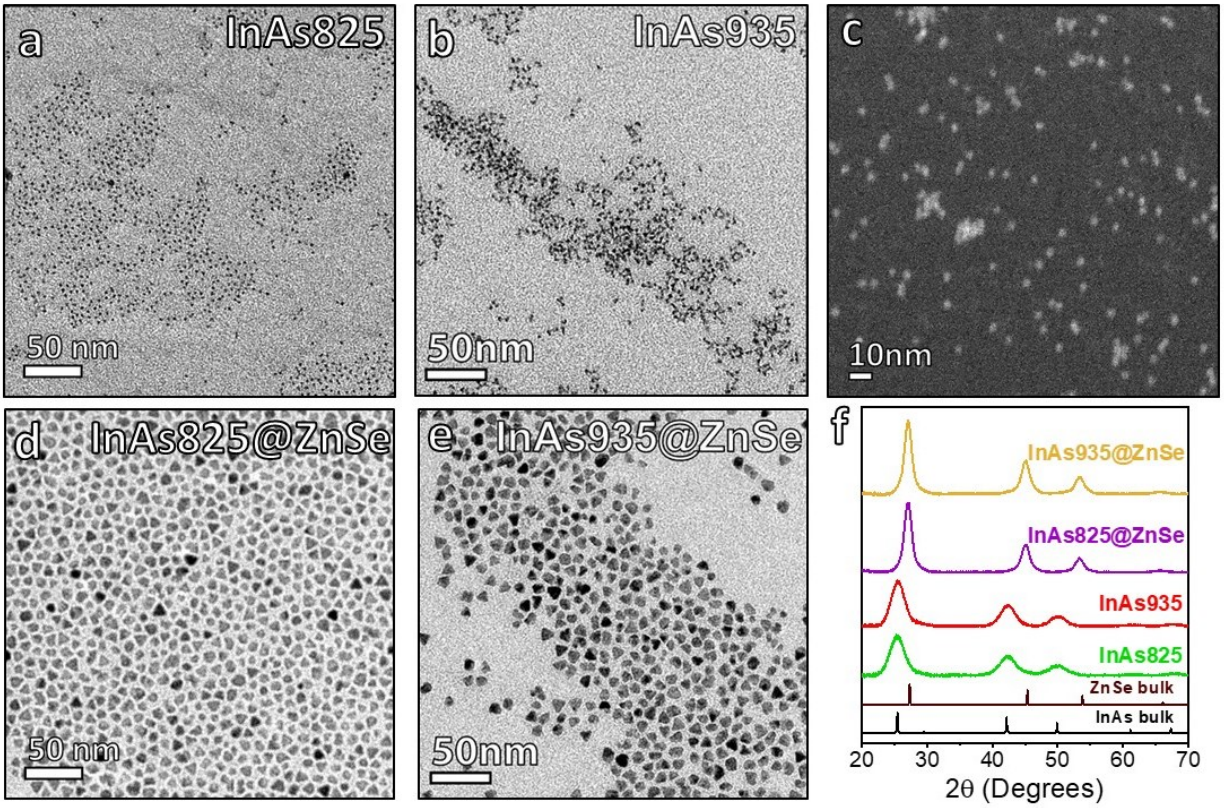

Figure 3.3.7. *Bright field (BF) - transmission electron microscopy (TEM) micrographs of (a) InAs825, (b) InAs935 quantum dots. (c) HAADF-STEM image of InAs935 QDs. (d, e) BF-TEM images of InAs825@ZnSe and InAs935@ZnSe core-shell structures. (f) XRD plots of InAs825 QDs, InAs935, InAs825@ZnSe, and InAs935@ZnSe QDs.*

Although both InAs825 and InAs935 displayed good size distributions, their photoluminescence was extremely weak, with PLQYs below 1%. To enhance the optical properties of these QDs, we overcoated them with a ZnSe shell using an optimized *in situ* shelling procedure previously developed in our group[42]. Briefly, 5.0 mL of a 0.8 M $ZnCl_2$ solution in Olam (corresponding to a final Zn/In precursor ratio of 30:1) and 7.5 mL of a 1.0 M TOP-Se solution (final Se/In ratio of 37.5:1) were injected into the crude InAs reaction mixture at 300 °C and allowed to react for 180 min (see Experimental Section for details). We note here that this shelling protocol was employed for all InAs@ZnSe samples described throughout this chapter.

Following shell growth, the resulting InAs825@ZnSe (Figure 3.3.7 d) and InAs935@ZnSe (Figure 3.3.7 e) core@shell QDs exhibited average diameters of 9.0 ± 0.8 nm and 9.9 ± 0.7 nm, respectively. These values correspond to ZnSe shell thicknesses of approximately 7 ML and 6 ML (Table 3.1 and Appendix A3.2). XRD confirmed that both samples retained the cubic zinc-blende structure without any detectable secondary phases (Figure 3.3.7 f). Shell thicknesses were estimated by combining TEM-derived particle sizes (Figure 3.3.7 d, e) with elemental composition obtained from inductively coupled plasma-optical emission spectroscopy (ICP-OES; Table 3.3) using a structural model comprising a tetrahedral InAs core surrounded by a ZnSe shell of variable

thickness (Table A 3.1). It is worth noting that ZnSe shell growth led to a marked increase in the In/As elemental ratio from ~1.15 in the cores to ~1.8 in the core@shell structures (Table 3.3). This trend, consistent with our previous observations[42, 43], indicates the formation of an In-Zn-Se interlayer at the core-shell interface, which is believed to partially relax lattice mismatch-induced strain and facilitate high-quality epitaxial shell growth.

Remarkably, the InAs825@ZnSe QDs exhibited strong PL centered at 905 nm with a PLQY of 75% and a FWHM of 190 meV (Figure 3.3.6 c and Table 3.1). This performance matches the best values previously reported for similar systems, which reached ~70% PLQY at ~900 nm with a broader FWHM of 220 meV using DMEA-AlH_3 as the reducing agent[42]. The InAs935@ZnSe QDs showed emission at 1000 nm with a FWHM of 185 meV and a PLQY of 60%, representing a record efficiency for amino-As based InAs QDs emitting at this wavelength (Figure 3.3.6 d and Table 3.1).

Table 3. 1. *Size, excitonic peak position and corresponding HWHM of InAs QDs. Size, ZnSe monolayers and optical properties of the corresponding InAs@ZnSe core@shell QDs.*

InAs			**InAs@ZnSe Core@shell**					
Size (nm)	**Excitonic peak (nm)**	**HWHM (meV)**	**Size (nm)**	**ZnSe MLs**	**PL Peak (nm)**	**PLQY (%)**	**FWHM (meV)**	**Avg. Lifetime (ns)**
2.9 ± 0.3	825	100	9.0 ± 0.8	7	905	75	190	55
3.7 ± 0.4	935	85	9.9 ± 0.7	6	1000	60	185	55

Overall, these results demonstrate the effectiveness of TOA-AlH_3 for the one-pot synthesis of amino-As based InAs QDs. Notably, the injection of the TOA-AlH_3 solution into the hot precursor mixture generated a far more stable reaction environment than that observed with DMEA-AlH_3. Specifically:

i. the reaction temperature dropped by only ~5 °C upon injection, compared to the 20-40 °C drop typically observed under analogous conditions with DMEA-AlH_3; and
ii. no boiling burst was observed, in contrast to the pronounced boiling and vapor formation characteristic of DMEA-AlH_3 injections (Figure 3.3.8 and 3.3.9).

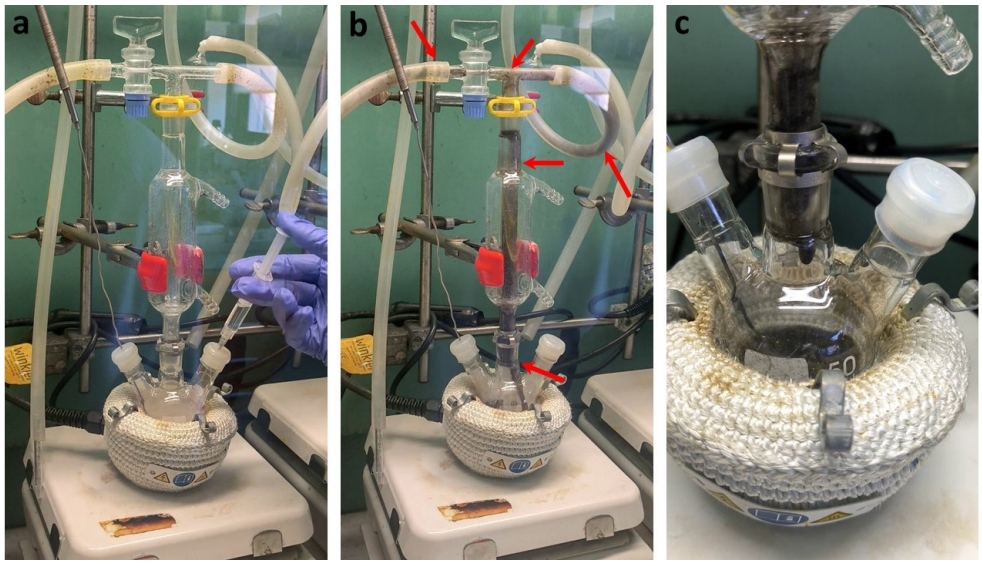

Figure 3.3.8. *Images of the reaction setup (a) before injection, (b) immediately after injection, and (c) 5 minutes after the injection of 0.8 mmol of DMEA-AlH3 into the reaction mixture. In panel (b), the red arrows highlight the sudden boiling burst, during which the reaction contents are rapidly propelled into the condenser and toward the Schlenk line, severely disrupting the setup. Panel (c) shows the continuous boiling of the reaction mixture throughout the reaction.*

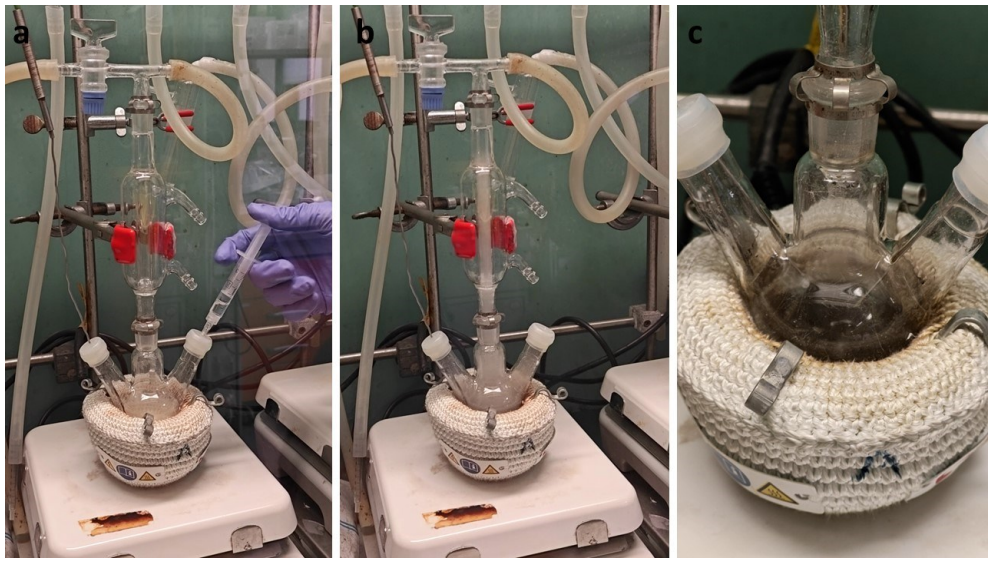

Figure 3.3.9. *Images of the reaction setup (a) before injection, (b) immediately after injection, and (c) 5 minutes after the injection of 0.8 mmol of TOA-AlH_3 into the reaction mixture. In contrast to the behavior observed with DMEA-AlH_3, the images demonstrate stable reaction conditions with no boiling bursts or disturbance of the reaction setup.*

As shown in the previous section, varying the one-pot synthesis parameters did not allow us to grow InAs QDs with excitonic absorption peaks beyond 1000 nm while simultaneously preserving narrow absorption linewidths. Extending the reaction time only broadened the size distribution, indicating the onset of Ostwald ripening and the loss of controlled growth. To overcome this

limitation and prolong the growth phase while maintaining monodispersity, we implemented a seeded growth strategy. In this approach, additional In and As precursors were introduced into the crude reaction mixture after the initial InAs QDs had reached a size of ~3.7 nm, corresponding to an excitonic absorption peak at approximately 935 nm (Figure 3.3.6d).

However, the seeded growth step requires the introduction of three different precursors, $InCl_3$, amino-As, and TOA-AlH_3, which can, in principle, be added individually or as mixtures and in various possible injection sequences. To determine the most effective approach, we systematically evaluated several injection protocols, summarized schematically in Figure 3.3.10. For this study, the InAs 'seed' QDs were first prepared following the optimized InAs935 synthesis conditions (0.2 mmol $InCl_3$, 2 mmol $ZnCl_2$, 3.3 mL Olam, 6.7 mL ODE, 0.2 mmol amino-As in 0.5 mL Olam, and 0.8 mmol TOA-AlH_3 in 0.5 mL ODE; injection at 240 °C and growth at 280 °C). After 60 min, the reaction was cooled to lower temperature to initiate the seeded growth step.

For the optimization of the seeded growth step, we employed a threefold excess of each precursor relative to the one-pot synthesis, which is 3 mL of 0.2 M $InCl_3$-Olam, 6 mL of 0.1 M amino-As in Olam, and 6 mL of 0.2 M TOA-AlH_3 in ODE. These components were then introduced via continuous injection at 240 °C. Multiple precursor-injection sequences were tested to identify the conditions that enable controlled growth while preserving narrow size distributions. The effectiveness of each route was assessed by monitoring the excitonic peak position, indicative of QD size, and the HWHM of the first excitonic peak, which reflects the size distribution.

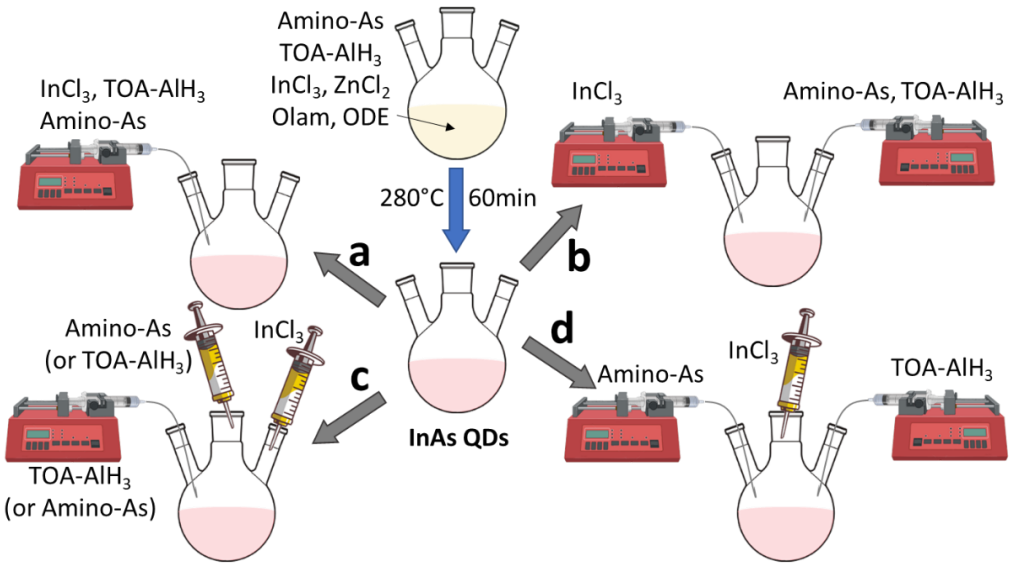

Figure 3.3.10. *Schematic representation of the seeded growth procedures tested in the present work: a) simultaneous continuous injection of all the reactants; b) continuous co-injection of two different reactant solutions; c) addition of two reactants followed by continuous injection of the third; d) addition of $InCl_3$ followed by continuous co-injection of amino-As and TOA-AlH_3.*

Simultaneous injection of all reactants mixed together.

In this strategy, all three precursors were premixed at room temperature and subsequently injected into the reaction flask using a syringe pump (Figure 3.3.10 a). The mixture turned deep purple-red within seconds (Figure 3.3.11 a), indicating rapid precursor interconversion. The resulting 15 mL solution (3 eq.) was loaded into a 20 mm diameter syringe and continuously injected at 0.05 mL/min into the InAs QD reaction mixture maintained at 240 °C. A thermocouple positioned at the syringe needle tip, where the solution drops into the reaction mixture, recorded temperatures exceeding 100 °C during injection (Figure 3.3.11 b), suggesting that the precursor mixture experienced significant heating before entering the flask. Aliquots were collected after 100, 200, and 300 min, corresponding to the addition of 1, 2, and 3 equivalents of precursors. This strategy resulted in the growth of InAs QDs which featured a broad excitonic absorption peak after a reaction time of 100 mins. However, with prolonged injection (200 min), aggregation was observed (orange and red curves Figure 3.3.11 c). We hypothesize that the precursors' reaction may initiate at the needle tip (where the temperature exceeds 100°C) before the droplet enters the reaction mixture, leading to broad size distributions.

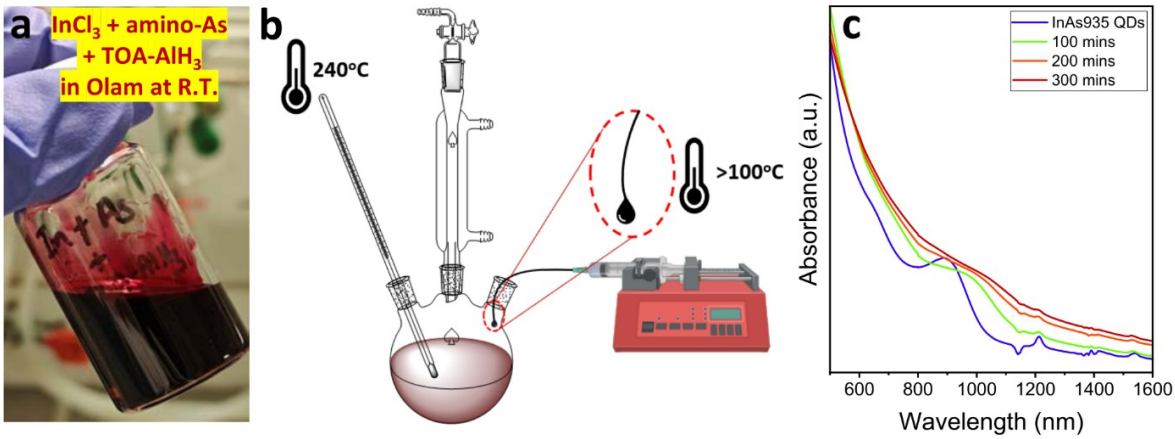

Figure 3.3.11. *(a) Image of mixture of $InCl_3$, amino-As and TOA-AlH_3 precursor solutions at room temperature. (b) Schematic showing the temperature conditions inside the reaction mixture. (c) Evolution of the absorption spectra of aliquots collected over time during the seeded growth of InAs QDs by continuous injection of the mixed precursor solution (3 eq. of extra $InCl_3$, amino-As, and TOA-AlH_3) into the seed reaction.*

Continuous co-injection of two different reactant solutions

Since premixing all three precursors led to their reaction before the droplets entered the reaction mixture, we next explored splitting them into pairs. In this approach, two precursors were combined at room temperature while the third was injected separately. The three possible combinations evaluated were: (i) $InCl_3$-Olam + TOA-AlH_3, (ii) amino-As + TOA-AlH_3, and (iii) amino-As + $InCl_3$-Olam. Each precursor pair and the remaining single precursor were delivered using two separate syringe pumps. The first combination, $InCl_3$-Olam mixed with TOA-AlH_3 was immediately ruled out because it led to the formation of metallic indium upon mixing. For the second strategy,

we attempted a two-syringe approach in which $InCl_3$-Olam was injected from one syringe and the amino-As + TOA-AlH_3 mixture from the other at 240 °C. However, the 0.2 M $InCl_3$-Olam precursor exhibited significant viscosity fluctuations as a function of the temperature (Figure 3.3.12 a-e) It was fluid at both 200°C and at room temperature but became highly viscous between 30 °C and 150 °C. As shown in the schematic (Figure 3.3.11 b), the needle tip reaches temperatures above 100 °C during injection, causing the $InCl_3$-Olam solution to thicken at the needle outlet (Figure 3.3.12 f). This viscosity increase made continuous and controlled injection impractical.

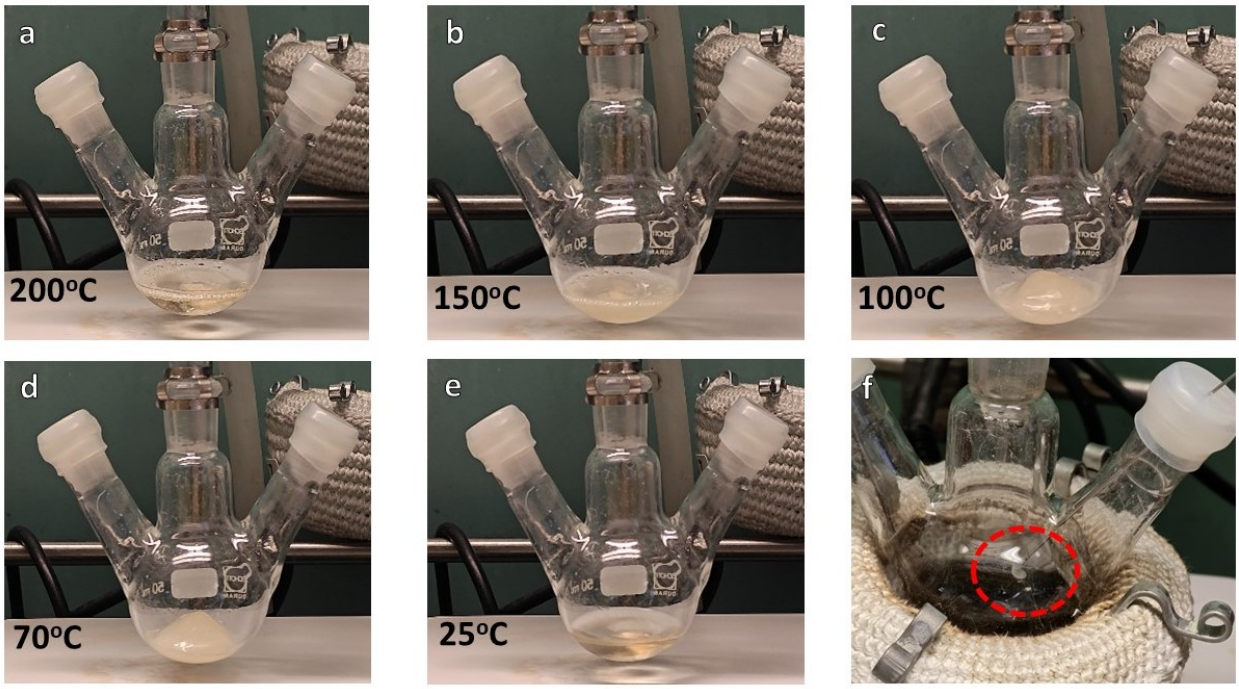

Figure 3.3.12. *(a-e) The variability in viscosity of 0.2M $InCl_3$-Olam solution with temperature. (f) The blockage in the continuous injection due to increased viscosity of the $InCl_3$-Olam solution inside the reaction flask.*

Direct addition of two precursors followed by the continuous injection of the third.

We next explored an approach in which two precursors were added directly to the InAs QD reaction mixture, followed by the continuous injection of the third precursor. Given the problems connected with the viscosity of the $InCl_3$-Olam solution, this solution was directly injected into the reaction medium. This left two possible injection sequences:

i. Direct injection of amino-As in Olam, followed by continuous injection of TOA-AlH_3 in ODE.

ii. Direct injection of TOA-AlH_3 in ODE, followed by continuous injection of amino-As in Olam.

In the first case, direct addition of amino-As to the reaction mixture led to immediate aggregation and precipitation of the InAs QDs. In the second case, direct injection of TOA-AlH_3 resulted in the

formation of metallic indium (In^0) and $AlCl_3$ as byproducts, as confirmed by the XRD pattern of the resulting material.

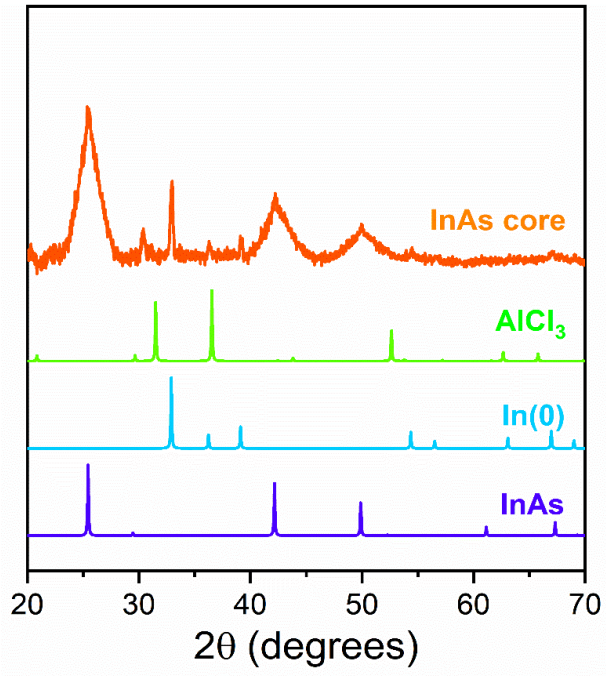

Figure 3.3.13. *XRD analysis of InAs QDs synthesized using seeded growth approach in which $InCl_3$-Olam and TOA-AlH_3 were directly added to the InAs QDs reaction mixture, followed by the continuous injection of amino-As in Olam.*

Direct addition of $InCl_3$ followed by the simultaneous co-injection of amino-As and TOA-AlH_3.

Taken together, the three precursor-injection routes described above proved unsuitable for controlled seeded growth. Each suffered from either (i) uncontrolled growth of the existing "seed" particles, (ii) aggregation and precipitation of the QDs, or (iii) precursor solutions that became too viscous to inject reliably. These limitations prompted us to explore an alternative strategy. We therefore developed an approach based on the direct addition of the required amount of $InCl_3$ to the crude InAs seed solution, followed by the simultaneous continuous co-injection of amino-As and TOA-AlH_3 (Figure 3.3.10 d).

After identifying this as the successful route, we optimized it by systematically varying both the injection temperature (which corresponds to the reaction temperature) and the relative injection rates of amino-As and TOA-AlH_3. The experiments revealed that the amount of TOA-AlH_3 delivered at any time must be approximately twice that of amino-As. When the reducing agent was injected too slowly (i.e., at less than twice the amino-As rate), aggregation occurred after ~80 min (Figure 3.3.14). Under such conditions, the excitonic absorption peak broadened and developed a pronounced low-energy tail (green and orange curves, Figure 3.3.14 b), indicative of light scattering from aggregates. After 100 min, aggregation became extensive enough to prevent reliable absorption measurements of the 120 min aliquot.

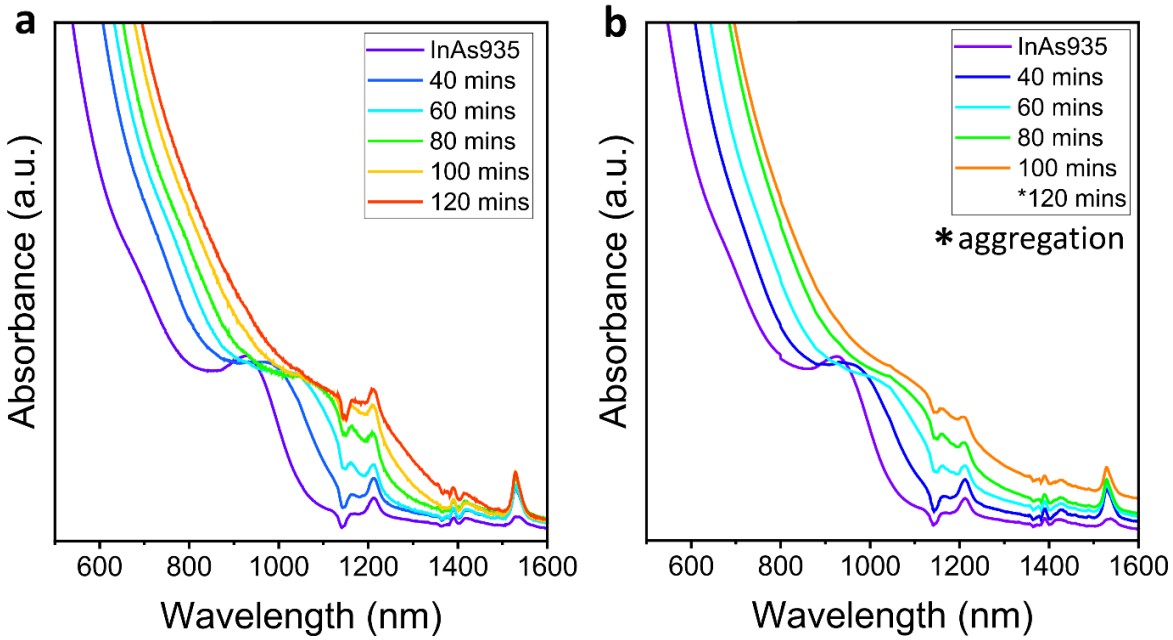

Figure 3.3.14. *Evolution of absorption spectra of reaction aliquots of InAs QDs with time when the injection rate of TOA-AlH_3 is (a) double (0.01mmol/min) and (b) equal (0.005mmol/min) as compared to the injection rate of amino-As (0.005mmol/min).*

We then optimized the injection rate by varying the amino-As delivery rate from 0.02 mmol/min (Figure 3.3.15 a) to 0.005 mmol/min (Figure 3.3.15 b) and 0.0025 mmol/min (Figure 3.3.15 c), while maintaining a fixed 2:1 TOA-AlH_3/amino-As injection-rate ratio. As shown in Figure 3.3.15, rates higher than 0.005 mmol/min (e.g., 0.02 mmol/min) led to progressively broader size distributions, reflected in the widening of the excitonic absorption feature over time. Conversely, reducing the injection rate below 0.005 mmol/min did not yield narrower size distributions and instead prolonged the total reaction time unnecessarily. Based on these observations, an injection rate of 0.005 mmol/min for amino-As and 0.01 mmol/min for TOA-AlH_3 was selected as optimal, providing controlled QD growth without excessive reaction durations.

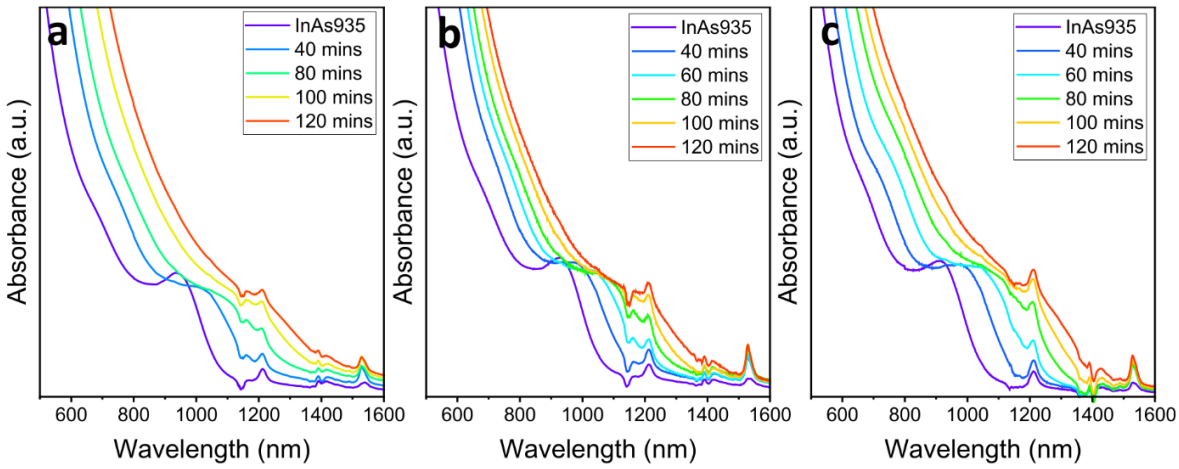

Figure 3.3.15. *Absorption spectra of reaction aliquots collected at different time points during the seeded growth of InAs QDs using amino-As injection rates of (a) 0.02 mmol/min, (b) 0.005 mmol/min, and (c) 0.0025 mmol/min, maintaining a (TOA-AlH_3/amino-As) injection rate ratio of 2:1.*

We next examined the effect of the injection (i.e., reaction) temperature on the final InAs QDs by varying the continuous-injection temperature from 200 °C to 260 °C while keeping all other parameters fixed (3 eq. of additional precursors; amino-As and TOA-AlH_3 injection rate of 0.005 mmol/min and 0.01 mmol/min). At 260 °C, rapid QD growth was observed, but this was followed by aggregation at longer reaction times (red curve, Figure 3.3.16). In contrast, injection temperatures ≤ 220 °C were insufficient to sustain significant growth. At 200 °C essentially no size increase occurred (blue curve, Figure 3.3.16), and at 220 °C only limited growth was achieved, with the excitonic peak reaching ~1050nm (green curve, Figure 3.3.16). By operating at 240 °C, however, controlled growth was obtained, yielding QDs with an excitonic absorption peak at 1170 nm after 120 min while maintaining narrow linewidths (HWHM ~100 meV).

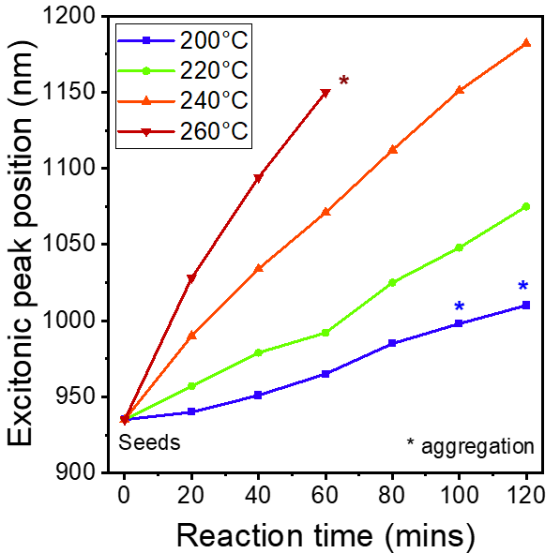

Figure 3.3.16. *Evolution of excitonic peak position with amount of precursor addition at varying temperatures. The * represents the point where aggregation of the QDs was observed.*

Using the optimized seeded-growth conditions, which consist of the direct addition of $InCl_3$ followed by continuous co-injection of amino-As (0.005 mmol/min) and TOA-AlH_3 (0.01 mmol/min) at 240 °C, we were able to precisely control the size of the InAs QDs by adding 2, 3, 5, or 7 equivalents of additional precursors (see Table 3.6, Experimental Section). By tuning the total amount of precursor added to the reaction mixture, the initial 3.8 nm seeds were successfully enlarged to particle sizes between 4.6 nm and 6.3 nm (Figure 3.3.17 and Appendix A 3.1).

Correspondingly, the excitonic absorption peaks could be tuned from 1090 to 1340 nm (the samples were named accordingly InAs1090, InAs1170, InAs1250 and InAs1340) with HWHM values in the 92-99meV range (Figure 3.3.18 and Table 3.4), with no need to perform a size selection. Such HWHM values are comparable to the best values reported so far for amino-As-based InAs QDs, namely ~95meV at 1380nm and 90meV at 1420 nm[45, 46]. The XRD patterns of these samples indicated the absence of secondary phases, such as metallic In or In- or As-oxides, and the presence of the expected cubic zinc-blende InAs phase only (Figure 3.3.19 a)

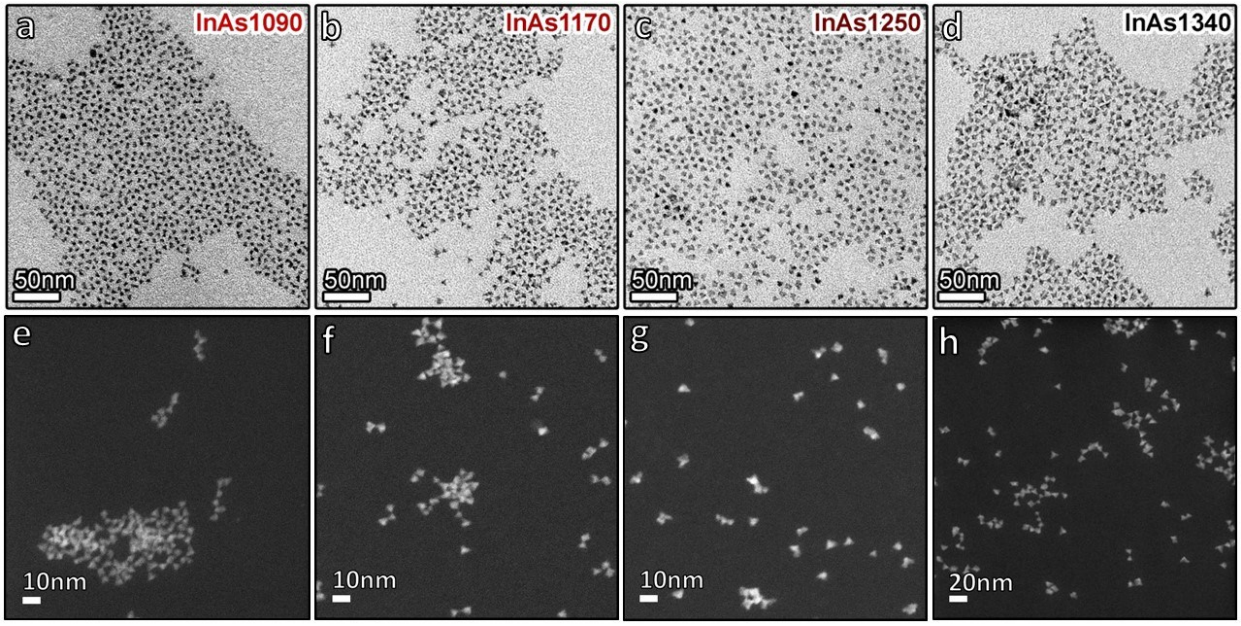

Figure 3.3.17. *BF-TEM micrographs of (a) InAs1090, (b) InAs1170, (c) InAs1250, and (d) InAs1340 QDs, and (e-h) the corresponding HAADF-STEM images.*

The InAs QDs obtained by seeded growth were subsequently overcoated with a ZnSe shell. After adding the shell precursors to the crude core solution, aliquots were collected at different times, purified, and analyzed.

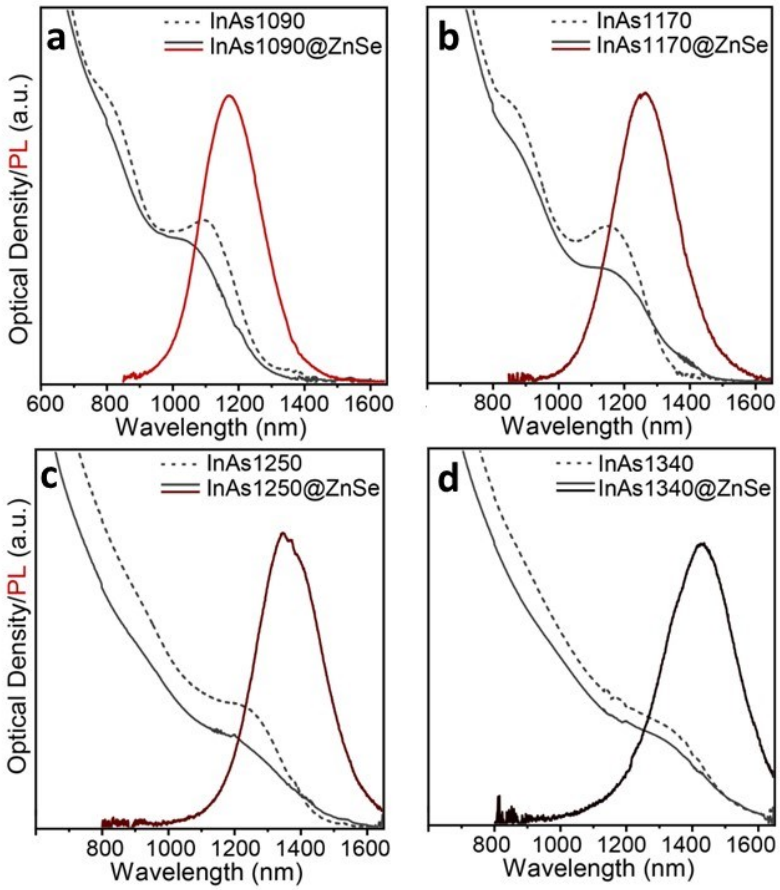

Figure 3.3.18. *(a-d) Absorption spectra (dotted lines) of the InAs QD samples, along with those of the corresponding core@shell (black lines) and PL spectra (various shades of red in panels a-d).*

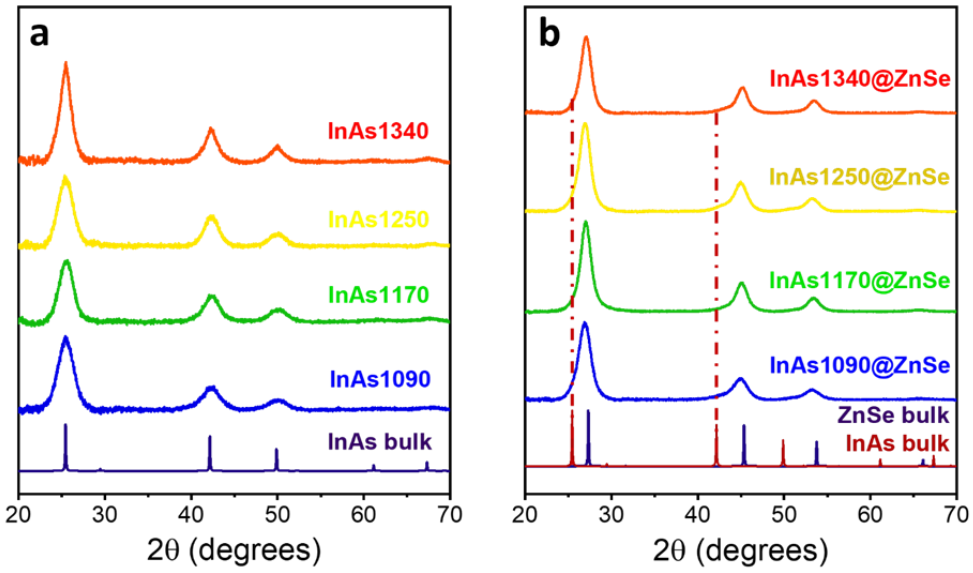

Figure 3.3.19. *XRD patterns of (a)InAs QDs and (b) the corresponding core@shell QD products together with the bulk reflections of zinc-blende ZnSe (ICSD 98-007-7092) and zinc-blende InAs (ICSD 98-002-4518).*

During ZnSe shell growth, both the excitonic absorption and PL peaks of the InAs cores initially redshifted and subsequently blue-shifted as shell deposition progressed, behavior consistent with previous observations for InAs-based core@shell structures. A possible explanation is that the first monolayer formed at the interface, likely with a composition close to In_2ZnSe_4, passivates surface traps and enhances PL but provides weaker carrier confinement, leading to an initial redshift[42, 43]. As the shell grows thicker, the composition and structure of this interfacial layer evolve, improving carrier confinement in the InAs core and resulting in the subsequent blueshift[42, 43].

For each core size, the shelling duration was optimized to achieve the highest PL efficiency (Figure 3.3.20 a, b). Under these optimized conditions, the resulting InAs@ZnSe QDs displayed remarkably high PLQYs of as high as 46% (1160 nm), 38% (1250 nm), 32% (1335 nm), and 23% (1430 nm), which are record values for these systems (Figure 3.3.20 b, Table 3.4). The average PL lifetimes (Table 3.2 and Figure 3.3.20 c) increased systematically with increasing core size, an expected trend given the weaker quantum confinement in larger InAs QDs, which reduces the radiative recombination rate and leads to longer PL lifetimes[52-54].

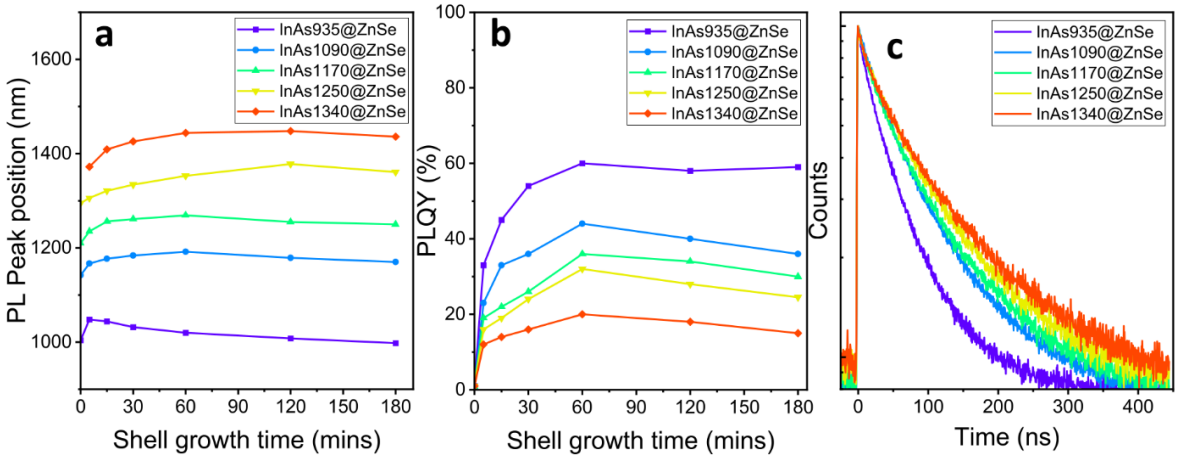

Figure 3.3.20. *Evolution of (a) PL peak position and (b) PLQY with increasing ZnSe shell growth time of InAs935@ZnSe, InAs1090@ZnSe, InAs1170@ZnSe, InAs1250@ZnSe and InAs1340@ZnSe QDs. (c) Time-resolved PL spectra of InAs935@ZnSe, InAs1090@ZnSe, InAs1170@ZnSe, InAs1250@ZnSe and InAs1340@ZnSe QDs.*

The PL decay curves were fitted with a biexponential decay function (shown as equation 3.3, 3.4)**,** where I(t) is the intensity at a given time, and τ_1 and τ_2 are the two time constants with amplitudes A_1 and A_2 respectively. The extracted values of the time constants and amplitudes are given in Table 3.2.

(Equation 3.3)

(**Equation 3.4)**

Table 3. 2. *Amplitudes and time constants extracted from biexponential fits of PL decay curves for InAs@ZnSe core@shell QDs.*

Sample	A_1	τ_1 (ns)	A_2	τ_2 (ns)	τ_{avg} (ns)
InAs935@ZnSe	0.28	32	0.72	64	55
InAs1090@ZnSe	0.26	22	0.74	84	67
InAs1170@ZnSe	0.26	28	0.74	93	78
InAs1250@ZnSe	0.22	25	0.78	103	86
InAs1340@ZnSe	0.25	22	0.75	119	95

BF-TEM analysis confirmed successful ZnSe shell growth, with the final InAs@ZnSe core@shell QDs exhibiting shell thicknesses of approximately 6-8 ML (Figure 3.3.21 a-d, Table 3.4, Appendix A3.2). XRD measurements further verified the crystalline structure of the core@shell nanocrystals, showing diffraction patterns consistent with the ZnSe phase (ICSD 98-007-7092) and no detectable secondary phases (Figure 3.3.19).

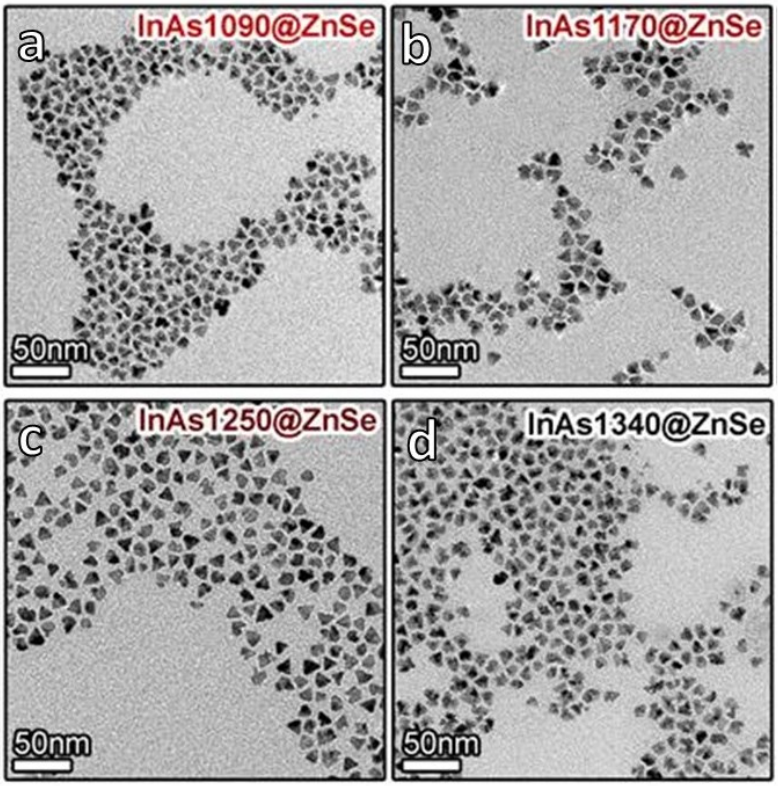

Figure 3.3.21. *BF-TEM micrographs of a) InAs1090@ZnSe, b) InAs1170@ZnSe, c) InAs1250@ZnSe, and d) InAs1340@ZnSe Core@shell QDs.*

Notably, the In/As elemental ratio increased upon ZnSe shelling (Table 3.3), suggesting the formation of an In-Zn-Se interlayer in these larger QD systems, consistent with our observations in smaller cores[42].

Table 3. 3. *Elemental ratios of InAs core QDs with different core sizes and their corresponding InAs@ZnSe core@shell QDs as measured by the ICP-OES.*

Sample Name	InAs QDs		Sample Name	InAs@ZnSe Cores@Shell QDs		
	In/As	Zn/In		In/As	Zn/In	Zn/Se
InAs825	1.14	0.06	InAs825@ZnSe	2.12	12.74	1.12
InAs935	1.18	0.08	InAs935@ZnSe	2.02	9.69	0.96
InAs1090	1.14	0.05	InAs1090@ZnSe	1.71	5.36	1.11
InAs1170	1.11	0.04	InAs1170@ZnSe	1.64	5.15	1.09
InAs1250	1.19	0.04	InAs1250@ZnSe	1.52	4.99	1.03
InAs1340	1.21	0.05	InAs1340@ZnSe	1.48	5.95	1.17

Table 3. 4. *Size, excitonic peak position, and HWHM of InAs QDs obtained via seeded growth. Size, ZnSe monolayers, and optical properties of the resulting InAs@ZnSe core@shell QDs.*

InAs		
Size (nm)	Abs. peak (nm)	HWHM (meV)
4.6±0.4	1090	99
5.2±0.5	1170	97
5.7±0.5	1250	98
6.3±0.7	1340	92

InAs@ZnSe Core@shell					
Size (nm)	ZnSe MLs	PL peak (nm)	PLQY (%)	FWHM (meV)	PL lifetime (ns)
10.2±0.9	6	1160	46	191	67
11.8±0.9	6	1250	38	177	78
12.1±1.0	6-7	1335	32	158	86
12.5±1.1	8	1430	23	154	95

High-resolution (HR) TEM analysis of the InAs@ZnSe QDs, exemplified here by the InAs1250@ZnSe sample, showed that most core@shell structures are monocrystalline, predominantly exhibiting a truncated tetrahedral morphology with an InAs core encapsulated by an epitaxial ZnSe shell (Figure 3.3.22). Tetrahedral QDs, such as the one shown in Figure 3.3.22a, rest on a truncated triangular facet on the carbon support film, oriented parallel to the [111] direction of the zinc-blende lattice (Figure 3.3.22 c, d). Strain mapping performed via peak-pair analysis (PPA; see Experimental Section for details) on the QD in Figure 3.3.22 revealed that the ZnSe shell possesses lattice parameters approximately 5.6% smaller than those of the core, slightly lower than the difference expected from the bulk values of the two materials.

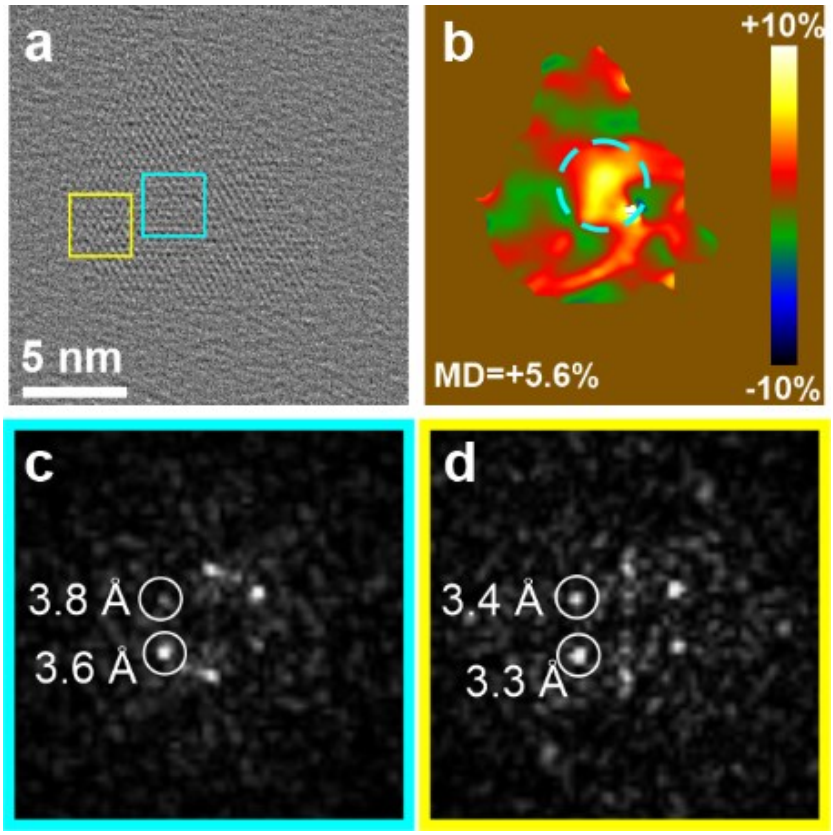

Figure 3.3.22. (*a) Average background subtraction-filtered HRTEM image of the InAs1250@ZnSe sample and b) the corresponding mean dilation (MD) map computed by the PPA method, with the core region enclosed in the cyan circle. The MD reported in the panel is the average mean dilation within the core area compared to the shell. (c-d) Fast Fourier transformations of areas enclosed in the (cyan) core and (yellow) shell areas of a), both matching with [111] direction of zinc-blende structures.*

PPA analysis performed on different QDs indicated that some InAs@ZnSe QDs feature a decentered InAs core (Figure 3.3.23), which can be explained by a partially anisotropic ZnSe shell growth in these core@shell structures.

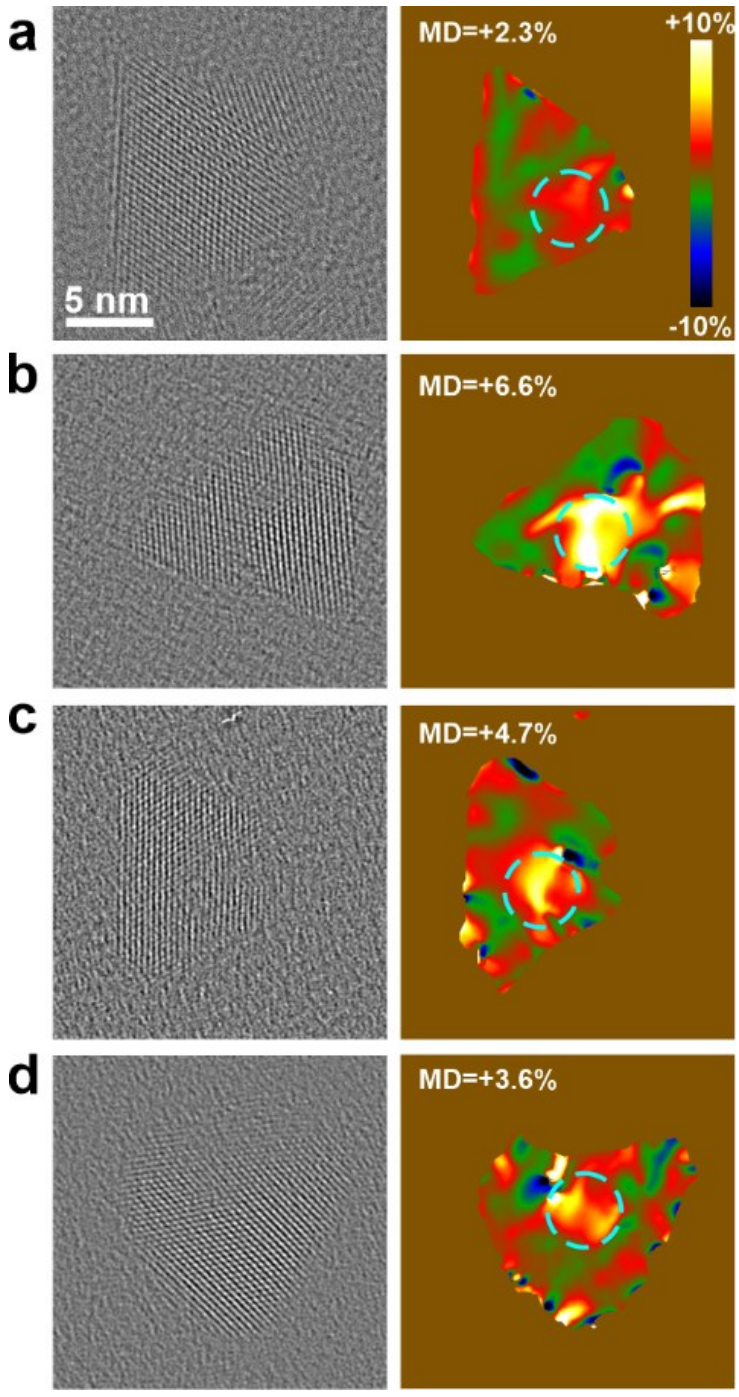

Figure 3.3.23. *(left) Average background subtraction-filtered HRTEM images of individual particles in the sample InAs1250@ZnSe and (right) corresponding mean dilation map computed by the PPA method. The MD values reported in the panels on the right are the average mean dilation values within the core area (within the cyan circles) as compared to the shell.*

We emphasize that amino-As-based InAs@ZnSe core@shell QDs with efficient emission above 1000 nm have not been reported prior to this work. This underscores the effectiveness of our reducing agent TOA-AlH_3 which was essential for achieving controlled growth and high PLQYs in

the SWIR region. Indeed, reducing agents dispersed in low-boiling-point solvents or those with a low boiling point themselves, such as DMEA-AlH_3, were observed to cause excessive boiling of the reaction mixture under analogous conditions, leading to unstable reaction conditions (Figure3.3.24).

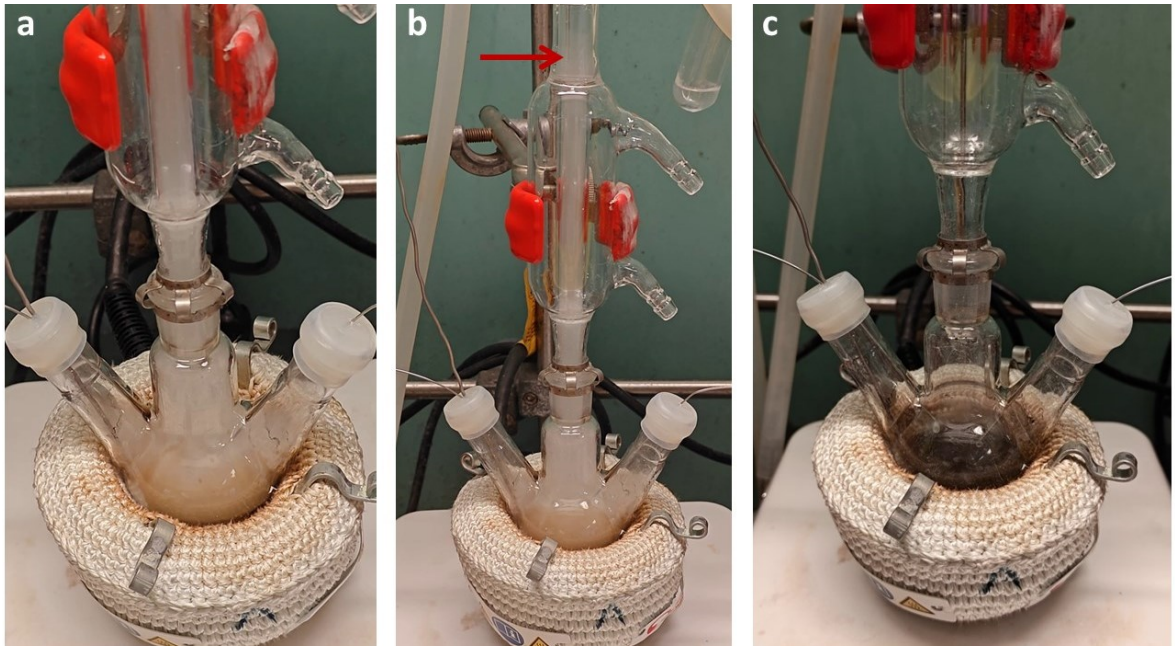

Figure 3.3.24. *Images of the reaction mixtures during continuous injection when 0.1 mmol of (a, b) DMEA-AlH_3 and (c) TOA-AlH_3 were injected into the reaction flask. The red arrow in panel (b) highlights the persistent boiling of the reaction mixture, which leads to a buildup of significant pressure inside the reaction flask.*

The Role of $ZnCl_2$

All the reaction schemes illustrated so far included the use of $ZnCl_2$ in the synthesis of InAs QDs. This additive was employed in the one-pot synthesis of InAs QDs (with a Zn/In precursors ratio of 10/1) and remained in the crude reaction solution in the whole seeded-growth procedure. Under the optimized reaction conditions described above, the absence of $ZnCl_2$ (details in Experimental Section) led to two main differences:

i. the formation of larger InAs QDs. In the one-pot synthesis, the QDs reached an absorption peak at 1020 nm (InAs1020-noZn), compared to 935 nm when $ZnCl_2$ was present (InAs935, Figure 3.3.25 a and Figure 3.3.6 d). Likewise, after three equivalents of precursors were added during seeded growth, the resulting QDs exhibited an excitonic peak at 1300 nm (InAs1300-noZn), whereas the $ZnCl_2$-containing synthesis produced QDs with a peak at 1170 nm (InAs1170, Figure 3.3.25 b and Figure 33.18 b). This size increase can be attributed to the absence of $ZnCl_2$, which acts as a Z-type ligand capable of binding to surface As sites and moderating monomer attachment. When $ZnCl_2$ is not present to

regulate surface reactivity, monomer addition proceeds more rapidly, leading to faster growth and the formation of larger QDs.

ii. poor optical quality even after ZnSe shelling. InAs QDs synthesized without $ZnCl_2$ displayed either very low PLQY after ZnSe shell growth (10% PLQY at 1100 nm for InAs1020-noZn@ZnSe; Figure 5a and Table S4) or no detectable emission (InAs1300-noZn@ZnSe; Figure 5b and Table S5). This aspect was studied in more details in one of our recent works[55].

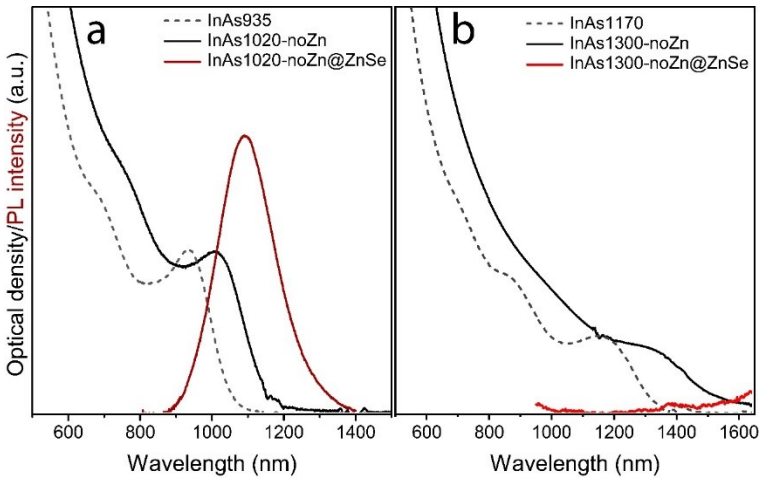

Figure 3.3.25. *a) Absorption curve (black line) of InAs QDs synthesized without $ZnCl_2$ via the one-pot procedure, along with the PL spectrum (dark red line) of the corresponding QDs after ZnSe shelling. b) Absorption spectrum of InAs QDs synthesized without $ZnCl_2$ via seeded growth approach using three equivalents of added precursors (black like), together with the PL spectrum (red line) of the resulting InAs@ZnSe QDs. The absorption spectra of InAs935 and InAs1170 QD samples are also included in panels a) and b), respectively (gray dotted lines).*

As shown in Table 3.5 and 3.6, the Zn/In ratios increased progressively with shell growth time, confirming the deposition of ZnSe on the InAs cores, consistent with what was observed when $ZnCl_2$ was used as an additive. However, despite successful shell formation, no meaningful improvement in PLQY was obtained for either the one-pot or seeded-growth samples. This indicates that, in the absence of $ZnCl_2$ during core formation, ZnSe shelling alone is insufficient to recover high emissive quality. The poor PLQYs suggest that the core surfaces formed without $ZnCl_2$ remain inadequately passivated, likely containing a higher density of nonradiative recombination sites that cannot be effectively passivated by subsequent ZnSe growth.

This interpretation is supported by recent work from our group, which demonstrated that introducing $ZnCl_2$ at the beginning of InAs synthesis enables selective passivation of defect-prone facets, particularly the (-1, -1, -1) surface. When $ZnCl_2$ is present during nucleation and growth, Zn incorporation occurs on the (100) and (-1, -1, -1) facets, suppressing trap formation and yielding highly emissive QDs. In contrast, post-synthetic exposure to $ZnCl_2$ results primarily in its adsorption as a Z-type ligand, with minimal lattice incorporation and therefore limited ability to passivate deep trap states.

Table 3. 5. *Elemental ratios and the corresponding PLQY values of reaction aliquots at various shell growth times for InAs935@ZnSe QD and InAs1020-noZn@ZnSe.*

Shell growth Time (mins)	**InAs935@ZnSe**			**InAs1020-noZn@ZnSe**		
	Zn/In	Zn/Se	PLQY (%)	Zn/In	Zn/Se	PLQY (%)
5	2.21	1.16	33	2.51	1.30	5
15	3.93	1.10	45	3.99	1.14	8
30	5.69	1.08	54	5.94	1.11	10
60	7.33	1.06	60	7.62	1.12	9
120	8.86	1.02	57	8.69	1.14	8
180	10.95	1.01	56	10.02	1.02	6

Table 3. 6. *Elemental ratios and the corresponding PLQY values of reaction aliquots at various shell growth times for InAs1170@ZnSe QD and InAs1300-noZn@ZnSe.*

Shell growth Time (mins)	**InAs1170@ZnSe**			**InAs1300-noZn@ZnSe**		
	Zn/In	Zn/Se	PLQY (%)	Zn/In	Zn/Se	PLQY (%)
5	1.03	0.92	19	0.86	0.80	No PL
15	1.99	1.14	22	1.12	0.82	No PL
30	2.63	1.08	26	2.60	0.93	No PL
60	4.24	1.07	36	3.25	0.97	No PL
120	5.64	1.06	34	4.82	0.99	No PL
180	6.76	1.04	30	6.24	1.05	No PL

3.4 Conclusion

In this chapter, we established a robust synthetic platform for producing highly emissive amino-As-based InAs and InAs@ZnSe quantum dots (QDs) with tunable optical responses extending deep into the short-wave infrared region. This result was achieved using TOA-AlH_3 as a reducing agent, which was synthesized in our lab and employed not only for the synthesis of InAs QDs through a hot-injection procedure, but also for their subsequent growth in-situ via a seeded-growth approach. TOA-AlH_3 can be dispersed in high-boiling-point solvents and has a high boiling point itself, enabling precise control over reaction conditions even during continuous addition in the seeded growth. This is in stark contrast to traditional reducing agents used in the amino-As route, which have a low boiling point and are dispersed in low-boiling-point solvents (e.g., DMEA-AlH_3, DIBAL-H, etc.). Moreover, TOA-AlH_3 is compatible with the $ZnCl_2$ additive in the InAs QDs reaction environment, a condition found to be essential to synthesize InAs@ZnSe core@shell QDs with efficient PL.

In developing the seeded-growth protocol, we established that the order of precursor addition is critical to avoid uncontrolled nucleation, precipitation, or aggregation. The most effective strategy involved the initial addition of $InCl_3$ to the crude InAs seed solution, followed by the continuous co-injection of amino-As and TOA-AlH_3 at controlled and distinct rates. This method enabled predictable and monodisperse size enlargement, ultimately yielding InAs cores with excitonic absorption up to 1340 nm and InAs@ZnSe QDs with PL emission extending to 1400 nm with a PLQY of 23%, record values for amino-As-derived InAs QDs in this spectral region.

Overall, the results presented in this chapter demonstrate that the combination of TOA-AlH_3 and $ZnCl_2$ provides a powerful and versatile platform for the synthesis of high-quality InAs@ZnSe QDs with emission across the NIR–SWIR range. These findings significantly advance the synthetic chemistry of RoHS-compliant infrared emitters and open promising opportunities for their integration into next-generation infrared optoelectronic technologies.

3.5 Experimental Section

Chemicals

Indium(III) chloride ($InCl_3$, 99.999%, Sigma-Aldrich), zinc(II) chloride ($ZnCl_2$, 99.999%, Sigma-Aldrich), lithium aluminum hydride ($LiAlH_4$, 95%, Sigma-Aldrich), aluminum(III) chloride ($AlCl_3$, 99.999%, Sigma-Aldrich), tris(dimethylamino)arsine (amino-As, 99%, Strem), alane N,N-dimethylethylamine complex solution (DMEA-AlH_3, 0.5 M solution in toluene, Sigma-Aldrich), oleylamine (Olam, 98%, Sigma-Aldrich), 1-octadecene (ODE, 90%, Sigma-Aldrich), selenium powder (Se, 99.99%, Strem), tri-n-octylphosphine (TOP, 97%, Strem), trioctylamine (TOA, 98%, Sigma-Aldrich), toluene (anhydrous, 99.8%, Sigma-Aldrich), pentane (anhydrous, 99%, Sigma Aldrich), tetrachloroethylene (TCE, anhydrous, 99%, Sigma-Aldrich), ethanol (anhydrous, 99.8%, Sigma-Aldrich). All the chemicals were used without further purification. Olam, TOA and ODE were degassed at 120°C under vacuum for 1.5h before use.

Synthesis of the TOA-AlH_3 adduct.

In a 250mL flat-bottom Florence flask, 3.7g (28.3mmol) of $AlCl_3$, 3.6g (94.9mmol) of $LiAlH_4$ and 100mL of pentane were added. 40.6 mL (93 mmol) of TOA was then added dropwise to the reaction mixture to prevent a sudden rise in temperature. The flask was sealed to minimize solvent evaporation and stirred overnight. Upon completion of the reaction, the mixture was filtered using Whatman filter paper to remove unreacted residues. The filtrate was then degassed under vacuum to remove pentane, yielding pure TOA-AlH_3. The reducing agent was stored under an inert atmosphere in a glovebox at low temperatures (-20°C) for subsequent use. Prior to injection into the reaction mixture, TOA-AlH_3 was mixed with a high-boiling solvent such as ODE to ensure compatibility with high-temperature reaction conditions.

Preparation of $InCl_3$-Olam (0.2M) precursor

0.88g (4mmol) of $InCl_3$ and 20mL of Olam were taken in a three-neck flask. The mixture was degassed at 120°C for 30 min, then heated up to 250°C for additional 30 min until the solution became clear. Afterwards, the solution was cooled down to room temperature and stored under inert atmosphere for use in subsequent synthesis.

Preparation of amino-As precursor solution

Inside a N_2 filled glovebox, 0.2 mmol of amino-As was dissolved in 0.5 mL of degassed Olam (that is 0.4M) in a vial at 60°C for 5 min, until no further bubbles were observed. The amino-As solutions in Olam employed for the seeded growth approaches were prepared with the same procedure with the only difference being the molarity that was set to 0.1M.

Preparation of 0.8M $ZnCl_2$-Olam precursor

In a N_2 filled glovebox, 8 mmol of $ZnCl_2$ was dissolved in 10 mL of OLAM in a 20 mL glass vial by heating the mixture up to 250°C under constant stirring for 30 min. $ZnCl_2$-Olam solidifies at room temperature, therefore the solution must be heated up to 100 °C before use.

Preparation of 1.0M TOP-Se precursor

In a N_2 filled glovebox, 20 mmol of Se powder was mixed with 20 mL of TOP in a 40 mL glass vial and heated at 120°C under stirring for 30 min. The resulting solution was cooled down to room temperature.

One-pot hot-injection synthesis of InAs@ZnSe core@shell QDs emitting at 905nm or 1000nm

In a typical synthesis, 0.2 mmol of $InCl_3$ and 2 mmol of $ZnCl_2$ were weighed into a 50 mL three-neck round-bottom flask. Varying amounts of Olam (5 mL, 3.3 mL, or 2.5 mL) and ODE (0 mL, 5 mL, 6.7 mL, or 7.5 mL) were added to the flask. InAs825 was synthesized using 5 mL of Olam and 5 mL of ODE, while InAs935 was synthesized using 3.3 mL of Olam and 6.7 mL of ODE. The mixture was degassed at room temperature for 15 minutes, followed by degassing at 120°C for 1 hour under vacuum. The temperature was then raised to 240°C under a nitrogen atmosphere, and the As precursor was injected at this temperature. Upon injection, the reaction temperature momentarily dropped by ~5°C and recovered to 240°C within ~20 seconds. Subsequently, 0.8 mmol of TOA-AlH_3 dissolved in 5 mL of ODE was swiftly injected into the reaction mixture at 240°C, and the temperature was increased to 280°C at a rate of ~5°C/min. The reaction was allowed to proceed for 60 minutes before quenching by removing the heating mantle and cooling the mixture to 90°C.

For the ZnSe shell growth, 5.0 mL of 0.8 M $ZnCl_2$-OLAM and 7.5 mL of 1.0 M TOP-Se solutions were injected into the crude reaction mixture at 90°C, followed by heating to 300°C under an inert atmosphere. After 120 minutes, the reaction was quenched by removing the heating mantle, followed by the addition of 5 mL of toluene. The mixture was centrifuged at 4000 rpm to remove aggregates and agglomerates. The resulting supernatant was collected, and the QDs were precipitated by adding ethanol, followed by centrifugation at 3000 rpm. The QDs underwent two additional washing steps before being dispersed in TCE for further characterization. All washing steps were performed inside a nitrogen-filled glovebox.

Synthesis of InAs@ZnSe core@shell QDs via the seeded growth approach

InAs QDs were synthesized following the procedure employed to produce InAs935 QDs. After 60 minutes, upon completion of InAs QDs synthesis, the reaction temperature was lowered to 240°C. At this stage, 2mL, 3mL, 5mL or 7mL of 0.2M $InCl_3$-Olam solution was injected into the crude reaction mixture in order to grow InAs QDs larger (details in table below). Immediately afterwards, 4mL, 6mL, 10mL and 14mL of 0.1M amino-As solution along with equal volumes of 0.2M TOA-AlH_3 solution, were loaded into two syringes (20 mm in diameter) and connected to two syringe pumps for continuous injection (details in Table 3.6).

Table 3. 7. *Injection amounts (in mmol) of additional precursors ($InCl_3$, amino-As, and TOA-AlH_3) and continuous injection durations used in the seeded growth of InAs935 QDs to obtain larger QDs with red-shifted excitonic absorption features.*

Excitonic peak position (nm)	Equivalents of precursors added	Amount of In precursor (mmol)	Amount of As precursor (mmol)	Amount of TOA-AlH_3 (mmol)	Cont. Inj. duration (min)
1090	2	0.4	0.4	0.8	80
1170	3	0.6	0.6	1.2	120
1250	5	1.0	1.0	2.0	200
1340	7	1.4	1.4	2.8	280

The continuous injection of the two precursors was performed at 240°C with a rate of 0.05 mL/min (which is 0.005mmol/min and 0.01mmol/min with respect to amino-As and TOA-AlH_3, respectively). After both precursors were completely injected, the heating mantle was removed, and the reaction mixture was cooled down to room temperature using compressed air. The samples were washed by addition of 10 mL of toluene followed by centrifugation at 4000 rpm to remove undesired byproducts and aggregates. The supernatant was collected and washed via the addition of ethanol followed by centrifugation at 4000 rpm. The purified InAs QDs were dispersed in 10 mL of Olam and transferred to a 50 mL three-neck flask under an inert atmosphere. The mixture was degassed at room temperature for 30 minutes to remove residual toluene or ethanol. Subsequently, the temperature was raised to 90°C under N_2 atmosphere. At this stage, 7.5mL of 0.8M of $ZnCl_2$-Olam and 6.0mL of 1.0M TOP-Se solutions were injected into the reaction mixture and the corresponding mixture was heated up to 300°C under N_2 atmosphere. After 120 min, the reaction was quenched by removing the heating mantle. 5 mL of toluene was added to the reaction mixture, and the solution was centrifuged at 4000 rpm to remove any unreacted impurities. The supernatant was further washed twice with toluene and ethanol, followed by centrifugation at 3000 rpm. The purified InAs@ZnSe QDs were dispersed in TCE and stored under an inert atmosphere for further characterization.

Synthesis of InAs@ZnSe QDs without using $ZnCl_2$ as an additive

The synthesis was performed by replicating the synthetic procedure used for InAs935 QDs and InAs1170 QDs respectively, excluding $ZnCl_2$ from the synthesis scheme.

In a typical reaction, 0.2 mmol of $InCl_3$, 3.33 mL of Olam, and 6.67 mL of ODE were loaded into a 50 mL three-neck round-bottom flask under an inert atmosphere and the synthesis was carried out as previously described in the experimental section. For the ZnSe shell growth, 7.5 mL of 0.8 M $ZnCl_2$ and 6.0 mL of 1.0 M TOP-Se were injected after quenching the InAs QDs growth at 60 min by lowering the reaction temperature to 90°C, following the standard shell growth procedure.

For the seeded growth approach, we followed the synthesis procedure for InAs1170 described in the "*Synthesis of InAs@ZnSe Core@Shell QDs via the Seeded Growth Approach*" section of the experimental section, again without employing any $ZnCl_2$.

Aliquots were collected at 5, 15, 30, 60, 120, and 180 minutes during the shell growth reaction and quenched in toluene. Each aliquot was washed twice with toluene and ethanol, precipitated via centrifugation at 3000 rpm, and then dispersed in TCE for further characterization.

Nuclear Magnetic Resonance (NMR)

All the NMR experiment were performed at 298K on a Bruker Avance III 400 MHz spectrometer fitted with a TBO broadband probe. The lock engage, the matching and tuning, and the homogeneity were automatically adjusted; the 90-degree excitation pulse instead was optimized manually.

^{1}H NMR spectra were acquired after a 90-degree pulse, with 16 transients (2 dummy scans), an inter pulse delay of 30 s, 65536 digit points for FID, over a spectral width of 20.49 ppm, with the offset positioned at 6.18 ppm. An exponential function equivalent to 0.3 Hz was used to smooth the FIDs prior to the Fourier Transform.

^{13}C NMR spectra were acquired with after a 30-degree pulse, with 256 scans (4 steady transients), a relaxation delay of 2.1 s, 49152 digit points for FID, over a spectral width of 236,6 ppm, centered at 100 ppm. FIDs were smoothed by an exponential function equivalent to 1 Hz before the Fourier transform to be applied.

Two different 1% v/v solutions of trioctylamine (TOA) or TOA-AlH_3 in benzene d-6 were prepared inside a N_2 filled glovebox and used for the NMR measurements.

Quantitative ^{1}H NMR spectra were acquired after a 90 degree pulse optimization, and homogeneity adjustment[56], with 32 transients (without dummy scans), an inter pulse delay of 30 s, 65536 digit points for FID, over a spectral width of 20.49 ppm, with the offset positioned at 6.18 ppm. An exponential function equivalent to 0.3 Hz was employed to smooth the FIDs prior to the Fourier Transform (FT).

Inductively Coupled Plasma Optical Emission Spectroscopy (ICP-OES)

The elemental analyses were performed via inductively coupled plasma optical emission spectroscopy (ICP-OES) with iCAP 6300 DUO ICP-OES spectrometer (ThermoScientific). The samples were dissolved in 1 mL of aqua regia (HCl/HNO_3 volume ratio of 3/1) overnight, and then diluted with 9 ml of Milli-Q water for measurements. The elemental analysis using ICP-OES was affected by a systematic error of ~5%.

X-ray Diffraction (XRD)

XRD patterns were acquired using a PANalytical Empyrean X-ray diffractometer equipped with a 1.8 kW Cu Kα ceramic X-ray tube and a PIXcel3D 2×2 area detector, operating at 45 kV and 40

mA. Specimens for XRD measurements were prepared by depositing a concentrated QD solution onto a silicon zero-diffraction single-crystal substrate. The diffraction patterns were recorded under ambient conditions using a parallel beam geometry in symmetric reflection mode. XRD data analysis was performed using HighScore 4.1 software (PANalytical).

Transmission Electron Microscopy (TEM)

Diluted QDs solutions were drop-cast onto copper TEM grids with an ultrathin carbon film. Overview BF-TEM images were acquired on a JEOL JEM-1400Plus microscope with a thermionic gun (LaB_6) operated at an acceleration voltage of 120 kV. HRTEM images were acquired by an image-Cs-corrected JEM-2200FS, operated at 200 kV, using a direct-electron-detection camera (Gatan K2 Summit) at a comparatively low dose rate (about 30 $e^-/(s \cdot Å^2)$) so as to minimize carbon contamination. The images presented here were extracted from original $(280\ nm)^2$ frames, obtained by cross-correlated sum of 40 frames, each obtained with 0.3 s exposure. The HRTEM images shown here were Fourier-filtered, using an average background subtraction filter (ABSF)[57], to minimize the contribution to the contrast from the amorphous component. The peak pair analysis (PPA)[58] method was used to compute the mean dilation map from the HRTEM image of individual core-shell particles, with the aim of identifying the position of the InAs core and the strain within the ZnSe shell.

Optical Characterization

The absorption spectra were recorded using a Varian Cary 5000 UV-Vis-NIR spectrophotometer. The samples were prepared by diluting the QDs solution in 3mL of TCE in 1 cm path length quartz cuvettes, sealed with airtight screw caps, inside a N_2 filled glovebox. Aliquots were taken directly from the reaction mixture using a glass syringe, diluted with toluene, and their absorption was measured under ambient conditions. Steady-state and time-resolved PL measurements were conducted using an Edinburgh Instruments FLS900 fluorescence spectrometer. Steady-state PL excitation was performed with a xenon lamp and a monochromator, while time-resolved PL was measured using a time-correlated single-photon counting (TCSPC) unit coupled with an Edinburgh Instruments EPL-510 pulsed laser diode (λ_{ex} = 508.2 nm, pulse width = 177.0 ps). PLQY measurements were carried out using the same spectrometer equipped with an integrating sphere, with excitation at 700 nm from the Xe lamp output. All QD solutions were diluted to an optical density of ~0.1 at the excitation wavelength.

Precursor Chemistry

Indium(III) chloride in oleylamine

When indium(III) chloride ($InCl_3$) is dissolved in oleylamine, the strongly Lewis-acidic indium centers are rapidly coordinated by the amine, which donates its lone pair as an L-type ligand. This ligand-metal interaction disrupts the polymeric In-Cl-In framework of the solid and generates a soluble molecular adduct typically represented as $[InCl_x(Olam)_y]$.

Amino-As

This precursor consists of contains three small and volatile dimethylamino groups. Upon injection into a hot-precursor solution of oleylamine, the first transformation that occurs is a transamination reaction. This process is thermodynamically favored due to the volatility difference between the amines involved. Oleylamine, acting as a nucleophile, attacks the arsenic center and progressively displaces the dimethylamido groups. The displaced leaving group, dimethylamine has a low boiling point (~7°C) and volatilizes rapidly under the reaction conditions. According to Le Chatelier's principle, this irreversible loss of the gaseous byproduct drives the equilibrium completely to the right, converting the small, reactive $As(NMe_2)_3$molecule into the sterically bulky tris(oleylamino)arsine, $As(Olam)_3$.

Conversion into As^{3-}

Unlike $(TMS)_3As$, amino-As cannot generate As^{3-} on its own. Similar to amino-P, it lacks self-reducing capability and thus requires an external reducing agent to convert $As^{3\delta+}$ to As^{3-}. While the exact reduction mechanism remains unclear, it is speculated to proceed via two possible pathways based on indirect evidence.

The first way is the reduction of $As^{3\delta+}$ to As^{3-}, which is facilitated by hydride ions (H^-) from the reducing agent. A hydride is effectively a proton carrying two electrons ($H^+ + 2e^-$), and when H^- attacks $As^{3\delta+}$, it donates electron density, reducing the arsenic center.

The second mechanistic way is not a simple electron transfer, rather a **σ-bond metathesis** mechanism. The reaction begins with coordination of the aluminum center in AlH_3 (a strong Lewis acid) to the nitrogen lone pairs of the As precursor, weakening the As-N bonds. A four-membered transition state then facilitates a concerted ligand exchange, in which a hydride ion (H^-) is transferred from Al to As, while an amido group (NR_2^-) simultaneously migrates to Al. This process is thermodynamically driven by the formation of strong Al-N bonds, which act as a thermodynamic sink. The net result is progressive replacement of amido ligands on arsenic with hydrides, forming reactive intermediates such as $H\text{-}As(NR_2)_2$ and ultimately arsine equivalents (AsH_3) that can combine with In^{3+} to nucleate InAs.

$$As(NR_2)_3 + H^- \rightarrow H\text{-}As(NR_2)_2 + (NR_2)^-$$

$$H\text{-}As(NR_2)_2 + H^- \rightarrow H_2\text{-}As(NR_2) + (NR_2)^-$$

$$H_2\text{-}As(NR_2) + H^- \rightarrow AsH_3 + (NR_2)^-$$

The Zinc precursor

The dissolution of zinc(II) chloride ($ZnCl_2$) in oleylamine leads to the formation of a well-defined coordination complex [$ZnCl_2(Olam)_x$] that remains structurally stable and can serve as a soft template for subsequent material growth. In analogous systems using shorter-chain amines such as octylamine, this Zn-amine adduct can even be isolated as a white crystalline solid[59].

The Selenium precursor

When elemental selenium is introduced into TOP, the phosphine acts as a strong nucleophile whose lone pair attacks the chalcogen-chalcogen σ* antibonding orbitals in the polymeric Se_n chains. This donor-acceptor interaction weakens and cleaves the Se-Se bonds, enabling phosphorus to insert into the chalcogen network and generate monomeric phosphine chalcogenide units. Once the R_3P-Se fragment is formed, a filled p orbital on the selenium donates electron density into an empty acceptor orbital on phosphorus, establishing a pπ-dπ dative π interaction. This π donation shortens and strengthens the P-Se linkage and yields the formal P=Se double bond notation, although the resulting bond remains highly polarized and nonclassical in character[60, 61].

Formation of ZnSe

When the $ZnCl_2$-Olam precursor and the TOP-Se precursor are mixed at high reaction temperatures, the two form a transient adduct. Oleylamine then functions as a nucleophile, with its nitrogen lone pair attacking the electrophilic phosphorus center of the $ZnCl_2$-activated TOP-Se complex[62]. Although alkylamines are generally weaker nucleophiles compared to oxygenated ligands, the strong Lewis acidity of $ZnCl_2$ sufficiently activates the P-Se bond, allowing oleylamine to cleave it effectively at elevated temperatures. This nucleophilic addition initiates a concerted process in which the P-Se bond breaks and a ZnSe monomer is released. Oleylamine then acts as a Bronsted base in the second step, neutralizing liberated chloride ions through protonation to form oleylammonium chloride ($RNH_3^+Cl^-$). In addition to oleylammonium chloride, the reaction produces amino-substituted trioctylphosphine species, including iminophosphoranes (TOP=NR) and aminophosphonium chloride salts (TOP(NHR)Cl)[62].

3.6 References

1. Chen, J.; Zheng, S.; Jia, D.; Liu, W.; Andruszkiewicz, A.; Qin, C.; Yu, M.; Liu, J.; Johansson, E. M. J.; Zhang, X., Regulating Thiol Ligands of p-Type Colloidal Quantum Dots for Efficient Infrared Solar Cells. *ACS Energy Letters* **2021,** *6* (5), 1970-1979.
2. Müller, T.; Skiba-Szymanska, J.; Krysa, A. B.; Huwer, J.; Felle, M.; Anderson, M.; Stevenson, R. M.; Heffernan, J.; Ritchie, D. A.; Shields, A. J., A quantum light-emitting diode for the standard telecom window around 1,550 nm. *Nat Commun* **2018,** *9* (1), 862.
3. Liu, S.; Xiong, K.; Wang, K.; Liang, G.; Li, M.-Y.; Tang, H.; Yang, X.; Huang, Z.; Lian, L.; Tan, M.; Wang, K.; Gao, L.; Song, H.; Zhang, D.; Gao, J.; Lan, X.; Tang, J.; Zhang, J., Efficiently Passivated PbSe Quantum Dot Solids for Infrared Photovoltaics. *ACS Nano* **2021,** *15* (2), 3376-3386.
4. Song, J. H.; Choi, H.; Pham, H. T.; Jeong, S., Energy level tuned indium arsenide colloidal quantum dot films for efficient photovoltaics. *Nat Commun* **2018,** *9* (1), 4267.
5. Geiregat, P.; Houtepen, A. J.; Sagar, L. K.; Infante, I.; Zapata, F.; Grigel, V.; Allan, G.; Delerue, C.; Van Thourhout, D.; Hens, Z., Continuous-wave infrared optical gain and amplified spontaneous emission at ultralow threshold by colloidal HgTe quantum dots. *Nature Materials* **2018,** *17* (1), 35-42.
6. Christodoulou, S.; Ramiro, I.; Othonos, A.; Figueroba, A.; Dalmases, M.; Özdemir, O.; Pradhan, S.; Itskos, G.; Konstantatos, G., Single-Exciton Gain and Stimulated Emission Across the Infrared Telecom Band from Robust Heavily Doped PbS Colloidal Quantum Dots. *Nano Letters* **2020,** *20* (8), 5909-5915.
7. Allen, P. M.; Liu, W.; Chauhan, V. P.; Lee, J.; Ting, A. Y.; Fukumura, D.; Jain, R. K.; Bawendi, M. G., InAs(ZnCdS) Quantum Dots Optimized for Biological Imaging in the Near-Infrared. *J. Am. Chem. Soc.* **2010,** *132* (2), 470-471.
8. Franke, D.; Harris, D. K.; Chen, O.; Bruns, O. T.; Carr, J. A.; Wilson, M. W. B.; Bawendi, M. G., Continuous injection synthesis of indium arsenide quantum dots emissive in the short-wavelength infrared. *Nat Commun* **2016,** *7* (1), 12749.
9. Goossens, S.; Navickaite, G.; Monasterio, C.; Gupta, S.; Piqueras, J. J.; Pérez, R.; Burwell, G.; Nikitskiy, I.; Lasanta, T.; Galán, T.; Puma, E.; Centeno, A.; Pesquera, A.; Zurutuza, A.; Konstantatos, G.; Koppens, F., Broadband image sensor array based on graphene–CMOS integration. *Nature Photonics* **2017,** *11* (6), 366-371.
10. Pradhan, S.; Di Stasio, F.; Bi, Y.; Gupta, S.; Christodoulou, S.; Stavrinadis, A.; Konstantatos, G., High-efficiency colloidal quantum dot infrared light-emitting diodes via engineering at the supra-nanocrystalline level. *Nature Nanotech* **2019,** *14* (1), 72-79.
11. Takemoto, K.; Takatsu, M.; Hirose, S.; Yokoyama, N.; Sakuma, Y.; Usuki, T.; Miyazawa, T.; Arakawa, Y., An optical horn structure for single-photon source using quantum dots at telecommunication wavelength. *Journal of Applied Physics* **2007,** *101* (8), 081720.
12. Vasilopoulou, M.; Fakharuddin, A.; García de Arquer, F. P.; Georgiadou, D. G.; Kim, H.; Mohd Yusoff, A. R. b.; Gao, F.; Nazeeruddin, M. K.; Bolink, H. J.; Sargent, E. H., Advances in solution-processed near-infrared light-emitting diodes. *Nature Photonics* **2021,** *15* (9), 656-669.
13. Rogalski, A., Infrared detectors: status and trends. *Progress in Quantum Electronics* **2003,** *27* (2), 59-210.

14. Kumar, S.; Pradhan, S., Colloidal Quantum Dot-Based Near and Shortwave Infrared Light Emitters: Recent Developments and Application Prospects. *Advanced Optical Materials* **2024,** *12* (n/a), 2400993.
15. De Franco, M.; Zhu, D.; Asaithambi, A.; Prato, M.; Charalampous, E.; Christodoulou, S.; Kriegel, I.; De Trizio, L.; Manna, L.; Bahmani Jalali, H.; Di Stasio, F., Near-Infrared Light-Emitting Diodes Based on RoHS-Compliant InAs/ZnSe Colloidal Quantum Dots. *ACS Energy Letters* **2022,** *7* (11), 3788-3790.
16. Roshan, H.; Zhu, D.; Piccinotti, D.; Dai, J.; De Franco, M.; Barelli, M.; Prato, M.; De Trizio, L.; Manna, L.; Di Stasio, F., Near Infrared Light-Emitting Diodes Based on Colloidal InAs/ZnSe Core/Thick-Shell Quantum Dots. *Advanced Science* **2024,** *11* (23), 2400734.
17. Schubert, J.; Riley, E. J.; Tyler, S. A., Combined effects in toxicology-a rapid systematic testing procedure: Cadmium, mercury, and lead. *Journal of Toxicology and Environmental Health* **1978,** *4* (5-6), 763-776.
18. Sobhanan, J.; Jones, P.; Kohara, R.; Sugino, S.; Vacha, M.; Subrahmanyam, C.; Takano, Y.; Lacy, F.; Biju, V., Toxicity of nanomaterials due to photochemical degradation and the release of heavy metal ions. *Nanoscale* **2020,** *12* (43), 22049-22058.
19. Keuleyan, S.; Lhuillier, E.; Guyot-Sionnest, P., Synthesis of Colloidal HgTe Quantum Dots for Narrow Mid-IR Emission and Detection. *J. Am. Chem. Soc.* **2011,** *133* (41), 16422-16424.
20. Bansal, A. K.; Antolini, F.; Zhang, S.; Stroea, L.; Ortolani, L.; Lanzi, M.; Serra, E.; Allard, S.; Scherf, U.; Samuel, I. D. W., Highly Luminescent Colloidal CdS Quantum Dots with Efficient Near-Infrared Electroluminescence in Light-Emitting Diodes. *The Journal of Physical Chemistry C* **2016,** *120* (3), 1871-1880.
21. McDonald, S. A.; Konstantatos, G.; Zhang, S.; Cyr, P. W.; Klem, E. J. D.; Levina, L.; Sargent, E. H., Solution-processed PbS quantum dot infrared photodetectors and photovoltaics. *Nature Materials* **2005,** *4* (2), 138-142.
22. Pietryga, J. M.; Schaller, R. D.; Werder, D.; Stewart, M. H.; Klimov, V. I.; Hollingsworth, J. A., Pushing the Band Gap Envelope: Mid-Infrared Emitting Colloidal PbSe Quantum Dots. *J. Am. Chem. Soc.* **2004,** *126* (38), 11752-11753.
23. European Union. Directive 2011/65/EU of the European Parliament and of the Council of 8 June 2011 on the Restriction of the Use of Certain Hazardous Substances in Electrical and Electronic Equipment (consolidated version 2025). EUR-Lex. https://eur-lex.europa.eu/legal-content/EN/TXT/?uri=CELEX:02011L0065-20250101.
24. George, E.; Pecht, M., RoHS compliance in safety and reliability critical electronics. *Microelectronics Reliability* **2016,** *65*, 1-7.
25. Gensch, C.-O.; Baron, Y.; Blepp, M.; Deubzer, O., Assistance to the Commission on Technological Socio-Economic and Cost-Benefit Assessment Related to Exemptions from the Substance Restrictions in Electrical and Electronic Equipment (RoHS Directive). *Öko-Institut eV, Freiburg, Germany* **2016**.
26. Ma, Y.; Zhang, Y.; Yu, W. W., Near infrared emitting quantum dots: synthesis, luminescence properties and applications. *Journal of Materials Chemistry C* **2019,** *7* (44), 13662-13679.
27. Yang, L.; Zhang, S.; Xu, B.; Jiang, J.; Cai, B.; Lv, X.; Zou, Y.; Fan, Z.; Yang, H.; Zeng, H., I–III–VI Quantum Dots and Derivatives: Design, Synthesis, and Properties for Light-Emitting Diodes. *Nano Letters* **2023,** *23* (7), 2443-2453.

28. Mir, W. J.; Sheikh, T.; Nematulloev, S.; Maity, P.; Yorov, K. E.; Emwas, A.-H.; Hedhili, M. N.; Khan, M. S.; Abulikemu, M.; Mohammed, O. F.; Bakr, O. M., One-Pot Colloidal Synthesis Enables Highly Tunable InSb Short-Wave Infrared Quantum Dots Exhibiting Carrier Multiplication. *Small* **2024,** *20* (19), 2306535.
29. Asor, L.; Liu, J.; Xiang, S.; Tessler, N.; Frenkel, A. I.; Banin, U., Zn-Doped P-Type InAs Nanocrystal Quantum Dots. *Advanced Materials* **2023,** *35* (5), 2208332.
30. Darwan, D.; Lim, L. J.; Wang, T.; Wijaya, H.; Tan, Z.-K., Ultra-Confined Visible-Light-Emitting Colloidal Indium Arsenide Quantum Dots. *Nano Letters* **2021,** *21* (12), 5167-5172.
31. Franke, D.; Harris, D. K.; Xie, L.; Jensen, K. F.; Bawendi, M. G., The unexpected influence of precursor conversion rate in the synthesis of III–V quantum dots. *Angewandte Chemie* **2015,** *127* (48), 14507-14511.
32. Schileo, G.; Grancini, G., Lead or no lead? Availability, toxicity, sustainability and environmental impact of lead-free perovskite solar cells. *Journal of Materials Chemistry C* **2021,** *9* (1), 67-76.
33. Battaglia, D.; Peng, X., Formation of High Quality InP and InAs Nanocrystals in a Noncoordinating Solvent. *Nano Letters* **2002,** *2* (9), 1027-1030.
34. Tamang, S.; Lee, S.; Choi, H.; Jeong, S., Tuning Size and Size Distribution of Colloidal InAs Nanocrystals via Continuous Supply of Prenucleation Clusters on Nanocrystal Seeds. *Chemistry of Materials* **2016,** *28* (22), 8119-8122.
35. Kim, T.; Park, S.; Jeong, S., Diffusion dynamics controlled colloidal synthesis of highly monodisperse InAs nanocrystals. *Nat Commun* **2021,** *12* (1), 3013.
36. Sheikh, T.; Mir, W. J.; Nematulloev, S.; Maity, P.; Yorov, K. E.; Hedhili, M. N.; Emwas, A.-H.; Khan, M. S.; Abulikemu, M.; Mohammed, O. F.; Bakr, O. M., InAs Nanorod Colloidal Quantum Dots with Tunable Bandgaps Deep into the Short-Wave Infrared. *ACS Nano* **2023,** *17* (22), 23094-23102.
37. Leemans, J.; Respekta, D.; Bai, J.; Braeuer, S.; Vanhaecke, F.; Hens, Z., Formation of Colloidal In(As,P) Quantum Dots Active in the Short-Wave Infrared, Promoting Growth through Temperature Ramps. *ACS Nano* **2023,** *17* (20), 20002-20012.
38. Bahmani Jalali, H.; De Trizio, L.; Manna, L.; Di Stasio, F., Indium arsenide quantum dots: an alternative to lead-based infrared emitting nanomaterials. *Chemical Society Reviews* **2022,** *51* (24), 9861-9881.
39. Liu, Z.; Pascazio, R.; Goldoni, L.; Maggioni, D.; Zhu, D.; Ivanov, Y. P.; Divitini, G.; Camarelles, J. L.; Jalali, H. B.; Infante, I.; De Trizio, L.; Manna, L., Colloidal InAs Tetrapods: Impact of Surfactants on the Shape Control. *J. Am. Chem. Soc.* **2023,** *145* (33), 18329-18339.
40. Srivastava, V.; Dunietz, E.; Kamysbayev, V.; Anderson, J. S.; Talapin, D. V., Monodisperse InAs Quantum Dots from Aminoarsine Precursors: Understanding the Role of Reducing Agent. *Chemistry of Materials* **2018,** *30* (11), 3623-3627.
41. Srivastava, V.; Janke, E. M.; Diroll, B. T.; Schaller, R. D.; Talapin, D. V., Facile, Economic and Size-Tunable Synthesis of Metal Arsenide Nanocrystals. *Chemistry of Materials* **2016,** *28* (18), 6797-6802.
42. Zhu, D.; Bahmani Jalali, H.; Saleh, G.; Di Stasio, F.; Prato, M.; Polykarpou, N.; Othonos, A.; Christodoulou, S.; Ivanov, Y. P.; Divitini, G.; Infante, I.; De Trizio, L.; Manna, L., Boosting the Photoluminescence Efficiency of InAs Nanocrystals Synthesized with Aminoarsine via a ZnSe Thick-Shell Overgrowth. *Advanced Materials* **2023,** *35* (38), 2303621.

43. Zhu, D.; Bellato, F.; Bahmani Jalali, H.; Di Stasio, F.; Prato, M.; Ivanov, Y. P.; Divitini, G.; Infante, I.; De Trizio, L.; Manna, L., ZnCl2 Mediated Synthesis of InAs Nanocrystals with Aminoarsine. *J. Am. Chem. Soc.* **2022,** *144* (23), 10515-10523.
44. Grigel, V.; Dupont, D.; De Nolf, K.; Hens, Z.; Tessier, M. D., InAs Colloidal Quantum Dots Synthesis via Aminopnictogen Precursor Chemistry. *J. Am. Chem. Soc.* **2016,** *138* (41), 13485-13488.
45. Skorotetcky, M. S.; Mir, W. J.; Sheikh, T.; Yorov, K. E.; Saidzhonov, B. M.; Daws, S.; Zhou, R.; Hedhili, M. N.; Abulikemu, M.; Mohammed, O. F.; Bakr, O. M., Si-H Hydrosilane Reducing Agents for Size- and Shape-Controlled InAs Colloidal Quantum Dots. *Advanced Materials* **2024,** *37* (n/a), 2412105.
46. Ginterseder, M.; Franke, D.; Perkinson, C. F.; Wang, L.; Hansen, E. C.; Bawendi, M. G., Scalable Synthesis of InAs Quantum Dots Mediated through Indium Redox Chemistry. *J. Am. Chem. Soc.* **2020,** *142* (9), 4088-4092.
47. Sagar, L. K.; Bappi, G.; Johnston, A.; Chen, B.; Todorović, P.; Levina, L.; Saidaminov, M. I.; García de Arquer, F. P.; Nam, D.-H.; Choi, M.-J.; Hoogland, S.; Voznyy, O.; Sargent, E. H., Suppression of Auger Recombination by Gradient Alloying in InAs/CdSe/CdS QDs. *Chemistry of Materials* **2020,** *32* (18), 7703–7709.
48. Liu, Z.; Llusar, J.; Karakkal, H. H.; Zhu, D.; Ivanov, Y. P.; Prato, M.; Divitini, G.; Brovelli, S.; Infante, I.; De Trizio, L.; Manna, L., Amino-Arsine and Amino-Phosphine Based Synthesis of InAs@InP@ZnSe core@shell@shell Quantum Dots. *Advanced Energy Materials* **2024,** *14* (47), 2402246.
49. Kim, M.; Lee, J.; Jung, J.; Shin, D.; Kim, J.; Cho, E.; Xing, Y.; Jeong, H.; Park, S.; Oh, S. H.; Kim, Y.-H.; Jeong, S., Surface-Originated Weak Confinement in Tetrahedral Indium Arsenide Quantum Dots. *J. Am. Chem. Soc.* **2024,** *146* (15), 10251-10256.
50. Humphries, T. D.; Munroe, K. T.; Decken, A.; McGrady, G. S., Lewis base complexes of AlH3: prediction of preferred structure and stoichiometry. *Dalton Transactions* **2013,** *42* (19), 6965-6978.
51. Wider, G.; Dreier, L., Measuring Protein Concentrations by NMR Spectroscopy. *J. Am. Chem. Soc.* **2006,** *128* (8), 2571-2576.
52. An, J. M.; Franceschetti, A.; Zunger, A., The Excitonic Exchange Splitting and Radiative Lifetime in PbSe Quantum Dots. *Nano Letters* **2007,** *7* (7), 2129-2135.
53. Du, H.; Chen, C.; Krishnan, R.; Krauss, T. D.; Harbold, J. M.; Wise, F. W.; Thomas, M. G.; Silcox, J., Optical Properties of Colloidal PbSe Nanocrystals. *Nano Letters* **2002,** *2* (11), 1321-1324.
54. Hours, J.; Senellart, P.; Peter, E.; Cavanna, A.; Bloch, J., Exciton radiative lifetime controlled by the lateral confinement energy in a single quantum dot. *Physical Review B* **2005,** *71* (16), 161306.
55. Zhu, D.; Llusar, J.; Asaithambi, A.; Liu, Z.; Bes, R.; Prieur, D.; Karakkal, H. H.; Prato, M.; Brovelli, S.; Saleh, G.; Panda, S.; Infante, I.; De Trizio, L.; Manna, L., Unveiling the Role of ZnCl2 in Enhancing the Photoluminescence Efficiency of Amino-As-Based InAs@ZnSe Quantum Dots. *ACS Nano* **2025,** *19* (39), 34807-34818.
56. Wu, P. S. C.; Otting, G., Rapid pulse length determination in high-resolution NMR. *Journal of Magnetic Resonance* **2005,** *176* (1), 115-119.
57. Kilaas, R., Optimal and near-optimal filters in high-resolution electron microscopy. *Journal of Microscopy* **1998,** *190* (1-2), 45-51.

58. Galindo, P. L.; Kret, S.; Sanchez, A. M.; Laval, J.-Y.; Yáñez, A.; Pizarro, J.; Guerrero, E.; Ben, T.; Molina, S. I., The Peak Pairs algorithm for strain mapping from HRTEM images. *Ultramicroscopy* **2007,** *107* (12), 1186-1193.
59. Dai, L.; Lesyuk, R.; Karpulevich, A.; Torche, A.; Bester, G.; Klinke, C., From Wurtzite Nanoplatelets to Zinc Blende Nanorods: Simultaneous Control of Shape and Phase in Ultrathin ZnS Nanocrystals. *The Journal of Physical Chemistry Letters* **2019,** *10* (14), 3828-3835.
60. Zhang, T.; Schwedtmann, K.; Weigand, J. J.; Doert, T.; Ruck, M., Dissolution behaviour and activation of selenium in phosphonium based ionic liquids. *Chemical Communications* **2017,** *53* (54), 7588-7591.
61. Krutin, D. V.; Zakharov, A. S.; Tupikina, E. Y.; Mulloyarova, V. V., Unveiling the electronic structure peculiarities of phosphine selenides as NMR probes for non-covalent interactions: an experimental and theoretical study. *Physical Chemistry Chemical Physics* **2024,** *26* (30), 20450-20461.
62. Mingabudinova, L.; Giordano, L.; Tessier, M. D.; Hens, Z.; Schiettecatte, P., Mechanistic study of ZnSe nanocrystal formation from zinc halides. *The Journal of Chemical Physics* **2023,** *158* (22).

3.7 Appendices

A 3.1. Size Distribution curves calculated from the TEM images using ImageJ software.

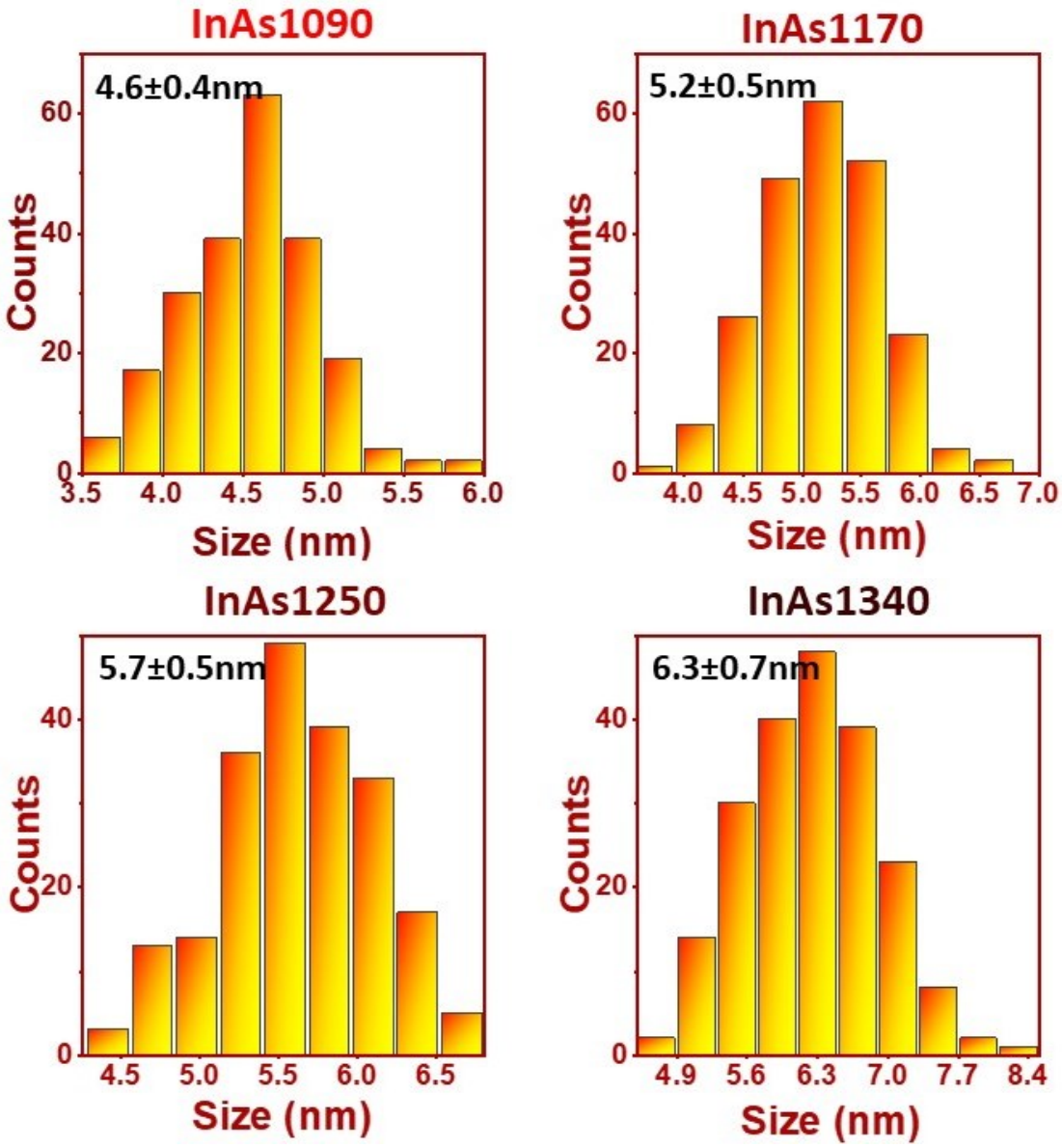

Figure A 3.1. Size distribution histograms for the (a) InAs1090, (b) InAs1170, (c) InAs1250 and (d) InAs1340 QD samples calculated by measuring the height of the tetrahedral QDs from the HAADF-STEM images.

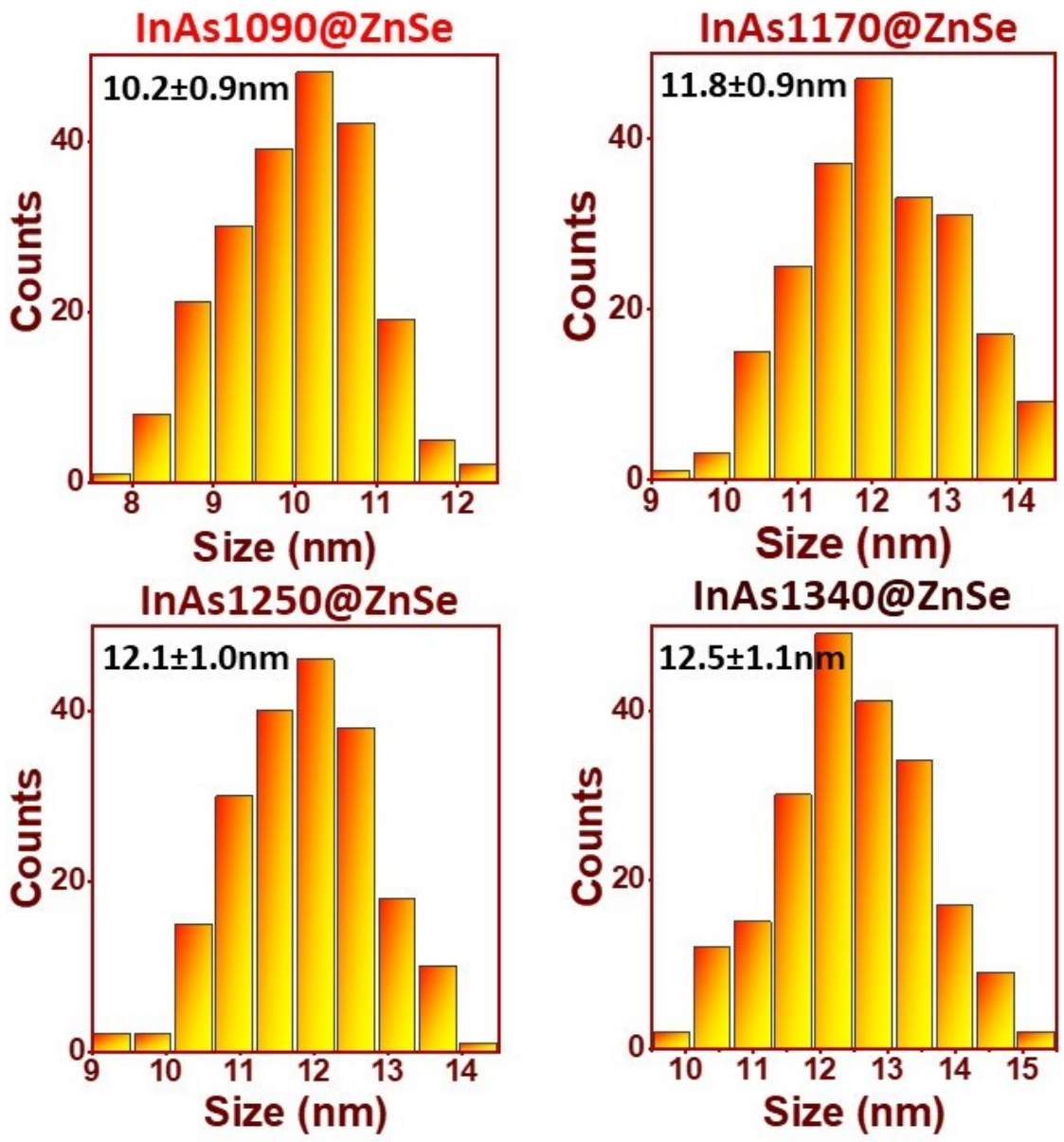

Figure A 3.2. Size distribution histograms for the (a) InAs1090@ZnSe, (b) InAs1170@ZnSe, (c) InAs1250@ZnSe and (d) InAs1340@ZnSe calculated from the TEM images reported in Figure 3.3.21.

A 3.2. Determination of number of monolayers in experimental samples through atomistic models.

To estimate the number of ZnSe monolayers forming the shell, we followed a procedure similar to that employed in a previous work from our group (see Note S2 of ref. [42] the latter hereinafter referred to as the "CS23 model". For the core, we used an atomistic structure that is less truncated compared to the one used in the CS23 model. This choice was made to better match the TEM images (e.g., Figure 3.3.17), which show QDs in the form of nearly untruncated tetrahedra, as inferred from the measured tetrahedral heights. With the adopted shape, the atomistic models could assume the following heights: 3.60 nm, 4.49 nm, 5.38 nm, 6.27 nm, 7.17 nm, 8.06 nm, etc. To determine the number of ZnSe monolayers, we followed the same procedure as in the CS23 model, specifically:

- The composition, and consequently the elemental ratios, were determined using non-truncated tetrahedra for simplicity. We consider the contribution of atoms located at the edges to be negligible; importantly, the error introduced by this approximation is expected to largely cancel out when calculating elemental ratios.

- The thickness of the each monolayer was determined as 2.5 times the lattice spacing of InAs along the {111} direction, as discussed in Note S2 and Figure S5 of ref. [42]
- In agreement with the findings of density functional theory (DFT) simulations, we deemed the first shell layer, the so-called interlayer, contains 15% of In and 15% of cation vacancies.[42] Moreover, the external layer of ZnSe contains 10% of cation vacancies. Note however that these are fine details, they change the elemental ratios by less than 10%.
- Importantly, matching the experimentally determined elemental ratios was only possible by assuming that a certain fraction of In was also present in the shell. We assumed that for every two In atoms, three Zn atoms were removed, based on quantum chemical simulations from ref.[42], which indicated that in the In-Zn-Se interlayers, In substitutes Zn and a cation vacancy is created for every two Zn-to-In cation substitutions. This assumption is also consistent with the generally observed increase in the In/As ratio as the shell thickness increases (see Table 1 of ref.[42] and Table A 3.1).

A 3. 1. *Determination of the number of ZnSe monolayers (MLs) in the shell of InAs@ZnSe QDs through the atomistic models (no quantum chemical simulations performed).*

Sample		ZnSe MLs	Core size (nm)	Total size (nm)	% In in shell	Zn/In ratio	In/As ratio	Zn/As ratio	Se/In ratio
InAs935	Model	6	3.60	8.57	3	10.27	1.84	18.85	10.40
	Exptl.	-[a]	3.7 ± 0.4	9.9 ± 0.7	-[a]	9.69	2.02	19.57	10.69
InAs1090	Model	6	4.49	9.46	9	4.49	2.31	10.36	5.09
	Exptl.	-[a]	4.6 ± 0.4	10.2 ± 0.9	-[a]	5.36	1.71	9.17	4.82
InAs1170	Model	6	5.38	10.35	5	4.93	1.56	7.70	5.22
	Exptl.	-[a]	5.2 ± 0.5	11.8 ± 0.9	-[a]	5.15	1.64	8.55	4.71
InAs1250	Model[b]	6-7	5.8	11.2	5	4.94	1.53	7.58	5.24
	Exptl.	-[a]	5.7 ± 0.5	12.1 ± 1.0	-[a]	4.99	1.52	7.59	4.87
InAs1340	Model	8	6.27	12.90	5	5.85	1.63	9.53	4.89
	Exptl.	-[a]	6.3 ± 0.7	12.5 ± 1.1	-[a]	5.95	1.48	8.80	5.09

[a] the number of ZnSe MLs and the In content of the shell are information not directly accessible from the experiment: they were determined through the model.

[b] in this sample, we found that the results could be fitted considering either an InAs core with a size of 5.38 nm and 6 ZnSe MLs, or a 6.27 nm InAs core with a 7 ZnSe MLs shell.

Chapter 4. Conclusions and Outlook

4.1 Conclusions

This thesis advances the synthesis of InAs quantum dots by modifying and refining the two major arsenic-based precursor routes. Through these developments, we were able to address long-standing challenges inherent to each synthetic approach and provide new mechanistic insights and methodologies that significantly improve the quality, reproducibility, and scalability of InAs QDs for short-wave infrared (SWIR) applications.

The first major contribution of this thesis is the modification of the most widely adopted synthesis procedure, which relies on tris(trimethylsilyl)arsine coupled with a secondary amine, namely dioctylamine, which modulates the reactivity of the former, and on a carboxylic acid, which acts as a surfactant. A key intrinsic limitation of this route is the reaction of the secondary amine with the carboxylic acid at high temperature, leading to the formation of water in the reaction environment. Through mechanistic analysis and supporting spectroscopic evidence, we proved the formation of water during the synthesis and we have ascertained that it does not react with InAs QDs forming any (surface) oxide. On the other hand, we discovered that the generated water reacts with TMS-based moieties producing TMS-OH, TMS-O-TMS and TMS-OLAc, which complicate QDs purification, often leading to material loss or to QD products containing a large fraction of organic residues. To overcome these issues, we replaced the secondary amine with a tertiary amine (i.e. trioctylamine), which, being not able to react with carboxylic acids, suppresses water formation and prevents the associated side reactions. Upon further optimization of reaction conditions, this modified approach yielded InAs QDs with excitonic absorption tunable up to 1100 nm with half-width-at-half-maximum values around 50 meV, and peak-to-valley ratios exceeding 2, representing record optical figures of merit for colloidal InAs QDs.

In the second part of this thesis (Chapter 3), we focused on one of the most promising As precursors, alternative to TMS-As, namely tris(dimethylamino)arsine (amino-As), which is non-pyrophoric, inexpensive, and commercially accessible. When employing this precursor to synthesize InAs QDs, the reaction kinetics are heavily dictated by the reducing agent which serves to reduce As3+, present in amino-As, to As3-. Commercially available reducing agents are either low boiling compounds or they are supplied in low-boiling solvents that vigorously boil at the high temperature required for the InAs QDs synthesis, causing unstable reaction conditions and limiting scalability and reproducibility. We addressed these issues by synthesizing a new reducing agent, namely trioctylamine-alane (TOA-AlH_3), which thermally decomposes releasing the AlH3 moiety (responsible of the $As^{3+} \rightarrow As^{3-}$ reduction) and trioctylamine, a compound with a high boiling point (i.e., 365°C), providing a stable, thermally robust reaction environment. Using TOA-AlH_3 in both hot-injection and seeded-growth synthesis routes, we could grow large InAs QDs with excitonic absorption tunable to ~1340 nm. Subsequent ZnSe shell growth yielded record photoluminescence quantum yields ranging from 60% at 1000 nm to 23% at 1430 nm.

Importantly, TOA-AlH_3 is fully compatible with $ZnCl_2$, a crucial additive for achieving high luminescence.

Overall, the advances presented in this thesis provide a unified framework for synthesizing high-quality InAs QDs through a deeper understanding of precursor chemistry, synthesis strategies, and reaction dynamics. By resolving key limitations in both the $(TMS)_3$-As and amino-As routes, this work establishes reliable and scalable methods for producing SWIR-active nanocrystals with record optical properties in both absorption and emission. The mechanistic insights and synthetic innovations developed here lay the foundation for future advances and further position colloidal InAs QDs as a promising platform for next-generation infrared optoelectronic technologies.

4.2 Outlook

4.2.1 From a device perspective

Through the synthesis modifications introduced in this thesis, we established a $(TMS)_3$-As based route to InAs QDs with excellent optical quality, peak-to-valley ratios exceeding 2, which already approach the figures of merit required for high-performance photodetectors. However, as-synthesized InAs QDs prepared via this route remain highly insulating due to their native long-chain ligand shell. A natural next step is therefore to develop ligand chemistries that preserve or minimally compromise the optical quality while rendering these QDs electrically conductive and compatible with device integration. This includes exploring compact inorganic or hybrid ligand systems, optimizing ligand-exchange protocols to avoid aggregation, and understanding how ligand coordination affects carrier mobility, and stability under electrical bias.

The InAs@ZnSe QDs developed via the amino-As-based synthetic platform exhibit record PLQYs in the SWIR spectral range, making them strong candidates for emissive device applications. Building on this foundation, an important future direction is the realization of SWIR light-emitting diodes (LEDs) based on these nanocrystals. This will require the translation of the colloidal synthesis into device-quality films with controlled thickness, minimized trap densities, and balanced charge injection. The combination of high PLQY, tunable emission, and improved synthetic control achieved in this work provides a promising starting point for demonstrating some of the first SWIR LEDs based on amino-As-derived InAs QDs.

4.2.2 From the materials perspective

One of the key challenges that remains for InAs@ZnSe core-shell systems is the relatively large lattice mismatch between InAs and ZnSe. Although ZnSe is an effective type-I shell for enhancing PLQY, its ~6.5% mismatch with InAs generates substantial interfacial compressive strain during shell growth. This strain increases with core size and can disrupt epitaxy, leading to structural defects that ultimately limit the optical performance of large InAs QDs. As interfacial strain energy grows with surface area, it becomes increasingly difficult to accommodate in larger cores, resulting in defects at the interface and a corresponding decline in PLQY.

A promising direction is the exploration of intermediate buffer layers with lattice parameters closely matched to InAs. Such layers could effectively mitigate strain before the deposition of wider-bandgap shells, improving strain relaxation and reducing the formation of interfacial trap states, thereby enhancing optical performance.

Another direction is the development of graded core-shell structures, where the shell composition is progressively varied from the core to the outer shell. This approach distributes lattice mismatch over multiple interfaces, reducing local strain and enabling the growth of thicker, defect-free shells. The design of such strain-engineered heterostructures represents a significant opportunity for achieving strong carrier confinement and high radiative efficiency across the SWIR range.

Beyond lattice mismatch, long-term stability remains a major bottleneck for the deployment of InAs-based nanocrystals in practical devices. Both bare and core/shell InAs QDs are susceptible to oxidative degradation, ligand desorption, and thermally or electrically induced surface reconstruction under ambient and operational conditions, which can introduce trap states and accelerate PL quenching. A rational route to address these limitations is the design of robust multishell architectures that combine lattice, electronic, and chemical passivation. In this context, overcoating InAs@ZnSe with an additional Zn(Se,S) or ZnS shell would introduce a wider-bandgap, chemically inert outer layer that more effectively blocks oxygen and moisture, stabilizes the ligand shell, and reduces surface reactivity.

Acknowledgements

This doctoral work represents the culmination of several years of research, learning, and personal growth, and it would not have been possible without the support and guidance of many individuals and institutions.

First and foremost, I would like to express my sincere gratitude to my supervisor, Prof. Liberato Manna, for his constant guidance, scientific insight, and encouragement throughout the course of my PhD. I am deeply thankful for the opportunity to work in his research group and for the stimulating scientific environment he fostered. His expertise, constructive criticism, and confidence in my ideas played a crucial role in shaping both this thesis and my development as an independent researcher. I am also sincerely grateful for the intellectual freedom provided during this work, which allowed me to explore new directions and develop original research approaches.

I would like to express my special thanks to my co-supervisor and mentor, Dr. Luca De Trizio, whose guidance, kindness, and constant availability made this PhD journey both smoother and more rewarding. He was always approachable and willing to discuss ideas, troubleshoot problems, and help me think critically about my results, which greatly improved my understanding and execution of the experiments. His deep expertise in nanocrystal chemistry, together with his ability to tackle scientific challenges from multiple perspectives, helped me build a strong foundation in this field. Beyond the laboratory, he also guided me through scientific communication and the publication process, teaching me how to write, structure, and refine manuscripts from the first draft to submission. Most importantly, his steady encouragement, optimism, and personal support during difficult periods were invaluable. Without his mentorship and support, this PhD journey would have been significantly more challenging.

I would like to thank all the scientists and collaborators who contributed to this work in various ways throughout my doctoral journey. I am grateful to Mirko Prato for his assistance with the XPS studies; Gabriele Saleh for his contributions to the theoretical calculations; and Giorgio Divitini and Rosaria Brescia for their support with high-resolution TEM and STEM analyses. I also thank Luca Goldoni for his significant help with the NMR measurements. I am grateful to the members of Quantum Solutions for their valuable support in developing the synthesis approaches. Finally, I would like to thank Enrico Bergamaschi for his help in synthesizing the reference standards used in the NMR experiments.

I would also like to thank the Nanochemistry technical staff, whose support greatly facilitated my day-to-day work in the laboratory. I am grateful to Gabriele La Rosa for his assistance with TGA analysis, Filippo Drago for his help with ICP measurements, and Francesco Di Donato and Simone Nitti for their invaluable support in the chemistry laboratories, especially in handling sensitive precursors. I also acknowledge Dorwal Marchelli for his assistance with optical measurements. I would like to extend my heartfelt gratitude to all the members of the Nanochemistry Laboratory for being an integral part of this journey.

I would also like to thank Iulia Manolache Orlatan and Simone Coralluzzo for their invaluable assistance with bureaucratic and administrative matters throughout my doctoral journey.

This journey would have been incomplete without the support of my friends and family, whose presence provided comfort, stability, and a sense of home throughout these years. I am sincerely grateful to Nikos, Clara, Ale, Alessandro, Martina, Anna, Hriday, Guncem, Ana, Zafer, Dongxu, Zheming, Zhanzhao, Sence, Ehsan, Jugal, Aswin, Manjunath, Aarya, Malavika, and Silvia for their friendship and for making everyday PhD life lighter and more enjoyable. I would like to express special thanks to my closest friends Hana, Mimi, Habib, Bharath, Bhargav, Mani, Arghya, Ashu, Vivek, MD, and Mukesh for always being there during difficult times, for listening, encouraging me, and helping me regain perspective when things felt overwhelming. Their companionship and support meant a great deal, and this journey would have been far more challenging without them.

I would like to express my deepest gratitude to my parents for their unconditional love, constant support, and countless sacrifices throughout my academic journey. Their belief in me and their encouragement at every stage provided the strength and motivation needed to persevere during challenging times. I am also sincerely thankful to my sibling for his support, understanding, and quiet encouragement, which helped me stay grounded throughout this journey. Above all, I would like to offer my heartfelt gratitude to Ganpati Bappa, from whom I have always drawn strength, resilience, and clarity to face the challenges encountered along this path. His presence and blessings were a constant source of motivation and inner strength.